THE ETHANOL OXIDATION REACTION AND PRODUCT DISTRIBUTIONS IN A DIRECT ETHANOL FUEL CELL

DAVID D. JAMES

The Ethanol Oxidation Reaction and Product Distributions in a Direct Ethanol Fuel Cell

by

David D. James

B.Sc. (Honours), Dalhousie University

Halifax, Nova Scotia 2008

A thesis submitted to the School of Graduate Studies in partial fulfillment of the requirements for the degree of

Doctor of Philosophy

Department of Chemistry

Memorial University

St. John's, Newfoundland

September 23rd, 2013

Abstract

A novel online system for quantifying product distributions of ethanol oxidation in direct ethanol fuel cells was developed. This system was shown to have many advantages over previously reported methodologies such as: ease of operation, quick response time, economical, and real time analysis. This system consisted of a non-dispersive infrared CO_2 detector coupled with a flow-through conductivity detector for CO_2 and acetic acid measurements, respectively. The third ethanol oxidation product, acetaldehyde, was shown to be accurately calculated using a Faradaic charge balance.

The effects of fuel and product crossover were closely examined. It was shown that the use of oxygen at the cathode can lead to an overestimation of ethanol oxidation products, mainly acetic acid, due to ethanol crossing through the membrane and reacting chemically with oxygen at the cathode. Furthermore, it was shown that significant amounts of acetaldehyde produced during ethanol oxidation were lost due to crossover, leading to an underestimation of its yield. To obtain more accurate product distributions, the fuel cell was operated using N_2/H_2 gas at the cathode (which eliminated the chemically oxidized ethanol reaction). To further improve the accuracy of product yields, a "crossover mode" approach to operating a fuel cell was examined. It was found that this method increased selectivity towards complete oxidation (carbon dioxide) by reducing poisoning of the electrode.

A kinetic and mechanistic study on the ethanol oxidation reaction was also carried out using an electrode stripping technique. It was found that applying a potential in the range where CO is oxidized, followed by allowing the cell to return to open circuit and then re-applying the potential led to significant increases in CO_2 yields. It was found that the CO_2 yield was dependent on the length of the pulse applied, the shorter the pulsing interval, the higher the yield. This suggests that the majority of the CO_2 produced was attributed to the oxidation of CO adsorbates. The time interval between pulses was also examined. It was found that the CO_2 yield was independent of the resting time, suggesting a rapid dissociation of ethanol on the electrode, which supports previous literature findings.

A Pt-$RuSnO_2$/C anode catalyst was developed and tested in our system. This catalyst was found to increase both the performance and the selectivity towards CO_2 in comparison to a Pt electrode, which is rarely reported in the literature.

Acknowledgements

I would first like to express my sincere gratitude to my supervisor Dr. Peter Pickup for the continuous support throughout my program. His patience, motivation, enthusiasm and immense knowledge had made my Ph.D an enjoyable and unforgettable experience. I could not have asked for a better advisor for my program.

I would like to thank my supervisory committee, Dr. Ray Poirier and Dr. Dave Thompson for the advice, support and time they have dedicated throughout my program. I want to thank all the faculty members of the chemistry department who sat on my comprehensive exam committee, examined my seminars and taught me courses throughout the years.

I acknowledge the support staff that have advised and trained me on the various instruments throughout Memorial University, especially the staff members of C-CART and the technicians working out of the Earth Science Department. I'd also like to thank the administration and physical science stores staff for all their help. I thank Dr. Guangchun Li for sharing his expertise with me and the Pickup group for all of their input and support towards my project.

I would like to extend my sincere gratitude to the funding agencies that made my program possible: School of Graduate Studies, the Chemistry Department, 3M Innovation

and the Natural Science and Engineering Research Council of Canada. A special thanks to NSERC for their generous funding through the Post Graduate Scholarship.

I would also like to thank all the friends I have made during my time in Newfoundland for their support and companionship. My deepest appreciation to my parents, who have taught me the value of hard work and determination which was needed to push me through my program. To my partner Leigh, I thank you for the love and support and for always lifting my spirits throughout the hard times.

Contents

List of Tables

List of Figures

List of Abbreviations

2, 4-DNPH	2, 4-Dinitrophenylhydrazine
AA	Acetic acid
AAEMFC	Alkaline anion exchange membrane fuel cell
AAL	Acetaldehyde
AC	Alternating current
AFC	Alkaline fuel cell
AOR	Alcohol oxidation reaction
CFP	Carbon fiber paper
CB	Carbon black
CO	Carbon monoxide
CO_2	Carbon dioxide
CV	Cyclic voltammetry
DAFC	Direct alcohol fuel cell
Dal	Dalhousie University
DC	Direct current
DEFC	Direct ethanol fuel cell
DEMS	Differential electrochemical mass spectrometry
DFAFC	Direct formic acid fuel cell
DFT	Density functional theory
DHE	Dynamic hydrogen electrode

DMFC	Direct methanol fuel cell
EDX	Energy dispersive x-ray microanalysis
EOR	Ethanol oxidation reaction
FAA	Flame atomic absorption
FTIR	Fourier transform infrared spectroscopy
GC	Gas chromatography
HFC	Hydrogen fuel cell
HPLC	High performance liquid chromatography
ICP-MS	Inductively coupled plasma mass spectroscopy
ICP-OES	Inductivity coupled plasma optical emission spectroscopy
M1	Method #1 for making Pt-RuSnO_2/C catalyst
M2	Method #2 for making Pt-RuSnO_2/C catalyst
MEA	Membrane electrode assembly
MOR	Methanol oxidation reaction
NDIR	Non-dispersive infrared
OCP	Open circuit potential
ORR	Oxygen reduction reaction
PEFC	Polymer electrolyte fuel cell
PEM	Proton exchange membrane
PEMFC	Proton exchange membrane fuel cell
PSA	Polystyrene sulfonic acid
RT	Room temperature

SCE	Saturated calomel electrode
SEM	Scanning electron microscopy
SHE	Standard hydrogen electrode
SPEFC	Solid polymer electrolyte fuel cell
TEM	Transmission electron microscopy
TGA	Thermogravitational analysis
XRD	X-ray diffraction

List of Symbols

A	Ampere
β	Rate of fuel consumption
B	Peak width at half height
C	Coulomb
ca.	Approximately
D	Mean particle diameter
D_E	Energy density
D_P	Power density
e^-	electron
E°	Standard potential
E	Potential
E_n	Energy
E_{rev}	Reversible cell potential
eV	Electron volt
F	Faraday constant
G	Gibb's energy
λ	Wavelength
h	Hour
i	Current

i_{lim}	Limiting current
i_o	Exchange current
I	Intensity
j	Current density
min	Minute
η	Overpotential
n	Electrons transferred in reaction
N	Moles of product
Θ	Diffraction angle
Ω	Ohm
ρ	Flow rate
ppm	Parts per million
Q	Charge
R	Gas constant
R_E	Electronic resistivity
s	Second
S	Siemens
ΔS	Entropy change
σ	Conductivity
τ	Efficiency
t	Time
T	Temperature

v	Volume
V	Voltage (volts)
W	Watts
X_{ads}	Species adsorbed on electrode surface

CHAPTER 1

Introduction

1.1 Introduction

With the slow depletion of fossil fuels, the search for new renewable energy sources has been an area of intense investigation. One area of focus that has been very attractive for many research groups is the development of fuel cell technology using hydrogen [1-4], methanol [5-10], ethanol [11-18], or formic acid [19, 20] as the primary fuel source. The conversion of chemical energy into electrical energy using fuel cells has been achieved and reported since the late 1830s [21]. The principles behind the fuel cell were first reported by German scientist Christian Schönbein in 1838, but a cell was not demonstrated experimentally until the following year [22]. Sir William Groove's serendipitous demonstration of the fuel cell in 1839 came from connecting the two electrodes of an electrolyzer together which were originally attached to a battery. He observed a consumption of hydrogen and oxygen, resulting in a reverse flowing current [21].

Due to the poor understanding of electrochemical theory, very little advancement in fuel cells was made until the 1950s. In 1959 Francis Bacon, working out of the department of chemical engineering at Cambridge University, constructed the first practical working fuel cell, using nickel based electrodes in an alkaline environment [23].

The first major commercial use of fuel cells dates back to the early 1960s with the use of solid polymer electrolyte fuel cells (SPEFCs – now known as polymer electrolyte fuel cells (PEFCs)) in the Gemini space missions [24, 25]. All space vehicles were equipped with these fuel cells which were used as auxiliary power sources; generating power for lighting, regulating gas pressures and producing drinking water aboard the space craft. These first generation fuel cells used hydrogen gas as the fuel and a polystyrene sulfonic

acid (PSA) proton exchange membrane that enabled high power densities [26]. However at the time, due to the extremely high cost of manufacturing and running these fuel cells their use was limited to space missions.

In the late 1960s, one of the biggest breakthroughs in PEFC technology was the development of a perfluorosulfonic acid membrane manufactured by Dupont, also known as Nafion® [27]. The high electronegativity of the side groups on the Nafion® membrane allowed for a two fold increase in proton conductivity compared to that of the PSA membrane. The increased conductivity of the membranes allowed for significant increases in both the power density and the cell efficiency [26, 28, 29]. The durability of the Nafion® membrane was exceptional, having a life time of about four orders of magnitude higher than that of the PSA membrane [30]. The exceptional durability of the Nafion® membrane sparked interest into the development of direct methanol fuel cells (DMFCs), direct ethanol fuel cells (DEFCs) and direct formic acid fuel cells (DFAFCs) in acid electrolytes.

Over the past couple of decades, fuel cell technology has progressed to the point of commercialization for many small portable applications [31-33] and also a few larger scale commercial products [34, 35]. Hydrogen fuel cells (HFC) have been at the top of the research ladder for almost all transportation manufacturers. Although there are currently no commercial HFC vehicles, there have been many prototype and demonstration vehicles produced from all the large vehicle manufacturers [36-38]. Ballard Power Systems, Toyota, Hydrogenics and a few other large scale fuel cell developers have introduced a three year HFC bus trial which is employed in many countries including: Cana-

da, US, Brazil, Germany, China and England [39, 40]. These HFC buses have been reported to be 39-141% more efficient for city driving compared to the diesel fuelled buses currently used [41]. Many wholesale and service companies including Sysco Foods, Federal Express Courier and Coca-Cola have taken advantage of the HFC technology by using forklifts powered by HFCs [42]. Other HFC vehicles recently manufactured include motorcycles, submarines, bicycles, boats and even airplanes.

DMFCs have been the most widely commercialized type of fuel cell [31, 32]. DMFCs are unable to produce large amounts of power, making them poor candidates for large machinery and vehicles. However, they do have the capability to store small amounts of energy over long time periods in small spaces [43]. This makes them ideal for small energy applications such as cell phones, laptops, cameras and in many military applications. In the mid 1990s, over 20,000 methanol "flex" vehicles were sold in the U.S. These vehicles had the capability to run on methanol or gas [44]. Due to high cost of methanol in the mid to late 1990s, the focus quickly shifted from methanol to ethanol as an alternative to gasoline. The commercialization of DEFCs could be considered lacking in comparison to HFCs and DMFCs. Few to none of the applications mentioned above have shown increased performance when replaced with DEFCs. However, due to the intrinsic advantages of ethanol as a fuel (see below), research and development into DEFCs has gained considerable attention.

Although hydrogen is the best candidate as a fuel for fuel cells from a weight energy density point of view (energy produced per mass of fuel = 33.3 kWh kg^{-1}), the danger and complications with the storage, transportation and use of hydrogen severely lim-

its its applications [45, 46]. The hydrogen fuel cell is the simplist of the fuel cells using H_2 at the anode and O_2 at the cathode, producing H_2O exclusively as a product and providing four electrons per mole of O_2 consumed. With water as the only reaction product, the kinetics at the anode are extremely facile leading to very high cell performances. Furthermore, since CO_2 is not a by-product of HFC devices, they are a "zero-emission" (no carbon footprint) energy source, making them ideal from an environmental point of view [23].

Methanol and ethanol on the other hand are liquid at room temperature, making the transportation and storage of the fuel safe and easy. The availability of both methanol and ethanol also make them very attractive, as heavy reformers (a device that extracts a desired product from a larger product) are not needed as is the case for hydrogen production. The energy densities for methanol and ethanol are 8.01 and 6.09 kWh kg^{-1} respectively [47, 48]. Although these alcohols use very similar components to the hydrogen fuel cell (anode, cathode and membrane), their performances are significantly lower due to intermediates adsorbed on the anode during oxidation [49,50].

The commercial production of methanol involves the reaction of carbon monoxide and H_2 gas. During the major coal mining days, synthetic gas was produced from the reaction of methane (which was a product of coal mining) with water in a process called steam methane reforming. The H_2 gas was then reacted with CO over a nickel, zinc oxide or alumina catalyst to produce methanol. Presently, methanol can be produced via three different methods; steam methane reforming, direct catalytic conversion of methane using Cu-zeolites or electrochemically from CO_2 using CuO or CuO_2 catalysts.

Methanol has been reported to have a much more simple reaction mechanism than that of ethanol in a fuel cell [51, 52]. In methanol oxidation, intermediates form at the anode and oxygen containing species are needed to oxidize these to CO_2. To produce the oxygen containing species, O_2 must be reduced at the cathode. This oxygen reduction reaction (ORR) is the rate determining step, and is extremely slow on the Pt cathode that is used in the hydrogen fuel cell. Although the thermodynamic reversible potential of ORR for MeOH is comparable to that of H_2 at the cathode (1.214 V and 1.23 V vs. SHE respectively), the methanol oxidation reaction (MOR) occurs at a much higher potential on the Pt cathode [53]. Due to the slow kinetics of the MOR, the Pt anode gets quickly covered with CO intermediates, limiting the available adsorption sites for oxygen containing species, hence, the oxidation to CO_2 [6,54,55]. This "poisoning" of the anode is the primary reason for the sluggish kinetics of DMFCs. Recent studies have shown that alloying Pt with a secondary metal (primarily Ru) has the ability to decrease the CO poisoning at the electrode, leading to significant increases in MeOH oxidation kinetics [eg. 51,56-58]. MeOH crossing through the membrane has also caused many problems with DMFCs. At all concentrations, MeOH has been shown to cross through the proton exchange membrane (PEM) from the anode to the cathode [59]. This causes a mixed potential at the cathode leading to a significant decrease in potential at the cathode and hence a decrease in overall cell performance.

Ethanol can be produced both naturally and synthetically. The majority of ethanol that is used in alcoholic beverages and as a fuel is produced naturally by the fermentation of sugars. This fermentation process involves yeast metabolizing sugar under certain

thermal conditions producing ethanol and CO_2. Ethanol used as a chemical solvent is typically made synthetically. This process is an acid-catalyzed hydration reaction involving ethylene and water producing ethanol exclusively.

Ethanol has been the focus of many research groups due to its ability to be produced in large quantities from the fermentation of biomass. This green, renewable fuel also has advantages over methanol in that it is non-toxic, and has a higher boiling point and higher energy density [60, 61, 62]. However, the ethanol oxidation reaction (EOR) in DEFCs follow an extremely complex mechanism involving many intermediate steps and pathways and is not fully understood [63-65]. Unlike methanol, ethanol contains a C-C bond that must be broken in order for it to be fully oxidized into CO_2. This complete process requires the transfer of 12 electrons for two moles of ethanol consumed. However many groups including our own have reported only partial oxidation into acetaldehyde (requiring a two electron transfer) and acetic acid (requiring a four electron transfer), making the EOR extremely inefficient [66-69]. Along with the problem of the C-C bond cleavage, similar barriers to those for MeOH oxidation are also present. CO poisoning of the electrode has been reported for EOR [14, 55, 70] and crossover of ethanol from anode to cathode causing a mixed potential [71, 72] has also been observed. These problems along with recent advances to their solutions and future objectives are all discussed in this work.

1.2. Types of Fuel Cells

1.2.1. Fuel Cell Composition

A fuel cell is a device that directly converts chemical energy into electrical energy by feeding the cell with an external fuel. Its main components are an anode, a cathode and an electrolyte membrane. The schematic in Figure 1.1 illustrates a typical fuel cell design. The fuel cell hardware consists of two metal support blocks with etched flow fields. The anode and cathode catalysts are designed with the exact dimensions of the flow field to minimize catalyst material. In most cases, polymer based gaskets are placed around the catalyst to limit the fuel and/or cathode gas from leaching out of the flow fields. At the anode plate, the fuel is passed directly through the plate to the flow field. The cathode gas also flows directly to the flow field. The metal plate supports must be non-reactive with the fuel and oxidant in order to optimize fuel cell reactions. Between the anode and cathode catalyst layers, there is an electrolyte membrane. With the help of the membrane, the fuel and oxidant gas are able to react and the oxidation products exit via the anode effluent stream. The electrons released from the fuel, pass through an external circuit (see Figure 1.2) from the anode to cathode and protons are transferred through the cell membrane to the cathode. At the cathode, oxygen gas accepts the transferred electrons and protons provided from the fuel and is converted to H_2O. Depending on the fuel used, the number of electrons that are transferred and the reaction products are varied. The proton exchange membranes (PEM) used in most fuel cells and in all of the work in this project,

are Nafion® membranes (see ref. [28-30]). These membranes aid in the transfer of protons from the anode to the cathode.

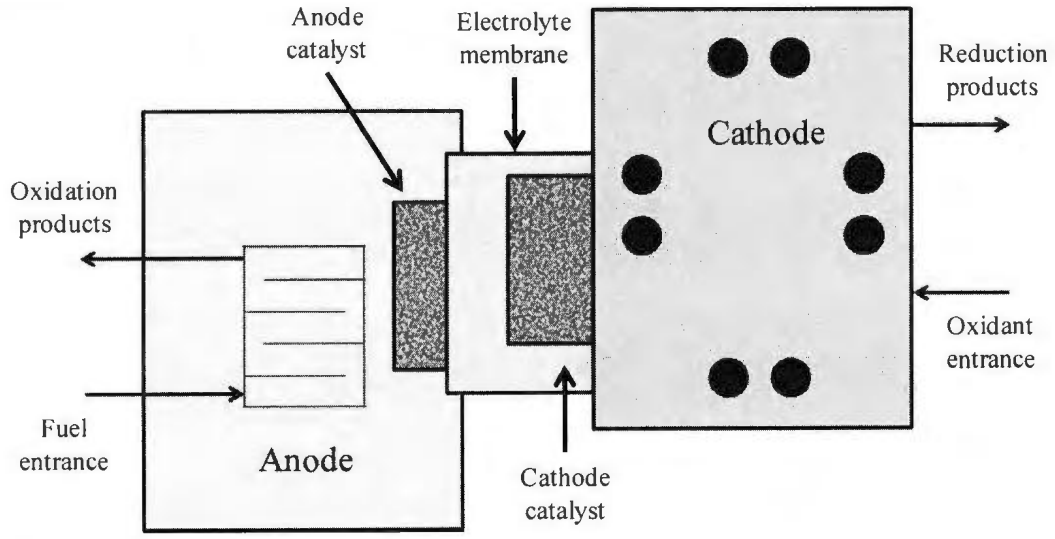

Figure 1.1: Schematic of a typical single cell solid electrolyte fuel cell composition.

The fuel cell has many similarities to a primary battery. The main distinguishing feature is that a fuel cell uses a continuous flow of both fuel and oxidant, making them long lasting devices. Batteries are considered energy storage devices, as they enclose the fuel and oxidant inside the casing. The lifetime and maximum amount of energy produced from a battery depends on the amount of active material stored and the rate at which it is consumed. Once all the chemical reactants have reacted, the battery can no longer produce energy, and is useless. There also exist secondary batteries which use external electricity to replenish the electro active-materials. A fuel cell could be considered a long lasting primary battery if the fuel container is included.

1.2.2. Proton Exchange Membrane Fuel Cells (PEMFC)

PEMFC (also referred to above as PEFC) are a type of fuel cell that relies on the use of a solid thin layer membrane to shuttle protons from the anode to the cathode. They are ideal for use in low to moderate temperature environments (usually up to 100 °C).The most distinguishing part of a PEMFC is the membrane electrode assembly (MEA). As shown in Figure 1.2, the MEA consists of a cathode, a proton exchange membrane and an anode. The thin membrane is sandwiched between the anode and cathode and the assembly is usually hot-pressed together. The anode and cathode typically use carbon fiber paper as a support, but glassy carbon and carbon cloth have also been used. The anode and cathode catalyst layers are usually comprised of a Pt-carbon mix or Pt-based alloyed Pt-metal-carbon mix.

Acting as probably the most important part of a PEMFC, the proton exchange membrane serves as both a proton conductor and the barrier separating the fuel and oxygen gas. Since Dupont's breakthrough with the Nafion® class of membranes, a significant amount of research has been conducted in an attempt to optimize the characteristics and cost of the membrane [73, 74].

The essential characteristic of a proton exchange membrane is the ability to conduct protons without conducting electrons (which would short-out the fuel cell). The membrane should be equipped with many proton conducting side groups and a very stable backbone which can withstand heat, the fuel and most importantly the harsh oxidative environment at the cathode [26, 75]. The membrane must also be resistant to fuel and gas crossover, as any leakage in the membrane would result in reduced efficiency. A low resistance to H^+ migration must also be present in the membrane. However, a low re-

sistance could also lead to hydrodynamic drag of H_2O and possibly ethanol from the anode to the cathode, leading to an increase in fuel crossover. Dupont

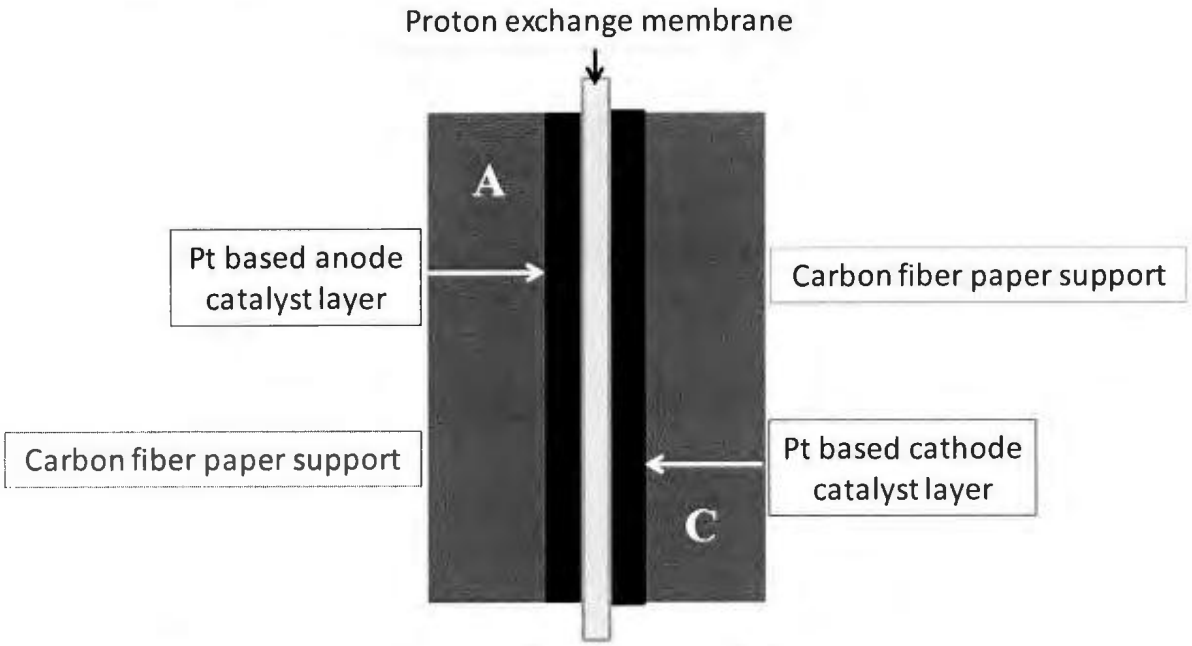

Figure 1.2: A schematic diagram of a typical MEA for a PEMFC.

successfully constructed membranes that fulfill all of the above criteria with the development of the Nafion® polymers shown in Figure 1.3.

As shown in the chemical structure, Nafion® was developed by the polymerization of a perfluoranated vinyl ether and tetrafluroethylene monomer [26]. These polymers are usually derived from the $-SO_2F$ precursor which is reacted with KOH in water and then soaked into acid to form the active side chain $-SO_3^-H^+$. With this very active side chain, the Nafion® membrane acts as a superacid, with the ability to conduct protons from the anode and transfer them to the cathode with ease [26].

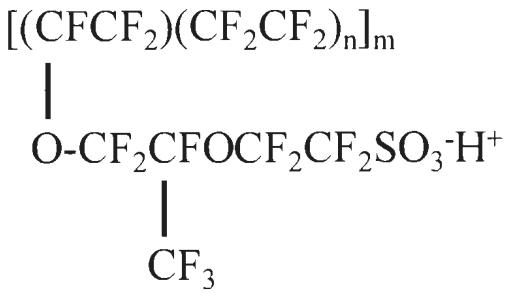

Figure 1.3: Chemical composition of the Nafion® membrane developed by Dupont [26].

Almost all anode catalysts for PEMFC-HFC are Pt (or Pt based alloys). The ability of Pt to oxidize H_2 into H^+, shown in equations 1.1 and 1.2, makes it ideal for providing electrons and protons to the cathode half-reaction.

$$2Pt + H_2 \rightarrow 2Pt - H_{ads} \tag{1.1}$$

$$Pt - H_{ads} \rightarrow Pt + H^+ + e^- \tag{1.2}$$

In HFCs, this is the only reaction that take place at the anode. This reaction takes place spontaneously on the Pt electrode, making it extremely efficient. A few minor problems that can lead to inefficiencies in the anode half-reaction of HFC are small amount of CO poisoning and dehydration of the anode. It has been reported that during the reforming process (production of H_2) small amount of CO are produced [76]. Even at very low concentrations, CO has the ability to compete for adsorption sites on the Pt anode, causing a decrease in available sites for H_{ads}, leading to inefficiencies in the cell [53].

Until recent years, Pt and Pt based catalysts have been strictly used in the oxygen reduction reaction (ORR) at the cathode. This half-reaction involves O_2 being reduced in

the presence of protons and electrons transferred from the anode to produce H_2O. The reaction mechanism for the ORR has been extensively researched on many different Pt surfaces [77,78]. Various mechanistic pathways have been identified for the ORR reaction, including a direct four electron transfer and a multi step transfer of four electrons [53, 79]. The mechanism for this complex reaction is still not fully understood, as theoretical studies have shown many different intermediate and radical formations prior to the final products [80]. A simplified schematic of the possible pathways is depicted in Figure 1.4. The O_2 at the cathode is first adsorbed onto the Pt surface with breakage of the double bond. Once the oxygen is adsorbed on the Pt surface, the reaction will take one of two accepted pathways. The desirable pathway, for a PEMFC, occurring at 1.23 V is a direct four electron-four proton transfer to H_2O. The second possible pathway occurring at a much lower thermodynamic electrode potential (0.70 V) is a two electron-two proton transfer to produce adsorbed H_2O_2. This mechanism is the preferred mechanism of the ORR in industry for the production of H_2O_2. From this step, the adsorbed hydrogen peroxide can take one of two paths. At high potentials of around 1.76 V, a second two electron-two proton reaction can take place to produced H_2O. The other possible pathway is the desorption at the electrode, forming H_2O_2 as a final product. Studies suggest that the desorption product is not likely in PEMFC since only small amounts of H_2O_2 were found in the ORR product analysis and the electron transfer number has been reported to be close to 4. Equations 1.3-1.5 summarize the direct and indirect pathways of O_2 reduction to and H_2O and H_2O_2, respectively. Equations 1.4 and 1.5 are coupled together to form the indirect pathway [53].

$$O_2 + 4H^+ + 4e^- \rightarrow 2H_2O \quad (1.3)$$

$$O_2 + 2H^+ + 2e^- \rightarrow H_2O_2 \quad (1.4)$$

$$H_2O_2 + 2H^+ + 2e^- \rightarrow 2H_2O \quad (1.5)$$

Comparing the complexity and potentials needed of the oxidation and reduction reactions, it is clear that the ORR is the rate determining step in HFC reactions.

The high cost of Pt metal coupled with the large overpotential required for reduction at the cathode have attributed to the limitation of fuel cells for many applications. Over the past decade, many research groups have devoted ample time into the development of new "low-Pt" [81-83] and "Pt-free" [84-86] cathode catalysts for ORR. These catalysts have shown fairly good activity towards ORR in the absence of ethanol. However, when ethanol was introduced, large increases in overpotential were observed. At the moment, the low ethanol tolerance coupled with significant decreases in performance (compared to Pt) have made these catalysts unsuitable for ORR in DEFCs.

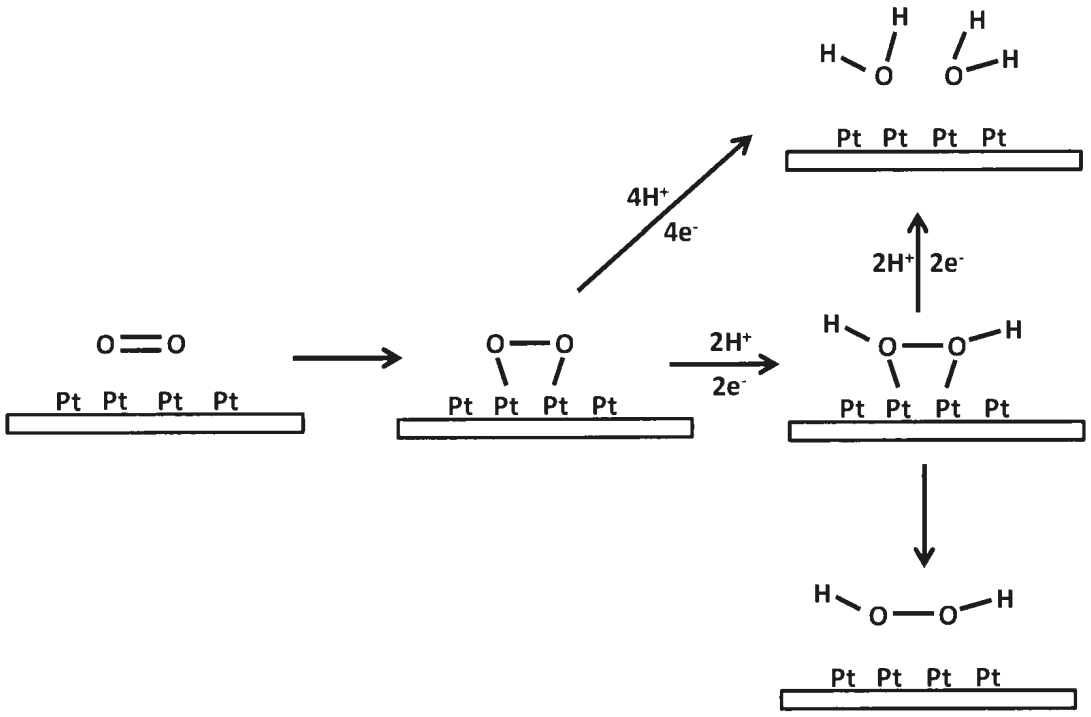

Figure 1.4: Mechanistic scheme of the oxidation reduction reaction occurring at a Pt cathode catalyst in an acidic environment (adapted from [53]).

1.2.3. Direct Alcohol Fuel Cell (DAFC)

DAFCs work in a very similar manner to that of the HFC, with the exception of small alcohols as the fuel at the anode instead of H_2. The components of DAFCs are the same as in HFCs with an anode, cathode and proton exchange membrane. Many different anode and cathode catalysts have been developed in attempts to optimize DAFCs efficiencies. As mentioned earlier, the inefficiencies of DAFCs arise from three main problems: large overpotentials at the cathode, the crossover of fuel from anode to cathode, and the

large overpotentials for the alcohol oxidation reaction (AOR) resulting from adsorbed intermediates. These problems will be further investigated in the subsections of this work.

1.2.3.1. Direct Methanol Fuel Cell (DMFC)

DMFCs use the simplest alcohol, methanol, as the fuel which is continually pumped to the anode of the fuel cell. Methanol reacts at the anode in the presence of water to produce CO_2, 6 protons and 6 electrons. The overall half-reaction at the anode is described as:

$$CH_3OH + H_2O \rightarrow CO_2 + 6H^+ + 6e^- \quad (1.6)$$

Unlike the hydrogen oxidation reaction (equations 1.1 and 1.2), methanol forms carbon based intermediates at the anode. These intermediates significantly lower the reaction rate at the anode as they need oxygen containing species, to be fully oxidized to CO_2. It cannot be determined for certain the exact mechanism that takes place in this reaction but the most accepted mechanism based on electrochemical theory is described by equations 1.7 and 1.8 [6].

$$Pt + H_2O \rightarrow Pt - OH + H^+ + e^- \quad (1.7)$$

$$Pt - CO + Pt - OH \rightarrow 2Pt + CO_2 + H^+ + e^- \quad (1.8)$$

During MOR, CO is strongly adsorbed onto the Pt anode surface. The removal of the CO involves the oxidation of water into surface bound hydroxyl radicals which then react with the CO to form CO_2. The major problem with the anode reaction is the large CO coverage on the anode surface. Due to very strong interactions between the CO and the Pt

electrode, the anode surface is easily and quickly covered with CO. This poisons the surface, leaving limited Pt adsorption sites to oxidize the water, leading to very slow overall oxidation kinetics at the anode surface [51, 56-58].

The reduction of oxygen at the cathode is very similar to that of HFCs (equations 1.3-1.5). As mentioned in section 1.1, the major problem in DMFCs arises from fuel crossover. Even at low concentrations, methanol can easily cross through the PEM. As its concentration increases, the rate of methanol flux through the membrane is significantly increased. Furthermore, when the temperature of the DMFC increases, the flux increases significantly [59]. When the methanol crosses from the anode to the cathode, it can be rapidly consumed by oxygen. This not only wastes fuel but also leads to a "mixed potential" at the cathode resulting in a significant decrease in reduction potential for O_2 and a decrease in overall cell performance. Although the mechanism for the oxidation of methanol (and ethanol) is fairly uncertain at the cathode, the reduction of the cell potential is indicative of the oxidation taking place. Furthermore, since low fuel concentrations and temperatures are needed to limit the effects of crossover, the overall number of electrons transferred and the kinetics of the overall reaction are decreased, hence reducing the maximum current.

1.2.3.2. Direct Ethanol Fuel Cell (DEFC)

All experimental results in this work use DEFCs, and these from here on out will be the focus of this report. DEFCs use the second smallest molar mass alcohol, ethanol, as the fuel at the anode and O_2 normally in air at the cathode as the oxidant. Since ethanol is a larger molecule than methanol, more electrons need to be transferred to fully oxidize it to

CO_2. This results in a much more complex mechanism for complete oxidation. Ethanol oxidation is very sensitive to many different parameters including fuel concentration, cell temperature, catalyst composition and cell potential [eg. 11, 14, 47-52]. The ideal complete EOR reaction in a DEFC is as follows:

$$CH_3CH_2OH + 3O_2 \rightarrow 2CO_2 + 3H_2O \tag{1.9}$$

The complexity of the EOR reaction occurs in the anode half-reaction. As ethanol is pumped through the anode compartment and reaches the electrode, many different adsorbed intermediates can form on the electrode surface. Depending on the cell potential, various suggested pathways have been reported. In the lower potential region, it has been reported that the major EOR product is acetaldehyde, which is produced by the following mechanism [87]:

$$Pt + CH_3CH_2OH \rightarrow Pt-(CH_3CH_2OH)_{ads} \tag{1.10}$$

$$Pt-(CH_3CH_2OH)_{ads} \rightarrow Pt-(CH_3CHOH)_{ads} + H^+ + e^- \tag{1.11}$$

$$Pt-(CH_3CHOH)_{ads} \rightarrow Pt-(CH_3CHO)_{ads} + H^+ + e^- \tag{1.12}$$

After EtOH is adsorbed, it undergoes a dehydrogenation reaction releasing an electron. Following this dehydrogenation step, the adsorbed ethanol radical releases a second electron, producing adsorbed acetaldehyde. The acetaldehyde is then desorbed from the surface producing the major product. The overall net half-reaction at low potentials for the major product is as follows:

$$CH_3CH_2OH \rightarrow CH_3CHO + 2H^+ + 2e^- \qquad (1.13)$$

As shown in this equation, the dissociation of water is not necessary to product acetaldehyde. Furthermore, it would not be expected to see any oxidation of water (hydroxyl adsorption) at the anode at low potential, since the dissociation of water occurs at high potentials. This partial oxidation of ethanol at low potentials severely decreases the efficiency of the fuel cell since only 2 of a possible 12 electrons are transferred, limiting the energy output.

In the high potential region, the ethanol oxidation reaction takes a completely different pathway [88]. With the dissociation of water molecules (into hydroxyl adsorbates), the oxygenated species are able to react with adsorbed ethanol to produce a reaction transferring more electrons. At the Pt surface, ethanol undergoes the same reaction as shown in equations 1.10 and 1.11 forming an adsorbed acetaldehyde intermediate. The water from the diluted ethanol fuel undergoes a dehydrogenation reaction forming hydroxyl species that are able to adsorb on the electrode. The acetaldehyde and hydroxyl adsorbates are then able to react to form the more oxygen rich species, acetic acid (equation 1.14).

$$Pt-(CH_3CHO)_{ads} + Pt-(OH)_{ads} \rightarrow Pt + CH_3COOH + H^+ + e^- \qquad (1.14)$$

The two electron transfer from the adsorbed acetaldehyde molecule coupled with a single electron transfer from the dissociation of water and a single electron transfer from equation 1.14 make the partial oxidation of ethanol to acetic acid a 4 electron transfer. The

overall reaction for EOR at high potential is represented by equation 1.15. Once again at high potential, the EOR reaction is significantly less efficient than the complete

$$CH_3CH_2OH + H_2O \rightarrow CH_3CO_2H + 4H^+ + 4e^- \quad (1.15)$$

oxidation, since only a third of the possible electrons are transferred. A second, less likely reaction can also occur in the high potential region. This is the complete oxidation to CO_2 which involves the transfer of 12 electrons (equation 1.16). The selectivity for this reaction is very low as the acetic acid pathway is dominant. For this reaction to take place, the C-C bond must be broken. Many theoretical studies into the direct and indirect pathways of complete oxidation of ethanol into CO_2 have been reported and are discussed in upcoming sections. The complete oxidation into CO_2 at the anode can be described as follows:

$$CH_3CH_2OH + 3H_2O \rightarrow 2CO_2 + 12H^+ + 12e^- \quad (1.16)$$

The reaction at the cathode is similar to both HFCs and DMFCs. The oxygen pumped through the cathode compartment accepts the electrons and protons produced at the anode and is reduced to water. Depending on which pathway the anode reaction takes will determine the amount of water produced at the cathode. As shown by the various pathways, the EOR mechanism at the anode is very complex, and multiple pathways resulting in multiple by-products for PEM cells are reported [63-65].

1.2.4. Alkaline Anion Exchange Membrane Fuel Cell (AAEMFC)

Another type of fuel cell that has recently gathered significant research interest for EOR are AAEMFCs. Some of the first fuel cells invented were alkaline fuel cells (AFC), such

as the cells used in the mid 1960s Apollo space missions [89]. These fuel cells used a liquid electrolyte (usually KOH). The research into these types of fuel cells quickly decreased as it was found that carbonates precipitated on the anode catalyst layer which was quickly deactivated [90]. With the development of solid anion exchange electrolytes, this problem was solved. This type of fuel cell uses a solid electrolyte membrane similar to PEMFCs to shuttle ions from one side of the fuel cell to the other. The oxidation of ethanol in the alkaline membrane cell involves hydroxyl ions that are produced from the cathode (equation 1.17) that migrate through the membrane to the anode. At the anode the ethanol reacts with the OH^- and is oxidized to CO_2 (equation 1.18).

$$3O_2 + 6H_2O + 12e^- \rightarrow 12OH^- \quad (1.17)$$

$$CH_3CH_2OH + 12OH^- \rightarrow 2CO_2 + 9H_2O + 12e^- \quad (1.18)$$

This process is depicted in Figure 1.5. The primary advantage over PEMFC is the ability to use Pt-free catalysts in the EOR. Although the complete oxidation to CO_2 has not been observed on Pt-free catalysts in alkaline media, the formation of by-products (acetaldehyde and acetic acid) has been. Furthermore, the major product produced in AAEMFC for EOR is acetate and the average number of electrons transferred is ~8; which is significantly higher than for the EOR in PEMFCs. Another possible advantage that alkaline media have over acidic media is the low overpotentials at which the ORR can occur on Pt [53, 91]. In alkaline media on a Pt catalyst, the direct 4 electron ORR (equation 1.3) occurs at a potential of 0.401 V, which is significantly lower than ORR in acidic media

(1.229 V). Consequently, alkaline media is not favored for the EOR, leading to an increase in overpotential at the anode, and no significant increase in cell potential.

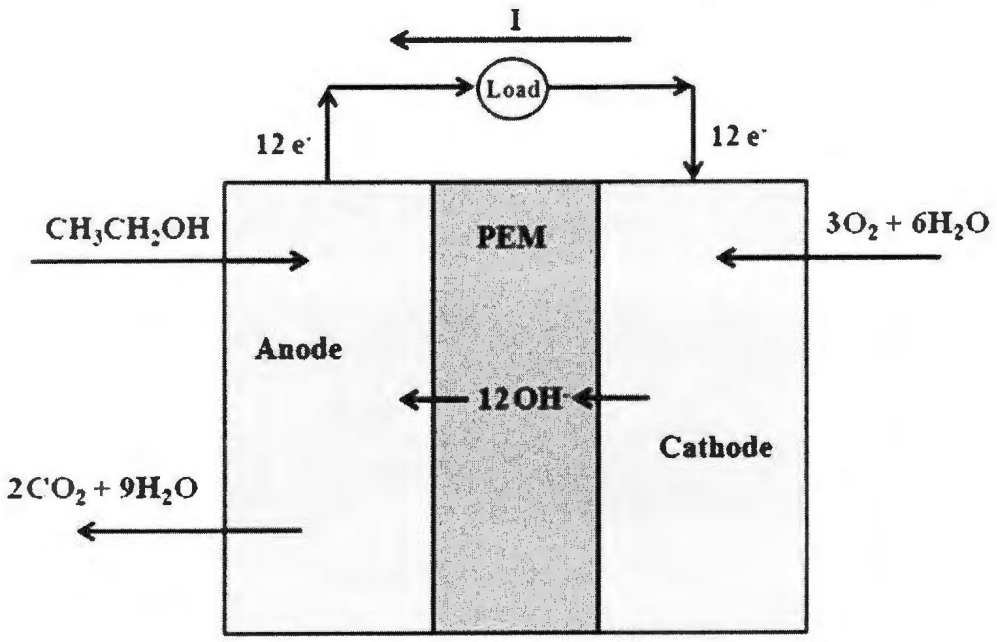

Figure 1.5. A Schematic of an AAEMFC for ethanol oxidation.

The less corrosive environment and the decrease in fuel crossover (due to the opposite direction of ion migration through the membrane) also add to the advantageous properties of AAEMFCs. The main disadvantage of AAEMFCs is the conductivity of the exchange membrane. Since the diffusion coefficient of H^+ is ca. twice that of OH^-, twice the amount of OH^- ions must be present to obtain similar results to PEMFCs [92]. This leads to a very basic environment (pH > 14) at the cathode and the MEA can easily be damaged. Many research groups have reported significant advancements in AAEMFC for EOR, but this is not discussed further as it is beyond the scope of this work.

1.3. Fuel Cell Theory

For the proceeding chapters, it is important for readers to have a general understanding of: the electrochemistry behind the fuel cell reactions, the definition of terms used, and the concept of faradaic processes.

1.3.1. Fuel Cell Performance

Understanding the basic thermodynamics of a fuel cell is very important when describing its "performance". To understand performance in a fuel cell, some terminology and definitions must first be introduced. The theory described in this subsection is all obtained from [93].

During the fuel cell process, electrons flow from the anode, through a load, to the cathode. This results in a current flowing opposite of the electron flow and a difference of potential from cathode to anode. The potential difference in the cell is one of the most important parameters when describing the behavior of the cell. When the cell is operating at the most thermodynamically reversible conditions, the potential difference between electrodes is called the "reversible cell potential" (E_{rev}). The E_{rev} is the highest possible cell potential a fuel cell can obtain. When analyzing thermodynamic properties such as enthalpy, entropy and Gibb's energy, equations can be derived to see the temperature, pressure and concentration dependence of E_{rev}. The derived formula for E_{rev} is as follows:

$$E_{rev}(T,P) = -\frac{\Delta G(T,P)}{nF} \tag{1.19}$$

Taking the derivative of the Gibb's function with respect to temperature, while leaving the pressure constant, results in the following:

$$\left(\frac{\partial \Delta G}{\partial T}\right)_p = -\Delta S \tag{1.20}$$

Substituting 1.19 into 1.20 gives:

$$\left(\frac{\partial E_{rev}\ (T,P)}{\partial T}\right)_p = \frac{\Delta S}{nF} \tag{1.21}$$

Based on equation 1.21, it is shown that the effect of the temperature will depend on the entropy of the reaction in the fuel cell. When the $\Delta S > 0$, the reversible cell potential will increase with increasing temperature. When the $\Delta S < 0$, the reversible cell potential will decrease with increasing temperature. When the system has $\Delta S = 0$, the reversible cell potential is not dependent on the temperature.

When the Gibb's function is differentiated with respect to the pressure, leaving the temperature constant, the following formula is derived:

$$\left(\frac{\partial G}{\partial P}\right)_T = \Delta v \tag{1.22}$$

where Δv is the change in volume between the products and reactants in the fuel cell reaction. Substituting equation 1.19 into 1.22, the following equation is derived:

$$\left(\frac{\partial E_{rev}}{\partial P}\right)_T = -\frac{\Delta v}{nF} \tag{1.23}$$

Based on this equation, it is clear that the reversible cell potential is dependent on the volumes of the products and reactants in the fuel cell equation. Rearranging the ideal gas equation for volume (equation 1.24), it is shown that the E_{rev} is dependent on the change in the number of moles of gas from products to reactants.

$$\Delta v = \Delta nRT/P \tag{1.24}$$

This being said, when the pressure is increased or decreased in the fuel cell, the change in E_{rev} is completely dependent on which side of the equation has the largest number of gas molecules. When $\Delta n > 0$, the E_{rev} will decrease with pressure. When $\Delta n < 0$, the E_{rev} will increase with pressure. Mostly all reactions in fuel cells will follow $\Delta n < 0$, as is the case with the hydrogen fuel cell $\left(H_{2(g)} + \frac{1}{2}O_{2(g)} \rightarrow H_2O_{(g)}\right)$. When $\Delta n = 0$ any change in pressure will not affect the system.

One major problem in fuel cells, particularly in ethanol fuel cells, is that the redox reactions are often not reversible. Such irreversible reactions lead to significant decreases in cell potential. The open circuit potential (OCP) is the potential difference observed between electrodes when no current is flowing in the cell. Once electrons start to migrate from the anode to the cathode, a current is produced and a decrease in the cell potential is observed. The difference in cell potential from the reversible cell potential is called the overpotential (η). As current density increases and the cell potential decreases (becoming further away from the reversible potential) the overpotential of the cell increases. The overpotential is reported to be a result of three separate issues in the fuel cell.

The best way to examine the performance of a fuel cell is by analyzing a polarization curve. The polarization curve is a plot of actual cell voltage (V) against the current density (j). Figure 1.6 illustrates a typical polarization curve for a DEFC. The straight line at the top represents the reversible cell potential. As shown, the zero current output potential (OCP) is significantly lower than the reversible cell potential. This drop in cell potential is due to parasitic processes that are not completely understood but are most likely a consequence of fuel crossover. As the current density is increased and the reaction proceeds, it can be seen that the cell potential drops until it reaches zero. The resulting current density when the potential is depleted is known as the "limiting current".

As shown in Figure 1.6, the polarization curve can be divided into three sections. These sections can be classified based on the main cause of the increased overpotential in each potential region. The first region of the polarization curve occurring at low overpotentials is often called the activation polarization (η_{act}) region and is shown to have a steep decrease in potential. The activation polarization occurs from the slow kinetics of the reactions occurring at the anode and cathode. Cell potential is quickly lost in this first region as energy is consumed to increase the rate of the electrochemical reactions to satisfy the current demand. The second region is often called the Ohmic polarization (η_{ohm}) region. This middle section of the polarization curve illustrates an almost linear relationship between the cell potential and the current density. This overpotential is caused by two factors. The first is the resistance to proton conduction through the electrolyte membrane. The second is caused from the resistance to electron flow in the electrodes, flow plates, and connectors. The third section of the polarization curve is known as the con-

centration polarization (η_{conc}) region. This overpotential arises from slow mass transfer of reactants to the electrode surfaces and to a lesser extent a build up of products at the active sites. In this high overpotential region, there is a significant imbalance of reactant and products at the active sites. To account for the quick depletion of reactants and to satisfy the high current output demand, the cell potential rapidly decreases until it reaches zero (limiting current).

The performance of a fuel cell is more of a comparative tool for fuel cell analysis. The cell voltage at a given current density or vice versa in a polarization curve is usually compared between various fuel cell experiments to determine which has the best performance. At a given current density, the fuel cell that exhibits the highest cell potential is said to have the best performance. Another characteristic often observed is the limiting current in a cell; the higher the limiting current, the better the performance of the fuel cell.

1.3.2. Fuel Cell Efficiencies

The overall efficiency of a fuel cell is another very important characteristic to examine when determining the overall quality of a fuel cell. There are efficiencies that must be taken into consideration when analyzing the overall efficiency of a fuel cell, such as voltage efficiency, current efficiency, reversible efficiency, Gibbs energy conversion efficiency, fuel cell system efficiency and auxiliary efficiency. For conciseness of this report, only voltage and current efficiencies are discussed.

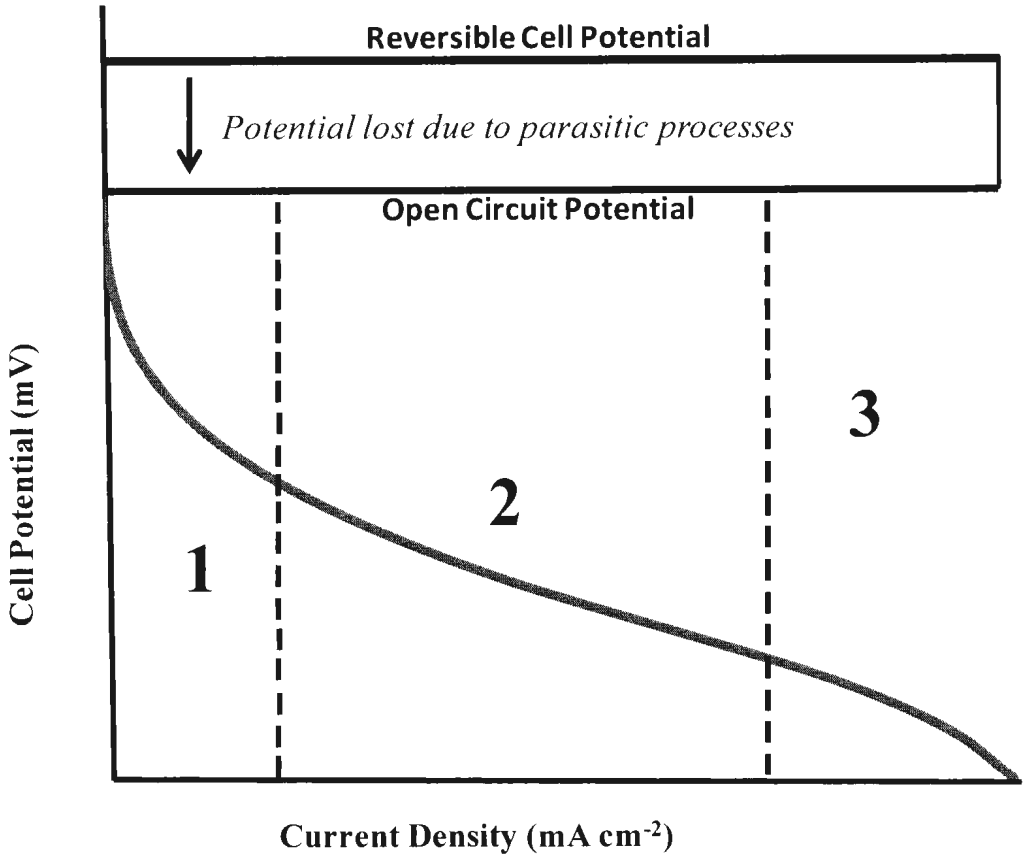

Figure 1.6: A typical polarization curve for a fuel cell. Regions: 1. Activation polarization. 2. Ohmic polarization. 3. Concentration polarization (Adapted from [93]).

Based on the fundamental relationship between voltage across two electrodes (V) and energy dissipated (E_n) as shown in equation 1.25 (where Q is the charge), the voltage efficiency is essentially a specific form of energy efficiency. As mentioned in the

$$V = \frac{E_n}{Q} \tag{1.25}$$

preceding section, the actual cell potential (E) is lower than the reversible cell potential (E_{rev}) due to the overpotentials. The ratio between E and E_{rev} is known as the voltage efficiency (τ_E) and is always less than one. The voltage efficiency describes how far away the cell potential is from the idealized cell potential at any given current density.

The current efficiency (τ_I) in a fuel cell is a relationship between current produced and amount of fuel that is consumed by the fuel cell. This measurement is based on Faraday's law and is described by the following equation:

$$\tau_I = \frac{I}{nF\beta} \tag{1.26}$$

where n is the theoretical number of electrons transferred, F is Faraday's constant and β is the rate of fuel consumption in the fuel cell. This efficiency measure is very important in DEFCs since one of the major problems is incomplete oxidation to CO_2. This causes the n value to vary depending on the anode products produced ($n_{AA} = 4$, $n_{AAL} = 2$, $n_{CO_2} = 12$), where acetic acid (AA) and acetaldehyde (AAL) are the dominant products in the EOR. The experimental n values are much lower than 12, resulting in low currents and a severe decrease in current efficiencies. The efficiencies described in the rest of this work are current inefficiency unless otherwise stated.

1.3.3. Energy and Power Density

Energy and power density are two very important parameters when describing a fuel cell. Energy density is defined as the amount of energy stored in a given system per unit volume or mass and can be represented by:

$$D_E = \frac{E_n}{V} \tag{1.27}$$

This parameter is very useful when describing and comparing various fuels. Table 1.1 summarizes the energy densities of some common fuels used today. Since the volume of a gas is much greater than that of a liquid, it is shown that for all of the gaseous fuels in the table, the energy density is very low in comparison to the liquid fuels. For the liquid fuels, as the molar mass is increased, the ability of the fuel to store energy also increases, increasing the energy density.

For fuel cell applications, an alternate energy density definition is often used. It is described as the amount of energy stored in a given system per unit mass. Comparing the energy density of hydrogen by unit volume and unit mass, H_2 ranks from one of the worst to the very best. This is due to the very low mass of hydrogen. This extremely high energy to mass ratio of hydrogen has been the primary reason for hydrogen becoming the most attractive fuel in the fuel cell community. However, the poor energy to volume ratio of hydrogen shows the inefficiency of the fuel when looking at storage and delivery of fuel to the cell.

Table 1.1: Energy densities per volume and per mass for many popular fuels used in combustion engines and fuel cells [Apadter from 94].

Fuel	Energy Density (kW h L^{-1})	Energy Density (kW h kg^{-1})
Hydrogen (g)	0.003	33.3
Hydrogen (l)	2.36	33.3
Methane	0.011	15.4
Methanol	4.33	6.09
Ethanol	6.67	8.01
Butanol	8.11	10.2
Gasoline	10	12.7

The power density is defined as the amount of power produced per unit volume, mass or area (equation 1.28) and power is defined as the amount of energy produced per unit time and has units of watts (W). Since power is proportional to power density, the rate at which energy is produced in a system will also be proportional to the power density. Moreover, the faster the kinetics in the fuel cell, the higher the power, hence the

$$D_P = \frac{P}{V} \tag{1.28}$$

higher the power density. In fuel cells, power density is often referred to as the amount of power produced per unit area having units of mW cm^{-2}. Since the power density is directly related to the kinetics of the fuel cell reactions, it will depend on many other parameters such as the temperature and pressure of the cell, the concentration of the fuel, and composition of the electrocatalyst.

1.3.4. Faradaic Processes

All theory described in this section was obtained from [95]. All calculations shown in the bulk of this work are based on the faradaic principles. In electrochemical experiments, concentrations of products can be directly related to the current that is produced during a redox reaction. Every redox couple has a certain standard potential (E°) where the electroactive species is neutral. At potentials < E°, the species will be in reduced and at potential > E°, they will be oxidized. At a given potential E, the Nernst equation (equation 1.29) can be employed to determine the concentration ratio of oxidized vs. reduced species at the electrode surface.

$$E = E^{\circ} + \frac{2.3RT}{nF} \log \frac{C_O(0,t)}{C_R(0,t)} \tag{1.30}$$

When a species loses or gains electrons, a current will be produced and is called the faradaic current. The resulting current is a direct measure of the rate of the reaction. When calculating concentrations and yields of the oxidized species (products) of the EOR, Faraday's law is used in order to determine the theoretical concentration of products. To obtain a yield and to determine product distributions, the number of "experimental moles" of product is divided by the "theoretical moles" of product obtained from the following equation:

$$N_{theo} = \frac{It}{nF} \tag{1.30}$$

where n is the number of electrons theoretically transferred in the reaction. All products yields reported in the proceeding chapters were calculated as follows:

$$\% \; yield = \frac{N_{exp}}{N_{theo}} \; x \; 100\% \tag{1.31}$$

1.4. Limitations of the EOR in DEFCs

This section will focus on the barriers, breakthroughs and future goals of EOR in DEFCs. There are many factors that contribute to the lack of commercialization of DEFCs as alternative energy sources. The barriers reviewed in this section include the sluggish kinetics of the EOR, the inefficiency of the EOR due to incomplete oxidation, the negative effects of fuel crossover, and the cost of electrode and Nafion® membranes.

1.4.1. Poor EOR Kinetics

The primary reason for the slow kinetics of the EOR is poisoning of the anode by intermediates adsorbed on the electrode surface. The effects of anode poisoning on a Pt catalyst are effectively shown by data from Oejten et *al.* [96] presented in Figure 1.7. This experiment involved poisoning of the H_2 anode stream with CO and observing the current density over time. It is clearly shown from the polarization curves that the performance of the cell was best for the pure H_2 stream. When CO was first introduced into the fuel stream, a significant decrease in cell potential was observed. As the time interval of the runs was increased, a trend of decreasing performance was reported. At short time intervals, H_2 and CO compete for active Pt adsorption sites. However, as time

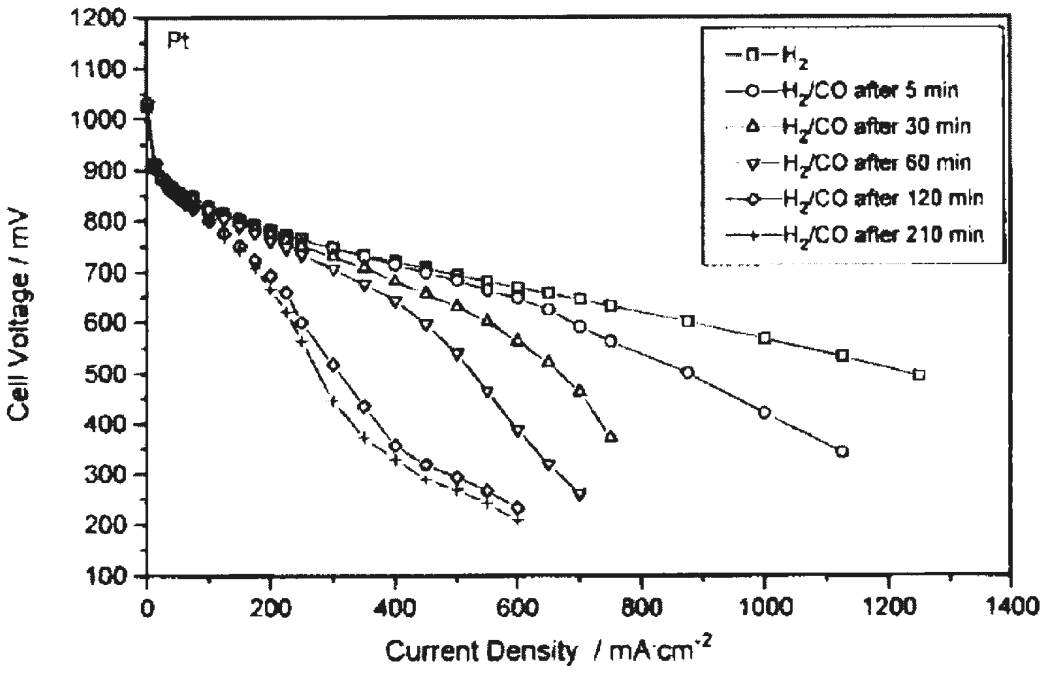

Figure 1.7: Polarization curves for H_2 oxidation at a 30% w/o Pt on Vulcan XC 72 anode at 80 °C at various steady-state time intervals. H_2 was doped with CO to demonstrate the effects of electrode poisoning (obtained with permission from [96]).

increased, the strongly adsorbed CO occupied most of the adsorption sites, leaving very little active surface area for the oxidation of H_2. This leads to a decrease in the rate of electron transfer and current density. Although these polarization curves are for hydrogen oxidation and CO was introduced into the cell, this is a very good representation of what occurs on a Pt anode in a DEFC.

To better understand why some anode catalysts are more susceptible to intermediate poisoning than others in DEFCs, the surface of the electrodes along with their mechanisms must be closely examined.

Pt anode catalysts have been the most widely researched for the EOR. Pt has been reported to have the best selectivity towards complete oxidation, but is known to be extremely susceptible to CO_{ads} poisoning. The mechanism to complete oxidation and poisoning of the electrode on Pt is depicted in Figure 1.8 a. and b. respectively. As shown, when ethanol is dissociated on the Pt electrode, the CO_{ads} forms linear and/or bridging interactions with the Pt surface [97]. These Pt-CO bonds on the surface are extremely strong, and require large overpotentials and oxygenated species to be fully oxidized to CO_2. Since the potential to dissociate ethanol into CO is much lower than the potential to dissociate H_2O into H^+ and OH_{ads}, most of the active Pt adsorption sites are already occupied by the CO before the OH_{ads} has the opportunity to form. As shown in the figure, for oxidation of CO into CO_2 to occur, adjacent CO_{ads} and OH_{ads} must be present. When there is a significant imbalance of the two adsorbates on the surface, CO is unable to oxidize further and the current density severely decreases.

To limit or eliminate the poisoning of the electrode, many research groups have been developing new anode catalysts that have the ability to lower the overpotential for the dissociation of H_2O and to decrease the bond strength of the CO on the electrode surface. To understand how to develop new electrocatalysts that can overcome these barriers, an explanation of the bifunctional mechanism and ligand (electronic) effects must be made.

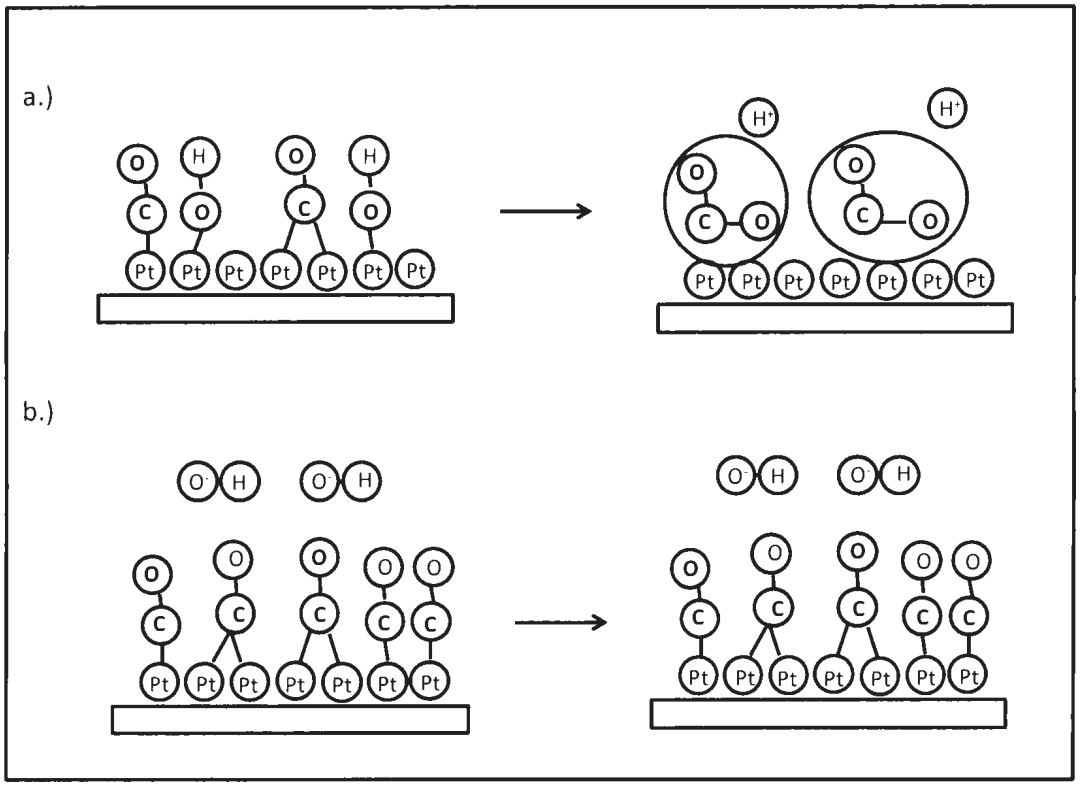

Figure 1.8. a.) Simplified mechanism for CO oxidation into CO_2. b.) Poisoning of the electrode by CO.

For ethanol oxidation, the bifunctional mechanism [70, 98] is a process where the Pt catalyst is alloyed with a secondary or tertiary metal to lower the overpotential for the oxidation of CO on the surface. The alloyed metal is able to dissociate H_2O and favors the adsorption of OH_{ads} rather than CO_{ads} at the anode. This eliminates the competition between CO and OH, and leaves sufficient active sites for the OH to adsorb on the surface. The close proximity of the CO and OH molecules enhance the kinetics of the CO oxidation to CO_2.

Many metals including Ru [16, 48, 87], Sn [98-102] and Ti [103] have been introduced into the Pt electrode surface and have shown increases in catalytic activity by increasing the CO tolerance at the surface. The secondary metal content has also been extensively examined in CO poisoning experiments. It has been shown that too much of a secondary metal can result in high OH_{ads} concentrations leading to significant OH poisoning [16, 48, 99] versus CO poisoning.

The second major problem leading to CO poisoning at the electrode is the strong interaction between the Pt on the surface and the adsorbed CO molecules. This barrier and the theory on how to overcome it was successfully described by Nøskov et al.[104-106] using density functional theory (DFT) calculations. Their work has described catalytic properties that can be altered with the incorporation of a secondary or tertiary metal in the catalyst composition. This theory, known as ligand (or electronic) effects, suggests that there are two main factors that contribute to the change in the electronic effects at the Pt surface which can result in weaker Pt-CO and Pt-OH bonds.

The first property is producing a strain on the surface of the electrode. By alloying the Pt electrode with a secondary and/or tertiary metal, the bond lengths of the atoms adsorbed on the surface of the electrode will be altered. This will result in either a tensile strain (which will lengthen the bond lengths) or a compressive strain (which will shorten the bonds). When an atom that is larger than Pt is introduced into the surface composition, the average bond lengths will increase leading to a tensile strain on the surface. When this occurs, the d-orbitals between atoms on the surface decrease in overlap which leads to a higher surface energy and stronger adsorption energy for the CO molecules.

When a smaller atom is incorporated into the surface composition, the average bond lengths on the surface are decreased, leading to an increase in d-orbital overlap and a decrease in surface energy. This decreased in surface energy leads to a decrease in adsorption energy, hence a weaker Pt-CO interaction.

The second property that can be altered is the electronic interactions between metal atoms in the composition of the catalyst. This is often referred to as the ligand effect. To investigate this effect, a layer of a secondary metal was placed just below the Pt surface layer [103]. No strain on the surface of the electrode was reported, therefore all of the results were solely due to electronic interactions between the two different metals. Their results were calculated computationally, by examining the d-band centers of each 3d transition metal – Pt compositions [103]. It was found that as they moved from right to left on the periodic table (decreasing atomic size) the d-band centers of the alloys decreased. Lowering of the d-band results in a weaker adsorption energy for OH_{ads} and easier removal of the CO_2. Out of all the 3d transition metals examined in this work, the Pt-Ti surface was found to have the weakest adsorption energy, hence was the best for limiting poisoning on the electrode.

1.4.2. Incomplete Oxidation of Ethanol

As mentioned earlier in this work, when ethanol is not fully oxidized into CO_2, transferring 12 electrons (equation 1.16), the reaction is very inefficient. The major obstacle in achieving complete oxidation to CO_2 is the cleavage of the C-C bond which is only seen at very high positive potentials. [12,107,108]. It has been reported from a number of theoretical studies (using DFT) [63-65] that out of all of the possible pathways by which eth-

anol oxidation can proceed, the C-C breakage is the most energetically demanding. As shown by a theoretical study carried out by Wang et *al.* [63] (Figure 1.9) on a Pt electrode, ethanol oxidation can follow a variety of pathways before being oxidized to one of the three main products. In each step of this reaction scheme, it is clearly shown that the energy barrier for the C-C cleavage is the highest.

This study shows a very high reaction barrier for an initial C-C cleavage (2.98 eV), and will most likely not occur at this stage of the reaction. After acetaldehyde is produced in the first step of the mechanism, a C-C bond cleavage is observed, with an energy barrier of less than half of the direct cleavage. This indicates that the CO_2 that is produced in the EOR is most likely a by-product from acetaldehyde production in the reaction.

It has also been reported in an experimental study carried out by Rao et al. [109] that acetaldehyde can easily be oxidized into CO_2 and acetic acid. However, once acetic acid is produced, it is a final product and cannot be further converted to CO_2. Based on these reports, it is suggested that the production of CO_2 primarily results from an acetaldehyde intermediate and only small amounts of CO_2 are produced from the direct oxidation from ethanol. The mechanism of ethanol oxidation is very complex and the understanding of what parameters of the catalyst must be altered to obtain the maximum efficiency and performance is still unclear. Since the production of acetic acid yields the transfer of 4 electrons and acetaldehyde only 2, one would think it more efficient to try to increase the selectivity towards acetic acid. However, as just mentioned, acetic acid is a

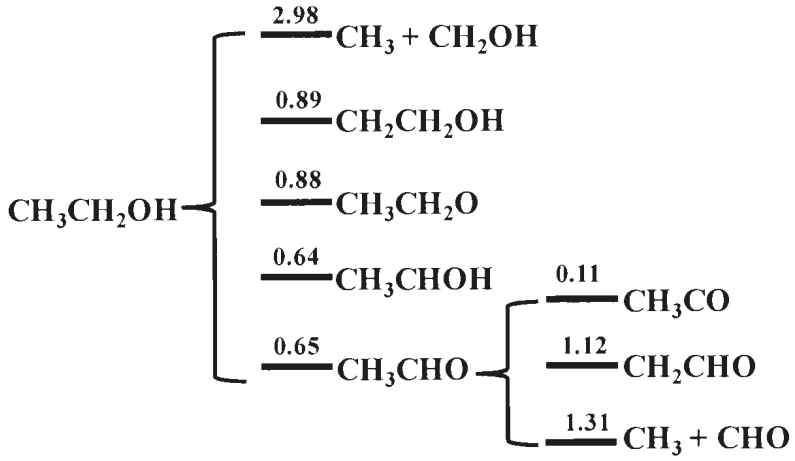

Figure 1.9: A scheme of possible EOR pathways along with the energy barriers calculated at each step using DFT, units of values in eV (adapted from [63]).

final product, whereas acetaldehyde can be further oxidized to obtain complete oxidation. For the commercialization of DEFC it is imperative that EOR gets as close as possible to complete oxidation. With this being said, the selectivity towards acetaldehyde would be preferred over acetic acid, as the product could be reused and converted to CO_2.

As mentioned earlier, the incorporation of a secondary or tertiary metal into the electrode composition can significantly increase the performance of the cell. PtRu and PtSn have been shown to give the best performance and the best power density for EOR in DEFCs. However, it has also been shown that when Ru or Sn is introduced into the lattice structure of the electrode, the selectivity towards CO_2 is significantly decreased (in comparison to pure Pt). Rousseau et al. [110] showed that the incorporation of Sn into a Pt electrode lowered both the yields of CO_2 and acetaldehyde, while significantly increas-

ing the acetic acid yield. This suggests that in order to adsorb dissociated ethanol on the surface and break the C-C bond, adjacent Pt sites are needed [111]. When the C-C bond in ethanol is not cleaved, adsorbed acetaldehyde covers the surface and by the bifunctional mechanism, the Sn activates H_2O forming OH_{ads}, and the acetaldehyde and OH_{ads} react to form acetic acid.

The development of new anode catalysts is a very complicated procedure as balance between performance and selectivity is needed. As the performance of a catalyst is increased, it is generally found that the selectivity towards complete oxidation is decreased [110], and vice versa. As Pt catalysts are typically the best for selectivity towards CO_2, one of the objectives for improving catalyst technology is to increase the performance of the electrode while leaving the CO_2 yield unchanged.

The best reported yields of CO_2 were obtained at very high cell temperature on Pt/Ru catalysts. Arico et *al.* [52] reported a CO_2 yield of 90% at 145 °C resulting in a power density of 110 mW cm^{-2} and Wang et *al.* [112] reported a CO_2 yield of 79% at 170 °C (77 mW cm^{-2}). Although these researchers have obtained very high CO_2 yields, the temperatures used are undesirable for functional use of a fuel cell. The most commonly used electrolyte membrane (Nafion®) can only withstand temperature up to ca. 100 °C, as they need to be continually hydrated. Moreover, high temperature fuel cells must be pressurized during operation. More recently, the focus has been shifted to low temperature fuel cells which would be much more suitable for commercial use. The best reported low temperature CO_2 yield was reported by Kowal et *al.* [65] using a novel Pt/Rh/SnO_2 cata-

lyst that can effectively split the C-C bond at moderate temperature (60 °C) to give a CO_2 product yield of ca. 50%.

1.4.3. Effects of Fuel Crossover

Fuel crossover has been one of the most concerning problems in DAFCs [eg. 14, 55, 59, 70]. In DEFCs ethanol crossover results in a decrease in fuel efficiency, hence energy density. As ethanol migrates from the anode to the cathode through the membrane, the usefulness of the fuel as an electron doner is lost. Furthermore, the ethanol can react with O_2 at the cathode at lower potentials for the ORR, resulting in a decrease in O_2 reduction potential. This results in an overall decrease in the cell potential and fuel efficiency (known as a "mixed potential").

The rate at which ethanol is able to diffuse through the membrane is highly dependent on the temperature of the cell, the concentration of the fuel and the thickness of the solid electrolyte membrane. Li et *al.* [72] effectively described how each of these parameters influenced the crossover rate in a DEFC using the limiting ethanol oxidation current. They reported that increasing the ethanol concentration by a factor of 4 resulted in a ca. 260% increase in crossover current. By increasing the thickness of the membrane from ca. 125 μm to ca. 175 μm, the crossover current was halved. Increasing temperature from 23 to 80 °C, increased the crossover current by a factor of 8. This study suggests that low ethanol concentration, thick membranes and low temperature is the recipe for low ethanol crossover in DEFCs. However, just like performance and selectivity, when overcoming one barrier in EOR, another problem is exemplified. Using low concentrations of ethanol is great for decreasing crossover rates and increasing the fuel efficiency,

however too much water at the anode can cause serious mass transport problems. Using a thick electrolyte membrane reduces crossover, but increases the proton migration resistance in the membrane. Low temperatures significantly decrease diffusion rates, but performances, efficiency and selectivity are also all reduced.

1.4.4. Cost Analysis of PEM-DEFCs

As mentioned above, one of the primary research areas in DEFC in recent years has been the development of low-Pt or Pt-free anode and cathode catalysts. In a recent statistic (July 2012) it was shown that Pt metal was the most expensive metal on the market at over 46 euros per gram [113]. Table 1.2 shows the average prices in euros of most of the reported metals found in DEFC catalysts over a one year period. From an economic point of view, it is clear that the Pt loading of catalysts must be reduced significantly to make DEFCs available for commercial products. In terms of Pt loading and alloying, significant advancements have been made over the past decade. In 2002, the cost of ethanol fuel cells (production) per unit of energy produced was ca. $275 per kW [113]. In 2011, it was reported that the cost had decreased by ca. 82% to ca. $49 per kW. To become commercially competitive with gasoline and internal combustion engines, the US department of energy estimated that the cost would need to be further reduced to $35 per kW. The high costs of PEM-DEFCs in 2002 were a consequence of high Pt electrode loadings, high cost of Nafion® membranes [26] and small scale manufacturing.

The best measurement for describing and comparing how economical a fuel cell is, is power density in terms of power produced per unit of mass (of Pt). The Pt/Ru

Table 1.2: Average price of metals used in catalysts for the EOR from July 2011-July 2012 in Europe (Reproduced from [113]).

Metal	Average Price (euros per g)
Pt	46
Rh	44
Au	42.5
Ir	31
Pd	19
Re	4.8
Ru	3
Ag	0.72
Co	0.02
Ni	0.01
Sn	0.01
Cu	0.00612
Al	0.00152

catalysts prepared by Arico and Wang [52,112] are the best in the field with power densities of 0.0275 mW μg^{-1}_{Pt} and 0.0115 mW μg^{-1}_{Pt}, repectively.

1.5. Research Objectives

The first goal of the current research project was to develop an online system to quantify product distribution in the EOR. As multi-catalyst screening techniques have been developed to quickly determine activity of electrodes and cell performance, it is very important to have a system that can determine EOR products in real time under working DEFC conditions. Current techniques used for product analysis are time consuming, costly and require a fair deal of expertise. The techniques described in this work are inexpensive, user friendly and can monitor product yields as they are being produced.

The second objective of this work was to examine crossover effects in DEFCs. It has been clearly shown that ethanol crosses through the membrane causing a mixed potential, however, there have been no reports on how crossover affects the EOR product distribution. The negative effects of fuel and product crossover leading to significant errors in product analysis will be examined.

A novel approach to operating a DEFC using a "crossover mode" to control the flux and concentration of ethanol at the anode was another aspiration of this project. By allowing ethanol to diffuse through the PEM before applying current, we were able to eliminate CO_2 crossover, and obtain more accurate CO_2 measurements. This method allows for control of ethanol concentration at the anode (eliminating crossover from anode to cathode) which can also lead to improved product analysis.

To better understand and help broaden the scope of the EOR, the kinetics of adsorption of ethanol are examined using stripping techniques. This technique involves al-

tering pulsing and resting intervals, which help in understanding poisoning of the electrode and the rate determining steps of the EOR.

Finally, the last objective of this project is the development and characterization of new anode catalysts which are able to increase the performance of the cell (compared to Pt) while maintaining selectivity towards CO_2.

1.6. References

[1] Trimm, D. L.; Önsan, Z. I. *Catal. Rev. Sci. Eng.* **2001**, *43*, 31-84.

[2] Ahmed, S.; Krumpelt, M. *Int. J. Hydrogen Energy* **2001**, *26*, 291-301.

[3] Girishkumar, G.; Rettker, M.; Underhile, R.; Binz, D.; Vinodgopal, K.; McGinn, P.; Kamat, P. *Langmuir*, **2005**, *21*, 8487-8494.

[4] Ross, D. K. *Vacuum*, **2006**, *80*, 1084-1089.

[5] Gasteiger, H. A.; Markovic, N.; Ross, P. N.; Cairns, E. J. *J. Phys. Chem.* **1993**, *97*, 12020-12029.

[6] Wasmus, S.; Küver, A. *J. Electroanal. Chem.* **1999**, *461*, 14-31.

[7] Kreuer, K. D. *J. Membr. Sci.* **2001**, *185*, 29-39.

[8] Liu, H.; Song, C.; Zhang, L.; Zhang, J.; Wang, H.; Wilkinson, D. P. *J. Power Sources* **2006**, *155*, 95-110.

[9] Salgado, J. R. C.; Alcaide, F.; Álvarez, G.; Calvillo, L.; Lázaro, M. J.; Pastor, E. *J. Power Sources* **2010**, *195*, 4022-4029.

[10] Lufrano, F.; Baglio, V.; Di Blasi, O.; Staiti, P.; Antonucci, V.; Aricò, A. S. *Solid State Ionics* **2012**, *216*, 90-94.

[11] Antolini, E. *J. Power Sources* **2007**, *170*, 1-12.

[12] Colmati, F.; Tremiliosi-Filho, G.; Gonzalez, E. R.; Berna, A.; Herrero, E.; Feliu, J. M. *Faraday Discuss.* **2008**, *140*, 379-397.

[13] Vigier, F.; Rousseau, S.; Coutanceau, C.; Leger, J. M.; Lamy, C. Top. Catal. 2006, 40, 111-121.

[14] Zhou, W.; Zhou, Z.; Song, S.; Li, W.; Sun, G.; Tsiakaras, P.; Xin, Q. *Appl. Catal. B* **2003**, *46*, 273-285.

[15] De Souza, R. F. B.; Silva, J. C. M.; Simões, F. C.; Calegaro, M. L.; Neto, A. O.; Santos, M. C. *Int. J. Electrochem. Sci.* **2012**, *7*, 5356-5366.

[16] Nakagawa, N.; Kaneda, Y.; Wagatsuma, M.; Tsujiguchi, T. *J. Power Sources* **2012**, *199*, 103-109.

[17] Song, S. Q.; Zhou, W. J.; Zhou, Z. H.; Jiang, G. Q.; Sun, Q.; Xin, Q.; Leontidis, V.; Kontou, S.; Tsiakaras, P. Int. J. Hydrogen Energy 2005, 30, 995-1001.

[18] Wang, Z.; Du, Y.; Zhang, F.; Zheng, Z.; Zhang, Y.; Wang, C. *J. Solid State Electrochem.* **2013**, *17*, 99-107.

[19] Yu, X.; Pickup, P. G. *J. Power Sources* **2008**, *182*, 124-132.

[20] Rees, N. V.; Compton, R. G. *J. Solid State Electrochem.* **2011**, *15*, 2095-2100.

[21] Grove, W. R. *Philos. Mag.* **1839**, *14*, 127-130.

[22] Bossel, U. *The Birth of the Fuel Cell*; European Fuel Cell Forum: Oberrohrdorf, 2000.

[23] Blomen, L. J. M. J.; Mugerwa, M. N. *Fuel Cell Systems*; Springer, 1993. pg. 27-28.

[24] Costamagna, P.; Srinivasan, S. *J. Power Sources* **2001**, *102*, 253-269.

[25] Bacon, F. T. *Electrochem. Acta* **1969**, *14*, 569-585.

[26] Mauritz, K. A.; Moore, R. B. *Chem. Rev.* **2004**, *104*, 4535-4585.

[27] Grot, W. G. *US Patents* 3,969,285 (1976), 4,026,783 (1977), 4,030,988 (1977)

[28] Lee, S. J.; Mukerjee, S.; McBreen, J.; Rho, Y. W.; Kho, Y. T.; Lee, T. H. *Electrochim. Acta* **1998**, *43*, 3693-3701.

[29] Litster, S.; McLean, G. *J. Power Sources* **2004**, *130*, 61-76.

[30] Tang, H.; Peikang, S.; Jiang, S. P.; Wang, F.; Pan, M. *J. Power Sources* **2007**, *170*, 85-92.

[31] Carrette, L.; Friedrich, K. A.; Stimming, U. *Fuel Cells* **2001**, *1*, 5-39.

[32] Kamarudin, S. K.; Achmad, F.; Daud, W. R. W. *Int. J. Hydrogen Energy* **2009**, *34*, 6902-6916.

[33] Shimiza, T.; Momma, T.; Mohamedi, M.; Osaka, T.; Sarangapni, S. *J. Power Sources* **2004**, *137*, 277-283.

[34] Cleghorn, S. J. C.; Ren, X.; Springer, T. E.; Wilson, M. S.; Zawodzinski, C.; Gottesfeld, S. *Int. J. Hydrogen Energy* **1997**, *22*, 1137-1144.

[35] Alves, H. J.; Junior, C. B.; Niklevicz, R. R.; Frigo, E. P.; Frigo, M. S.; Coimbra-Araujo, C. H. *Int. J. Hydrogen Energy*, **2013**, in press.

[36] http://corporate.ford.com/microsites/sustainability-report-2011-12/environment-products-plan-migration-fcv - accessed March 2nd, 2013.

[37] http://pressroom.toyota.com/article_display.cfm?article_id=1840 – accessed March 2nd, 2013.

[38] http://www.fuelcelltoday.com/media/1713685/fct_review_2012.pdf - accessed March 2nd, 2013.

[39] http://www.nrel.gov/hydrogen/proj_fc_bus_eval.html - accessed March 2nd, 2013.

[40] http://www.crest-au.com/docs/alt_CBA.pdf - accessed March 6th, 2013

[41] http://www.hydrogen.energy.gov/pdfs/progress10/viii_0_technology_validation_overview.pdf – accessed March 3rd, 2013

[42] http://fchea.org/core/import/PDFs/Materials%20Handling%20Fact%20 Sheet.pdf – accessed March 2nd, 2013.

[43] Heinzel, A.; Hebling, C.; Müller, M.; Zedda, M.; Müller, C. *J. Power Sources* **2002**, *105*, 250-255.

[44] Vancoillie, J.; Demuynck, J.; Sileghem, L.; Van De Ginste, M.; Verhelst, S.; Brabant, L.; Van Hoorebeke, L. *Appl. Energy* **2013**, *102*, 140-149.

[45] Murray, L. J.; Dincă, Long, J. R. *Chem. Soc. Rev.* **2009**, *38*, 1294-1314.

[46] Tanaka, T.; Azuma, T.; Evans, J. A.; Cronin, P. M.' Johnson, D. M.; Cleaver, R. P. *Int. J. Hydrogen Energy* **2007**, *32*, 2162-2170.

[47] Zhou, W. J.; Zhou, B.; Li, W. Z.; Zhou, Z. H.; Song, S. Q.; Sun, G. Q.; Xin, Q.; Douvartzides, S.; Goula, M.; Tsiakaras, P. *J. Power Sources* **2004**, *126*, 16-22.

[48] Antolini, E.; Colmati, F.; Gonzalex, E. R. *Electrochem. Commun.* **2007**, *9*, 398-404.

[49] Song, S.; He, C.; Liu, J.; Wang, Y.; Brouzgou, A.; Tsiakaras, P. *Appl. Catal. B* **2012**, *119*, 227-233.

[50] Maab, H.; Nunes, S. P. *J. Power Sources* **2010**, *195*, 4036-4042.

[51] Leger, J. M.; Rousseau, S.; Coutanceau, C.; Hahn, F.; Lamy, C. *Electrochim. Acta* **2005**, *50*, 5118-5125.

[52] Aricò, A. S.; Cretì, P.; Antonucci, P. L.; Antonucci, V. Electrochem. *Solid-State Lett.* **1998**, *1*, 66-68.

[53] Zhang, J. *PEM Fuel Cell Electrocatalysts and Catalyst Layers*; Springer; 2008, 89-134.

[54] Leger, J. M. *J. Appl. Electrochem.* **2001**, *31*, 767-771.

[55] Wang, D.-Y.; Chou, H.-L.; Lin, Y.-C. *J. Am. Chem. Soc.* **2012**, *134*, 10011-10020.

[56] Chrzanowski, W.; Wiechokski, A. *Langmuir* **1998**, *14*, 1967-1970.

[57] Velázquez-Palenzuela, A.; Brillas, E.; Arias, C.; Centellas, F.; Garrido, J. A.; Rodriguez, E. M.; Cabot, P.-L. *J. Power Sources* **2012**, *208*, 306-315.

[58] Velázquez-Palenzuela, A.; Brillas, E.; Arias, C.; Centellas, F.; Garrido, J. A.; Rodriguez, E. M.; Cabot, P.-L. *J. Catal.* **2013**, *298*, 112-121.

[59] Scott, K.; Taama, W. M.; Argyropoulos, P.; Sundmacher, K. *J. Power Sources* **1999**, *83*, 204-216.

[60] Miesse, C. M.; Jung, W. S.; Jeong, K. J.; Lee, J. K.; Lee, J.; Han, J.; Yoon, S. P.; Nam, S. W.; Lim, T. H.; Hong, S. A. *J. Power Sources* **2006**, *162*, 532-540.

[61] Lamy, C.; Lima, A.; LeRhun, V.; Delime, F.; Coutanceau, C.; Leger, J. M. *J. Power Sources* **2002**, *105*, 283-296.

[62] Lamy, C.; Belgsir, E. M.; Leger, J. M. *J. Appl. Electrochem.* **2001**, *31*, 799-809.

[63] Wang, H.-F.; Liu, Z.-P. *J. Am. Chem. Soc.* **2008**, *130*, 10996-11004.

[64] Kavanaugh, R.; Cao, X.-M.; Lin, W.; Haracre, C.; Hu, P. *J. Phys. Chem. C* **2012**, *116*, 7185-7188.

[65] Kowal, A.; Li, M.; Shao, M.; Sasaki, K.; Vukmirovic, M. B.; Zhang, J.; Marinkovic, N. S.; Liu, P.; Frenkel, A. I.; Adzix, R. R. *Nature Mater.* **2009**, *8*, 325-330.

[66] Wieckowski, A.; Sobrowski, J.; Zelenay, P.; Franaszczuk, K. *Electrochim. Acta* **1981**, *26*, 1111-1119.

[67] Kokoh, K. B.; Hahn, F.; Belgsir, E. M.; Lamny, C.; de Andrade, A. R.; Olivi, P.; Motheo, A. J.; Tremiliosi-Filho, G. Electrochim. Acta 2004, 49, 2077-2083.

[68] Farias, M. J. S.; Camara, G. A.; Tanaka, A. A.; Iwasita, T. *J. Electroanal. Chem.* **2007**, *600*, 236-242.

[69] James, D. D.; Bennett, D. V.; Li, G.; Ghumman, A.; Helleur, R. J.; Pickup, P. G. *Electrochem. Commun.* **2009**, *11*, 1877-1880.

[70] Lamy, C.; Rousseau, S.; Belgsir, E. M.; Coutanceau, C.; Leger, J. M. *Electrochim. Acta* **2004**, *49*, 3901-3908.

[71] Meyer, M.; Melke, J.; Gerteisen, D. *Electrochim. Acta* **2011**, *56*, 4299-4307.

[72] Li, G.; Pickup, P. G. *J. Power Sources* **2006**, *161*, 256-263.

[73] Zhang, L. W.; Chae, S. R.; Hendren, Z.; Park, J. S.; Wiesner, M. R. *Chem. Eng. J.* **2012**, *204*, 87-97.

[74] Snyder, J. D.; Elabd, Y. A. *J. Power Sources* **2009**, *186*, 385-392.

[75] Peighambardoust, S. J.; Rowshanzamir, s.: Amjadi, M. *Int.J. Hydrogen Energy* **2010**, *35*, 9349-9384.

[76] Oh, S. H.; Sinkevitch, R. M. *J. Catal.* **1993**, *142*, 254-262.

[77] Marković, N. M.; Schmidt, T. J.; Stamenković, V.; Ross, P. N. *Fuel Cells* **2001**, *1*, 105-117.

[78] Paulus, U. A.; Schmidt, T. J.; Gasteiger, H. A.; Behm, R. J. *J. Electroanal. Chem.* **2001**, *495*, 134-145.

[79] Damjanovic, A.; Sepa, D. B.; Vojnovic, M. V. *Electrochim. Acta* **1979**, *24*, 887-889.

[80] Hyman, M. P.; Medlin, J. W. *J. Phys. Chem. B* **2006**, *110*, 15338-15344.

[81] Gasteiger, H. A.; Kocha, S. S.; Sompalli, B.; Wagner, F. T. *Appl. Catal. B: Environ.* **2005**, *56*, 9-35.

[82] Simões, F.; Olivi, P. *Electrocatalysis* **2010**, *1*, 163-168.

[83] Morales-Acosta, D.; Lopez de la Fuente, D.; Arriaga, L. G.; Vargas Guilierrez, G.; Rodriguez Varela, F. J. *Int. J. Electrochem. Sci.* **2011**, *6*, 1835-1854.

[84] Rodriguez Varela, F. J.; Gonzalez Ramirez, S. E.; Klapco, R. D. *J. New Mater. Electrochem. Syst.* **2009**, *12*, 9-15.

[85] Rao, C. V.; Viswanathan, B. *Electrochim. Acta* **2010**, *55*, 3002-3007.

[86] Song, S.; Wang, Y.; Tsiakaras, P.; Shen, P. K. *Appl. Catal. B* **2008**, *78*, 381-387.

[87] Li, H.; Sun, G.; Cao, L.; Jiang, L, Xin, Q. *Electrochim. Acta* **2007**, *52*, 6622-6629.

[88] Liu, J.; Ye, J.; Xu, C.; Jiang, S. P.; Tong, Y. *Electrochem. Commun.* **2007**, *9*, 2334-2339.

[89] Markgraf, S.; Hörenz, M.; Schmiel, T.; Jehle. W.; Lucas, J.; Henn, N. *J. Power Sources* **2012**, *201*, 236-242.

[90] Danks, T. N.; Slade, R. C. T.; Varcoe, J. R. *J. Mater. Chem.* **2003**, *13*, 712-721.

[91] Spendelow, J. S.; Wieckowski, A. *Phys. Chem. Chem. Phys.* **2007**, *9*, 2654-2675.

[92] Jiang, L.; Hsu, A.; Chu, D.; Chen, R. *J. Electroanal. Chem.* **2009**, *629*, 87-93.

[93] Li, X. Principles of Fuel Cells; Taylor and Francis Group; New York, 2006.

[94] http://web.archive.org/web/20100825042309/http://www.ior.com .au/ecflist.html – accessed March 17th, 2013.

[95] Wang, J. Analytical Electrochemistry; John Wiley & Sons, 2001, pgs 3-18.

[96] Oetjen, H.-F.; Schmidt, V. M.; Stimming, U.; Trila, F. *J. Electrochem. Soc.* **1996**, *143*, 3838-3842.

[97] Xia, X. H.; Iwasita, L. T. *J. Electroanal. Chem.* **1997**, *437*, 233-240.

[98] Vigier, F.; Coutanceau, C.; Hahn, F.; Belgsir, E. M.; Lamy, C. *J. Electroanal. Chem.* **2004**, *563*, 81-89.

[99] Antolini, E.; Gonzalez, E. R. *Electrochim. Acta* **2010**, *55*, 6485-6490.

[100] Lim, D.-H.; Choi, D.-H.; Lee, W.-D.; Lee, H.-I. *Appl. Catal. B* **2009**, *89*, 484-493.

[101] Antolini, E.; Gonzalez, E. R. *Catal. Today* **2011**, *160*, 28-38.

[102] Dupont, C.; Jugnet, Y.; Loffreda, D. *J. Am. Chem. Soc.* **2006**, *128*, 9129-9136.

[103] Kitchen, J. R.; Nørskov, J. K.; Barteau, M. A.; Chen, J. *J. Chem. Phys.* **2004**, *120*, 10240-10246.

[104] Ruban, A.; Hammer, B.; Stolzte, P.; Skriver, H. L.; Nørskov, J. K. *J. Mol. Catal. A Chem.* **1997**, *155*, 421-429.

[105] Mavrikakis, M.; Hammer, B.; Nørskov, J. K. *Phys. Rev. Lett.* **1998**, *81*, 2819-2822.

[106] Liu, P.; Logadottir, A.; Nørskov, J. K. *Electrochim. Acta* **2003**, *48*, 3731-3742.

[107] Mann, J.; Yao, N.; Bocarsly, A. B. *Langmuir* **2006**, *22*, 10432-10436.

[108] Lai, S. C.; Koper, M. T. *Faraday Discuss.* **2008**, *140*, 379-397.

[109] Rao, V.; Cremers, C.; Stimming, U.; Cao, L.; Sun, S.; Yan, S.; Sun, G.; Xin, Q. *J. Electrochem. Soc.* **2007**, *154*, B1138-B1147.

[110] Rousseau, S.; Coutanceau, C.; Lamy, C.; Leger, J. M. *J.Power Sources* **2006**, *158*, 18-24.

[111] Del Colle, V.; Berná, A.; Tremiliosi-Filho, G.; Herrero, E.; Feliu, J. M. *Phys. Chem. Chem. Phys.* **2008**, *10*, 3766-3773.

[112] Wang, Q.; Sun, G. Q.; Cao, L.; Jiang, L. H.; Wang, G. X.; Wang, S. L.; Yang, S. H.; Xin, Q. *J. Power Sources* **2008**, *177*, 142-147.

[113] Brouzgou, A.; Podias, A.; Tsiakaras, P. *J. Appl. Electrochem.* **2013**, *43*, 119-136.

CHAPTER 2

Experimental

2.1. Chemicals and Materials

All chemicals and materials, with the exception of the anode support plate of the fuel cell, were used as received. The inlet and outlet portions of the anode support plate of the fuel cell were modified to eliminate any contact between the anode solution and the metal of the plate. For acetic acid measurements, a large background was detected and was suspected to be caused by metal ions dissolving from the metal block into the anode stream.

The fuel cell used in all of the reported experiments of this work was a 5 cm^2 single cell fuel cell from Fuel Cell Technology Inc. Nafion® 115 membranes were the only PEM used in this work. All homemade electrodes used Toray™ (0.26 mm) carbon fiber paper (CFP).

Commercial Pt anodes and cathodes (4 mg cm^{-2} loading of Pt black on Toray™ CFP) that were used in many of the experiments were donated by Ballard Power Systems.

Chemicals used include: Anhydrous ethanol (Commercial Alcohols Inc.), acetic acid (Fisher Scientific), acetaldehyde (Sigma-Aldrich), 2,4-dinitrophenol hydrazine (Sigma-Aldrich), hydrochloric acid (Sigma-Aldrich), methanol (Fisher Scientific), sodium hydroxide (Sigma-Aldrich), potassium hydroxide (ACP Chemical Inc.), methyl orange indicator (Sigma-Aldrich), phenolphatlein pH indicator (Sigma-Aldrich), sulphuric acid (Fisher Scientific), sodium borohydride (Sigma-Aldrich), carbon black (Vulcan XC-72, Cabot), sodium citrate (Anachemia), potassium perruthenate (Alfa Aesar), chloroplatinic acid hexahydrate (Alfa Aesar), tin (IV) chloride pentahydrate (Fisher Scientific) and Nafion® solution (5%, Dupont).

Industrial grade nitrogen, oxygen and 5% H_2/N_2 from Air Liquide were used in fuel cell experiments. CO_2 (Air Liquide) was used in detector calibrations.

2.2. Preparation of Electrodes and MEAs

Homemade electrodes described in this work were prepared in a similar fashion to Li et *al.* (eg. [1,2]). A catalyst ink was prepared by first dispersing the catalyst in sufficient 5% Nafion® solution (Aldrich) and the resulting mixture was sonicated for ca. 30 min. The ink was then well dispersed over a 5 cm^2 piece of CFP (Toray™). The catalyst was then allowed to dry overnight in a fumehood.

For low or room temperature (RT) experiments, MEAs were prepared by hot-pressing the electrodes and a Nafion® 115 membrane together at a temperature of 135 °C for 90 sec at a pressure of 200 kg cm^{-2} using a Carver laboratory press.

2.3. Electrochemical Measurements

Electrochemical measurements (galvanostatic and potentiostatic) were carried out with a Solartron 1286 electrochemical interface coupled with a 1250 frequency analyzer or with an Arbin® Instruments multi-channel potentiostat. CorrWear and E-DAQ software were used for measuring and recorded potential/current and conductivity responses respectively. Logger Pro software was used for recording CO_2 detector signals.

Cyclic voltammetry measurements were carried out in a conventional three electrode cell using an EG&PAR 273 potentiostat/galvanostat. This instrument used M270 commercial software for recording results.

2.4. Product Analysis Instrumentation

To determine the product selectivity in the EOR, three main instruments were used. For CO_2 analysis, a commercial CO_2 detector was used. In acetic acid analysis, a commercial flow-through conductivity detector was used. Acetaldehyde measurements were carried out using gas chromatography (GC).

2.4.1. Non-Dispersive Infrared (NDIR) Carbon Dioxide Detector

Most of the CO_2 measurements reported in this work were carried out using a commercial Telaire 7001 CO_2 detector. The detector uses a dual beam absorption infrared method with a gas flow-through inlet. It consists of an IR lamp which delivers waves of light through a tube of air (Figure 2.1). The detector uses an optical filter which eliminates wavelengths from all likely interferences. When the tube is flushed with N_2 none of IR waves are absorbed and all of the light is detected at the far end of the tube. Once CO_2 is introduced into the detector, the IR waves are absorbed by the CO_2, leading to a decrease in light detected. The difference in IR light detected (CO_2/N_2 to N_2) is used to determine the concentration of CO_2 present in the detector. Beer's law represents the correlation between analyte concentration and intensity of light by the following:

$$I = I_0 e^{kc} \tag{2.1}$$

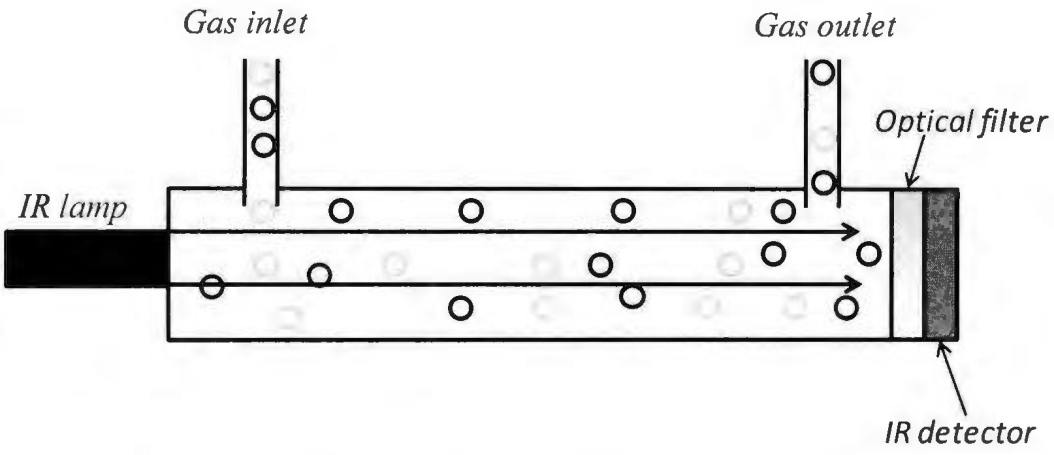

Figure 2.1: Gas chamber tube of a NDIR CO_2 monitor consisting of an IR lamp, optical filter and IR detector.

where I is the intensity of the light striking the detector, I_0 is the measured intensity of the light in the empty gas chamber, k is a system dependent constant and C is the concentration of the gas to be measured. CO_2 calibration gases are use to obtain k for the device.

The CO_2 detector and product analysis are further discussed in the upcoming chapters of this report.

2.4.2. Flow-Through Conductivity Detector

A commercial liquid flow-through conductivity pod from E-DAQ was used in many of the acetic acid measurements throughout this work. This device detects substances that

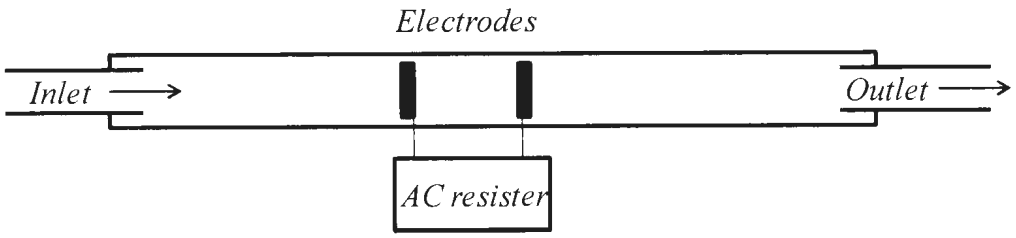

Figure 2.2: A schematic of a simple liquid flow-through conductivity detector.

ionize in solution, and is therefore great for inorganic and organic acids, bases and salts. These systems are frequently used in environmental studies and many biotechnology applications.

This simple detector consists of two electrodes which are both exposed to the liquid feed (Figure 2.2). Once the solution is in contact with the electrodes, the ions cause an electrical conductance between the electrodes. A potential pulse is applied across the pair of electrodes and the alternating current (AC) (0.5, 1 or 10 kHz frequency) is measured. A direct current (DC) voltage signal is produced that is proportional to the conductance. The conductivity is the reciprocal of the electrical resistivity and can be represented by the following formula:

$$\sigma = \frac{1}{R_E} \tag{2.2}$$

The units of conductivity are usually expressed as $\mu S\ cm^{-1}$ or $mS\ cm^{-1}$, where S is Siemens and is the reciprocal of Ohms (Ω^{-1}).

For acetic acid concentration analysis, standards of various acid concentrations were made and fed through the cell. A linear relationship between $[H^+]$ and signal was observed and used as a calibration curve. Accuracy of the conductivity cell results were frequently checked by titrating the anode product solution. The conductivity results and discussion are presented in chapter 3 of this work.

2.4.3. Gas Chromatograph

Gas chromatography was used in the determination of acetaldehyde produced in the EOR. A Varian 3400 GC was used with a RTX® - 1301 molecular sieve column (Restek: 60 m x 0.25 mm, 1.4 μm thickness) and flame-ionization detector were used. Ethanol present in the samples and used as the fuel was used as an internal standard.

Due to the high volatility of acetaldehyde it was important that all samples from the anode and cathode exhausts were cooled quickly after exiting the fuel cell (also for acetic acid measurements as σ is T dependent). At the anode, the outlet line was a metal coil that was cooled in an ice bath to limit the loss of acetaldehyde due to vaporization. For collection of product at the cathode, a liquid nitrogen trap was placed directly below the collection flask. The liquid nitrogen was able to freeze the acetaldehyde produced, and the resulting solid acetaldehyde was collected and refrigerated at temperatures below its boiling point (4 °C).

Gas chromatography is an analytical technique for separating and analyzing compounds by vaporization. Once the compounds in a solution are in the gas phase, they interact with the walls of the column. The walls of the column are composed of an inert solid coated with liquid or polymer known as the stationary phase. The mobile phase in GC

is an inert gas (usually helium or nitrogen) and is used to carry the vaporized compounds through the column. Every compound will pass through the column at a different rate (depending on the strength of the interaction between compound and material on the column wall), and the time required is known as the retention time. The difference in retention times between compounds and the strength of the signal produced is what gives GC its analytical properties.

Various acetaldehyde standards were made using the same concentration of ethanol that was used in the fuel cell experiments. The peak area ratios between the acetaldehyde and ethanol peaks were used to produce a linear calibration curve for acetaldehyde analysis. The GC analysis will be discussed in the proceeding chapter.

2.5 Catalyst Characterization Techniques

2.5.1. X-Ray Diffraction (XRD)

Powder XRD was used in these experiment to identify crystalline components of the catalysts synthesized in this work and to determine particle sizes. The sample is exposed to a fixed wavelength of x-ray waves and the intensity of the diffracted waves are recorded and analyzed based on the degree of constructive and destructive interference This method is able to determine various properties of the catalyst structure including unit cell parameters by altering the angle of x-ray waves on the surface and recording their scattering patterns.

XRD patterns of the catalysts examined were obtained on an X-ray diffractometer (Rigaku Ultima IV) using a Cu-Kα source (1.5418 Å) which was generated at 40 kV and 44 mA by Wanda Aylward of CREAIT working in the Earth Science building. Continu-

ous mode was used with a count time of 1.000 degrees per sec. The scan ranged from 10 to 90 degrees, with an overall scan time of 1.33 h.

2.5.2. Inductively Coupled Plasma Mass Spectroscopy (ICP-MS)

ICP-MS is an analytical technique for determining elemental contents in a sample. The sensitivity of this technique is extremely good as it can detect elements at concentrations as low as 1 part per trillion. It uses an inductively coupled plasma to ionize samples and is then quantified using mass spectroscopy.

ICP-MS measurements were carried out using an Elan DRC II ICPMS by Lakmali Hewa of CREAIT working out of the Earth Science building. To first dissolve the metals from the catalyst samples, 2 mL of 8 mol L^{-1} nitric acid was added to 8 mg of the sample in a Teflon screw capped jar and left to heat at 70 °C two days. The sample did not go into solution. The sample was then diluted to 8 mL with nanopure water. Assuming the elements have leached out into the final 8 mL solution, a dilution (M37367a) of the final solution was analyzed.

2.5.3. Inductively Coupled Plasma Optical Emission Spectroscopy (ICP-OES)

ICP-OES is another analytical technique very similar to ICP-MS in that the atoms in the solution are ionized by an inductively coupled plasma. The main difference between the two techniques is that ICP-OES uses the electromagnetic emissions from ionized atoms to determine concentrations, whereas the ICP-MS uses the mass of the ionized atoms.

ICP-OES measurements were carried out on a Perkin Elmer 5300 DV by Dr. Geert Van Biesen. Samples were first diluted with aqua regia and then further diluted

with 2% HNO_3 for ICP-OES analysis. Yttrium was used as an internal standard. Calibration curves were prepared using various concentrations of Pt, Sn and Ru in 2% HNO_3.

2.5.4. Thermogravimetric Analysis (TGA)

TGA is a method of thermal analysis used in this work in which increasing the temperature of a sample leads to changes in the composition of the sample. Due to the very high vaporization temperatures of the transition metals involved (in comparison to the combustion of carbon, water and surface oxygen functional groups), by setting the temperature of the instrument to temperatures just above the evaporation temperature of water, oxygen groups and carbon (in separate steps), the content of each was determined by the difference in mass.

TGA experiments were conducted using a TA instrument Q500 thermogravimetric analyzer with thermal advantage software by Julie Collins of CREAIT. The scan rate ranged from 1 to 50 °C min^{-1} depending of the rate of the mass loss, using a dynamic, high resolution scan option. Experiments were conducted under an air atmosphere.

2.5.5. Energy Dispersive X-Ray Microanalysis (EDX)

In EDX experiments, high energy electrons are applied to the surface of a sample and x-rays are produced as a result of the electrons ionizing the core shells of the atoms. The energies and intensities of the x-rays are measured, and since each atom has unique energies for each core electron shell, atoms in the sample can be distinguished.

EDX analysis of the catalysts were carried out using a Bruker XFlash dual 5030 energy dispersive X-ray analyzer by Michael Shaffer at Memorial University.

2.5.6. Transmission Electron Microscopy (TEM)

TEM is a microscopy technique that passes an electron beam through a thin layer sample. As the electrons pass through the sample, an image is produced. The extremely high resolution of these images can help in characterizing a sample at a molecular level.

TEM experiments were carried out at the University of New Brunswick (The Microscopy and Microanalysis Facility) by Louise Weaver using a JEOL 2011 200 keV scanning transmission electron microscope. The sample was prepared by carefully scraping Pt-$RuSnO_2$/C powder off of an electrode and was dispersed in ethanol and sonicated. A drop of the sample solution was then placed on a 200 mesh, carbon coated copper grid and allowed to dry overnight. The chemical analysis was carried out using a EDAX analysis system.

2.6. References

[1] Li, G.; Pickup, P. G.; *Electrochem. Acta* **2006**, *52*, 1033-1037.

[2] Li, G.; Pickup, P. G.; *J. Power Sources* **2007**, *173*, 121-129.

CHAPTER 3

A Novel Methodology for Online Analysis of Products from a DEFC

3.1. Introduction

Parts of this chapter were written by Dr. Peter Pickup and have been published in a peer-reviewed journal [1]. This work was initiated by Dwayne Bennett (in collaboration with Dr. Azra Ghumman, and Dr. Robert Helleur), who demonstrated the basic concepts of the methodology, and obtained preliminary results with the DEFC. None of these earlier results are used in this thesis. The guidance of Dr. Guangchun Li with the instrumentation and fuel cell theory is gratefully acknowledged.

The quantitative detection of ethanol oxidation products has been a recently growing sub-field of direct ethanol fuel cell (DEFC) chemistry. The significant increase in DEFC performance may perhaps now be sufficient to justify commercialization; however their efficiency and undesirable formation of by-products could be a challenge. The main products of the ethanol oxidation reaction (EOR) are acetic acid (AA) and acetaldehyde (AAL), which result in much less energy production than for complete oxidation to CO_2. In additions these products would need to be collected and somehow recycled. The development of practical PEM-based DEFC technology requires new anode catalysts that can accomplish almost complete oxidation of ethanol to CO_2 at moderate temperatures (preferably below 100 °C). With the search for new catalysts gathering momentum [2-9], and the use of multi-electrode sputtering deposition techniques [10-12], product analysis is becoming an increasingly important topic. The literature has discussed results obtained with both liquid electrolyte cells [13] and fuel cells [14]. Differential electrochemical mass spectrometry is the preferred method for liquid electrolytes cells, and has been used at elevated temperatures and pressures [13]. This technique is well suited for mechanistic

studies, but measurements on fuel cells are necessary to evaluate the transferability of knowledge and optimize catalysts and conditions for the fuel cell environment.

Measurements of product distributions from DEFCs have taken many different paths with the surge in DEFC technology. Figure 3.1 illustrates a complex methodology that Lamy and co-workers [15] use for quantitative product analysis. This three step process begins with the anode solution entering the first flask in which the liquids (AA and non-volatilized AAL) are extracted for HPLC analysis. The gaseous products (CO_2 and volatilized AAL) are purged into a second flask and bubbled through a solution of 2,4-dinitrophenylhydrazine (2,4-DNPH) solution. The 2, 4-DNPH solution acts as an aldehyde test solution and the AAL, in its gas phase, reacts to form a precipitate. This precipitate is then solubilised in ethyl acetate and is analyzed by HPLC. The CO_2 is then purged into a third flask in which it reacts with sodium hydroxide forming carbonate that is once again collected for high performance liquid chromatography (HPLC). Many other groups have successfully analyzed product distributions by gas chromatography [2,16-18], and/or titration [2,19]. Transmission IR measurements of CO_2 have also been reported for the oxidation of formic acid [20] and methanol [21,22].

Although most studies have been shown to give accurate and reproducible product distributions; the time, money, effort and expertise required for these experiments could delay the screening and advancement of new anode catalysts. Furthermore, most of the techniques described above do not allow for real time monitoring of products during ethanol oxidation.

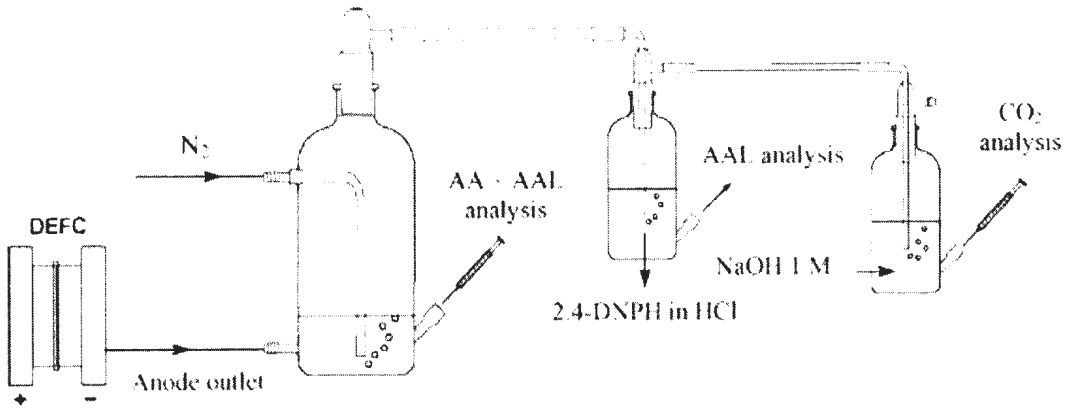

Figure 3.1: Schematic of methodology used by Lamy et *al.* for the detection of ethanol oxidation products from a direct ethanol fuel cell (Obtained with permission from [15]).

In this work, we report a novel way of quantifying ethanol oxidation products in a DEFC that is time efficient, inexpensive, requires little expertise, and most importantly can monitor the concentrations of EOR products moments after they are produced. This methodology couples a liquid feed conductivity detector for AA detection along with a non-dispersive infrared CO_2 detector. It is demonstrated that the AAL yield can be accurately obtained from these measurements using a faradaic charge balance, resulting in a simple online system for rapid evaluation of anode catalysts in DEFCs. Furthermore, we examine problems in product analysis that result from fuel crossover from the anode and oxygen crossover from the cathode.

Since this work has been published, Andreadis et *al.* [23] have successfully developed an on-line system for product analysis by coupling a GC with a MS and three IR gas analyzers. The anode products were first heated to ca. 200 °C to ensure the AA, water

and unreacted ethanol were vaporized for analysis. The anode port outlet was directly connected to a GC/MS for AA and AAL measurements. The CO_2 produced in the EOR was analyzed using an IR detector selective for CO_2. Although this system can monitor products produced in real time (delayed ca. 20 min by retention times) expensive instrumentation and equipment expertise are still required.

The work described in this chapter was originally in collaboration with the Jeff Dahn group at Dalhousie University. They had used a 64-electrode fuel cell for high throughput screening of Pt and PtRu catalysts. A sputtering system was used to alter the composition of the catalyst. A constant 0.15 mg cm^{-2} was first applied to the catalysts followed by a linear gradient of the metal (s). Activities of the catalysts were determined in the multi-electrode cell using cyclic voltammertry (CV). Once the best composition for the PtRu catalyst was determined, based on its activity, 5 cm^2 catalysts were prepared and sent to us for product analysis. On this end, it was our objective to develop a fast, simple and inexpensive way of testing these catalysts in a DEFC for product analysis. Although the performance and selectivity towards CO_2 for the prepared catalysts did not show significant enhancements, the results will still be briefly described in this chapter.

3.2. Experimental

3.2.1. Materials

Electrodes used in this work consisted of 4 mg cm^{-2} Pt black on Toray^{TM} carbon fiber paper donated by Ballard Power Systems. Anhydrous ethanol was obtained from Commercial Alcohols Inc., while acetic acid and acetaldehyde were obtained from Sigma–Aldrich.

3.2.2. The Fuel Cell

A 5cm^2 commercial cell (Fuel Cell Technology Inc.) was used. The anode inlet and outlet were both modified to prevent the anode solution from contacting any metal parts of the hardware since corrosion within the ports was found to lead to large background conductivity readings. Membrane and electrode assemblies were prepared by hot pressing a 5 cm^2 anode and a 5 cm^2 cathode onto a Nafion® 115 membrane (Dupont) at a pressure of 200 kg cm^{-2} at 135 °C for 90 s. The cell was operated with an anode feed of 0.50 mol L^{-1} ethanol solution at 0.50 mL min^{-1}. The cathode feed was 5% H_2 in N_2 (v/v) at 10 cm^3 min^{-1} to provide a stable reference potential and prevent the formation of oxidation products from ethanol crossing through the membrane. Electrochemical (galvanostatic) measurements were made using a Solartron 1286 electrochemical interface.

3.2.3. Product Analysis

A schematic of the online product analysis system is shown in Figure 3.2. A flow-through conductivity cell (eDAQ Inc.) was used to measure the conductivity due to AA (see section 2.4.2.). After cooling to approximately RT, and passing though the conductivity cell, the exhaust from the fuel cell was collected in a 100 mL flask that was continually flushed with N_2 (at 90 mL min^{-1}) to extract the CO_2. The CO_2 concentration in the exiting N_2 was measured with a Telaire 7001 non-dispersive infrared CO_2 monitor (see section 2.4.1.). Calibration of the CO_2 monitor is described in Ref. [14] and will be described in chapter 4.

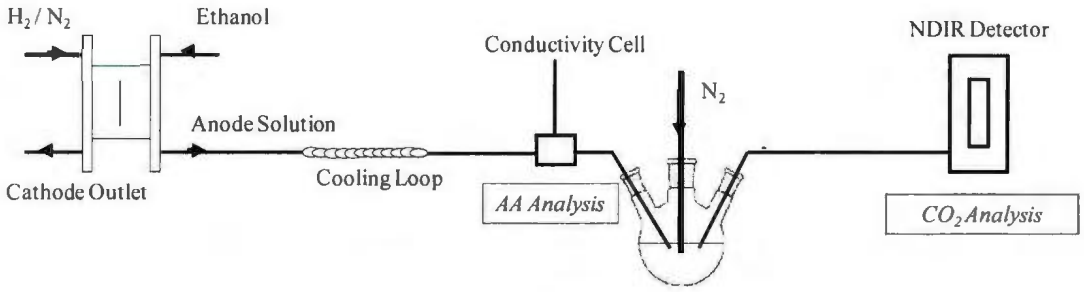

Figure 3.2: Schematic of the online system for product analysis from the direct ethanol fuel cell (adapted from [1]).

Gas chromatography (GC) was periodically used to measure AAL levels in the solution from the anode, without extraction of the CO_2 which would cause loss of AAL. A Varian 3400 GC was used with a RTX®-1301 molecular sieve column (Restek: 60 m x 0.25 mm, 1.4 μm thickness) and flame-ionization detector. Ethanol present in the samples and used as the fuel was used as an internal standard (see section 2.4.3).

All yields reported in this work are faradaic yields based on the current passed by the fuel cell. To calculate the product yields, the experimental number of moles of each of the products was first determined and using Faraday's law of electrolysis, theoretical moles were calculated. A simple % yield calculation followed and these were the values reported in this chapter. For experimental moles of CO_2 (N_{CO2}), the following formula converts the measured concentration (in ppm s^{-1}) to moles s^{-1} taking into consideration the total number of moles of gas passed through the detector per unit time:

$$\frac{CO_2(ppm)}{t} = \frac{N_{CO_2}}{N_{CO_2} + N_{N_2}} 10^6 \qquad (3.1)$$

Experimental moles of AA are easily calculated as each method (conductivity detector

and titration) gives the concentration of AA in the solution. Using the flow rate of the ethanol at the anode and the concentration, the experimental moles s^{-1} are calculated as follows:

$$\frac{N_{AA}}{t} = [AA] \cdot \rho \tag{3.2}$$

where [AA] is the concentration of AA in mol L^{-1}, ρ is the flow rate of ethanol in L s^{-1} and t is time in s.

Using the current passed at the anode, the theoretical number of moles of each product is calculated using equation 1.30. For CO_2, AA and AAL the n values are 6, 2, and 4, respectively.

More in depth non-faradaic methods to calculate product yields are also reported in the literature [15,23]. Andreadis et al. [23] use a more complex method to calculate product yields based on ethanol conversion (X_{EtOH}) and product selectivity (eg. S_{CO_2}) by the following formula:

$$Yield_{CO_2} = X_{EtOH} \cdot S_{CO_2} \tag{3.3}$$

where ethanol conversion is calculated from ethanol concentration ($EtOH_{in}$) , ethanol crossover ($EtOH_{cross}$), the volume fluxes at the inlet and outlet (V_{in} and V_{out}), and the concentrations of each by-product by the following formula:

$$X_{EtOH} = \frac{(0.5\ x\ [CO_2] + [CH_3CHO] + [CH_3COOH]) x\ V_{out}}{(EtOH_{in} - EtOH_{cross}) x\ V_{in}} x\ 100 \tag{3.4}$$

The selectivities towards each product are dependent on the concentrations of each by-product and the volume of the product at the outlet (V_{out}). An example of selectivity towards acetic acid is as follows:

$$S_{CH_3COOH} = \frac{([CH_3COOH])x\ V_{out}}{(0.5\ x\ [CO_2] + [CH_3CHO] + [CH_3COOH])x\ V_{out}}\ x\ 100 \qquad (3.5)$$

3.3. Results and Discussion

3.3.1. Conductimetric Analysis of Acetic Acid

The analysis of acetic acid used here is based on the fact that this is the only component of the fuel cell anode exhaust stream that should contribute to its ionic conductivity. Thus the conductivity measured with a simple flow-through cell can be used to monitor acetic acid production.

The use of a conductivity flow-through cell for the analysis of acetic acid is a novel approach to online fuel cell product analysis. To evaluate the method, calibration curves were obtained by pumping standard solutions of acetic acid through the conductivity cell until a steady reading was obtained. The results did not vary significantly depending on whether the solution was passed though the anode compartment of the fuel cell first, or simply pumped directly into the conductivity cell, although the background conductivity was higher when the fuel cell was used. Plots of conductivity versus $[H^+]$ (e.g.

Figure 3.3) were linear, indicating that the primary contributor to the conductivity is from dissociation of acetic acid.

The origin of the relatively high background conductivity was examined using flame atomic absorption spectroscopy (FAA). It was first presumed that this background was due to metal ions that were leaching out of the fuel cell block supports and into the liquid stream of the anode. A number of metals including: Fe, Ni, Zn, Pb, Cu and Na were tested as they were the most likely candidates for the background problem. No signal was observed for any of the transition metals tested, however a signal was observed for Na. Na standards ranging from 1 – 20 ppm were made and a calibration curve was constructed and is observed in Figure. 3.4. A quadratic curve fit the standards very nicely.

Based on this curve we calculate the Na concentration in our sample to be ca. 2.3 ppm. It was speculated from these experiments that the source of Na was from the Nafion® membrane that was used in the MEA of the cell. As Nafion® is a cation exchange membrane, some H^+ in the membrane could have been replaced by Na^+ ions extracted from the walls of the glass container used to store the Nafion®. It was calculated that the conductance of 0.1 mmol L^{-1} (ca. 2.3 ppm Na) corresponds to ca. 0.1 mS cm^{-1} of the signal in the detector. The background observed was ca. 0.2 mS cm^{-1}(at the time of this experiment), so it was concluded that approximately half of the background conductivity was due to Na^+ ions. The other half of the background was thought to be a consequence of AA leaching from the graphite blocks of the fuel cell. This was presumably AA that had permeated into the blocks during previous experiments, and we have not been able to effectively remove it. It was assumed that this relatively stable background

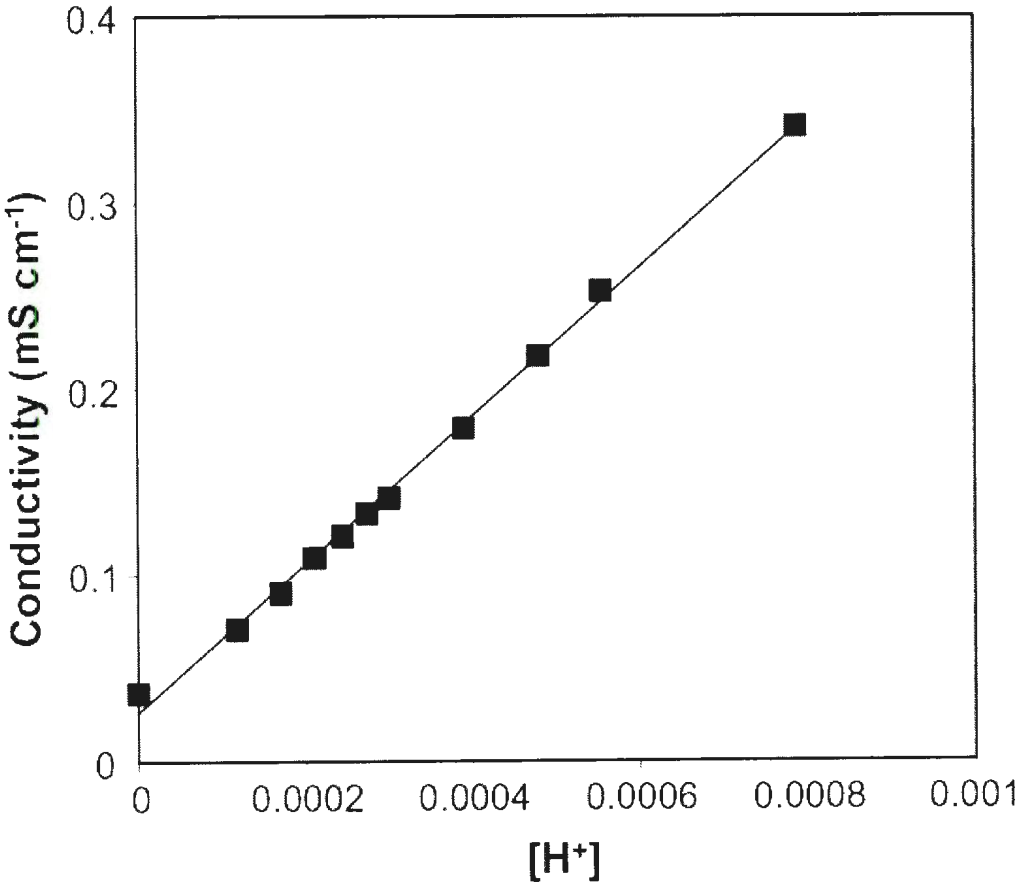

Figure 3.3: Conductivity versus hydrogen ion concentration for acetic acid standards passed through the fuel cell prior to the conductivity detector (Obtained with permission from [1]).

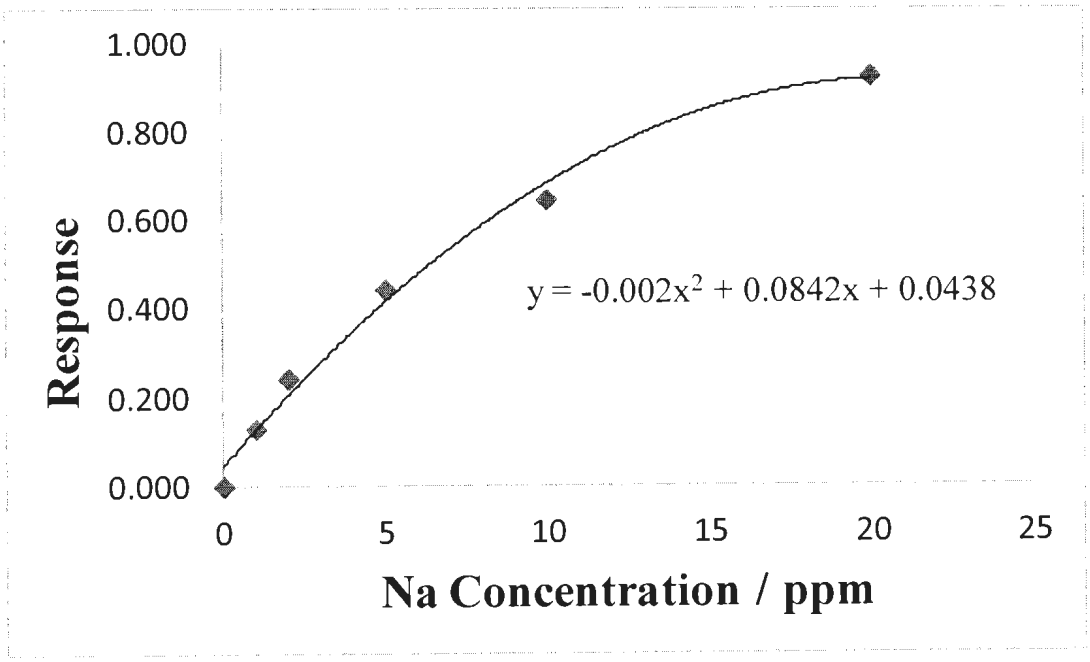

Figure 3.4: Na calibration curve for flame atomic absorption (FAA) testing for ionic conductivity background in fuel cell.

would have a similar effect on both the standards and unknowns, and so unknown AA concentrations were determined from the uncorrected conductivity, and the regression parameters from Figure 3.3. Solutions collected from the fuel cell were regularly titrated with base to check the accuracy of results from the conductivity measurements.

Recent studies have suggested that background conductivity in a typical DEFC could be a result of a different problem. Experiments performed by Jablonski et al. [24,25] in 2011 and 2012 have shown that oxygen gas has the ability to permeate through a Nafion® 117 membrane. They report that under fuel cell conditions, (oxygen is used at the cathode) the oxygen is able to diffuse through the PEM from the cathode to anode and

is able to chemically oxidize ethanol at the anode to produce acetic acid and acetaldehyde. Their results stem from the observed AA and AAL at OCP where no current was passed through the cell. Significant amounts of both products were observed. Furthermore, they reported that at high cell potentials (above 0.3 V) and low current densities, where water is not activated at the anode, the production of AA is not feasible and any reported AA must be a consequence of oxygen permeation. Temperature dependence experiments for oxygen permeation through Nafion® 117 membrane were also carried out. It was reported that an almost exponential relationship was observed between temperature increase and oxygen permeation [25].

Since H_2/N_2 gas was used at the cathode for the experiments described in this chapter, oxygen permeation did not affect the results. If oxygen were used, it would be expected that oxygen permeation would affect the results that were reported in this chapter, since Nafion® 115 membranes (thinner than Nafion® 117) were used and would be more susceptible to oxygen diffusion. Jablonski et al. [24,25] had not reported oxygen permeation at RT, therefore the RT experiments described in the proceeding chapter (using O_2 at cathode and cell voltages below 0.3 V) should not be significantly affected.

Another problem that could add to an increase in background conductivity and could significantly affect the results for product analysis in the literature is the crossover of ethanol from the anode to the cathode. It is well known that significant amounts of fuel (based on cell parameters, MEAs and fuel type) are able to diffuse through the PEM. In a subsequent paper [26] (see chapter 4), we have shown that when fuel crosses through the membrane it is able to react chemically with the oxygen at the cathode. This leads to not

only a large decrease in fuel efficiency and a depolarization (mixed potential) at the cathode, but it can result in excess production of EOR products. When AAL and CO_2 are produced, they will mainly be carried out by the gas stream since they are in the gas phase. However, when acetic acid is produced in the liquid phase, it mainly diffuses back to the liquid anode stream. This will lead to an overestimation of the AA yield since faradaic yields are calculated from the observed current in the cell and this chemical reaction is not accounted for.

The conductimetric system was first tested by using a DEFC operated at ambient temperature with a Pt black anode catalyst. Figure 3.5 shows a conductivity vs. time plot for operation of the cell at a current density of 12 mA cm^{-2} with H_2/N_2 as the cathode gas. The initial decline in conductivity, before the current was switched on, is due to slow removal of AA from the cell following the previous experiment. Diffusion of AA into the membrane and cathode catalyst layer creates a reservoir of AA that can only slowly be removed. After the current was started, the conductivity rose slowly to a plateau of 0.172 mS cm^{-1}. Based on the calibration data in Figure 3.3, this corresponds to an AA concentration of 8.8 mmol L^{-1}, while NaOH titration of the solution collected from the cell over the final 30 min gave 8.4 mmol L^{-1}.

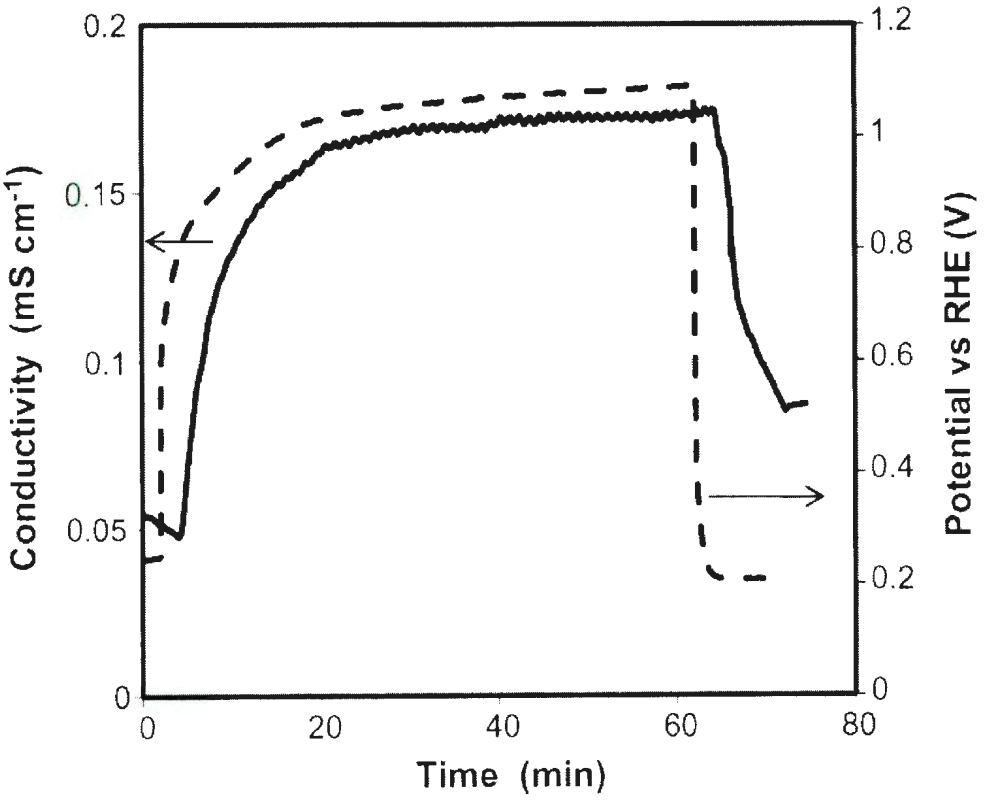

Figure 3.5: Conductivity of the exhaust solution (solid) and potential (dashed) vs. time at 60 mA and room temperature for a DEFC with a Pt anode (obtained with permission from [1]).

Since the detector works on detecting conductivity in a liquid feed, when large amount of CO_2 are produced, a large fluctuation in the signal is observed. The liquid is cooled to RT before the conductivity measurements; therefore the fluctuation would not be caused by evaporated water in the stream. Figure 3.6 illustrates the behavior of the conductivity detector at various temperatures and applied currents. At ambient temperature and a relatively low current of 80 mA (Figure 3.6.a), a smooth conductivity curve was observed. The curve plateaued at ca. 10 min and remained constant at ca. 0.183 mS

cm^{-1} for the duration of the run. Based on the calibration curve in Figure 3.3, this represents an AA concentration of 0.0141 mol L^{-1}. To verify all our conductivity results, a simple acid-base titration was performed in each case. Here the titration gave an AA concentration of 0.0145 mol L^{-1}, which is a deviation of only ca. 2.8%. In Figure 3.6.b, the temperature of the fuel cell was increased to 80°C and the current was increased to 200 mA. It is expected that at elevated temperatures and currents the amount of CO_2 produced in the system would significantly increase and that is what was observed from this conductivity trace. This graph is much choppier than that in Figure 3.6.a due to the higher production of CO_2. As the CO_2 bubbles are formed and exit the cell, the liquid feed is interrupted and that is why we observed a much more noisy response in the conductivity trace. In this trace, it was less obvious where the conductivity became stable. For this reason we once again titrated the liquid feed and found that using the upper limit of the trace gave the appropriate conductivity traces. Using the upper portion of the trace and comparing it to the titration we obtained a deviation of ca. 3.0% between the concentrations from the conductivity and titration. Figure 3.6.c illustrates a conductivity trace where the temperature was ramped to 100°C and 200 mA was once again applied. As shown, the quality of the trace is further degraded as the fluctuations increased. However, once again taking the upper portion of the trace gave a very acceptable percent difference of ca. 7.3%. In Figure 3.6.d, the temperature remained at 100 °C, but the current was doubled to 400 mA. The percent difference in this trace was very small at 3.4%.

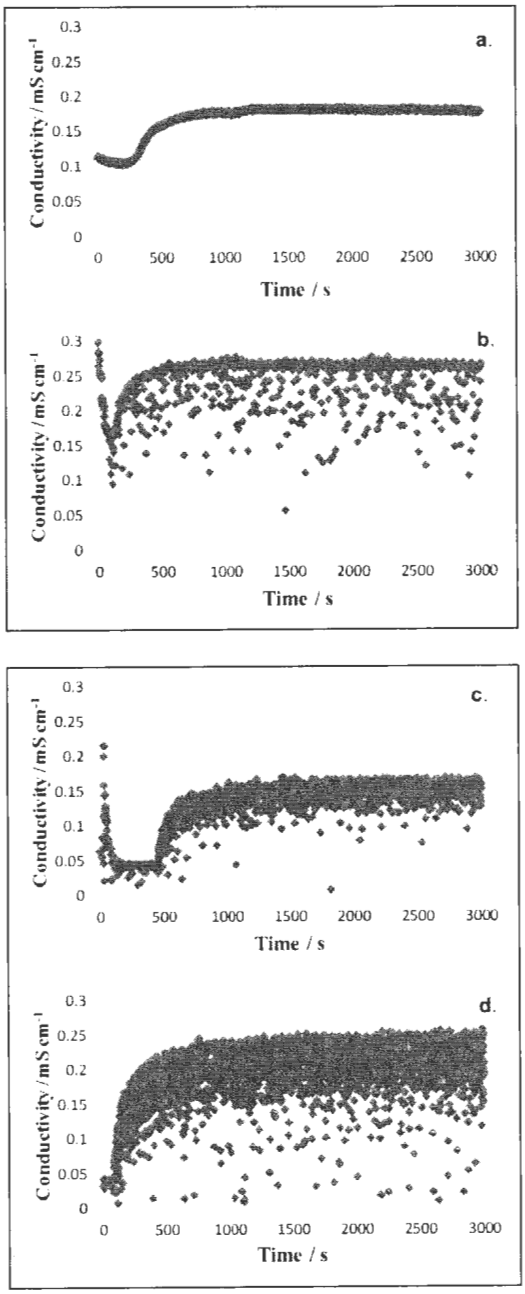

Figure 3.6:.Conductivity traces obtained for acetic acid quantification at various temperatures and currents. **a.)** Ambient temperature and 80 mA, **b.)** 80°C and 200 mA, **c.)** 100°C and 200 mA, and **d.)** 100°C and 400 mA. All measurements were obtained using a commercial 40% Pt anode and cathode (Ballard) in a direct ethanol fuel cell.

The slow response observed in the conductivity traces is due mainly to the large volume of the fuel cell's flow channels and outlet tubing relative to the solution flow rate (0.5 mL min^{-1}). The total dead volume of ca 1.4 mL was found to result in a ca. 15 min response time when an impermeable separator was placed between the two flow fields of the cell. The response time in Figure 3.5 is only slightly higher than this, indicating that the effects of diffusion of acetic acid out of the MEA are relatively minor. While the flux of AA between the cell (graphite blocks and MEA) and ethanol solution will influence changes in the AA concentration in the anode exhaust, it will become negligible relative to the rate of electrochemical acetic acid production under steady state conditions. AA concentrations and yields reported here are therefore based on steady state conductivities.

Results from the data in Figure 3.5 and other room temperatures experiments are summarized in Table 3.1, together with results from titration of the AA produced. There was generally good agreement between the calculated AA yields measured by the two methods, indicating that the conductivity cell provides accurate online measurements. The yield of AA was found to increase somewhat with increasing current density, and this is discussed below with the analytical data for CO_2 and AAL. The reason for the anomalously low conductivity result at 80 mA is unclear. An experiment on another MEA (with 40% Pt/C as the anode catalyst) at 80 mA gave good agreement between the AA yields determined from the conductivity and by titration, and good agreement between the titrations results for the two MEAs (Table 3.1).

Table 3.1: Faradaic yields from conductivity, titration, GC, and CO_2 measurements on the anode exhaust solution from a DEFC with a Pt anode operated at constant current and ambient temperature. Values in parentheses are based on the titration results (reproduced from [1]).

Current (mA)	Acetic acid		CO_2 (%)	Acetaldehyde	
	Conductivity (%)	Titration (%)		Charge Balance (%)	GC[a] (%)
20	29.9	26.5	5.7	64.4 (67.8)	58.3
40	36.3	34.8	2.7	61.0 (50.9)	56.5
60	47.3	45.2	1.7	50.9 (53.0)	48.4
80	40.1	55.5	1.4	57.9 (43.1)	43.8
80 (40% Pt/C)	56.7	58.3	3.0	40.3 (38.7)	Not measured

[a] relative standard deviations for multiple measurement were 3-6%

Table 3.2: Faradaic yields of the EOR products from conductivity, titration, GC and CO_2 measurements on the anode exhaust solution from a DEFC with a Pt anode operated at constant current and 80 °C. Values in parentheses are based on the titration results (Reproduced from [1]).

Current (mA)	Acetic acid		CO_2 (%)	Acetaldehyde	
	Conductivity (%)	Titration (%)		Charge Balance (%)	GC (%)
50	26.1	28.0	14.1	59.8 (57.9)	8.4
100	30.9	34.6	13.5	55.6 (51.9)	4.3
150	37.6	40.9	15.6	46.8 (43.5)	3.0
200	39.5	40.7	18.6	41.9 (40.7)	2.4
250	37.3	39.4	6.1	56.6 (54.5)	2.0

Results for Figure 3.6.b and other 80 °C experiments are reported in Table 3.2. Once again it is shown here that there seems to be a trend between the AA yields and the current applied to the cell. As mentioned above, the values of the titrated AA concentrations and those obtained from the conductivity detector (using the upper limit) are in very good agreement ranging from 3.0-10.7% difference, with all conductivity results slightly underestimating those of the titration.

3.3.2. CO_2 Measurements with a NDIR Based Detector

The use of the Telaire® 7001 NDIR detector for online CO_2 measurements has been previously described [14]. The CO_2 yield vs. time trace recorded concurrently with the conductivity trace shown in Figure 3.5 is shown in Figure 3.7. The peak at ca. 24 min was caused by admission of air into the collection flask when it was emptied, and so is excluded from the following analysis. The peak in CO_2 yield at ca. 8 min is attributed to stripping of adsorbed CO from the anode, as previously discussed [14].

The average CO_2 yield over 1 h from the data in Figure 3.7 was 1.7%, and data for other currents at ambient temperature are presented in Table 3.1. These results are consistent with previously reported values [14], although somewhat lower because of averaging over a longer time period. The decrease in average yield with increasing current is thought to be due to a decreasing influence of the fixed amount of pre-adsorbed CO [14].

When the temperature was increased to 80 °C, the CO_2 yields significantly increased as expected [27]. The CO_2 values shown in Table 3.2 are in good agreement with previous reported literature results under similar cell conditions [15,23].

3.3.3. Acetaldehyde Analysis and Charge Balance

Two of the main products of the electro-oxidation of ethanol were analyzed with the conductivity cell (AA) and the CO_2 monitor. The concentration of the third significant product, AAL, can be estimated by difference because only trace amounts of other products are produced by PEM DEFCs [15,28]. In this work, product yields (faradaic) have been calculated based on the current produced by the cell. Thus the percentage of the current producing AAL (i_{aal}) is calculated as:

$$i_{aal} = 100\% - (i_{aa} + i_{CO2}) \tag{3.6}$$

where i_{aa} and i_{CO2} are the percentages of the current producing AA and CO_2, respectively. To check the validity of using equation 3.6, the AAL level in the solution exiting the anode was measured by GC. The results of these calculations and the GC analyses are given in Table 3.1. The yield of AAL has been calculated from the AA yield from both the conductivity and titration measurements.

To determine the concentration of AAL from GC, acetaldehyde standards ranging from 0.00635 to 0.100 mol L^{-1} were made using ethanol as an internal standard. Due to the broad peaks of both AAL and ethanol (Figure 3.8), peak height ratios were not suitable for calibrating our system. Instead we found that AAL/EtOH area ratios were more acceptable. As shown in Figure 3.9, a linear relationship between the [AAL] and AAL/EtOH peak area ratios was obtained. The shoulders observed in some of the peaks are most likely due to the degradation of the column that was used in these experiments.

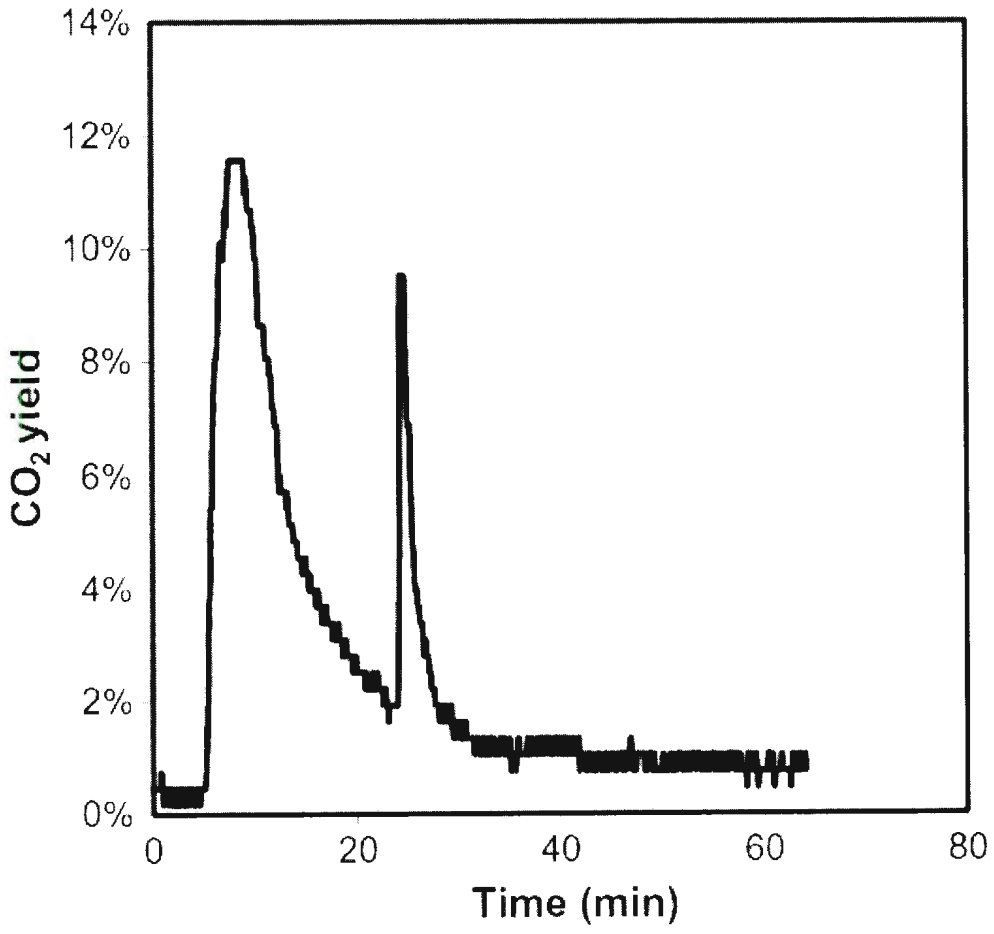

Figure 3.7. Carbon dioxide yield vs. time at 60 mA for a DEFC with a Pt anode (obtained with permission from [1]).

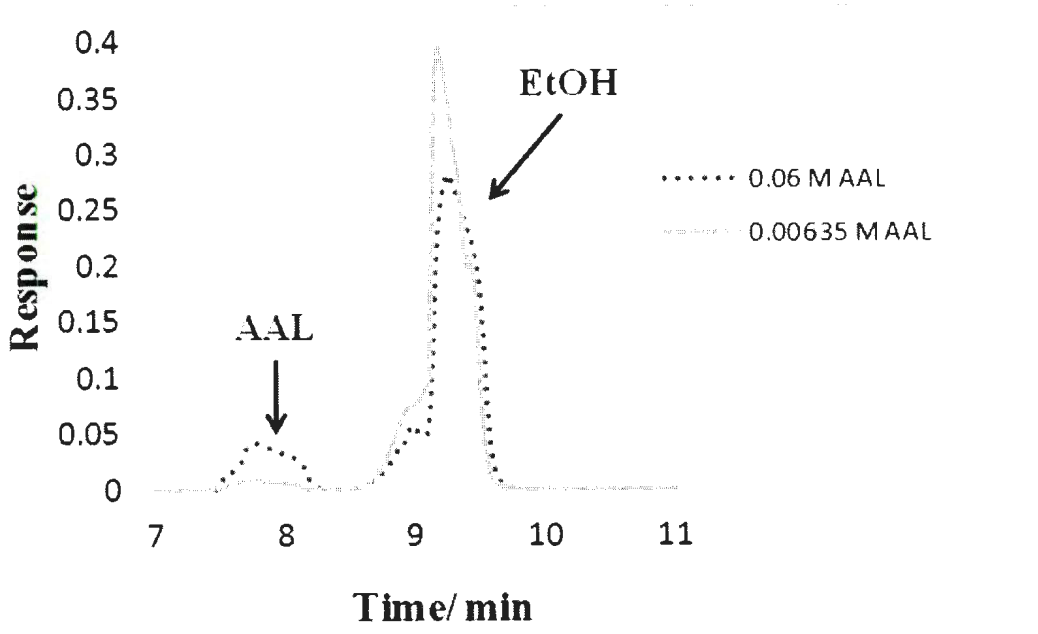

Figure 3.8: Chromatograms for 0.00635 mol L^{-1} and 0.0600 mol L^{-1} AAL standards. Peak area ratios were used to calibrate the GC for AAL sample analysis.

The calculated AAL yields in Table 3.1 are generally in reasonable agreement with the values measured by GC. In all but one case (titration at 80 mA), the GC results are low. Since some AAL should be lost from the cell by crossover, it is very likely that the GC results underestimate the true yield. The results from equation 3.6 are therefore likely to be more accurate. Since it was reported that O_2 is able to cross through the PEM [24,25], it can be assumed that the smaller diatomic gas (H_2) will also diffuse from the cathode. This could lead to oxidation of H_2 at the anode resulting in an overestimation of AAL yield by equation 3.6.

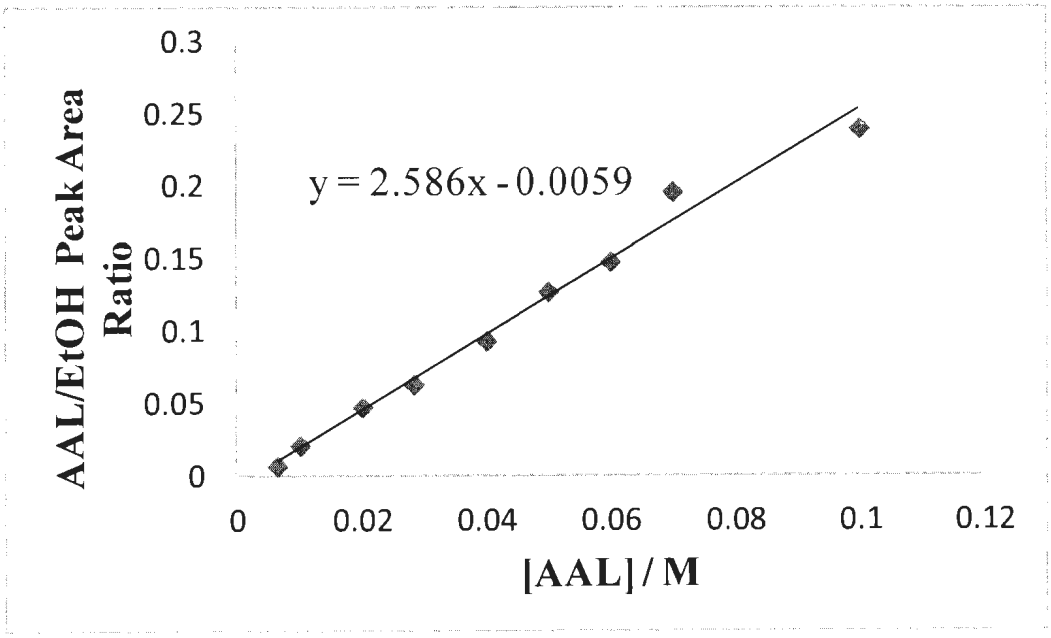

Figure 3.9: Calibration of GC for acetaldehyde analysis. AAL/EtOH peak area ratios were used.

Whichever AAL result is used, the general trend is the same with the yield decreasing somewhat with increasing current. The CO_2 yield also decreases, and these two trends are compensated by an increasing yield of AA. This is consistent with reports that AAL production takes place at lower potentials on Pt than AA production [23,29,30]. The ratios of AA to AAL are similar to values reported at ambient temperature for ethanol oxidation in liquid electrolyte cells [31,32].

GC experiments were also performed with the fuel cell operated at 80 °C. The anode exhaust was cooled with an ice bath in an attempt to lose as little volatilized AAL as possible (see section 2.4.3). However, as shown in Table 3.2, GC analysis of the cooled solution indicated that very low amounts of AAL were collected. For example, at a current of 200 mA (40 mA cm^{-2}), the yield of acetic acid was 39.5% from the conductivity

(40.7% by titration) and the CO_2 yield was 18.6%. These results give a calculated (equation 3.6) acetaldehyde yield of 41.9%, while GC analysis gave only 2.4%. Since the CO_2 and AA measurements were made following cooling of the exhaust, their accuracy does not depend on the cell temperature.

It therefore appears that at elevated temperatures, most of the AAL produced in the cell is lost, presumably via crossover to the cathode and evaporation. Since the low volatility of AA and low solubility of CO_2 would result in much lower loss of these products by crossover, the AAL yield from equation 3.6 should be much more accurate than the value determined by GC. The crossover of AAL into the cathode stream was later confirmed (see chapter 4).

3.3.4. Pt and PtRu Anodes Prepared from Dalhousie University

Catalytic activities of Pt and PtRu catalysts were monitored for a variety of different catalyst loadings by Professor Jeff Dahn's group at Dalhousie University (Dal). Electrodes prepared with the most active Pt and PtRu catalysts were sent from Dalhousie University for us to evaluate under our standard DEFC conditions with product analysis. Figure 3.10 illustrates the polarization curves of these catalysts at 80 °C and 0.5 mol L^{-1} ethanol solution. As shown, the performances of both the Pt and PtRu electrodes were almost identical to that of a commercial Pt black electrode from Ballard Power Systems. It was anticipated that the Pt catalyst would be similar to the commercial Pt catalyst, but based on literature results and the Dalhousie results, the PtRu should exhibit significant

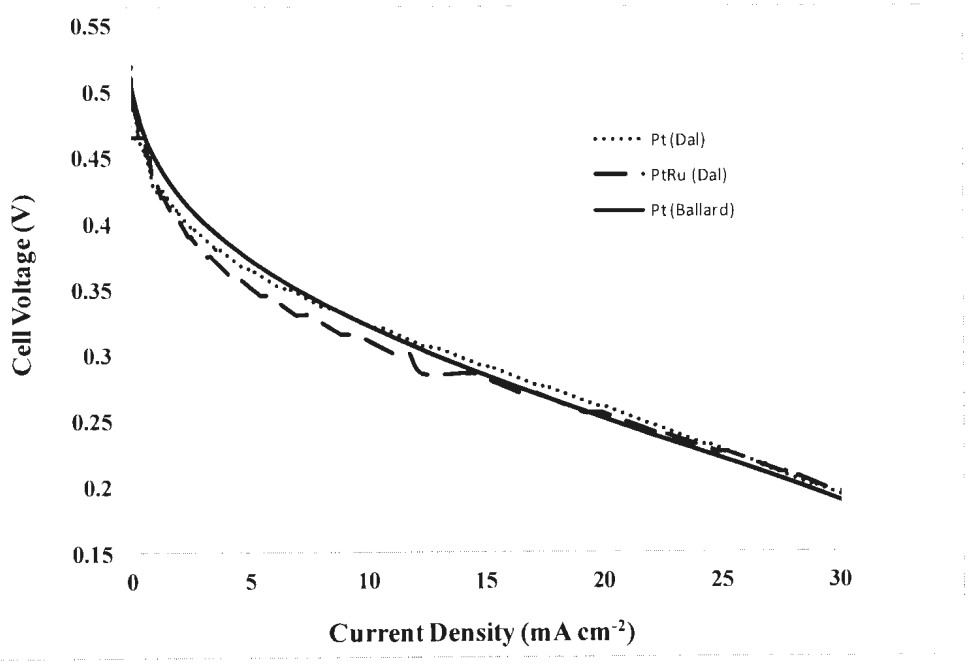

Figure 3.10: Polarization curves for the Pt and PtRu anode catalysts prepared by Dahn et *al.* and a commercial Pt catalyst from Ballard Power Systems.

enhancements in performances. The OCP for all three of the catalysts shown in Figure 3.10 was ca. 575 mV.

Product analyses for the Pt and PtRu electrodes were carried out using the method described in this chapter. The results are described in Table 3.3. When comparing the selectivity towards CO_2 of these catalysts to the Ballard Pt electrode described in Table

Table 3.3: Faradaic yields of the EOR products for Pt and PtRu catalysts prepared at Dalhousie University. CO_2 yields were measured with the NDIR detector, AA yields were calculated from conductivity cell and AAL yields were calculated with equation 3.6. Experiments were conducted at 80 °C, using 0.5 mol L^{-1} ethanol solution and H_2/N_2 gas at the cathode.

Pt (Dalhousie)			
Current (mA)	CO_2 (%)	Acetic Acid (%)	Acetaldehyde (%)
50	14.2	11.7	74.1
100	8.9	8.7	82.4
200	8.1	14.6	77.3
250	7.7	13.8	78.5
PtRu (Dalhousie)			
Current (mA)	CO_2 (%)	Acetic Acid (%)	Acetaldehyde (%)
50	16.0	14.0	70.0
100	8.9	24.2	66.9
200	7.1	29.5	63.4
250	7.4	31.6	61.0

3.2, a significant decrease in shown. Furthermore, both catalysts show a significant decrease in AA production and increase in AAL production. As expected [15] the PtRu catalyst shows a larger yield of AA than the Pt catalysts, however the decrease in CO_2 yield that has been reported for PtRu alloys is absent.

Based on reports in the literature, a few conclusions can be made about these catalysts. First, the significant decrease in CO_2 selectivity of the Pt catalyst compared to that of the commercial Pt catalyst suggests that the Pt loading was too low (0.15 mg cm^{-2}, where that of the Ballard electrode was 4 mg cm^{-2}). In a Ballard electrode, much of the AAL produced within the catalyst layer will be able to react to AA and CO_2 before it can diffuse out of the electrode. Due to the thin catalyst layer in the Dal electrodes, they are more permeable and more of the AAL will escape, resulting in higher AAL yields. This behaviour is observed for methanol oxidation and similar behavior would be expected for ethanol oxidation [33,34].

Although these results are not encouraging in terms of the efficiencies of the new electrodes, they illustrate the value of our analysis system and provide useful information on the kinetics and properties of electrode surfaces in the EOR.

3.3.5. Product Analysis for Homemade High Performance Catalysts

Many catalysts have been tested for performance for the EOR in DEFCs, but very few studies have reported product distribution. Dr. Guangchun Li prepared a series of catalysts using the methods described in [35,36] to be used for product analysis using the methodology described above. Electrodes were prepared on CFP with compositions of Pt, PtRh, PtSnRh, PtSnRu, and PtSnPb. It is known from the literature that Rh is able to in-

crease the selectivity towards CO_2, but tends to show a decrease in performance [6,37]. On the other hand, the incorporation of Sn into the catalyst has been shown to decrease CO_2 selectivity but increase cell performance [8,38]. Using our product analysis methodology, we were able to quickly assess product selectivities for Dr. Li's catalysts.

Table 3.4 describes our results in a DEFC at 100 °C using 0.5 mol L^{-1}ethanol and at O_2 gas at the cathode. As shown in this table, there was a small increase in CO_2 selectivity at the low currents when Pt was alloyed with Rh. This is consistent with literature reports [6,37]. When Pt is was alloyed with Sn and/or Pb a large decrease in CO_2 and increase in acetic acid was observed. This is also consistent with previous experimental values [8,38]. When Sn and Rh were simultaneously introduced into the Pt catalyst, only a slight decrease in CO_2 yield was observed. This was probably due to opposing effects on the CO_2 selectivity. When Sn and Pb were introduced, a very large decrease was observed, and at the higher currents, very little CO_2 was produced.

It should be noted that in some of these experiments, it was calculated that the combined CO_2 and acetic acid yields were over 100%. This would suggest that no acetaldehyde was produced. It is shown in the proceeding chapters that at high temperature using O_2 at the cathode, crossover, resulting in inaccurate acetic acid yields occurs. Therefore the acetic acid measurements in table 3.4 are most likely inaccurate. The CO_2 measurement in table 3.4 should however be fairly accurate as will be described in chapter 4.

Table 3.4: Faradaic yields for CO_2 and acetic acid with various anode catalysts, at 100 °C, 0.5 mol L^{-1} ethanol solution with O_2 at the cathode.

Catalyst	Current (mA)	CO_2 (%)	Acetic Acid (%)
Pt	50	80	31
PtRh	50	90	32
PtSnPb	50	14	58
PtSnRh	50	35	53
Pt	100	66	28
PtRh	100	68	17
PtSnPb	100	6	65
PtSnRh	100	50	68
Pt	200	58	22
PtRh	200	55	15
PtSnPb	200	3	66
PtSnRh	200	47	60

3.4. Conclusion

A system for continuous monitoring of CO_2 and AA levels from a DEFC has been demonstrated. AAL levels can be determined by difference from the applied current, providing continuous monitoring of the distribution of all major (>1%) products from ethanol oxidation in a DEFC. Although it could not be shown that the charge balance is accurate at high temperatures due to loss of AAL, we believe that this system provides a more accurate account of AAL produced during EOR. Since it has been shown that even at elevated temperatures, CO_2, AA and AAL are the only significant products [39]; it can be assumed that the charge balance equation (equation 3.6) is an accurate way of determining AAL production. By using H_2/N_2 at the cathode to provide a reference potential, the negative effects are fuel crossover and oxygen permeation on product selectivity are eliminated.

3.5. References

[1] James, D.D.; Bennett, D.V.; Guangchun, L.; Ghumman, A.; Helleur, R.J.; Pickup, P.G. *Electrochem. Commun.* **2009**, *11*, 1877-1880.

[2] Wang, Q.; Sun, G.Q.; Cao, L.; Jiang, L.H.; Wang, G.X.; Wang, S.L.; Yang, S.H.; Xin, Q. *J. Power Sources* **2008**, *177*, 142-147.

[3] Bergamaski, K.; Gonzalez, E.R.; Nart, F.C. *Electrochim. Acta* **2008**, *53*, 4396-4406.

[4] Lima, F.H.B.; Gonzalez, E.R. *Electrochim. Acta* **2008**, *53*, 2963-2971.

[5] Purgato, F.L.S.; Olivi, P.; Leger, J.M.; de Andrade, A.R.; Tremiliosi, G.; Gonzalez, E.R.; Lamy, C.; Kokoh, K.B. *J. Electroanal. Chem.* **2009**, *628*, 81-89.

[6] Kowal, A.; Li, M.; Shao, M.; Sasaki, K.; Vukmirovic, M.B.; Zhang, J.; Marinkovic, N.S.; Liu, P.; Frenkel, A.I.; Adzic, R.R. *Nat. Mater.* **2009**, *8*, 325-330.

[7] Li, M.; Kowal, A.; Sasaki, K.; Marinkovic, N.; Su, D.; Korach, E.; Liu, P.; Adzic, R. R. *Electrochim. Acta* **2010**, 55, 4331-4338.

[8] Hsieh, C.-T.; Liu, Y.-Y.; Chen, W.-Y.; Hsieh, Y.-H. *Int. J. Hydrogen Energy* **2011**, *36*, 15766-15774.

[9] Su, B. J.; Wang, K. W.; Cheng, T. C.; Tseng, C. *J. Mater. Chem. Phys.* **2012**, *135*, 395-400.

[10] Huang, R. H.; Chiu, T. W.; Lin, T. J.; Sun, C. H.; Chao, W. K.; Tsai, D. C.; Hsueh, K. L.; Shieu, F. S. *J. Power Sources* **2013**, *227*, 229-236.

[11] Park, K. W.; Lee, Y. W.; Sung, Y. E. *Appl. Catal. B* **2013**, *132*, 237-244.

[12] Casic, S.; Gunther, B. H. *Chem. Eng. Tech.* **2012**, *84*, 2204-2209.

[13] Sun, S.; Halseid, M.C.; Heinen, M.; Jusys, Z.; Behm, R.J. *J. Power Sources* **2009**, *190*, 2-13.

[14] Ghumman, A.; Li, G.; Bennett, D.V.; Pickup, P.G. *J. Power Sources* **2009**, *194*, 286-290.

[15] Rousseau, S.; Coutanceau, C.; Lamy, C.; Leger, J.M. *J. Power Sources* **2006**, *158*,18-24.

[16] Arico, A.S.; Creti, P.; Antonucci, P.L.; Antonucci, V. Electrochem. *Solid State Lett.* **1998**, 1, 66-68.

[17] Taneda, K.; Taniyama, T.; Yamazaki, Y. *Electrochemistry* **2004**, *72*, 700-702.

[18] Nakagawa, N.; Kaneda, Y.; Wagatsuma, M.; Tsujiguchi, T. *J. Power Sources* **2012**, *199*, 103-109.

[19] Li, G.; Pickup, P.G. *J. Power Sources* **2006**, *161*, 256-263.

[20] Gao, L.; Huang, H.L.; Korzeniewski, C. *Electrochim. Acta* **2004**, *49*, 1281-1287.

[21] Huang, H.L.; Korzeniewski, C.; Vijayaraghavan, G. *Electrochim. Acta* **2002**, *47*, 3675-3679.

[22] Sanicharane, S.; Bo, A.; Sompalli, B.; Gurau, B.; Smotkin, E.S. *J. Electrochem. Soc.* **2002**, *149*, A554-A557.

[23] Andreadis, G.; Stergiopoulos, V.; Song, S.; Tsiakaras, P. *Appl. Catal. B* **2010**, *100*, 157-164.

[24] Jablonski, A.; Kulesza, P. J.; Lewera, A. *J. Power Sources* **2011**, *196*, 4714-4718.

[25] Jablonski, A.; Lewera, A. *Appl. Catal. B* **2012**, *115*, 25-30.

[26] James, D. D.; Pickup, P. G. *Electrochim. Acta* **2010**, *55*, 3824-3829.

[27] Wang, J.; Wasmus, S.; Savinell, R. F. *J. Electrochem. Soc.* **1995**, *142*, 4218-4224.

[28] Song, S.Q.; Zhou, W.J.; Zhou, Z.H.; Jiang, L.H.; Sun, G.Q.; Xin, Q.; Leontidis, V.; Kontou, S.; Tsiakaras, P. *Int. J. Hydrogen Energy* **2005**, *30*, 995-1001.

[29] Vigier, F.; Coutanceau, C.; Hahn, F.; Belgsir, E.M.; Lamy, C. *J. Electroanal. Chem.* **2004**, *563*, 81-89.

[30] Hitmi, H.; Belgsir, E.M.; Leger, J.M.; Lamy, C.; Lezna, R.O. *Electrochim. Acta* **1995**, *39*, 407-415.

[31] Wang, H.; Jusys, Z.; Behm, R.J. *J. Phys. Chem. B.* **2004**, *108*, 19413-19424.

[32] Vigier, F.; Coutanceau, C.; Perrard, A.; Belgsir, E.M.; Lamy, C. *J. Appl. Electrochem.* **2004**, *34*, 439-446.

[33] Jusys, Z.; Kaiser, J.; Behm, R. J. Electrochim. Acta 2002, 47, 3693-3706.

[34] Masdar, M. S.; Tsujiguchi, T.; Nakagawa, N. J. Power Sources 2009, 194, 618-624.

[35] Li, G.; Pickup, P. G. *Electrochim. Acta* **2006**, *52*, 1033-1037.

[36] Li, G.; Pickup, P. G. *J. Power Sources* **2007**, *173*, 121-129.

[37] Li, M.; Cullen, D. A.; Sasaki, K.; Marinokovic, N. S.; More, K.; Adzic, R. R. *J. Am. Chem. Soc.* **2013**, *135*, 132-141.

[38] Antolini, E.; Gonzalez, E. R. *Electrochim. Acta* **2010**, *55*, 6485-6490.

[39] Lamy, C.; Belgsir, E. M.; Leger, J. M. *J. Appl. Electrochem.* **2001**, *31*, 799-809.

CHAPTER 4

Effects of Ethanol and Product Crossover on the EOR

4.1. Introduction

Parts of this chapter were written by Dr. Peter Pickup and have been published in a peer-reviewed journal [1].

Because of the overriding influence of product distributions on the efficiencies of DEFCs [2], and the problems that would be associated with recycling of the by-products, product analysis is becoming a central feature of DEFC research. There has also been a great deal of fundamental research on product distributions from the electrooxidation of ethanol in conventional cells (e.g. [2, 3-9]). However, since this chapter is focussed on complications related to the fuel cell configuration, only methods that have been applied to fuel cells are reviewed here.

Products from DEFCs have been measured by gas chromatography (GC) [10], liquid chromatography (HPLC) [11], titration [12], non-dispersive infrared spectrometry (NDIR) [13,14], differential electrochemical mass spectrometry [15], and ionic conductivity measurements [14]. In all cases, it has been assumed that all products exit the cell via the anode exhaust of the fuel cell, and there has been no consideration of possible losses of products via crossover to the cathode. Furthermore, in most cases (except [14,15]) the cell has been operated with oxygen or air passing over the cathode. Although this represents normal operation of the DEFC, it complicates the product analysis problem because of ethanol crossover from the anode to the cathode, where it can react with oxygen to produce oxidation products. To avoid the production of ethanol oxidation products at the cathode, results have been reported for experiments with an N_2/H_2 mixture at the cathode [14,16]. Oxygen permeating through the membrane from cathode to anode

has also been recently reported [17,18]. This leads to oxygen reacting with ethanol at the anode leading to a chemical reaction that can produce acetic acid and acetaldehyde. At OCP, significant amounts of both acetic acid and acetaldehyde were detected. Recent papers reporting on product analysis have corrected for both the ethanol/product crossover from the anode and oxygen crossover from the cathode [19,20].

Lamy and co-workers [11] have reported a comprehensive analysis of product distributions from DEFCs with various anode catalysts. HPLC was used to measure acetic acid, acetaldehyde, and CO_2. The charge needed to generate the measured levels of these products was summed and compared with the charge passed by the cell (Table 4.1). Excellent agreement was obtained, apparently indicating that acetic acid, acetaldehyde, and CO_2 were the only significant products (except at high currents where it was thought that there might be significant formation of ethyl acetate). The good charge balance obtained also suggests that loss of products via crossover to the cathode was negligible, although significant crossover of ethanol was observed.

We have also attempted to obtain a charge balance for products measured at the anode exhaust of a DEFC, using a combination of NDIR (CO_2), ionic conductivity (acetic acid), titration (acetic acid), and GC (acetaldehyde) (see chapter 3) [14]. A reasonable balance was obtained at ambient temperature with N_2/H_2 at the cathode, although it did appear that some acetaldehyde was lost to crossover. However, the charge could not be fully accounted for when the temperature was increased to 80 °C, suggesting considerable loss of acetaldehyde to crossover or lost during product collection. Li and Pickup [12] have previously described the influence of elevated temperatures on ethanol crossover. It

Table 4.1. Product analysis for the EOR on a Pt-Sn (9:1) anode catalyst at 80 °C, 3 bar and 2 mol L^{-1} ethanol solution using O_2 gas at the cathode (adapte from [11]).

Current density (mA cm^{-2})	Acetic Acid	CO_2	Acetaldehyde	Total
24	74.8%	8.0%	17.2%	100%
32	76.9%	7.7%	15.4%	100%
40	79.7%	4.4%	15.9%	100%

was reported that the current density as a function of temperature showed an almost exponential relationship. From room temperature to 80 °C, the current density increased by more than 8 times. By increasing the temperature, the kiSince the current density is a good measure for the concentration of ethanol reaching the anode, it is also an appropriate measurement of ethanol flux through the proton exchange membrane. Since it was shown that liquid ethanol is able to cross through the membrane to the gas stream of the cathode, it is very likely that any gaseous products (CO_2 and AAL) formed when operating a DEFC normally would also diffuse through the membrane. Jablonski et *al.* have reported on oxygen permeation from the cathode to the anode [17,18]. It was shown in these studies that the concentration of oxygen diffusion through the membrane also increases in an exponential way as temperature was increased.

In these studies, N_2/H_2 instead of O_2 or air was used at the cathode to prevent the formation of oxidation products from ethanol crossing through the membrane and oxygen diffusion from the cathode.

The purpose of these experiments is to document the effects of ethanol and product crossover on product distributions measured at the anode exhaust of a DEFC. The main objective is to explain the apparent discrepancies between the charge balance results reported in [11,14] and to suggest a more accurate method of product analysis.

4.2. Experimental

4.2.1. Materials

Electrodes consisted of 4 mg cm^{-2} Pt black on Toray™ carbon fiber paper donated by Ballard Power Systems. Anhydrous ethanol was obtained from Commercial Alcohols Inc., while acetic acid and acetaldehyde were obtained from Sigma–Aldrich.

4.2.2. The Fuel Cell

A 5 cm^2 commercial cell (Fuel Cell Technology Inc.) was used. The anode inlet and outlet were both modified to prevent the anode solution from contacting any metal parts of the hardware. Membrane and electrode assemblies were prepared by hot pressing a 5 cm^2 anode and a 5 cm^2 cathode onto a Nafion® 115 membrane (Ion Power) at a pressure of 200 kg cm^{-2} at 135 °C for 90 s. The cell was operated with an anode feed of 0.50 mol L^{-1} ethanol solution at 0.50 mL min^{-1}. The cathode feed was 5% H_2 in N_2 at 10 mL min^{-1} or dry O_2 at 30 mL min^{-1}. Electrochemical measurements were made using an Arbin Instruments potentiostat.

4.2.3. Product Analysis

A flow-through conductivity cell (eDAQ Inc.) was used to measure the conductivity of the anode exhaust solution, which is due to acetic acid. After passing though the conduc-

tivity cell, the exhaust from the fuel cell was collected in a 100 mL flask that was continually flushed with N_2 (at 90 mL min^{-1}) to extract the CO_2. The CO_2 concentration in the exiting N_2 stream was measured with a Telaire 7001 non-dispersive infrared CO_2 monitor. The CO_2 measurements were performed as previously described in section 3.3.2, and calibration of the detector is described in the proceeding sub-section. Conductivity measurements and calibration of the conductivity cell were carried out as described in section 3.3.1. Gas chromatography (GC) was used to measure acetaldehyde levels in the solution from the anode, without extraction of the CO_2 which would cause loss of acetaldehyde, as previously described section 3.3.3. To prevent loss of acetaldehyde by evaporation, the solution exiting the anode was passed through a metal coil cooled with ice and collected in a flask cooled with ice. The good charge balances obtained at ambient temperature (Table 4.3) confirm the efficacy of the acetaldehyde collection procedure. All yields reported in this work are faradaic yields based on the current passed by the fuel cell.

4.2.4. Calibration of the NDIR Detector with Pure CO_2

The calibration of the CO_2 detector was performed in two different manners. A pure CO_2 method which will be described here and a methanol crossover method which will be described in the suceeding chapter (section 5.3.1).

The sensitivity of the detector to atmospheric CO_2 caused many problems when using this system for CO_2 detection in our experiments. In some cases the concentration of CO_2 produced was lower than atmospheric CO_2 (ca. 450 ppm), resulting in large background readings when the N_2 flush rate was low. Furthermore, the detector gave varied background readings based on the amount of use of the detector. For this reason, the de-

tector needed to be calibrated before each series of experiments and was periodically calibrated during a series. For this reason, a quick and easy method for calibrating the system was needed.

The calibration of the detector used pure CO_2 which was obtained directly from the gas line with a 1 cm^3 gas-tight syringe. An initial reading on the syringe was taken and a set administration rate of the CO_2 was implemented. N_2 was passed directly to the CO_2 detector (bypassing the fuel cell). A 3 way valve was placed in the N_2 stream for delivery of the CO_2 to the N_2 stream and into the detector. The CO_2 was passed for 300 s and a final CO_2 reading on the detector was obtained at the end of the time interval. Based on the flow rate of CO_2 and the time passed, the theoretical moles of CO_2 per s was calculated. The reading obtained on the detector was then converted to moles per s and was plotted against the theoretical moles per s. The linear equation obtained from this graph was used to correct for the experimental readings obtain on the detector throughout the experiments.

4.3. Results and Discussion

4.3.1. The Effects of Ethanol Crossover

The crossover of ethanol from the anode to the cathode in DEFCs has been quantified in a number of publications [12,21-23]. One of the major problems associated with crossover is the creation of a mixed potential at the cathode due to simultaneous reduction of oxygen and oxidation of ethanol (equation 4.1).

$$CH_3CH_2OH + nO_2 \rightarrow xCO_2 + yCH_3CHO + zCH_3CO_2H + mH_2O \qquad (4.1)$$

This reaction generates CO_2, acetaldehyde and acetic acid in the cathode catalyst layer. These products can exit the fuel cell via the cathode stream, or they can crossover through the membrane and exit with the fuel stream. In addition, the acetaldehyde can undergo further electrochemistry as it passes through the anode catalyst layer. O_2 crossover to the anode has also been reported [17,18] and can generate ethanol oxidation products at the anode via reaction (4.1). It is important to note that the production of CO_2, acetaldehyde and acetic acid by reaction (4.1) does not produce a current in the external circuit. If these products cross over to the anode they will cause overestimation of the product yields measured in the anode exhaust.

In order to investigate the effects of reaction (4.1) on the apparent product yields from a DEFC, results were compared for experiments with either O_2 or N_2/H_2 passing through the cathode compartment. Use of O_2 corresponds to the normal operation of the DEFC (use of air would not significantly change the results, except for a decrease in cell performance), while use of N_2/H_2 prevents reaction (4.1) from occurring. The H_2 was included to provide a stable reference potential, but was diluted with N_2 to minimize the effects of H_2 crossover.

Initial experiments were conducted with the cell at open circuit with O_2 at the cathode in order to assess the non-electrochemical formation of acetic acid via reaction (4.1). Since reaction (4.1) will occur under all operating conditions when O_2 is present at the cathode, the open circuit data provide an assessment of the errors that can be produce in the measurement of electrochemical product yields. Since the publication of these re-

sults, other research group have calculated products yields by first correcting for the products produced at open circuit [19,20].

4.3.2. Acetic Acid Produced by Ethanol Crossover

A conductivity cell was used to monitor acetic acid levels in the anode exhaust from the fuel cell. This method has been shown to provide accurate online measurements of acetic acid yield [14] and has provided a very convenient way of making a preliminary assessment of the effects of crossover. Figure 4.1 shows a conductivity trace for the anode exhaust with the fuel cell at ambient temperature under various open circuit conditions. Initially, N_2/H_2 was passed through the cathode compartment and deionised water was passed through the anode compartment, in order to establish a background reading. The high initial conductivity was due to residual acetic acid from previous experiments. As seen in Figure 4.1, there was still a significant concentration of acetic acid leaching from the cell after an hour of flushing with water at 0.5 mL min^{-1}. This was traced to acetic acid that had absorbed into the graphite blocks of the cell and sodium ions in the Nafion® membrane (see section 3.3.1). Since, this background acetic acid was also present during calibration, it has little effect on the accuracy of acetic acid yields determined from steady-state conductivity readings [14], except at very low acetic acid concentrations. It is important to note that the accumulation of acetic acid and other products in the fuel cell plates is probably very common, but has not previously been reported.

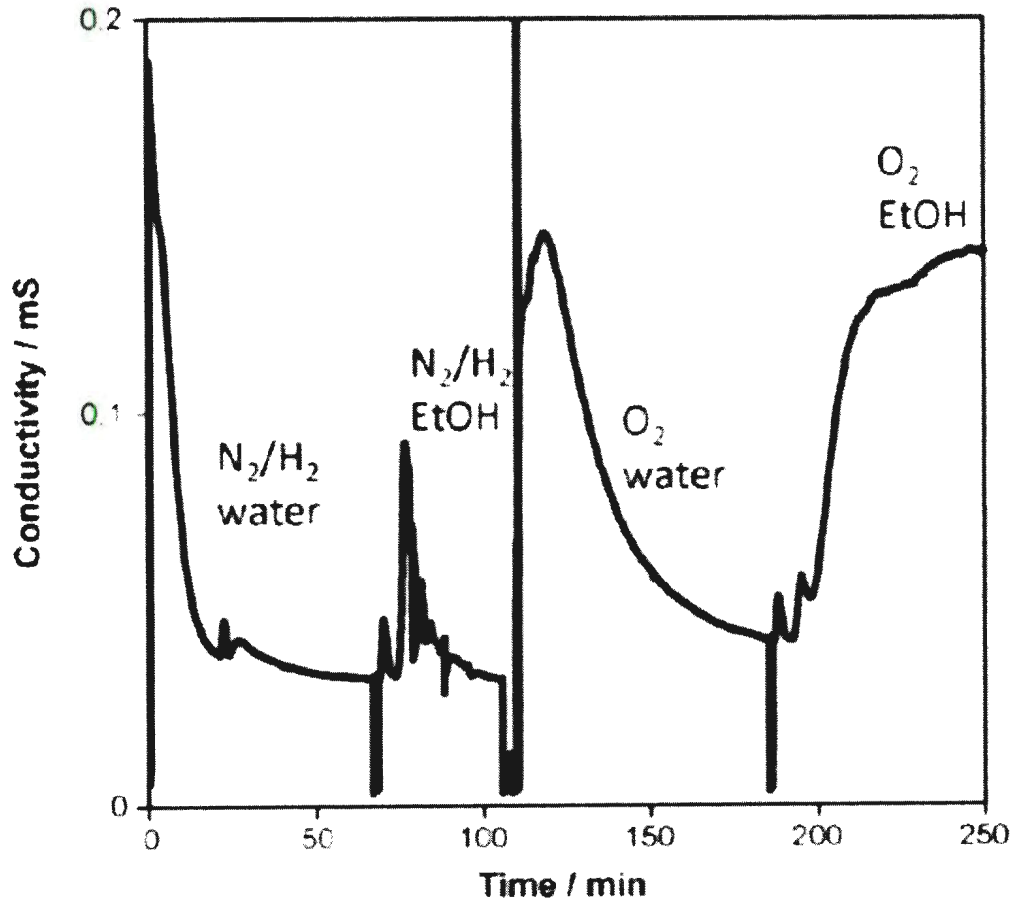

Figure 4.1: Ionic conductivity of the anode exhaust of a DEFC at open circuit and ambient temperature with N_2/H_2 at the cathode and water at the anode (0–67 min), N_2/H_2 at the cathode and 0.5 mol L^{-1} ethanol at the anode (75–105 min), O_2 at the cathode and water at the anode (110–185 min), and O_2 at the cathode and 0.5 mol L^{-1} ethanol at the anode (190–250 min) (Obtained with permission from [1]).

Once the background reading was reasonable stable (33 μS), the anode stream was changed to 0.5 mol L^{-1} ethanol to check whether the reaction with oxygen dissolved in the ethanol solution would contribute to the apparent acetic acid yield. There was a transient increase in conductivity due to leaching of acetic acid from the cell during the

switch over (while the anode flow was off), but the reading fell back to the 33 μS background relatively quickly (the dead volume limits the response to ca. 15 min [14]). Then, the anode stream was switched back to water, and the cathode stream was switched to O_2. There was a larger transient increase in conductivity this time because the O_2 was able to react with residual ethanol in the cell that had crossed over to the cathode. However, again the conductivity fell reasonably quickly, and would presumably have reached the previous value of 33 μS given sufficient time. Finally, the anode stream was switched to 0.5 mol L^{-1} ethanol with O_2 at the cathode. The conductivity of the anode exhaust rose over a period of an hour to reach an approximately constant value of 140 μS. This conductivity corresponds to an acetic acid concentration of ca. 5 mmol L^{-1}, which can be attributed to the reaction of ethanol with O_2 at the cathode. More recent results suggest that a portion of this acetic acid produced is likely caused by the oxygen permeating through the Nafion® membrane reacting with ethanol at the anode [19,20]. However, at ambient temperatures, it is most likely due to ethanol crossover.

An assessment of the fraction of the acetic acid produced at the cathode that is detected in the anode exhaust can be made by considering the flux of ethanol that crosses to the cathode. Under the conditions used here, the flux of ethanol reaching the cathode can be estimated to be ca. 1.6×10^{-8} mol cm^{-2} s^{-1} (based on n = 4 and 6 mA cm^{-2}; Nafion® 115, 0.5 mol L^{-1} ethanol) [12]. This flux of acetic acid crossing back to the anode would yield a concentration in the anode exhaust of 9.3 mmol L^{-1} (0.5 mL min^{-1}). Since the data in Figure 4.1 show that ca. 5 mmol L^{-1} acetic acid was detected, and the yield of acetic acid would not be expected to be much greater than 50% (see Table 4.2), it appears that

most of the acetic acid produced at the cathode exits the cell via the anode. This is presumably because the low volatility of acetic acid favours crossover relative to evaporation into the cathode gas stream.

Confirmation that acetic acid crosses through the membrane was obtained by passing 0.5 mol L^{-1} acetic acid through the cathode compartment of the cell (5 mL min^{-1}) and measuring the conductivity of water passing through the anode compartment (5 mL min^{-1}). Changing from pure water at the cathode to 0.5 mol L^{-1} acetic acid produced an increase in the conductivity at the anode from the background level to a new steady-state level. At ambient temperature, the conductivity of the solution exiting the anode corresponded to an acetic acid concentration of 0.1 mmol L^{-1}, while at 80 °C the acetic acid concentration at the anode rose to 21 mmol L^{-1}. Although these concentrations may appear to be too low to be consistent with the interpretation of the data in Figure 4.1, it should be noted that the concentration of acetic acid in the cathode catalyst layer in that experiment is determined by the balance of the flux of ethanol to the cathode and the rate of evaporation of the acetic acid produced. Because of its low volatility, very high concentrations of acetic acid can quickly accumulate in the cathode.

Table 4.2: Faradaic yields from titration (acetic acid) and NDIR (CO_2) measurements on the anode exhaust solution from a DEFC with a Pt anode. The cathode gas was either N_2/H_2 or O_2 (adapted from [1]).

Current (mA)	T (°C)	Acetic Acid		CO_2	
		N_2/H_2	O_2	N_2/H_2	O_2
20	Ambient	26.5%	42.1%	5.7%	6.6%
40	Ambient	34.8%	48.4%	2.7%	4.0%
60	Ambient	45.2%	57.1%	1.7%	2.5%
80	Ambient	55.5%	61.8%	1.4%	2.0%
50	80	28.0%	49.4%	14.1%	20.0%
100	80	34.6%	54.2%	13.5%	25.4%
150	80	40.9%	46.7%	15.6%	25.0%
200	80	40.7%	46.1%	18.6%	24.0%

Some results previously reported in chapter 3.

The results shown in Figure 4.1 clearly demonstrate that reaction (4.1) at the cathode produces acetic acid that exits the cell via the anode exhaust. It should be noted that all of the data shown in Figure 4.1 were obtained at open circuit, and that the acetic acid produced at the cathode is not the result of current passed by the cell. In order to assess the effects of reaction (4.1) on the measured faradaic yields of acetic acid when the cell is operating, yields measured with O_2 and N_2/H_2 at the cathode were compared. Results for operation of the cell at ambient temperature and 80 °C are shown in Table 4.2. Under all conditions, the apparent yield of acetic acid in the anode stream was significantly higher when O_2 was used at the cathode, indicating that the contribution from reaction (4.1) caused large errors. At both ambient temperature and 80 °C, the absolute error in the acetic acid yield decreased significantly with increasing current density. This is ex-

pected because the amount of acetic acid produced by reaction (4.1) would be expected to be almost constant, regardless of the applied current, while the total amount of acetic acid increases with increased current density.

4.3.3. CO_2 Yields

CO_2 yields measured with the NDIR detector are reported in Table 4.2. At both ambient temperature and 80 °C, the yield was higher at all currents when O_2 was used at the cathode. It seems unlikely that significant amounts of CO_2 produced at the cathode would cross the membrane to the anode, since it can much more readily diffuse into the O_2. The effect is more likely a consequence of the higher CO_2 concentration in the cathode catalyst layer, which would inhibit CO_2 crossover from the anode. The error in the CO_2 yield (here the result with O_2 is presumably most accurate) generally decreased with increasing current density (Table 4.2), as expected for a constant flux of CO_2 produced at the cathode. However, the effect is less clear cut than for acetic acid because of the greater uncertainties in the CO_2 results (resulting from the lower yields and greater time dependence).

4.3.4. Acetaldehyde Crossover

Acetaldehyde production at the cathode by reaction (4.1) would be expected to be small relative to acetic acid production because of the low flux of ethanol and high concentration of oxygen. In addition, acetaldehyde produced at the cathode would be expected to exit the cell primarily via the cathode gas stream because of its high volatility. No attempts were therefore made to measure crossover of acetaldehyde from the cathode to the anode. Much more of a concern is the crossover of acetaldehyde from the anode to the

Table 4.3: Faradaic yields from titration, GC, and NDIR measurements on the anode exhaust solution from a DEFC with a Pt anode. The cathode gas was N_2/H_2 (adapted from [1]).

Current (mA)	T (°C)	Acetic Acid	CO_2	Acetaldehyde	Total
20 [a]	Ambient	26.5%	5.7%	58.3%	90.5%
40 [a]	Ambient	34.8%	2.7%	56.5%	94.0%
60 [a]	Ambient	45.2%	1.7%	48.4%	95.3%
80 [a]	Ambient	55.5%	1.4%	43.8%	100.7%
50	80	28.0%	14.1%	8.4%	50.5%
100	80	34.6%	13.5%	4.3%	52.4%
150	80	40.9%	15.6%	3.0%	59.5%
200 [a]	80	40.7%	18.6%	2.4%	61.7%

[a] Results previously reported in chapter 3.

cathode during operation of the cell, which would result in underestimation of acetaldehyde yields. In order to investigate this, full product analyses were performed with N_2/H_2 at the cathode to avoid complications due to reaction (4.1). In these experiments, the CO_2 yield was determined with a commercial NDIR monitor interfaced to the anode exhaust [13], while acetic acid in the anode exhaust was titrated with NaOH (conductivity measurements gave similar results [14]). Acetaldehyde in the anode exhaust was determined by GC [14]. Apparent yields of all products measured at the anode exhaust with the cell operated at ambient temperature and 80 °C are listed in Table 4.3.

At ambient temperature, a reasonable charge balance was obtained at all current densities employed. There did appear to be some loss of products at low currents, but this

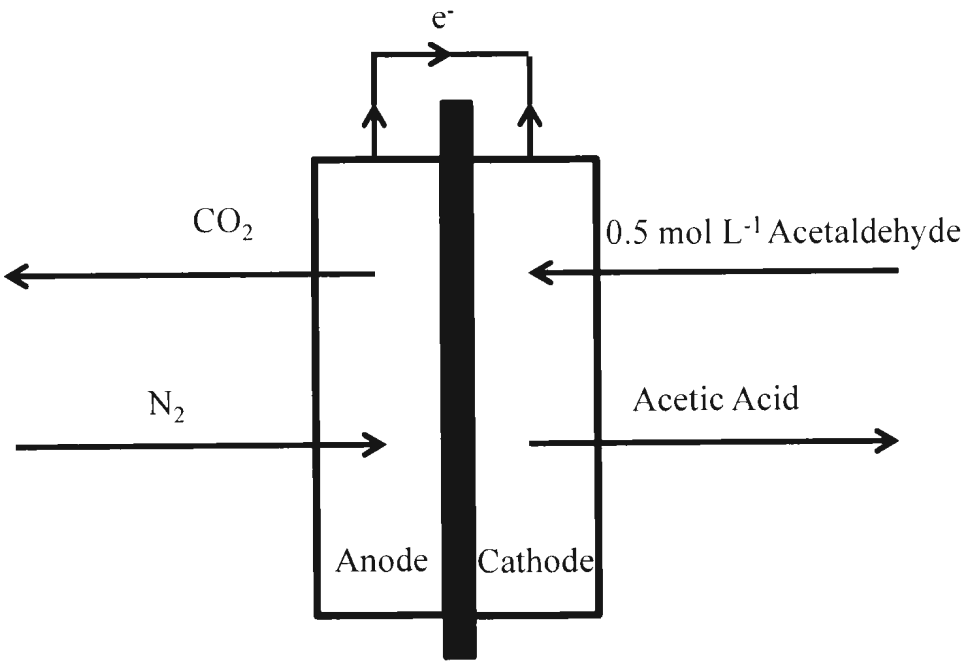

Figure 4.2: Schematic of DEFC setup in crossover mode with 0.5 mol L^{-1} acetaldehyde at the cathode and N_2 at the anode for determination of acetaldehyde flux through membrane.

is more likely to be due to a systematic error that is more significant at low concentrations. If it were due to loss of acetaldehyde by crossover (or during collection of the acetaldehyde), a similar discrepancy would be observed at each current.

In contrast, the charge balance was poor when the cell was operated at 80 °C, indicating substantial product loss at all currents employed. The low acetaldehyde concentrations measured and the fact that the loss increases with increasing acetaldehyde concentration both suggest that acetaldehyde loss (by crossover) is the main factor, although crossover of CO_2 and acetic acid must also occur. It should be noted that the low total

product yield at 80 °C should not be due to inaccuracies in the product analyses, since these were all performed after cooling of the anode exhaust stream to ambient temperature.

In order to confirm that acetaldehyde crossover does occur, and to attempt to quantify its rate, experiments were conducted with aqueous acetaldehyde as the fuel with the cell operated in "crossover mode" (Figure 4.2). Thus 0.5 mol L^{-1} aqueous acetaldehyde was passed through the cathode compartment and N_2 was passed through the anode, as originally reported for measuring methanol crossover [24]. In this mode, acetaldehyde crossing the membrane is oxidized at the anode while water is reduced at the cathode, which acts as a dynamic hydrogen electrode (DHE). The limiting current should provide a measure of the acetaldehyde flux across the membrane.

At ambient temperature, the current due to acetaldehyde crossover was too small to be unambiguously detected. However, at 80 °C substantial currents due to acetaldehyde oxidation at the N_2 flushed anode were measured. Unlike in similar experiments with methanol, the current at constant potential did not reach a steady state, continuing to decay over the ca. 30 min measurement times employed. This is illustrated in Figure 4.3, where the current range over ca. 30 min at each potential is shown as a series of points at 5 s intervals. The highest currents were seen at 700 and 800 mV vs. DHE (depending on the time). The lower currents at higher potentials appear to be due to changes in product distributions (see below), which change the effective n-value (electrons per acetaldehyde molecule) of the reaction.

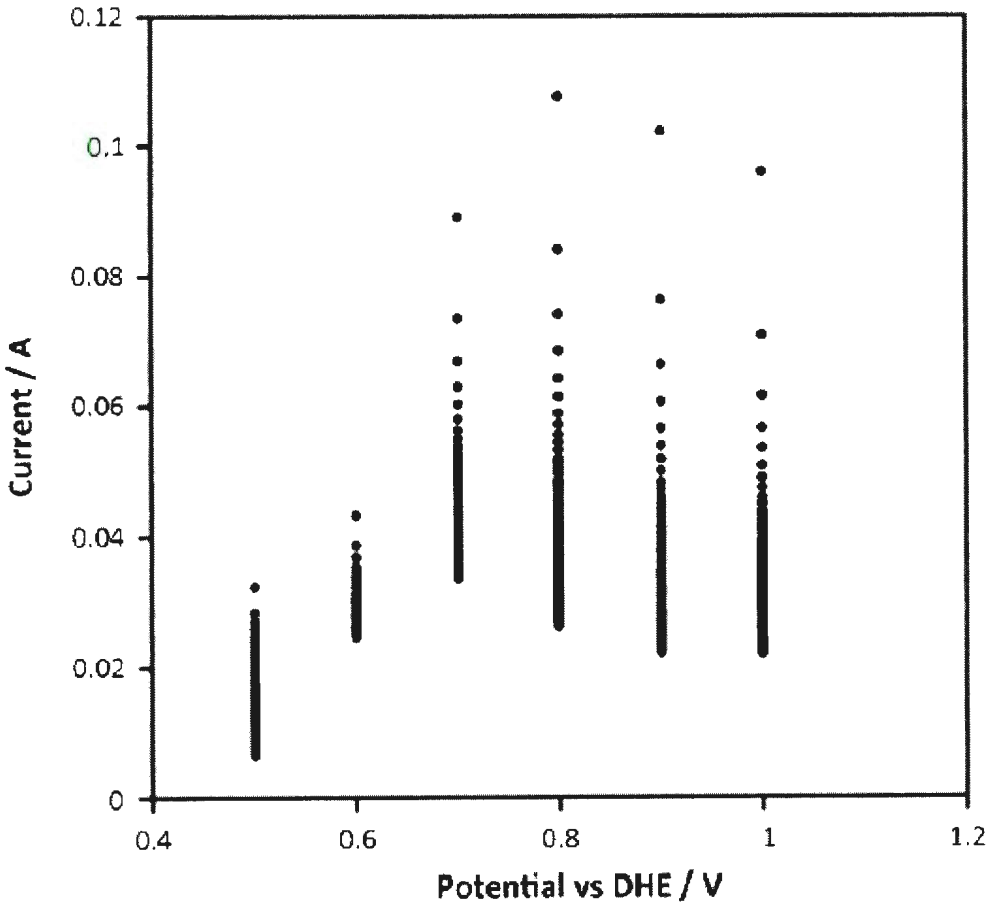

Figure 4.3: Current vs. potential for acetaldehyde oxidation in crossover experiments with 0.5 mol L^{-1} acetaldehyde at the cathode (DHE) and N_2 at the anode. Individual points show the currents (decreasing with time) at 5 s intervals at each potential (obtained with permission from [1]).

In order to convert the currents in Figure 4.3 to acetaldehyde fluxes, it is necessary to know the n-value. The yields of CO_2 and acetic acid were therefore measured by passing the N_2 from the anode through the NDIR detector (after condensing vapours) and passing the liquid cathode exhaust through a conductivity detector, respectively. The liquid cathode exhaust was also titrated with NaOH(aq) to obtain more accurate average

Table 4.4: Average Faradaic yields from titration (acetic acid) and NDIR (CO_2) measurements during acetaldehyde crossover measurements at 80 °C (reproduced from [1]).

Potential (mV vs. DHE)	CO_2	Acetic Acid
600	87%	21%
700	90%	18%
800	54%	20%
900	33%	27%
1000	25%	30%

acetic acid yields. Average yields from these experiments are reported in Table 4.4. It is assumed here that most of the acetic acid crosses through the membrane to the cathode because of its low volatility

At all potentials, the yield of CO_2 was found to decrease with time, from values above 100% (e.g. 140% at 700 mV), while the yield of acetic acid increased somewhat. The high apparent initial CO_2 yields can be attributed to stripping of CO from the anode [13] which requires only two electrons versus five electrons (per mole of CO_2) for production of CO_2 from acetaldehyde. The additional current due to CO oxidation accounts in part for the observed current decay, particular at short times. However, there was also an increase in acetic acid (n=2) to CO_2 (n=5) ratio with time, which would result in a current decay at constant acetaldehyde flux.

At the end of the 700 mV run, the measured CO_2 yield (with n=5) was ca. 70%, while the acetic acid yield was ca. 20% (averages for the full run were ca. 90% and 18%,

respectively). The charge balance here is satisfactory in light of the complications from adsorbed CO and the changing product distribution. However, the CO_2 yield dropped sharply at higher potentials, while the acetic acid yield increased only slightly, leading to large fractions of the charge unaccounted for (Table 4.4). This must be due to a combination of acetic acid evaporation into the gas stream, and crossover of CO_2 to the liquid stream.

An estimate of the steady-state flux of acetaldehyde across the membrane was made using the current and product distribution measured at the end of the run at 700 mV. The n-value (per acetaldehyde molecule) was taken as 8.2, which is a product weighted average of n = 2 for acetic acid production and n = 10 for CO_2 production. A flux of 4.3×10^{-8} mol s^{-1} was obtained. This corresponds to only ca. 1% of the acetaldehyde entering the cell, which appears to indicate that acetaldehyde crossover cannot account for the very low apparent acetaldehyde yields observed for ethanol oxidation at 80 °C (Table 4.3). However, it is possible that the very low boiling point of acetaldehyde could result in evaporation of a large fraction before it can be oxidized in the crossover experiments. To test this, the N_2 flow at the anode was stopped during a crossover experiment at 700 mV in order to slow down the evaporation of acetaldehyde. The result, shown in Figure 4.4, was a large jump in the current to a relatively stable value. This provides clear evidence that the electrochemical method greatly underestimates the crossover of acetaldehyde.

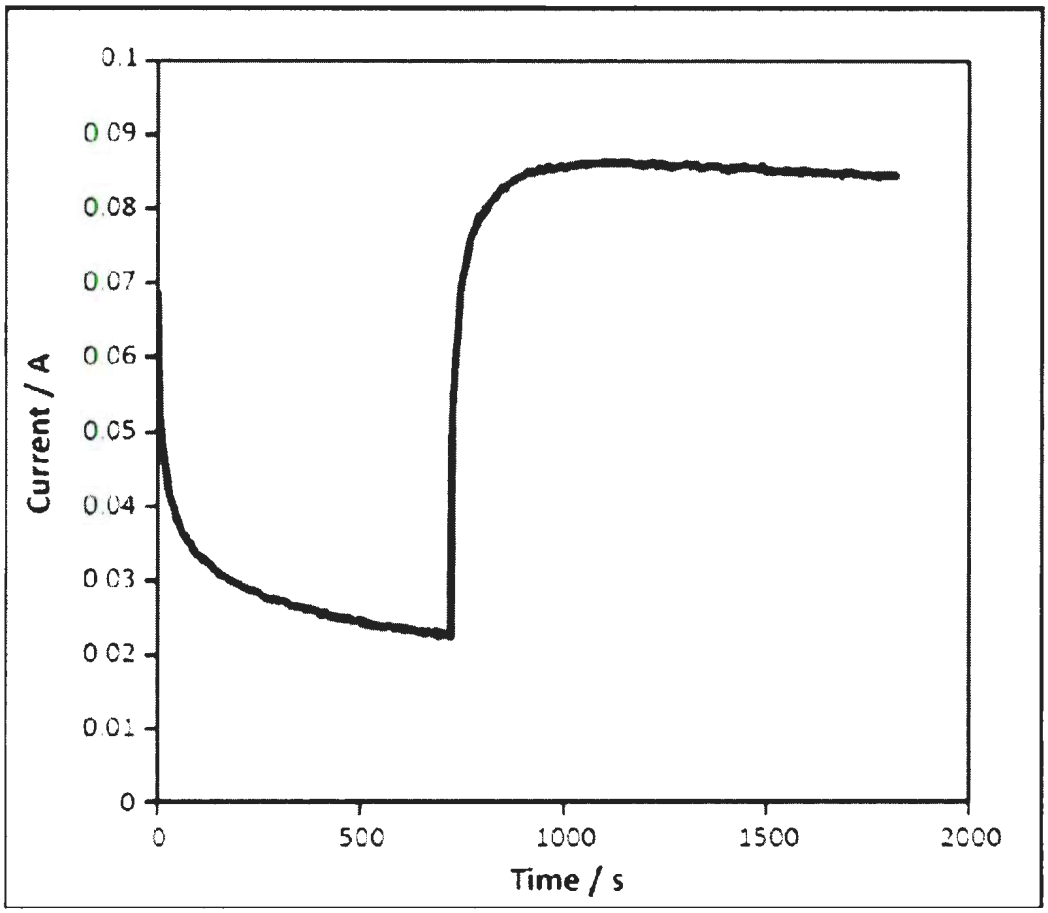

Figure 4.4: Current vs. time at 700 mV vs. DHE for acetaldehyde oxidation during a crossover experiment with 0.5 mol L^{-1} acetaldehyde at the cathode (DHE) and N_2 at the anode. The N_2 flow was stopped at ca. 700 s (obtained with permission from [1]).

4.3.5. Product Analysis at the Cathode

It is clear from the results presented above that accurate analysis of product yields and distributions from electrochemical oxidation of ethanol in a DEFC requires analysis of products exiting at both the anode and the cathode, as well as the absence of oxygen at the cathode (which would lead to a mixture of chemical and electrochemical products). In order to assess the loss of CO_2 via the cathode, the CO_2 concentration was measured in the N_2/H_2 exhaust from the cathode following collection of the liquid products in a cooled flask. The results are reported in Table 4.5 as the percentage of the charge passed required to produce the CO_2 measured at the cathode. Based on the CO_2 yields measured at the anode (Table 4.3), which increased slightly with increasing current, the yield at the cathode due to crossover should also increase slightly. The decreasing yields actually observed at the cathode therefore suggest a systematic error in the measurements. This can be attributed to the effect of the background CO_2 reading which can lead to significant overestimation of CO_2 yields at low currents. At 200 mA, where the results should be most accurate, it can be seen by comparing the result in Tables 4.3 and 4.5 that ca. 23% of the CO_2 produced at the anode crossed to the cathode, and that the total CO_2 yield was ca. 24%.

In another set of experiments, acetaldehyde and acetic acid in the cathode gas (N_2/H_2) were collected with a cold trap (cooled with liquid N_2) and analysed by CG (acetaldehyde) and titration (acetic acid). The results are reported in Table 4.5 as faradaic yields. It is clear from these results that there was substantial crossover of both acetic acid and acetaldehyde to the cathode. However, the precision and accuracy of the results is

Table 4.5: Faradaic yields from titration, GC, and NDIR measurements on the cathode exhaust gas from a DEFC operated at 80 °C with a Pt anode. The cathode gas was N_2/H_2 (adapted from [1]).

Current (mA)	Acetic Acid (%)	CO_2 (%)	Acetaldehyde (%)
50	0	13	26
100	8	7.4	12
150	136	6.2	7.5
200	72	5.4	41

obvious very poor. For acetic acid, the problem appears to be due to its low volatility, which causes it to exit the cell randomly in water droplets that condense in the cathode gas stream. For acetaldehyde, the high volatility makes it difficult to avoid losses during trapping and preparation of the sample for analysis. The main issue in the experiments reported here appears to be loss of acetaldehyde during the rapid release of CO_2 that was also collected in the cold trap. Further work is focussed on developing better methodology for a complete and simultaneous measurement of all products from both sides of the cell.

4.4. Conclusions

The results presented here show that it is very difficult to make accurate measurements of product distributions from a DEFC, particularly at elevated temperatures. Even if all products where determined at both the anode and cathode exhausts, it would be extremely

difficult to divide the results into individual values for the anode (due to the current flow) and cathode (due to reaction with O_2). At ambient temperature, acceptable accuracies for acetic acid and acetaldehyde yields can be obtained by analysing the anode exhaust with N_2/H_2 at the cathode. However, the cell is no longer a fuel cell under these conditions, and the CO_2 yield measured at the anode may be inaccurate.

At elevated temperatures, all crossover rates are greatly elevated, and there is the added complication of acetaldehyde crossover. Product yields should be determined with N_2/H_2 at the cathode and by summing the products at both exhausts.

Finally, it is necessary to consider the origin of the excellent charge balances, based on analysis of the anode exhaust only, reported by Lamy and co-workers for a DEFC operated at 80 °C with O_2 at the cathode [11]. Under these conditions, the acetic acid yield would be overestimated because of the contribution from reaction (4.1), while the acetaldehyde and CO_2 would be underestimated because of their crossover to the cathode. It therefore appears that these two effects cancelled each other in Lamy's work.

4.5. References

[1] James, D.D.; Pickup, P.G. *Electrochim. Acta* **2010**, *55*, 3824-3829.

[2] Vigier, F.; Rousseau, S.; Coutanceau, C.; Leger, J.M.; Lamy, C. *Top. Catal.* **2006**, *40*, 111-121.

[3] Fujiwara, N.; Friedrich, K.A.; Stimming, U. *J. Electroanal. Chem.* **1999**, *472*, 120-125.

[4] deSouza, J.P.I.; Queiroz, S.L.; Bergamaski, K.; Gonzalez, E.R.; Nart, F.C. *J. Phys. Chem. B* **2002**, *106*, 9825-9830.

[5] Wang, H.; Jusys, Z.; Behm, R.J. *J. Phys. Chem. B* **2004**, *108*, 19413-19424.

[6] Santos, V.P.; Del Colle, V.; de Lima, R.B.; Tremiliosi-Filho, G. *Langmuir* **2004**, *20*, 11064-11072.

[7] Vigier, F.; Coutanceau, C.; Hahn, F.; Belgsir, E.M.; Lamy, C. *J. Electroanal. Chem.* **2004**, *563*, 81-89.

[8] Camara, G.A.; Iwasita, T. *J. Electroanal. Chem.* **2005**, *578*, 315-321.

[9] Sun, S.; Halseid, M.C.; Heinen, M.; Jusys, Z.; Behm, R.J. *J. Power Sources* **2009**, *190*, 2-13.

[10] Arico, A.S.; Creti, P.; Antonucci, P.L.; Antonucci, V. Electrochem. *Solid State Lett.* **1998**, *1*, 66-68.

[11] Rousseau, S.; Coutanceau, C.; Lamy, C.; Leger, J.M. *J. Power Sources*, **2006**, *158*, 18-24.

[12] Li, G.; Pickup, P.G. *J. Power Sources* **2006**, *161*, 256-263.

[13] Ghumman, A.; Li, G.; Bennett, D.V.; Pickup, P.G. *J. Power Sources* **2009**, *194*, 286-290.

[14] James, D.D.; Bennett, D.V.; Guangchun, L.; Ghumman, A.; Helleur, R.J.; Pickup, P.G. *Electrochem. Commun.* **2009**, *11*, 1877-1880.

[15] Rao, V.; Cremers, C.; Stimming, U.; Cao, L.; Sun, S.G.; Yan, S.Y.; Sun, G.Q.; Xin, Q. *J. Electrochem. Soc.* **2007**, *154*, B1138-B1147.

[16] James, D. D.; Pickup, P. G. *Electrochim. Acta* **2012**, *78*, 274-278.

[17] Jablonski, A.; Kulesza, P. J.; Lewera, A. *J. Power Sources* **2011**, *196*, 4714-4718.

[18] Jablonski, A.; Lewera, A. *Appl. Catal. B* **2012**, *115*, 25-30.

[19] Nakagawa, N.; Kaneda, Y.; Wagatsuma, M.; Ysujiguchi, T. *J. Power Sources* **2012**, *199*, 103-109.

[20] Seweryn, J.; Lewera, A. *J. Power Sources* **2012**, *205*, 264-271.

[21] Song, S.; Wang, G.; Zhou, W.; Zhao, X.; Sun, G.; Xin, Q.; Kontou, S.; Tsiakaras, P. *J. Power Sources* **2005**, *140*, 103-110.

[22] Song, S.; Zhou, W.; Tian, J.; Cai, R.; Sun, G.; Xin, Q.; Kontou, S.; Tsiakaras, P. *J. Power Sources* **2005**, *145*, 266-271.

[23] Paganin, V.; Sitta, E.; Iwasita, T.; Vielstich, W. *J. Appl. Electrochem.* **2005**, *35*, 1239-1243.

[24] Ren, X.M., Springer, T.E.; Zawodzinski, T.A.; Gottesfeld, S. *J. Electrochem. Soc.* **2000**, *147*, 466-474.

CHAPTER 5

Measurement of Carbon Dioxide Yields for Ethanol Oxidation by Operation of a Direct Ethanol Fuel Cell in Crossover Mode

5.1. Introduction

Parts of this chapter were written by Dr. Peter Pickup and have been published in a peer-reviewed journal [1].

In assessing the efficiency of anode catalysts, and operating conditions, for breaking the C-C bond of ethanol it is crucial to employ reliable and accurate methodology for measuring CO_2 yields. Spectroscopic methods such as in situ FTIR [2-12] and differential electrochemical mass spectrometry (DEMS) [7,13-21] are extremely valuable for mechanistic studies, but the results are generally dominated by transient (from adsorbed CO) rather than steady-state CO_2 production. In addition, such experiments do not usually represent fuel cell operating conditions. Measurements on the anode exhaust from DEFCs [22] can provide CO_2 yields averaged over periods of hours, as well as real time monitoring of CO_2 production [23]. However, they suffer from crossover effects [24,25] due to the diffusion of oxygen, ethanol, and its oxidation products across the Nafion® membrane (PEM). It is also possible that the build-up of ethanol oxidation products in the anode flow field can cause product distributions to vary along the length of the flow field.

In order to minimize the effects of CO_2 crossover and variations in concentrations along the flow field on measured CO_2 yields in a DEFC we report here on the effects of controlling the flux of ethanol to the anode, by operating the cell in crossover mode, where the rate of ethanol oxidation is limited by its rate of diffusion

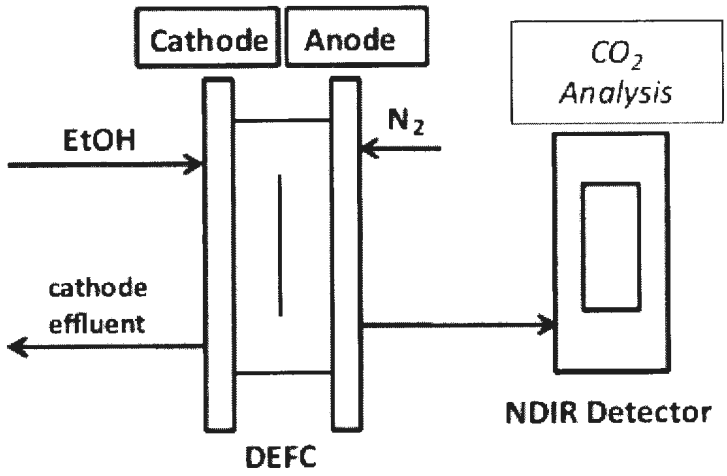

Figure 5.1: Schematic diagram of a DEFC operated in crossover mode with CO_2 monitoring of the anode exhaust using a non-dispersive infrared (NDIR) detector (obtained with permission from [1]).

though the Nafion® membrane (crossover). The experimental set-up is illustrated schematically in Figure 5.1. A conventional PEM fuel cell was used with Pt black electrodes sandwiching a Nafion® 115 membrane. Aqueous ethanol was delivered to the cathode and N_2 was passed through the anode compartment. The CO_2 concentration of the anode exhaust gas was continuously monitored with a non-dispersive infrared (NDIR) CO_2 detector. We demonstrate that this configuration virtually eliminates inaccuracies due to crossover effects (ethanol, oxygen, and carbon dioxide) and produces high yields of CO_2.

5.2. Experimental

5.2.1. Materials

Electrodes consisted of 4 mg cm^{-2} Pt black on Toray™ carbon fiber paper donated by Ballard Power Systems. Anhydrous ethanol was obtained from Commercial Alcohols Inc.

5.2.2. The Cell

A 5 cm^2 commercial cell (Fuel Cell Technology Inc.) was used. The cathode inlet and outlet were both modified to prevent the ethanol solution from contacting any metal parts of the hardware. Membrane and electrode assemblies were prepared by hot pressing a 5 cm^2 anode and a 5 cm^2 cathode onto a Nafion® 115 membrane (Ion Power) at a pressure of 200 kg cm^{-2} at 135 °C for 90 s. The cell was operated with a cathode feed of 0.10–1.0 mol L^{-1} ethanol or methanol solution at 0.50 mL min^{-1}. The anode feed was N_2 at 45 or 90 cm^3 min^{-1}. Electrochemical measurements were made using a Solartron 1286 potentiostat operated with Corrware software.

5.2.3. CO_2 Analysis

The N_2 exhaust from the fuel cell was passed through a 125 mL flask to collect condensates and then into a Telaire 7001 non-dispersive infrared CO_2 monitor [23]. All CO_2 yields reported in this work are faradaic yields based on the current passed by the fuel cell. Since it was found that the accuracy of the detector deteriorated with time when used in these experiments over long periods (weeks), it was necessary to recalibrate regu-

larly either with known concentrations of CO_2 in N_2 or using methanol in crossover mode and assuming a 100% yield of CO_2 (see below).

5.3. Results and Discussion

5.3.1. Testing and Calibration of the System with Methanol

The accuracy of the system for measuring CO_2 yields was first evaluated using methanol as the fuel, which was expected to give close to a 100% faradaic yield. A 1 mol L^{-1} methanol solution was fed through the cathode compartment of the cell at a flow rate of 0.50 mL min^{-1}. At the anode, N_2 gas was passed at a rate of 90 mL min^{-1}. Methanol crossing through the Nafion® 115 membrane was oxidized at the anode, using constant currents ranging from 5 to 80 mA, while the cathode acted as a dynamic hydrogen electrode (DHE). As shown in Figure 5.2, the CO_2 concentrations measured in these experiments agreed well with the calculated concentrations based on a 100% faradaic yield of CO_2. The slope of the data shown in Figure 5.2 was 1.03, indicating that the system provides an accurate measure of the CO_2 yield, and that methanol is almost exclusively oxidized to CO_2 under the conditions employed. Crossover of CO_2 to the cathode must also have been insignificant in these experiments.

Many of the previously reported measurements of CO_2 yields from methanol oxidation have shown yields below 100% due to incomplete oxidation to formaldehyde and formic acid [26,27]. However, since these two intermediates can both be oxidized to

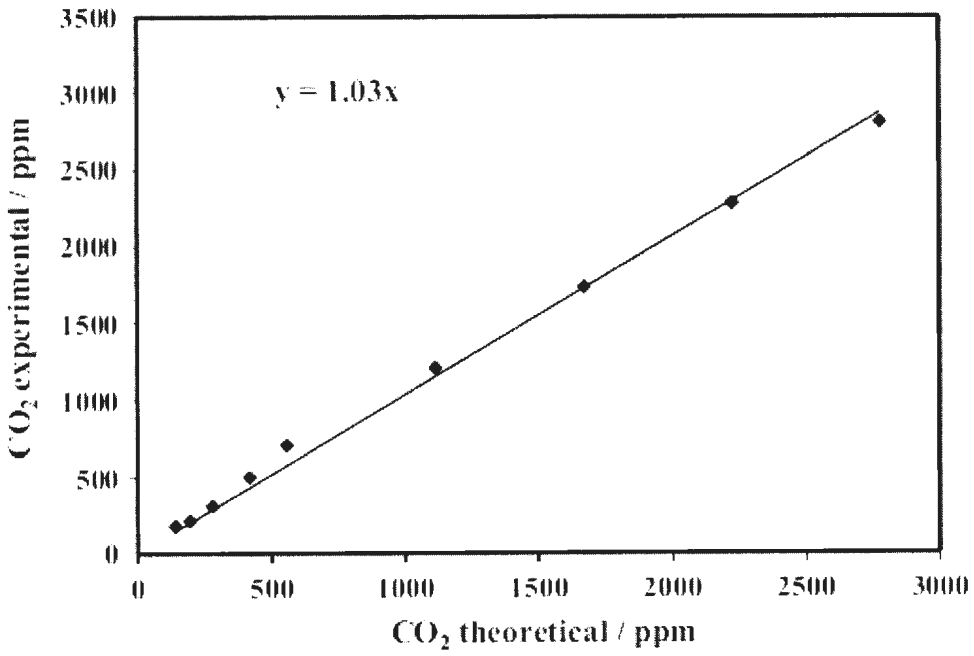

Figure 5.2: Measured CO_2 concentration in the anode exhaust vs. theoretical concentration for a 100% faradaic yield for constant current (5–80 mA) oxidation of methanol crossing through a Nafion® 115 membrane (T = 80 °C) (obtained with permission from [1]).

CO_2 within the porous structure of a fuel cell electrode [28,29], high CO_2 yields and low levels of formaldehyde and formic acid are achieved in direct methanol fuel cells [30].

In order to assess the effects of CO_2 crossover in conventional measurements (i.e. measuring the CO_2 in the fuel stream exhaust; "normal" mode), the anode and cathode connections in Figure 5.1 were reversed. Thus, in these experiments the cathode was flushed with N_2 and acted as a DHE and the anode was supplied with 0.1 mol L^{-1} methanol. The CO_2 concentration was measured in the N_2 exiting the cathode chamber and in the 0.1 mol L^{-1} methanol exiting the anode chamber (following extraction into an N_2 stream [23]). It was found that at 30 mA, ca. 34% of the measured CO_2 exited the cell in

the N_2 stream from the cathode, while 66% exited in the anode exhaust. Clearly, there was a great deal of CO_2 crossover from the anode to the cathode, as would be expected given the high activity of CO_2 at the anode (ca. 0.53 for CO_2 gas saturated with water at 80 °C) and low activity at the cathode (close to 0 for ca. 650 ppm CO_2 in N_2). These results confirm [24] that conventional measurements of CO_2 yields in direct alcohol fuel cells (i.e. measurement of CO_2 in the anode exhaust only) underestimate the true yield due to crossover. Indeed, such measurements on the DMFC here gave significantly lower CO_2 yields (ca. 70% on average over a 2–30 mA current range) than the measurements reported in Figure 5.2.

5.3.2. Ethanol Oxidation

The crossover of ethanol through proton exchange membranes in fuel cells has been described in a number of papers [24,31-33]. The effects of oxygen permeation from the cathode compartment of a fuel cell through the membrane have also recently been described [25]. It has been shown that the use of oxygen at the cathode can result in both a misinterpretation of ethanol oxidation products, due to ethanol crossing through the membrane and chemically reacting with oxygen at the cathode [24] and also acetic acid and acetaldehyde formation at the anode due to oxygen permeation [25]. In order to avoid these problems, the experiments reported here employed N_2 at the cathode, and a reference potential was provided by the cathode acting as a dynamic hydrogen electrode. The main focus of these experiments was not to measure the rate of ethanol crossover but to provide a controlled and limited flux of ethanol to the anode by delivering it from the cathode via diffusion through the membrane.

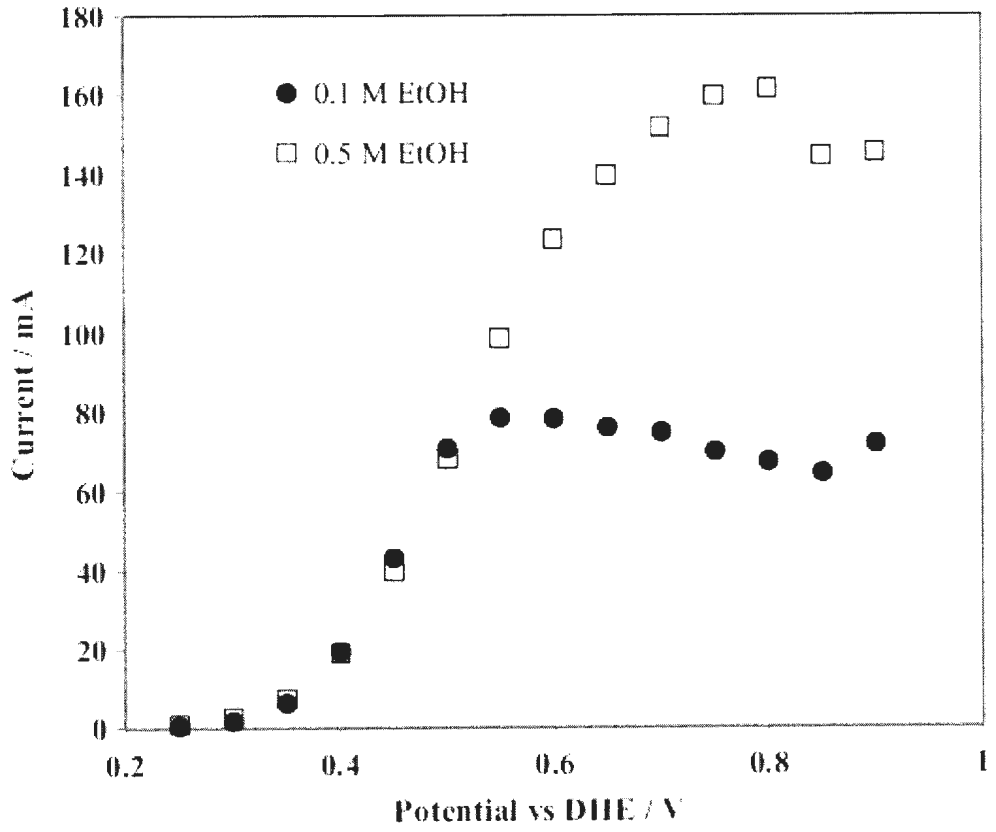

Figure 5.3: Polarization curves at 80 °C recorded in the crossover mode shown in Fig. 1. Current measurements were made (averaged over 30–100 s) following ca. 4 min at each potential. N_2 was passed over the anode at 45 mL min^{-1} while 0.1 or 0.5 mol L^{-1} ethanol solution was supplied to the cathode which acted as a DHE (obtained with permission from [1]).

It is well known that the rate of diffusion of ethanol through a Nafion® membrane is dependent on the concentration of the ethanol solution [32,33]; this is illustrated in Figure 5.3 which show polarization curves for the oxidation of ethanol crossing the

membrane from 0.1 to 0.5 mol L^{-1} ethanol solutions on the cathode side of the cell. The diffusion limited flux of ethanol across the membrane is indicated by the approximately constant (limiting) currents at potentials above 0.5–0.7 V, and can clearly be controlled by varying the concentration of the ethanol feed solution. However, it is curious that increasing the ethanol concentration by a factor of 5 only increased the limiting current by a factor of ca. 2.1. This suggests that the average number of electrons released per ethanol molecule must have been significantly higher at the lower concentration. This is confirmed by the higher CO_2 yields measured at lower ethanol concentrations (see below). Figure 5.4 shows a typical CO_2 concentration vs. time trace for constant potential oxidation of ethanol crossing through the membrane from 0.1 mol L^{-1} ethanol at the cathode, together with the current vs. time curve. The rise in CO_2 concentration was slow because of the large dead volume of the tubing and glassware used to condense and remove water from the anode exhaust gas (N_2 + CO_2 + water vapor, etc.) before it was passed through the CO_2 detector, which is easily damaged by water condensation. However, a steady CO_2 reading was established after ca. 5 min, and the current was also reasonably stable. The faradaic yield of CO_2 ($\%CO_2$) was calculated from the average CO_2 concentration (ppm CO_2) and average current (I), after the first 5 min, to be 63% using Equation (5.1),

$$\frac{\%CO_2}{100\%} = \frac{nF\rho(ppm\ CO_2)}{(2.42\ x\ 10^7)I} \qquad (5.1)$$

where n = 6 and ρ is the N_2 flow rate in L s^{-1}.

Table 5.1 shows the faradaic CO_2 yields for ethanol oxidation at various potentials and ethanol concentrations. As the ethanol concentration was decreased, a significant increase in CO_2 selectivity was seen. When comparing the 0.5 mol L^{-1} to the 0.1 mol

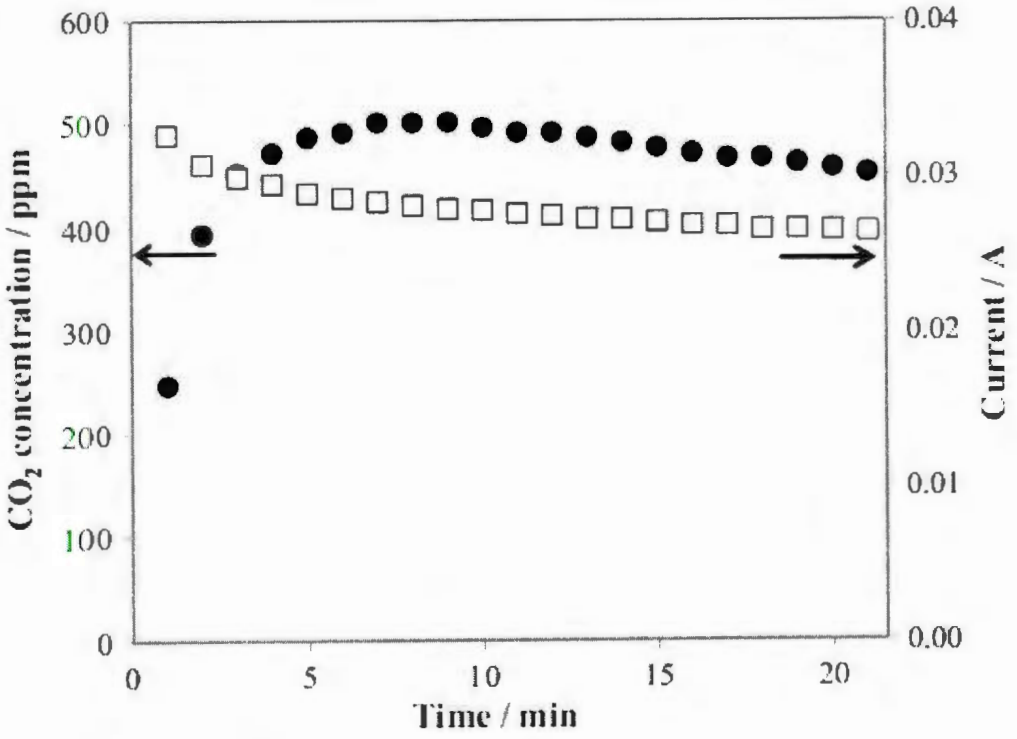

Figure 5.4: CO_2 concentration and current vs. time traces recorded during the oxidation of ethanol at 80 °C and 0.70 V vs. DHE. N_2 was passed over the anode at 45 mL min^{-1} while 0.1 mol L^{-1} ethanol solution was supplied to the cathode (obtained with permission from [1]).

L^{-1} concentrations, the faradaic CO_2 yield was more than four times higher for 0.1 mol L^{-1} ethanol at the lowest potential (500 mV) and two times higher at the limiting current (700 mV). Since the rate of diffusion through the membrane increases with increasing EtOH concentration, it is evident from these results that a lower diffusion rate is preferred for optimal selectivity toward CO_2.

Table 5.1: Faradaic yields of CO_2 for oxidation of ethanol crossing over through a Nafion® 115 proton exchange membrane at 80 °C in a DEFC. The anode gas was N_2 (adapted from [1]).

[Ethanol] (mol L^{-1})	Cell Potential (mV)	CO_2 (%)
0.1	500	42±6
0.1	600	60±3
0.1	700	64±2
0.3	500	27±3
0.3	600	39±2
0.3	700	43±2
0.5	500	<10
0.5	600	21±1
0.5	700	28±2

Uncertainties are standard deviations based on the standard deviations of the calibration parameters and the average CO_2 readings.

In order to investigate whether the high yields with 0.1 mol L^{-1} ethanol reported in Table 5.1 were due to limitation of the flux of ethanol by the membrane, additional experiments were performed in which CO_2 yields were compared for operation of the cell in "normal" and "crossover" modes with 0.1 mol L^{-1} ethanol. These experiments were performed at constant current (10, 20, 30,.and 50 mA). The measured CO_2 yields are plotted as a function of cell potential in Figure 5.5. Interestingly, the highest CO_2 yield (68%) was obtained in normal mode at the lowest potential (~0.34 V vs. DHE; 10 mA). Yields

dropped with increasing current in normal mode, but increased in crossover mode, reaching limiting values in both cases. It has commonly been reported that CO_2 yields from ethanol oxidation decrease as the potential [13,34] or current density [23,35] is increased, which is the trend seen here in normal mode. The increasing yields with increasing potential and current seen here for crossover mode in both Table 5.1 and Figure 5.5 are therefore anomalous. This effect may be due to the decreasing ethanol concentration at the anode as the current increases. Based on a linear concentration gradient across the membrane, the ethanol concentration at the anode would be proportional to $(i_{lim} - i)/i_{lim}$, where i_{lim} (~72 mA) is the limiting crossover current. When compared at similar cell potentials, yields were clearly higher in crossover mode than in normal mode. This can be attributed to loss of CO_2 though the cathode in normal mode, which was demonstrated to result in a ca. 30% underestimation of the CO_2 yield in the methanol oxidation experiments. Since the yields in normal mode at the lowest potentials should have been similarly underestimated, the actual yield at 10 mA (ca. 0.34 V vs. DHE) must have been significantly greater that 68%.

The highest yields of CO_2 observed in this work (64–68% in Figure 5.5 and Table Figure 5.1) are significantly higher than the highest previously reported yields for ethanol oxidation at 80 °C in DEFCs. We have previously reported a yield of 15% for oxidation of 0.5 mol L^{-1} ethanol at 40 mA cm^{-2} [23], while Rousseau et al. [22] obtained a faradaic yield of 35% at 8 mA cm^{-2} with 2 mol L^{-1} ethanol. A yield of 62.1% has been reported for ethanol oxidation at 80 °C (86.9% at 100 °C) in a high- temperature/high-pressure DEMS study with 0.01 mol L^{-1} ethanol [13].

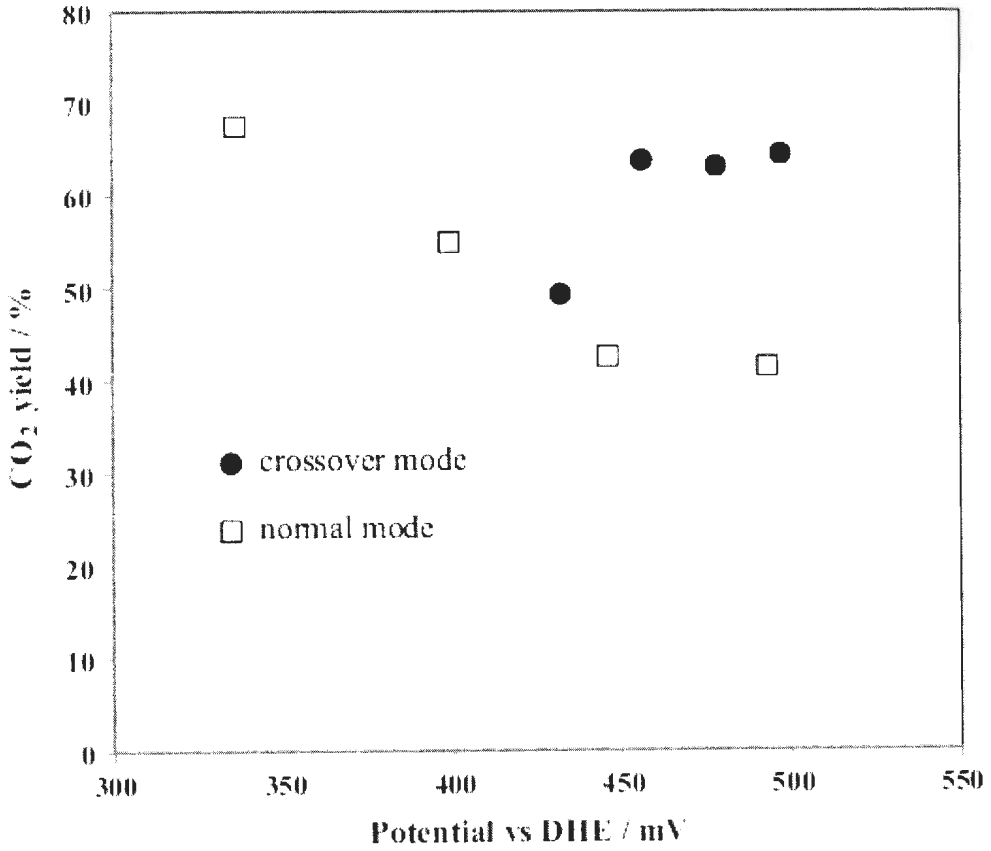

Figure 5.5: Measured CO_2 yield vs. cell potential for DEFCs operated in normal and crossover modes with 0.1 mol L^{-1} EtOH at 80 °C. In each case, the CO_2 was measured only in the anode exhaust stream (obtained with permission from [1]).

The high yields in the current work are clearly due in part to the lower ethanol concentration employed (0.1 mol L^{-1}), and also to the lower current densities (2–8 mA cm^{-2}). Insight into the origins of such sensitivity of the CO_2 yield, or product distribution, to operating conditions has recently been provided by a density functional theory study of

the key steps in the mechanisms for CO_2 and acetic acid formation during ethanol oxidation [36]. It was shown that the activation barriers for these steps were influenced by both the presence of surface hydroxyl groups (OH_{ads}) on the catalyst, and the presence of water molecules. The route to acetic acid requires the OH_{ads} functionality while the route to CO_2 is inhibited by OH_{ads}. In contrast, the presence of water increases the rates of both routes, but speeds up CO_2 production more than acetic acid production. The high yields of CO_2 seen here at low currents/potentials in normal mode can reasonably be attributed to low OH_{ads} coverage and high water activities. The lower yield in crossover mode at the lowest current may be due to a lower water activity at the anode, which was flushed with dry N_2 at 80 °C in these experiments. At higher currents, this effect may be compensated by the decreasing ethanol concentration at the anode, as suggested above. Although further work is needed to explore these effects in more detail, it seems clear from both experimental and theoretical perspectives that it will be possible to further increase the selectivity of ethanol oxidation for breaking the C-C bond by tuning the cell operating conditions.

5.4. Conclusions

Operation of a direct methanol fuel cell (DMFC) in crossover mode has been shown to produce CO_2 quantitatively without significant crossover of CO_2 to the fuel stream (cathode). In contrast, ca. 30% of the CO_2 produced when the cell was operated normally crossed to the cathode gas stream. Consequently, measurements of CO_2 in the anode exhausts of both DMFCs and DEFCs greatly under-estimate the yield of CO_2. Making these measurements in crossover mode should therefore be the preferred method

for fundamental studies and for comparing and screening catalysts. An additional advantage of using crossover mode, not explored here, is that measurements of CO_2 in the anode gas exhaust can be made with a much faster response time [37] than measuring CO_2 in a liquid anode exhaust.

5.5. References

[1] James, D.D.; Pickup, P.G. *Electrochim. Acta* **2012**, 78, 274-278.

[2] Li, M.; Kowal, A.; Sasaki, K.; Marinkovic, N.; Su, D.; Korach, E.; Liu, P.; Adzic, R.R. *Electrochim. Acta* **2010**, 55, 4331-4338.

[3] Freitas, R.G.; Pereira, E.C.; Christensen, P.A. *Electrochem. Commun.* **2011**, 13, 1147-1150.

[4] Vigier, F.; Coutanceau, C.; Hahn, F.; Belgsir, E.M.; Lamy, C. *J. Electroanal. Chem.* **2004**, 563, 81-89.

[5] dos Anjos, D.M.; Hahn, F.; Leger, J.M.; Kokoh, K.B.; Tremiliosi, G. *J. Solid State Electrochem.* **2007**, 11, 1567-1573.

[6] Shao, M.H.; Adzic, R.R. *Electrochim. Acta* **2005**, 50, 2415-2422.

[7] Wang, Q.; Sun, G.Q.; Jiang, L.H.; Xin, Q.; Sun, S.G.; Jiang, Y.X.; Chen, S.P.; Jusys, Z.; Behm, R.J. *Phys. Chem. Chem. Phys.* **2007**, 9, 2686-2696.

[8] Colmati, F.; Tremiliosi, G.; Gonzalez, E.R.; Berna, A.; Herrero, E.; Feliu, J.M. *Phys. Chem. Chem. Phys.* **2009**, 11, 9114-9123.

[9] Heinen, M.; Jusys, Z.; Behm, R.J. *J. Phys. Chem. C* **2010**, 114, 9850-9864.

[10] Kutz, R.B.; Braunschweig, B.; Mukherjee, P.; Behrens, R.L.; Dlott, D.D.; Wieckowski, A. *J. Catal.* **2011**, 278, 181-188.

[11] Garcia-Rodriguez, S.; Rojas, S.; Pena, M.A.; Fierro, J.L.G.; Baranton, S.; Leger, J.M. *Appl. Catal. B* **2011**, 106, 520-528.

[12] Cantane, D.A.; Gonzalez, E.R. *J. Electrochem. Soc.* **2012**, 159, B355-B359.

[13] Sun, S.; Halseid, M.C.; Heinen, M.; Jusys, Z.; Behm, R.J. *J. Power Sources* **2009**, 190, 2-13.

[14] Wang, J.; Wasmus, S.; Savinell, R.F. *J. Electrochem. Soc.* **1995**, 142, 4218-4224.

[15] Fujiwara, N.; Friedrich, K.A.; Stimming, U. *J. Electroanal. Chem.* **1999**, 472, 120-125.

[16] Neto, A.O.; Giz, M.J.; Perez, J.; Ticianelli, E.A.; Gonzalez, E.R. *J. Electrochem. Soc.* **2002**, 149, A272-A279.

[17] Gonzalez Pereira, M.; Davila Jimenez, M.; Elizalde, M.P.; Manzo-Robledo, A.; Alonso-Vante, N. *Electrochim. Acta* **2004**, 49, 3917-3925.

[18] Wang, H.; Jusys, Z.; Behm, R.J. *J. Power Sources* **2006**, 154, 351-359.

[19] Wang, H.; Jusys, Z.; Behm, R.J. *J. Phys. Chem. B* **2004**, 108, 19413-19424.

[20] Rao, V.; Cremers, C.; Stimming, U.; Cao, L.; Sun, S.G.; Yan, S.Y.; Sun, G.Q.; Xin, Q. *J. Electrochem. Soc.* **2007**, 154, B1138-B1147.

[21] *Structure and Bonding: Fuel Cells and Hydrogen Storage;* Wang, H.S.; Abruna, H.D.; Bocarsly, A.; Mingos D.M.S. (Eds.); Springer-Verlag, Berlin, **2011**; Vol 141, p. 33.

[22] Rousseau, S.; Coutanceau, C.; Lamy, C.; Leger, J.M. *J. Power Sources*, **2006**, 158,18-24.

[23] Ghumman, A.; Li, G.; Bennett, D.V.; Pickup, P.G. *J. Power Sources* **2009**, 194, 286-290.

[24] James, D.D.; Pickup, P.G. *Electrochim. Acta* **2010**, 55, 3824-3829.

[25] Jablonski, A.; Kulesza, P.J.; Lewera, A. *J. Power Sources* **2011**, 196, 4714-4718.

[26] Wang, H.S.; Wingender, C.; Baltruschat, H.; Lopez, M.; Reetz, M.T. *J. Electroanal. Chem.* **2001**, 509, 163-169.

[27] Wang, H.; Loffler, T.; Baltruschat, H. *J. Appl. Electrochem.* **2001**, 31, 759-765.

[28] Jusys, Z.; Kaiser, J.; Behm, R.J. *Electrochim. Acta* **2002**, 47, 3693-3706.

[29] Gao, L.; Huang, H.L.; Korzeniewski, C. *Electrochim. Acta* **2004**, 49, 1281-1287.

[30] Masdar, M.S.; Tsujiguchi, T.; Nakagawa, N. *J. Power Sources* **2009**, 194, 618-624.

[31] Song, S.; Wang, G.; Zhou, W.; Zhao, X.; Sun, G.; Xin, Q.; Kontou, S.; Tsiakaras, P. *J. Power Sources* **2005**, 140, 103-110.

[32] Song, S.; Zhou, W.; Tian, J.; Cai, R.; Sun, G.; Xin, Q.; Kontou, S.; Tsiakaras, P. *J. Power Sources* **2005**, 145, 266-270.

[33] Li, G.; Pickup, P.G. *J. Power Sources* **2006**, 161, 256-260.

[34] Nakagawa, N.; Kaneda, Y.; Wagatsuma, M.; Tsujiguchi, T. *J. Power Sources* **2012**, 199, 103-107.

[35] Andreadis, G.; Stergiopoulos, V.; Song, S.; Tsiakaras, P. *Appl. Catal. B* **2010**, 100, 157-164.

[36] Kavanagh, R.; Cao, X.M.; Lin, W.F.; Hardacre, C.; Hu, P. *Angew. Chem. Int. Ed.* **2012**, 51, 1572-1575.

[37] Ghumman, A.; Pickup, P. G. *J. Power Sources* **2008**, *179*, 280-285.

CHAPTER 6

Kinetic and Mechanistic Study

6.1. Introduction

Poisoning of the electrode by CO and other ethanol oxidation intermediates is a major concern in direct ethanol fuel cells. It has been reported for decades that Pt catalysts are severely susceptible to CO poisoning due to strong interactions between Pt and CO molecules on the surface of the electrode (see section 1.4). Although most of the highest yields towards CO_2 (complete oxidation of ethanol) have been reported for Pt catalysts [1-3], their voltage efficiencies are moderate to low compared to those of bi- and tri- metallic alloyed catalysts [4-6]. As mentioned in the introduction of this work, computational studies of Pt catalysts show that the CO and other ethanol oxidation intermediates formed on the surface of the catalyst from the dissociation of ethanol are highly attracted to Pt. The energy released when CO adsorbs on the Pt surface is much higher than that of oxygenated species [7]. Since oxygenated species are needed for further oxidation to the more oxygenated products (CO_2 and acetic acid), the poisoning of the electrode decreases the average number of electrons transferred by forming large amounts of the least oxygenated product, acetaldehyde.

Two very important aspects to examine when trying to understand the inefficiencies of ethanol oxidation are the dissociation of ethanol on the surface of the electrode and the kinetics of the oxidation of CO into CO_2 at the electrode surface. The rate determining steps in ethanol oxidation have been reported to be a combination of the dissociation of ethanol into CO, CH_x and CH_xO species arising from the difficulty in cleaving the C-C bond and the oxidation of CO into CO_2 arising from strong CO surface adsorption energies. To better understand and improve catalyst performances, many research groups

have developed new anode catalysts that have been shown to increase ethanol oxidation efficiencies by altering product distributions. The primary objectives of this work were to gain insight into both the ethanol adsorption/desorption processes and to increase CO_2 yields in DEFCs.

It has been reported in chapter 3 of this work that at the start of each experiment at RT (Figure 3.7), there is a large amount of CO_2 that is produced and high cell efficiencies are observed. However, after short periods of time, large decreases in both the CO_2 yield and efficiencies are seen. This is due to a build up of CO and other intermediates on the electrode surface. This poisoning of the electrode (using Pt catalysts) can be mitigated by periodically oxidizing the adsorbed species and this is the main focus of this chapter.

In this work, we report a series of electrode surface cleaning experiments in which potential steps are applied to the anode at small time intervals. After each of the pulsing intervals, the cell is allowed to return to open circuit. During the rest period, ethanol was able to adsorb to the surface. Different pulsing and resting time intervals were monitored, giving an indication of the times needed for ethanol adsorption and oxidation of CO to CO_2. Various magnitudes of pulses, pulse times and rest times were examined and conclusions about the adsorption and desorption kinetics are made.

The motivation behind these stripping experiments can be attributed to previous work done by the Pickup group in 2008 [8]. They had used stripping techniques to increase the CO_2 yield to more than 60% at room temperature. As shown in Figure 6.1, 2 s pulses were applied to the anode followed by 30 s rest intervals at open circuit and room temperature. The 2 s pulse at 0.82 V vs. H2 seemed to be sufficient to strip the intermedi-

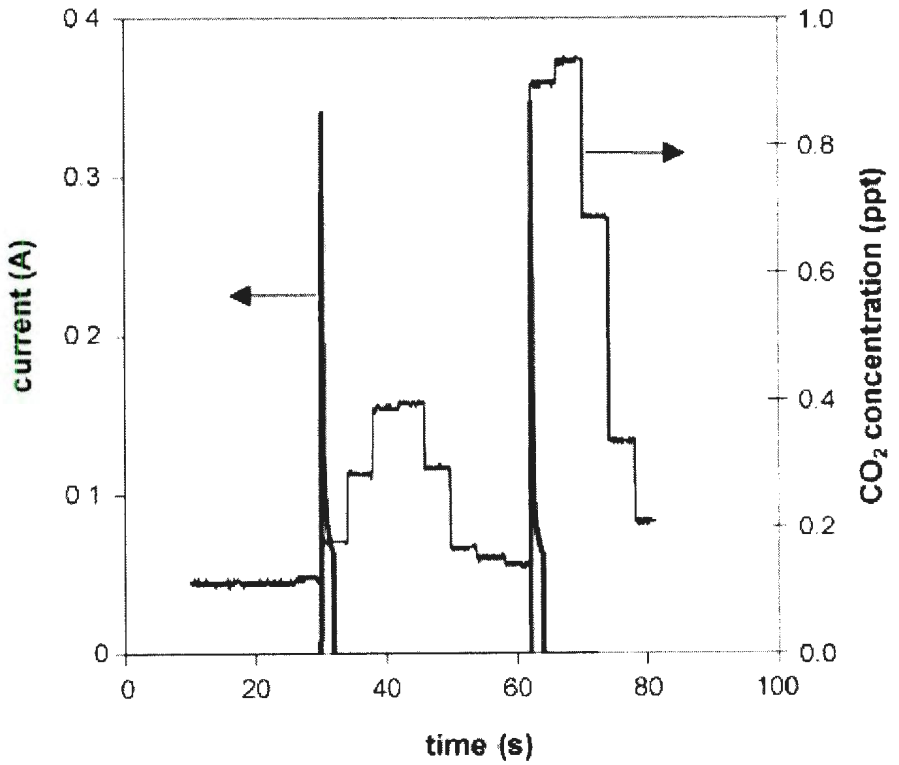

Figure 6.1: Current and concentration of CO_2 produced during stripping experiment with 2 s pulses at 0.82 V and 30 s resting intervals between pulses at open circuit [8].

ates from the surface. The long resting interval was applied to make sure there was ample time for the ethanol to dissociatively re-adsorb on the surface. In this instance, the first pulse gave a CO_2 yield of ca. 34% and the second pulse more than 60%, based on the assumption that the CO_2 was due to the 12 electron oxidation of ethanol. The significant increase in CO_2 can be attributed to the clean surface of the electrode after the first pulse stripped the adsorbed intermediates from the surface. The first pulse may have been lower because of long period at open circuit before the first pulse was applied, leading to a large build up of adsorbates that were not CO. After the first pulse, the cell was allowed

to return to open circuit, but during the slow relaxation period, the anode was still at a higher potential than the original OCP allowing the majority of the ethanol to dissociate into CO. Therefore, prior to the second pulse, the surface contain more CO adsorbates that were then oxidized to CO_2. This increase in CO_2 concentration at the second pulse was observed in most of the experiments described in this chapter. Comparing these results to some of the room temperature results obtained in chapter 3 of this work, yields are significantly enhanced using the stripping method. This study also reported that the large peak current observed early in a potentiostatic experiment is primarily due to adsorbates such as CO being oxidized to CO_2 and the current produced throughout the rest of the experiment is increasingly due to acetic acid and acetaldehyde formation.

In this work, the resting period between pulses is closely examined and altered to give the shortest resting period possible without losing selectivity towards CO_2. Also, the magnitude of the potential applied and the pulsing time is analyzed to determine the shortest pulse times and smallest magnitudes of potential needed to optimize the system.

Various trends in results are reported in this chapter and will be further discussed giving some insight into the mechanism of ethanol oxidation at the surface of the electrode. All results for pulsing experiments are at room temperature unless stated otherwise.

The oxidation of acetaldehyde in direct ethanol fuel cells will also be reviewed in this chapter. It has been reported from various theoretical studies (see section 1.4.2) that one of the most energetically favored first steps of the complex mechanism of the oxidation of ethanol is the production of acetaldehyde [9-11]. The final section of this chapter will be focussed on the oxidation of acetaldehyde in a fuel cell at various fuel cell condi-

tions. By testing known concentrations of acetaldehyde directly fed into the fuel cell and examining the product distributions, we were able to gain some insight into the overall reaction mechanism. Conclusions will be made on the accuracy of the theoretical calculations and assumptions reported in literature.

6.2. Experimental

6.2.1. Materials

Electrodes used in this work consisted of commercial 4 mg cm^{-2} Pt black on Toray™ carbon fiber paper donated by Ballard Power Systems. Anhydrous ethanol was obtained from Commercial Alcohol Inc. Acetaldehyde (99.5%) was obtained from Sigma-Aldrich.

6.2.2. The Fuel Cell

A commercial 5 cm^2 fuel cell was used for all experiments in this chapter. The anode and cathode inlets were both modified to avoid any corrosion of metal in the cell which could affect results. Membrane and electrode assemblies were prepared using the same method as mentioned in previous chapters with 5 cm^2 electrodes and Nafion®115 ion exchange membranes from Dupont. The cell was operated in both normal and crossover mode. In normal mode, 0.1, 0.5, and 1 mol L^{-1} ethanol was used as the fuel. The ethanol solution was purged with N_2 at a flow rate of ca. 27 mL min^{-1} in a 500 mL sealed metal cylinder (Figure 6.2). The gas stream containing N_2 and ethanol vapour was fed through the anode compartment of the fuel cell where the oxidation took place. 5% H_2 in N_2 gas was used at the cathode at a feed of 10 mL min^{-1} to provide a stable reference potential. H_2/N_2 was

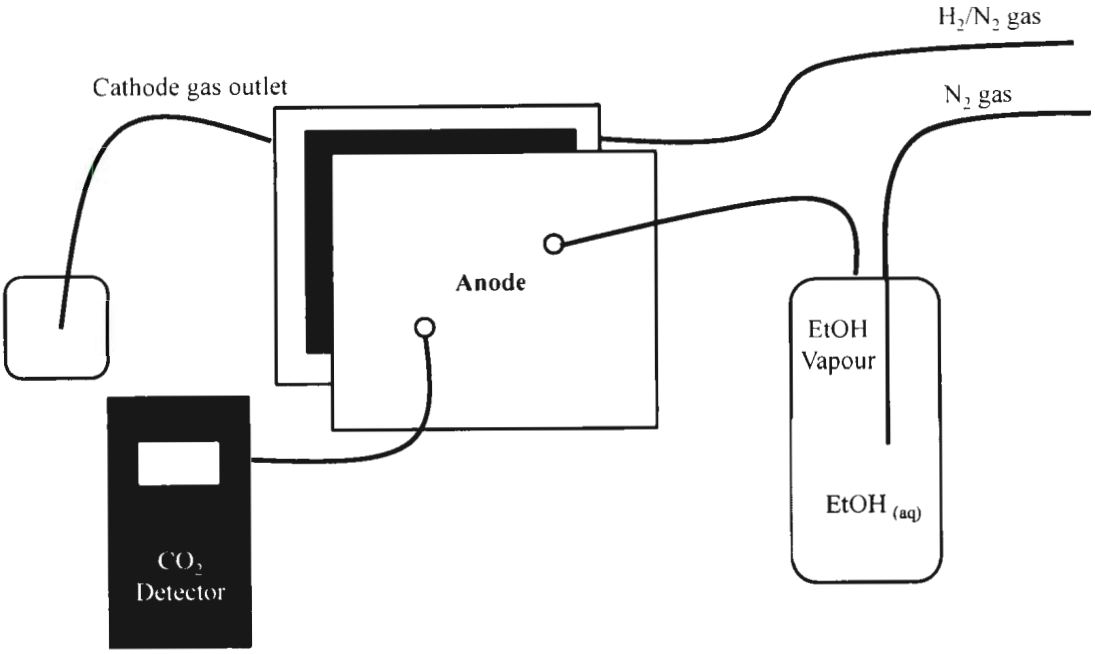

Figure 6.2: Schematic of the system used for room temperature adsorbate stripping experiments in normal mode with H_2/N_2 as the cathode gas.

used in these experiments at the cathode instead of O_2 to limit the amount of chemically produced products of EOR as previously mentioned in chapter 4.

Stripping experiments carried out in crossover mode used 0.1 and 0.5 mol L^{-1} ethanol solution and were performed at ambient temperature. The ethanol solution was fed through the cathode at 0.50 mL min^{-1}. The ethanol was allowed to cross through the Nafion® membrane to the anode where oxidation took place. At the anode, N_2 was fed at a rate of 27 mL min^{-1} which carried the CO_2 to the detector for analysis. All anode prod-

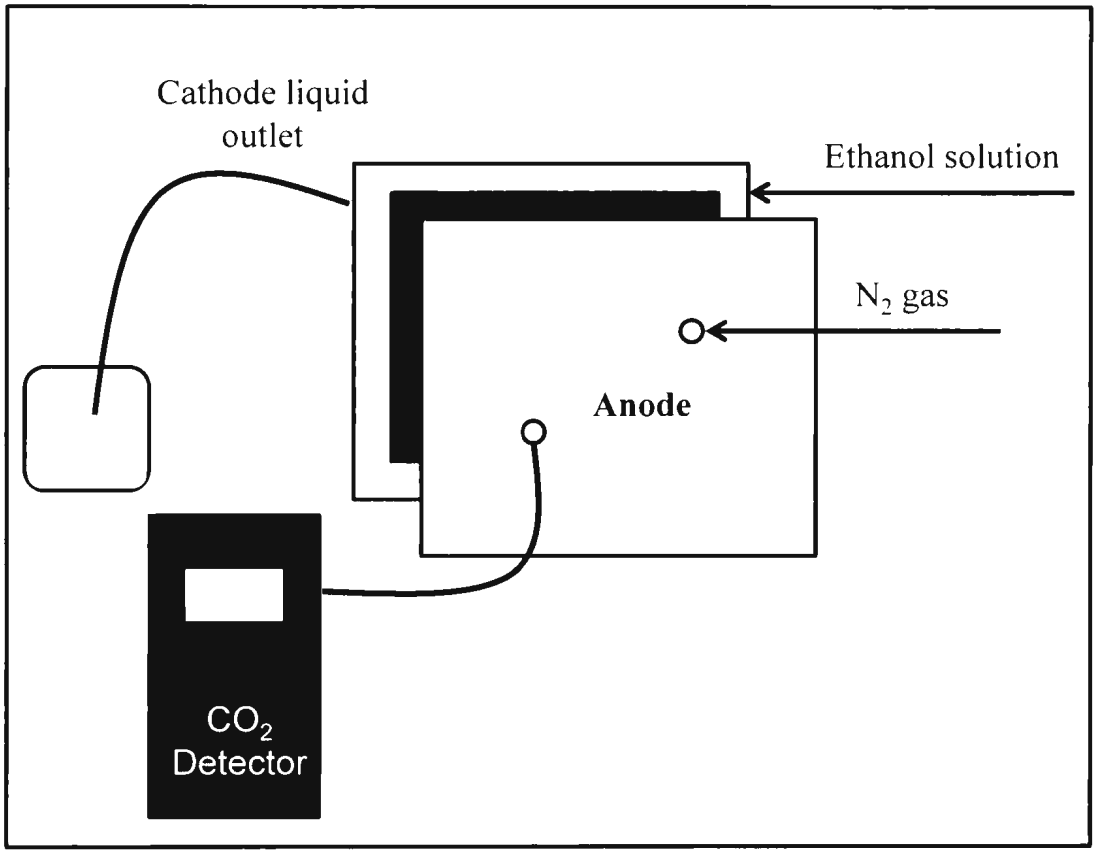

Figure 6.3: Schematic of the fuel cell setup for stripping experiments carried out in crossover mode.

ucts were found to be in the gas phase suggesting that the acetic acid produced in the N_2 anode stream crossed back through the membrane and exited via the liquid cathode stream. Since the anode outlet contained no liquids, a collection flask was not needed and the CO_2 detector was directly linked to the anode outlet (Figure 6.3).

For acetaldehyde oxidation experiments (normal mode), 0.5 mol L^{-1} acetaldehyde solution was pumped through the anode compartment at 0.50 mL min^{-1}. At the cathode,

distilled water (0.50 mL min^{-1}) or H_2/N_2 (~10 mL min^{-1}) were used to give a stable reference potential (DHE for water). These experiments were carried out at room temperature, 40, 60, 80, and 100°C.

6.2.3. CO_2 Analysis

As illustrated in Figure 6.2, after oxidation, the anode products are passed directly through the NDIR detector for CO_2 concentration analysis. The tubing from the anode to the detector was shortened to allow quick readings and good resolution of CO_2 peaks. At room temperature, this system worked very well as all of the products were in the gas phase and there were no problems due to condensation of products. At higher temperatures, it was found that small amounts of condensed liquids which were formed in the gas stream entered the detector. The detector was found to be very liquid sensitive and major problems occurred at elevated temperatures.

Due to the very short pulsing intervals that were used in this work, the faradaic CO_2 yields were a bit more challenging to calculate. For calculations of the theoretical moles of CO_2, the charged passed by the cell must be used, as shown in chapter 3. When pulsing the cell with a known potential it is seen (Figure 6.4) that the current quickly drops over the interval, even at very small pulsing intervals. Therefore, we needed to integrate the current vs. time plots to obtain the total charge over the given interval. Figure 6.4a illustrates the significant drop in current with a 15 s pulsing interval at 0.8 V. In this experiment, the resting intervals were at open circuit. In some experiments using a smaller concentrations of ethanol (0.1 mol L^{-1}), it was found that in order to obtain significant and distinguishable CO_2 concentration peaks, the cell needed to be discharged

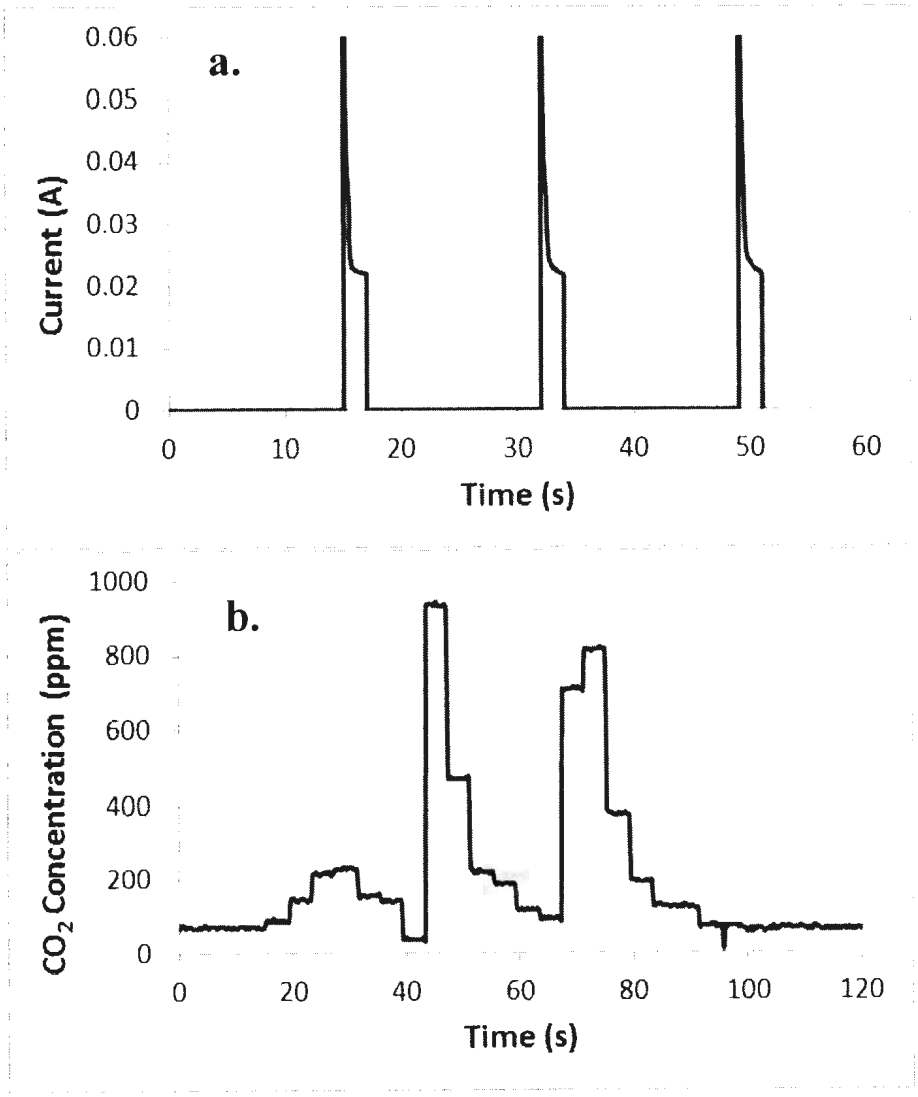

Figure. 6.4: 1 mol L^{-1} ethanol stripping experiment in normal mode at ambient temperature. 2 s pulsing intervals at 0.8 V (vs. H_2) followed by 15 s resting intervals at open circuit potential. **a.)** Current vs. time trace, **b.)** CO_2 concentration vs. time.

during the resting intervals. To do this, we set the resting interval to 0 V vs. H_2 instead of leaving the cell at open circuit. For calculating faradaic yields in these experiments, it was important for us to integrate over both the pulsing and resting potentials to correct for the negative (discharging) current. By integrating over the complete interval, we were able to obtain the net charge for the pulses, and hence able to calculate the theoretical moles of CO_2. Figure 6.4b illustrates the CO_2 production obtained from applying pulses of 0.8 V of potential (vs. H_2). To obtain our net experimental moles of CO_2, the traces recorded from the CO_2 detector were converted to mol s^{-1} then integrated.

6.2.4. Acetic Acid Analysis

Acetic acid yields reported in this chapter were only calculated for the acetaldehyde oxidation experiments. Only the anode solution was collected for titration in these experiments. It is possible that small amounts of acetic acid could have crossed through the membrane and therefore our reported results could be slightly overestimated in this chapter.

6.3. Results and Discussion

6.3.1. Linear Sweep Experiments

To first investigate an optimal pulsing potential for oxidizing CO into CO_2 from the anode under our fuel cell conditions, linear sweep experiments were carried out. (Note: In this section, "CO" refers to both CO and other adsorbates on the electrode surface

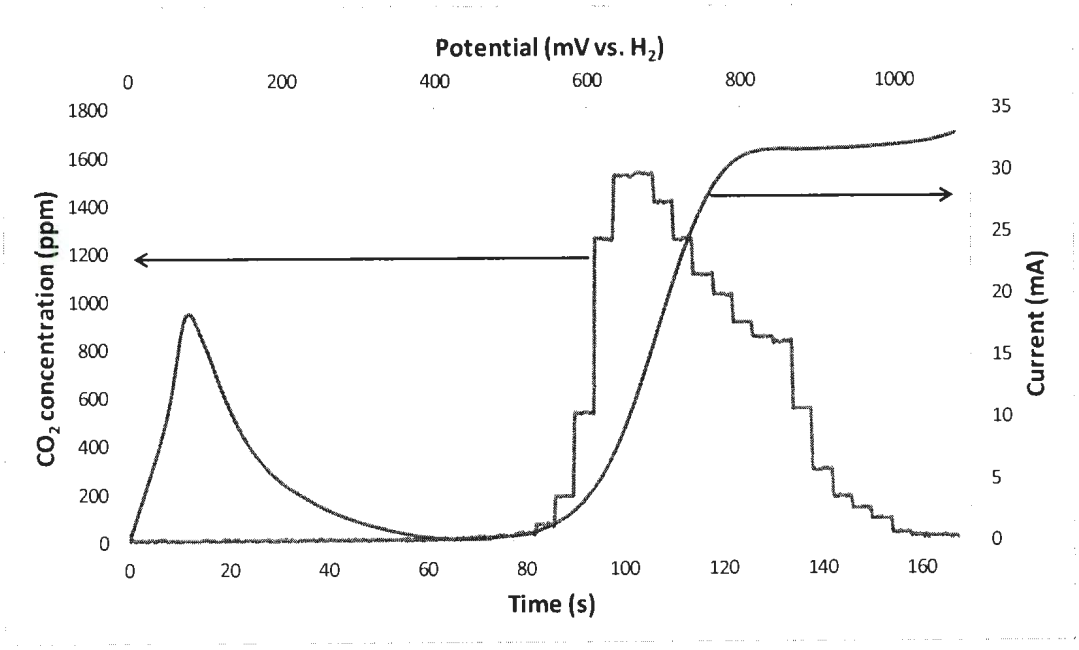

Figure 6.5: Current and CO_2 concentration measurements by applying a linear potential sweep from 0 to 1.1 V (vs. H_2). Room temperature experiment using 1.0 mol L^{-1} ethanol vapor as the fuel and H_2/N_2 at the cathode to obtain a stable reference potential.

resulting from the dissociation of ethanol). Ethanol vapor (from 1 mol L^{-1} EtOH (aq)) was used as the fuel and H_2/N_2 as the cathode gas. The sweep rate was 10 mV s^{-1} and experiments were performed at room temperature. These experiments involved increasing the potential from 0 to 1.1 V (vs. H_2). The current and CO_2 produced were both monitored as a function of time and potential and are shown in Figure 6.5. As shown in this graph, there was a rise in current starting at ca. 700 mV which continued to rise throughout the high potential region. This increase in current in this potential region is the oxidation of ethanol and its adsorbates on Pt and is well documented in the literature [8,12,13]. Monitoring of the CO_2 produced in this region also suggests the stripping CO into CO_2 as

a large burst was observed. Calculation of the CO_2 faradaic yield for the entire sweeping experiment was carried out (assuming that n=6 for CO_2 formation) and was found to be ca. 43%. However, between 0 and 0.3 V (vs. H_2) a large peak in current was observed. This peak is the desorption of hydrogen, and this region should be excluded from the CO_2 yield calculations. It should be noted that this peak appears to be larger than normal (usually O_2 or N_2 is used at the cathode) and may be due to crossover of the hydrogen that is used in the cathode stream or H_2 produced at the anode at 0 V. The CO_2 yield was calculated to be ca. 52% from 0.3 V onwards. These experiment show a significant increase in CO_2 yield on Pt at room temperature compared to those reported in the literature (highest yield ca. 13%) [14]. This suggests that applying a potential in the CO oxidation region (0.7-0.9 V vs. H_2) can strip the CO from the electrode and reduce the amount of CO poisoning on the electrode.

The pulsing potential for the stripping experiments is very important when trying to obtain the highest yields of CO_2. If the chosen potential is too low the oxidation of CO to CO_2 may not be carried out fully, resulting in CO poisoning and the formation of acetaldehyde could be favored. A potential too high (vs. H_2 $\rightarrow$low cell potential) could result in large production of OH adsorbates which will then favor the production of acetic acid, which is known to be formed at high currents.

To monitor the high current / high CO_2 potential range, constant potential experiments were carried out. These potentiostatic experiments used 700, 800, 900, and 1000 mV (vs. H_2) over 180 s intervals. The current vs. time traces were integrated to obtain

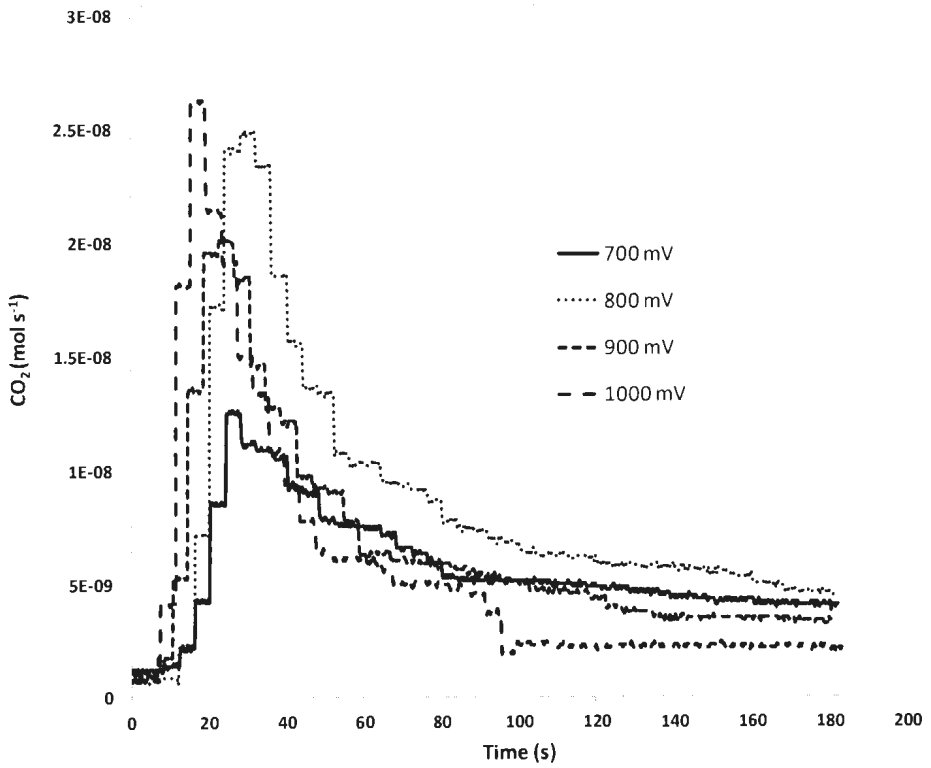

Figure 6.6: CO_2 traces for constant potential experiments for 700, 800, 900, and 1000 mV (vs. H_2) using vapour from 1.0 mol L^{-1} ethanol at room temperature.

charges, and the CO_2 vs. time traces were integrated to obtain the total moles of CO_2 produced. The CO_2 vs. time traces for each potential are shown in Figure 6.6. In each of the traces in Figure 6.6, it is shown that a large burst of CO_2 occurs at the start of the experiment. This spike in CO_2 is caused by adsorbed CO, formed on the electrode prior to the run while the system was at open circuit, which is oxidized to CO_2. For each potential, the faradaic CO_2 yields were calculated for the entire run, for the first 50 s and for the final 50 s. As shown in Table 6.1 (and can be interpreted from Figure 6.6), high CO_2

Table 6.1: Faradaic CO_2 yields for potentiostatic experiments at 700, 800, 900 and 1000 mV (vs. H_2). CO_2 yields were calculated for the entire run and for various regions of the experiment.

Potential (mV vs. H_2)	CO_2 yield (total)	CO_2 yield (first 50 s)	CO_2 yield (final 50 s)
700	31.0 %	37.9 %	23.0 %
800	31.9 %	51.8 %	21.9 %
900	21.4 %	29.8 %	16.4 %
1000	19.8 %	30.9 %	11.2 %

yields were observed for the first 50 s (29.8-51.8%). After the CO was stripped from the electrode, the concentration of CO_2 decreased until it became relatively steady at ca. 120 s. The CO_2 yields decreased with time as the concentration decreased but the current remained steady from ca. 50 s onwards. These results suggest that the current produced at the start of these experiments was primarily due to the formation of CO_2 from adsorbed CO, and at longer times was from the production of acetic acid and acetaldehyde.

The sharp spike observed at the beginning of each run indicates that each potential tested is sufficient for CO stripping. However, the 800 mV (vs. H_2) was shown to have the largest CO_2 production in the first 50 s (which will be the important time interval for pulsing) and was therefore chosen to be the optimal potential to use for the pulsing experiments. To further demonstrate the importance of the pulsing potential, a 500 mV (vs. H_2) constant potential experiment was carried out. Absolutely no CO_2 was produced in this run, indicating that the potential was not high enough for CO stripping.

6.3.2. Increasing CO_2 Yield Using Pulsing Techniques

As mentioned in the introduction of this work, the complete oxidation of ethanol into CO_2 is normally very minor on Pt at room temperature. Using galvanostatic (constant current) experiments and liquid ethanol, the highest CO_2 yield reported at room temperature is ca. 13% [14]. As just shown in the linear sweep and constant potential experiments, yields much higher than 13% can be achieve when a proper potential is applied to the anode. By applying a potential in the CO oxidation region and stripping the CO and other intermediates into CO_2, then allowing the system to return to open circuit (where ethanol is able to re-adsorb to the surface) and re-applying the potential, the high yields seen in the first 50 s of Figure 6.6 can be continually achieved. By allowing the cell to return to open circuit between pulses, all of the current will be anodic and will all contribute to the CO_2 yield calculations.

To demonstrate the effects on CO_2 yield using this technique, a pulsing experiment using 5 s pulses at 0.8 V (vs. H_2) followed by 5 s resting intervals at open circuit was carried out. In this experiment 5 pulses were applied to the anode and the resulting current and CO_2 concentration were recorded (Figure 6.7). It is shown that the first pulse produced a fairly low concentration of CO_2. This has been observed in previous pulsing experiments [8] and is observed in almost all of our pulsing experiments. As mentioned earlier in this chapter, this low CO_2 concentration produced during the first pulse (in comparison to the proceeding pulses) is thought to be caused by a large concentration of

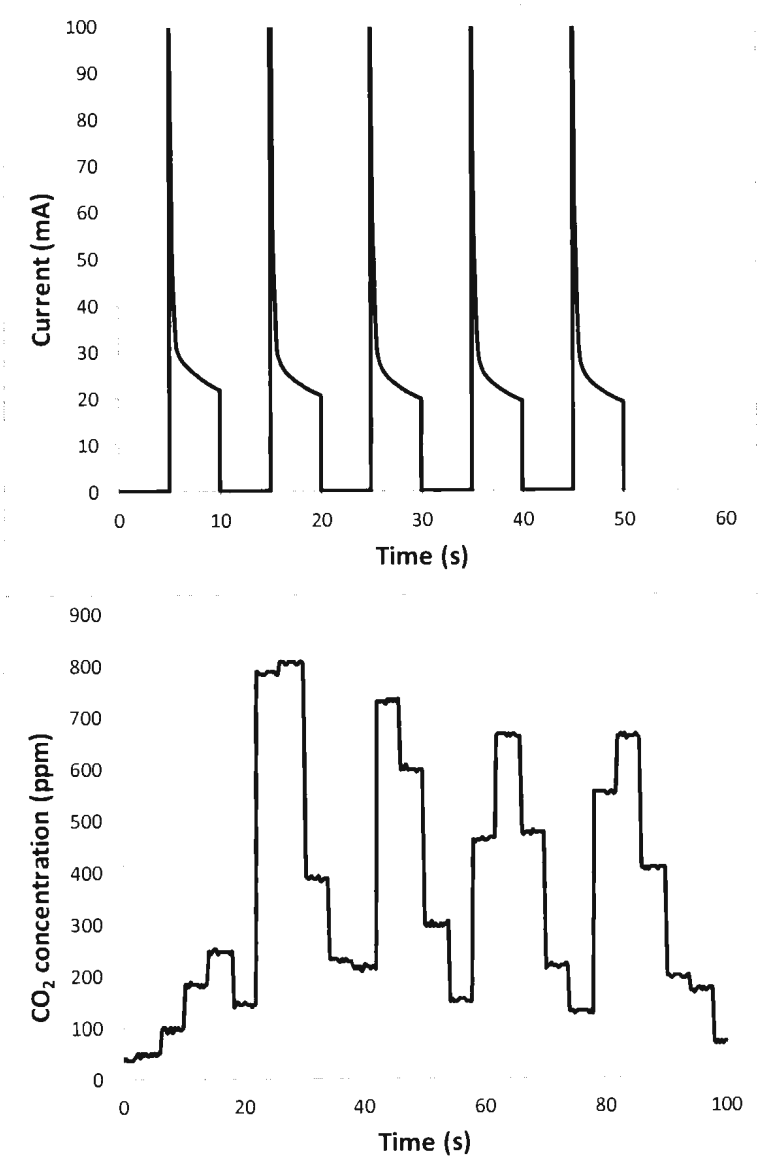

Figure 6.7: Pulsing experiment using 5 s pulses at 0.8 V (vs. H_2) with 5 s resting intervals at open circuit between pulses. The slow response time of the CO_2 measurements was corrected for.

non-CO adsorbates on the electrode surface. In each of the following pulses, CO was produced on the electrode at the high anode potentials while the cell was returning to its OCP. It would seem that the 5 s resting interval was enough time for ethanol to dissociate to CO on the surface.

As shown in Table 6.2, the first pulse (based on the first current peak) gave a CO_2 yield of 28.2%. The following peaks (2-5) gave yields between ca. 74-91% and the overall yield for the 5 peaks was calculated to be ca. 76%. It should be noted that the percent yield of all of the pulsing experiments would be most likely overestimated due to the oxidation of CO into CO_2. As mentioned earlier, as the cell is returning to open circuit potential, ethanol is oxidized to CO on the surface of the electrode. Once the potential is reapplied to the cell, the CO gets oxidized into CO_2 which would only require the transfer of 2 electrons. For all the calculations for theoretical moles of CO_2 in this chapter, it is assumed that ethanol is completely oxidized into CO_2 and the number of electrons transferred are 6 per mole of CO_2. Since the oxidation into CO_2 in these experiments involves a complex oxidation mechanism in which a mixture of ethanol, acetaldehyde and CO would be further oxidized to CO_2, the true number of electrons transferred would be most likely less than 6, resulting in an overestimation of the faradaic yields. The true number of electrons transferred in these experiments would be a much more complicated calculation that is beyond the scope of this work. Many of the calculated CO_2 yields are larger than 100% in this section, and are therefore only used as a comparison between other parameters and methods.

Table 6.2: Charges and moles of CO_2 obtained from graphs in Figure 6.7.

Pulse	Charge / C	Moles of CO_2 / 10^{-7}	CO_2 yield / %
#1	0.146	0.71	28.2
#2	0.150	2.20	84.9
#3	0.136	1.74	74.1
#4	0.132	2.03	89.0
#5	0.133	2.09	90.9
Total	0.697	9.18	76.2

6.3.2.1. Resting Time Dependence on CO_2 Yield

By varying the resting intervals between pulses, insight into the adsorption/dissociation rate of ethanol on the electrode surface can be gained. If the open circuit resting interval is too short, the ethanol will not have time to dissociate on the electrode and only small CO_2 yields will be observed. Since the adsorption of ethanol on Pt is known to be very quick and not the rate determining step (in the low potential region), very short intervals between pulses would most likely be sufficient. If the resting interval is too long (cell is allowed to return to open circuit potential) the ethanol could possible favor to dissociate into non-CO adsorbates (such as an acetaldehyde intermediate) and reduce the CO_2 produced for the pulse. In this work, pulsing experiments were performed in which the open circuit resting intervals were varied between pulses. These experiments were performed using 1 mol L^{-1} ethanol vapor from aqueous ethanol at room temperature. For this series of experiments, a complete run consisted of three pulsing intervals of 2 s each at 0.8 V (vs. H_2) each with various resting intervals in between.

Table 6.3: CO_2 yields for pulsing experiments using 2 s pulses of 0.8 V of with various resting intervals at open circuit. Ethanol vapor from 1 mol L^{-1} aqueous ethanol was used as the fuel. Experiments carried out at room temperature.

Resting Interval / s	Charge / C	Moles of CO_2 / 10^{-7}	Apparent CO_2 Yield / %
0.5	0.177	2.71	88.4
1	0.175	2.69	89.0
5	0.187	2.95	91.3
10	0.189	3.56	109
15	0.185	4.41	138

The resting intervals applied between pulses were 0.5, 1, 5, 10 and 15 s. The open circuit potential prior to these experiments ranged from 0.41 to 0.43 V (vs. H_2). The results for this series of experiments are shown in Appendix A and summarized in Table 6.3. It is shown from these results that the rest time between pulses does not seem to significantly influence the overall CO_2 yield throughout the run. The calculated faradaic CO_2 yields for the shorter resting intervals (0.5, 1 and 5 s) were all fairly close ranging from 88.4 to 91.3 %. This could suggest that 0.5 s is sufficient time for the ethanol to dissociate into CO on the surface of the electrode. It appears that at the higher resting intervals (10 and 15 s), there is an increase in CO_2 yield. This could be a result of slow diffusion of CO_2 through the membrane. The longer resting intervals could allow for all of the CO_2 that is produced to reach the detector before the proceeding pulse. This can be verified by observing the steady state moles s^{-1} of CO_2 between pulses. For example, for the 5

s resting interval, the lowest CO_2 reading between pulses was found to be ca. 2.71×10^{-9} moles s^{-1}, whereas that for the 15 s resting interval was found to be ca. 8.33×10^{-10} moles s^{-1} (see Appendix A). This could suggest that the longer resting interval may be needed for the system to record all of the CO_2 produced from each pulse.

Another interesting observation from these results is that at the highest resting interval (15 s) there was no significant change in current. This could suggest that the amount of CO that is produced on the electrode during the relaxation period (to open circuit) is similar for the 0.5 and 15 s resting interval, suggesting quick kinetics, making these pulsing experiments rest-time independent.

The traces found in Appendix A show a similar trend for this series of experiments in that the first pulse gives a significantly lower number of moles compared to the proceeding pulses. In the short resting interval experiments, there is very poor resolution between peaks, and would be very tough to associate a CO_2 yield per peak. At the longer resting interval experiments (10 and 15 s), where there is good resolution between peaks, it is shown that the number of moles of CO_2 produced are ca. 2 times larger for the second and third peak compared to that of the first. Again, this trend can be attributed to the formation of CO intermediates on the surface of the electrode as the anode is returning to open circuit.

6.3.2.2. CO_2 Yield Dependence on Pulse Time

By altering the pulse time and comparing CO_2 yields and/or moles of CO_2 produce, some insight into the oxidation of CO to CO_2 could be gained. Since it is thought that the rate determining step in the complete oxidation of ethanol in a DEFC is the oxidation of CO

into CO_2 [15], monitoring the CO_2 yield as a function of pulsing time could be of importance.

This series of experiments once again used ethanol vapor from 1 mol L^{-1} aqueous ethanol as the fuel and H_2/N_2 gas at the cathode as reference potential. The resting intervals were held at 5 s to ensure that the ethanol had sufficient time to re-adsorb and dissociate on the electrode. The pulsing times used were 0.5, 1, 5, 10, and 15 s and the pulsing potential was 0.8 V (vs. H_2). The CO_2 yields calculated for the entire run are reported in Appendix B and summarized in Table 6.4. It is shown that at low pulsing times, large CO_2 yields were obtained. This could suggest that only short pulsing times at an appropriate potential are needed to completely strip the CO from the electrode into CO_2. The yields above 100% at low pulsing intervals indicate that the number of electrons transferred is most likely less than 6. This is an indication that the CO_2 produced at these low intervals is primarily due to CO that is adsorbed to the electrode (where the number of electrons transferred is 2). As the pulsing time was increased, a significant decrease in CO_2 yield was observed. These results suggest that once all of the CO on the electrode is oxidized to CO_2, the ethanol will most likely react with the dissociated water (OH^-) to form significant amounts of acetic acid. The formation of acetic acid during the pulsing interval will significantly decrease the production of CO_2, leading to an overall decrease in the CO_2 yield for the entire run. Comparing the total number of moles produced at the 0.5 and 1 s pulsing intervals, only a small increase in CO_2 is reported (2.46×10^{-7} to 3.04×10^{-7} moles). If it is assumed that 0.5 s is sufficient time to strip all the CO into CO_2, then the majority of the CO_2 observed at 0.5 s would be attributed to CO oxidation (with

Table 6.4: Faradaic CO_2 yields for pulsing experiments using 0.8 V (vs. H_2) pulsing potential and a constant resting interval of 5 s at open circuit.

Pulsing Interval / s	Charge / C	Moles of CO_2 / 10^{-7}	Apparent CO2 Yield / %
0.5	0.081	2.46	176
1	0.124	3.04	142
5	0.394	5.02	74.3
10	0.689	7.71	65.2
15	0.971	9.30	55.1

an n value of 2). As the pulsing interval increased to 1 s, it is likely that the increase in moles of CO_2 would be attributed to ethanol dissociation and oxidation on the clean electrode surface (in the final 0.5 s of the 1 s pulse) resulting in an n value closer to 6 and lowering the apparent faradaic yield.

Determining the actual faradaic CO_2 yield is very difficult in this set of experiments due to the number of electrons varying from the oxidation of mixed intermediates. It can be assumed that these yields are much more overestimated at the lower pulsing potential where the majority of the CO_2 produced is attributed to the oxidation of CO. However, at the lower pulsing intervals, the charge passed is most likely significantly overestimated as well. Since the charging current would account for a large portion of the overall charge at the low pulsing interval, the theoretical moles calculated would be overestimated and the faradaic yield would be underestimated. As the pulsing times increase, the charging current becomes much less significant and would therefore not affect the faradaic yield as much.

Once again for this set of experiments, a low CO_2 yield was observed for each of the initial pulses (see Appendix B). The second and third pulses showed much high yields, which support our assumption of CO being produced at potentials between 0.8 V and OCP (ca. 0.42 V).

6.3.2.3. Temperature Dependence on CO_2 Yield

The production of CO_2 has been reported to be dependent on the temperature of the fuel cell. As temperature increases, the cleavage of the C-C bond occurs more easily resulting in high production of CO_2. The highest CO_2 yield ever reported was ca. 95% and occurred at 145 °C [16]. However, most Nafion® membranes can only withstand temperatures to ca. 100 °C due to low water transport resulting in dehydration and degradation of the membrane.

In this set of experiments, the temperature of the fuel cell was increased from ambient temperature to 50 °C and the corresponding yields using pulsing were measured. Temperatures beyond 50 °C resulted in small production of liquid products in the anode line which could significantly affect the detector and possibly compromise the results; therefore only experiments at 50 °C and below were carried out using this method.

To show the temperature dependence on CO_2 yield using the stripping method, 2 s pulses at 0.8 V (vs. H_2) with 15 s rest intervals at open circuit were used. The CO_2 concentration traces for the various temperatures are depicted in Figure 6.8. It is clear from these traces that as the temperature was increased, significant increases in CO_2 production were observed. Table 6.5 reports the calculated charges and faradaic CO_2 yields for the experiments at 30, 40 and 50 °C. As would be expected, increasing temperature

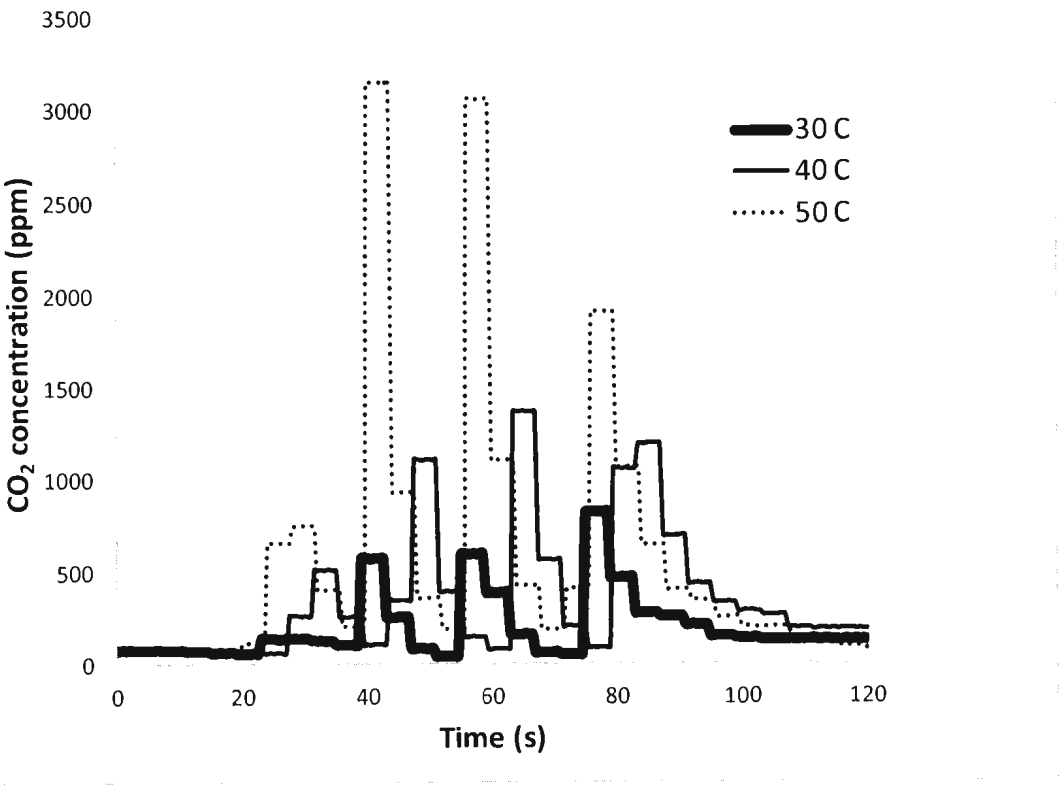

Figure 6.8: CO_2 traces for stripping experiments using various fuel cell temperatures. Vapour from 1 mol L^{-1} ethanol solution, 2 s pulses at 0.8 V (vs. H_2) with 15 s resting intervals at open circuit.

Table 6.5: Apparent faradaic CO_2 yield calculated using the integrated moles of CO_2 and the charge produced in the cell using 2 s pulsing intervals at 0.8 V (vs. H_2) and 15 s resting intervals at open circuit between pulses.

Temperature (°C)	Charge (C)	CO_2 (mols 10^{-7} s^{-1})	CO_2 yield (%)
30	0.2485	6.71	156
40	0.2635	8.06	175
50	0.4859	19.60	234

showed an increase in yield. When the temperature was increased from ambient temperature (Table 6.3) to 30 and 40 °C, only a small hike in CO_2 yield was observed. However, the increase from 40 to 50 °C showed a very large jump in the CO_2 yield (175-234%). This could be indicative of an exponential relationship between CO_2 yield and temperature. Also, as expected, the performance of the cell (current produced) at elevated temperatures was also increased.

6.3.2.4. Pulsing in Crossover Mode

As shown in chapter 5, running a DEFC in crossover mode can increase the Faradic CO_2 yield by more than 30% at low concentrations of ethanol. This increase is most likely due to slow diffusion of the ethanol through the membrane resulting in a decrease in CO poisoning at the anode. In this series of experiments, the stripping technique was employed to the crossover method of running a fuel cell (described in chapter 5). The concentra-

tions of ethanol used for these experiments were 0.1 and 0.5 mol L^{-1} since it was shown in the previous chapter that lower concentrations lead to high yields in crossover mode. This series of stripping experiments used 5 s pulses at 0.7, 0.8 and 0.9 V (vs. H_2) and 5 s resting intervals at open circuit between pulses. Only two pulses were applied for each run. All CO_2 and current traces can be found in Appendix C.

Table 6.6 reports the results obtained at room temperature for anode stripping experiments in crossover mode. As shown, the average yield using 0.1 mol L^{-1} ethanol throughout the CO oxidation potential region (700-900 mV) was ca. 49%. If compared with the results obtained using normal mode (see section 6.3.2.1) there is a significant decrease in CO_2 yield using the crossover stripping method. For example, the highest CO_2 yield reported in this chapter for the RT normal mode stripping experiments was ca. 176% (see Table 6.4), whereas in crossover mode, the highest yield was calculated to be ca. 50%. This significant decrease in CO_2 yield in crossover mode could suggest that the crossover method limits the amount of CO build-up on the electrode, hence, limiting the amount of CO_2 produced from CO stripping. If this is the case, then these calculations would most likely be fairly accurate as a smaller percentage of the CO_2 produced would be from CO adsorbants and the number of electrons transferred would be closer to 6.

These results were very interesting, as the trends in fuel concentration using stripping method and normal method in crossover mode on CO_2 yield were reversed (see chapter 5). In the regular crossover mode, it was shown that decreasing the ethanol concentration increased the CO_2 yield. Using the stripping technique, where the CO poisoning of the anode is assumed to be eliminated, the more concentrated fuel showed a higher

Table 6.6: Faradaic CO_2 yields calculated in crossover mode using stripping methodology. The pulse times were 5 s and the resting time between pulses was 5 s at open circuit.

[EtOH]	Potential (mV vs. H_2)	CO_2 yield (%)
0.1	700	45.1
0.1	800	47.7
0.1	900	54.0
0.5	700	50.5
0.5	800	51.9
0.5	900	57.6

yield than that of the lower concentrated fuel. These results suggest that our assumption that the high yields in crossover mode, at low concentrations of ethanol, are a consequence of decreased poisoning of the electrode. Since less ethanol is reaching the electrode in crossover mode and is dependent on the fuel concentration, smaller amounts of CO and other intermediates are occupying the adsorption sites reducing the poisoning of the electrode.

6.3.3. Acetaldehyde Oxidation

In almost all theoretical studies involved in proposing the EOR mechanism, the formation of acetaldehyde is the most kinetically favoured and is therefore the most likely first product produced at the electrode surface. From adsorbed acetaldehyde, further oxidation can take place to form CO_2 which involves 10 electron transfers or to acetic acid which involves 2 electron transfers. The desorption of acetaldehyde is also very commonly ob-

served in the EOR especially at low current densities.

In these experiments, 0.5 mol L^{-1} acetaldehyde (in distilled water) was used as the fuel and was passed through the anode compartment of the fuel cell. Distilled water was used at the cathode to obtain a DHE. The cell was operated at constant current. The oxidation reactions at the anode for the production of CO_2 and acetic acid are shown in equation 6.1 and 6.2 respectively.

$$CH_3CHO + 3H_2O \rightarrow CO_2 + 10H^+ + 10e^- \quad (6.1)$$

$$CH_3CHO + H_2O \rightarrow CH_3COOH + 2H^+ + 2e^- \quad (6.2)$$

The results for these experiments are shown in Table 6.7 and all CO_2 traces can be found in Appendix D. In most of the experiments, we were able to obtain a charge balance (100% total yield) using the CO_2 detector or the conductivity cell for CO_2 and acetic acid analysis. In some cases, usually at low currents, the combined CO_2 and acetic acid yields gave yields > 100%. This is most likely due to calibration errors in the detection systems. At low currents there are only small concentrations of products being produced which leads to higher errors in the calibration of the system.

As shown in Table 6.7, at low currents, the production of CO_2 was the highest. When the current was increased, the acetic acid yield also increased which is shown for the EOR as well. At RT, the oxidation of AAL to AA is dominant and only small CO_2yields are observed. As temperature is increased, a significant increase in CO_2 yield

Table 6.7: Acetaldehyde oxidation (0.5 mol L^{-1} in distilled water) product analysis at various temperatures and currents. Water was passed through the cathode in these experiments.

Temperature (°C)	I (mA)	CO_2 Yield (%)	AA Yield (%)	Total Yield (%)
ambient	20	39.1	79.6	118.7
ambient	50	15.1	87.3	102.4
ambient	100	11.8	82.7	94.5
40	20	18.9	76.1	95.0
40	50	22.9	85.2	108.1
40	100	13.2	78.4	91.6
60	20	58.8	53.2	112.0
60	50	25.2	77.4	102.6
60	100	14.1	76.5	90.6
80	20	63.2	64.3	127.5
80	50	36.4	68.4	104.8
80	100	27.3	63.4	90.7
100	50	57.2	59.0	116.2
100	100	55.5	45.0	100.5
100	200	48.9	42.5	91.4

is observed resulting in a large decrease in AA yield.

Table 6.7 is great for understanding the behaviour of acetaldehyde at various temperatures and currents when it is produced in a DEFC. The trends in CO_2 yield for ethanol oxidation based on temperature and current are very similar to those for acetaldehyde oxidation. This data can suggest that ethanol undergoes oxidation to acetaldehyde prior to formation of CO_2 and most like to acetic acid as well.

6.4. Conclusions

Pulsing the anode to a potential in the region where CO oxidation takes place can strip the CO from the surface to produce CO_2. This results in a clean surface for ethanol to re-adsorb and dissociate. This method had been shown to significantly increase the CO_2 yield at ambient temperature. The calculated yields in this chapter for the pulsing experiments are overestimated as the oxidation taking place is for a mixture of CO and ethanol which require 2 and 6 electrons, respectively. All our calculations assumed only ethanol oxidation and a 6 electron transfer, resulting in an underestimation of theoretical moles of CO_2. The pulsing times were examined and it was found that at the shorter the pulsing times, the CO_2 yield was higher. This is a result of quick stripping of CO into CO_2 during the first instances of the pulse, and production of more acetic acid and/or acetaldehyde later in the pulse. The resting interval between pulses was also examined. It was shown that the dissociation of ethanol on the anode surface seems to occur very quickly and 0.5 s rests between pulses at open circuit were sufficient time for re-adsorption of ethanol.

The initial pulse in each series of experiments showed a lower CO_2 yield than the following pulses and could be caused by non-CO intermediates adsorbing to the electrode

surface at open circuit. It can be suggested that as the cell slowly returns to open circuit during the resting intervals, the potential remains high enough for CO to form on the electrode surface resulting in higher CO concentrations on the surface and higher CO_2 yields for the second and third pulses.

The temperature dependence was also briefly examined. It was shown that increasing the temperature to 50 °C from ambient temperature can increase the CO_2 yield by ca. 58%. Increasing the temperature in the cell higher than 50 °C resulted in formation of liquid products in the anode feed, which can destroy the detector. A detector which is liquid friendly would be needed to conduct experiments at high temperatures.

Pulsing experiments in crossover mode were carried out and it was found that the CO_2 yields were significantly lower using this mode than in normal mode. This could be due to the slow build-up of CO on the electrode surface in crossover mode compared to that in normal mode, leading to a smaller CO concentration and in turn a smaller CO_2 concentration.

Acetaldehyde oxidation in a DEFC was examined at various temperatures and currents to determine the product distribution. It was shown that acetaldehyde oxidation products are affected in a similar manner to the EOR. For example, as the current is increased, the production of acetic acid is also increased and when the temperature is elevated, the CO_2 yield significantly increases.

6.5. References

[1] Rousseau, S.; Coutanceau, C.; Lamy, C.; Leger, J. M. *J. Power Sources* **2006**, *158*, 18-24.

[2] Nakaguwa, N.; Kaneda, Y.; Wagatsuma, M.; Tsujiguchi, T. *J. Power Sources* **2012**,

[3] Linares, J. J.; Zignami, S. C.; Rocha, T. A.; Gonzalez, E. R. *J. Appl. Electrochem.* **2013**, *43*, 147-158.

[4] Song, S. Q.; Zhou, W. J.; Zhou, Z. H.; Jiang, L. H.; Sun, G. Q.; Xin, Q.; Leontidis, V.; Kontou, S.; Tsiakaras, P. *Int. J. Hydrogen Energy* **2005**, *30*, 995-1001.

[5] Zignami, S. C.; Baglio, V. Linares, J. J.; Monforte, G.; Gonzalez, E. R.; Aricò, A. S. *Electrochim. Acta* **2012**, *70*, 255-265.

[6] Pugato, F. L. S.; Pronier, S.; Olivi, P.; de Andrade, A. R.; Leger, J. M.; Tremiliosi-Filho, G.; Kokoh, K. B. *J. Power Sources* **2012**, *198*, 95-99.

[7] Dupont, C.; Jugnet, Y.; Loffreda, D. *J. Am. Chem. Soc.* **2006**, *128*, 9129-9136.

[8] Ghumman, A.; Pickup, P. G. *J. Power Sources* **2008**, *179*, 280-285.

[9] Wang, H.-F.; Liu, Z.-P. *J. Am. Chem. Soc.* **2008**, *130*, 10996-11004.

[10] Zang, J.; Cao, X.-M.; Zhang, Z.; Borgma, A.; Wu, P. *J. Phys. Chem. C* **2011**, *115*, 22429-22437.

[11] Kavanaugh, R.; Cao, X.-M.; Liu, W.; Hardacre, C.; Hu, P. *J. Phys. Chem. C* **2012**, *116*, 7185-7188.

[12] Blanco, T. C.; Pierna, A. R.; Barroso, J. *J. Power Sources* **2011**, *196*, 4337-4341.

[13] D'Urso, C.; Bonesi, A.; Triaca, W. E.; Castro Luna, A. M.; Baglio, V.; Arico, A. S. *Int. J. Electrochem. Sci.* **2012**, *7*, 9909-9919.

[14] Wang, H.; Jusys, Z.; Behm, R. J. *J. Phys. Chem. B* **2004**, *108*, 19413-19424.

[15] Zhou, W.; Zhou, Z.; Song, S.; Wenzhen, L.; Sun, G.; Tsiakaras, P.; Xin, Q. *Appl. Catal. B* **2003**, *456*, 273-285.

[16] Arico, A. S.; Creti, P.; Antonucci, P. L.; Antonucci, V. *Electrochem. Solid-state. Lett.* **1998**, *1*, 66-68.

CHAPTER 7

Enhanced Performance and CO_2 Selectivity with a Pt-$RuSnO_2$/C Catalyst

7.1. Introduction

Direct alcohol fuel cells (DAFC) are a continually growing field of electrochemistry. Their ability to use a liquid feed at moderate temperatures to generate significant energy makes them very attractive as a futuristic bulk energy source [1-5]. Methanol and ethanol fuels have been the most widely researched alcohols for DAFCs. Methanol, which is currently used in many small commercial applications such as cell phones and laptops, has been a very promising candidate due to its low cost, ease of storage and transport, and ease of oxidation [6, 7]. However, the toxicity of methanol and its oxidation products has limited its use in large commercial applications. Ethanol on the other hand is non-toxic, renewable, easily produced in large quantities, and has a higher energy density than methanol (8.01 vs. 6.09 kWh kg^{-1}), making it an excellent candidate for mass commercialization [8, 9]. However, there are many obstacles that must be overcome in making ethanol a competitive fuel in DAFCs [2, 3].

The main drawbacks of direct ethanol fuel cells (DEFC) are performance and selectivity towards carbon dioxide (CO_2). The ethanol oxidation reaction (EOR) involves complex mechanisms that are concentration and temperature dependent [10-12], and is still not completely understood by researchers. In the case of complete oxidation to CO_2, 12 electrons are transferred. When oxidation is not complete, acetic acid (AA) and acetaldehyde (AAL) are produced, needing 4 and 2 electrons to be transferred, respectively. The production of the AA and AAL by-products significant decreases the performance (energy density) of the reaction and may cause concern about disposal of the by-products [3, 11, 13].

To increase the efficiency of the EOR, metal catalysts are needed. Pt catalysts have been shown to exhibit the highest CO_2 yields in DEFCs [11, 13] (besides a study Arico et al. [12] using a PtRu catalyst and a study by Kowal et al. [14] using a $PtRhSnO_2/C$ catalyst). Despite the high selectivity towards CO_2, Pt catalysts show very poor overall efficiency due to low cell voltage. The poor efficiency of Pt electrodes can be attributed to the strong interactions between the Pt surface and the adsorbed CO and CH intermediates (CO_{ads} and $CH_{x,\ ads}$), leading to high overpotentials for the EOR to occur. For the adsorbed species on the surface of the electrode to be oxidized, a sufficient amount of oxygen containing species must be present and in close proximity with the CO_{ads} and $CH_{x,\ ads}$. At low potentials, all adsorption sites are occupied by the CO_{ads} and $CH_{x,\ ads}$ and no hydroxyl (OH_{ads}) are able to adsorb on the surface, poisoning the electrode [15].

To improve the performance of the EOR, many secondary and tertiary metal catalysts have been investigated. Studies have shown that the best binary catalysts for EOR are PtSn [16, 17] and PtRu [12, 18, 19], the former being the best. Since Sn and Ru atoms can exist in their oxidized forms, they can supply the catalyst with the oxygenated species, lower the onset potential of the EOR, and limit poisoning of the electrode. In the case of PtSn, the highest performances were reported at low potentials, due to its ability to dissociate adsorbed ethanol on the surface of the electrode. Whereas, for PtRu the best performances were obtained at high potentials, suggesting that the Ru atoms aid in the dissociation of water and the oxidation of adsorbates to form the EOR products [20]. Although the incorporation of Sn, Ru and other metals has been shown to significantly increase the electroactivity of the catalyst, significant decreases in CO_2 yields (in compar-

ison with pure Pt) have been observed [13]. The drop in CO_2 yield with an increase in current density can suggest an increase in the unfavorable AA product yield. Many groups have also tried alloying Pt with both Sn and Ru [13,21,22]. Rousseau and his colleagues have shown that incorporating a small amount of Ru into a PtSn catalyst can increase the performance and the selectivity towards CO_2 in comparison to the PtSn and PtRu catalysts [13]. Although the reported yields were still significantly lower than those obtained using a Pt catalyst, the PtRuSn system has shown potential to be an ideal candidate for the EOR in DEFCs.

Taking into consideration the importance of Pt for selectivity towards CO_2 along with the reported enhanced performances of Sn and Ru, Pt-$RuSnO_2$/C catalysts have been synthesized. A slow deposition of Pt nanoparticles on carbon black coated with a mixed Ru and Sn oxide has allowed us to synthesize a catalyst that exhibits the benefits of Ru and Sn while maintaining the selectivity of Pt towards CO_2. To gain insight into the mechanism and product distribution of the EOR; CO_2 and AA products were analyzed and reported. Characterization of the catalysts was carried out using energy dispersive x-ray spectroscopy (EDX), x-ray diffraction (XRD), inductively coupled plasma optical emission spectroscopy (ICP-OES), thermogravimetric analysis (TGA) and transmission electron microscopy (TEM).

7.2. Experimental

7.2.1. Chemicals and Materials

Anhydrous ethanol (Commercial Alcohols Inc.), sulphuric acid (Fisher Scientific), carbon black (Vulcan XC -72, Cabot), $KRuO_4$ (Alfa Aesar), $SnCl_4 \cdot 5H_2O$ (Fisher Scientific)

$H_2PtCl_6 \cdot 6H_2O$ (Alfa Aesar), sodium citrate (Anachemia), potassium hydroxide (ACP Chemical Inc.), Nafion® solution (5% Dupont) and sodium borohydride (Sigma Aldrich) were used as received. Double distilled water was used throughout all experiments. Commercial electrodes (used where indicated in this work) consisted of 4 mg cm^{-2} Pt black on Toray™ carbon fiber paper.

7.2.2. Cells

Initial electrochemical measurements (cyclic voltammetry) were carried out in a conventional three electrode cell with an EG&G PAR 273 A model Potentiostat/Galvanostat using M270 commercial software. A 5 cm^2 commercial cell (Fuel Cell Technology Inc.) was used for fuel cell testing. The cathode inlet and outlet were both modified to prevent the ethanol solution from contacting any metal parts of the hardware. Membrane and electrode assemblies were prepared by hot pressing a 5 cm^2 anode and a 5 cm^2 cathode onto a Nafion® 115 membrane (Ion Power) at a pressure of 200 kg cm^{-2} at 135 °C for 90 s. The cell was operated with an anode feed of 0.50 mol L^{-1} ethanol solution at 0.50 mL min^{-1}. The cathode feed was O_2 or N_2 at 50 mL min^{-1}. Use of N_2 allows the cathode to act as a dynamic hydrogen electrode (DHE). Electrochemical measurements in fuel cell experiments were made using a Solartron 1286 potentiostat operated with Corrwear software.

7.2.3. Electrochemical Measurements

Cyclic voltammograms of the Pt-$RuSnO_2$/C electrodes were performed in a standard 3 electrode cell. To prepare the working electrodes, 10 drops of methanol was added dropwise to 10.4 mg of the catalyst powder, to form a suspension of the catalyst that would

adhere to carbon fiber paper. The catalyst and methanol mixture were then spread across a 0.5 cm by 0.5 cm section of a strip of carbon fiber paper to give a catalyst area of 0.25 cm^2. The 3 electrode cell contained an Ag/AgCl reference electrode and a Pt counter electrode. The 0.25 cm^2 tip of the electrode was placed in 15 mL of 0.1 mol L^{-1} H_2SO_4. The cell was purged with nitrogen for 15 min before measurements.

7.2.4. Product Analysis

Both the anode solution and the cathode gas were passed through a 125 mL flask. The O_2 or N_2 at the cathode was purged through the solution of the collection flask and into a Telaire 7001 non-dispersive infrared CO_2 detector for CO_2 analysis. The CO_2 detector was calibrated using a methanol crossover method and a controlled CO_2 concentration method (see section 5.2.3 and ref [23]) regularly throughout the runs as it was found that the detector readings tended to decrease with extensive use. Anode and cathode solutions were periodically titrated to check CO_2 yield accuracy. This two step titration began with the combined anode and cathode exhausts being bubbled through a cold condensing flask containing 1 mol L^{-1} NaOH solution. The CO_2 first reacted with the NaOH to form Na_2CO_3 (equation 7.1). This solution was then titrated with 0.100 mol L^{-1} HCl using a phenolphthalein indicator to remove all excess NaOH in the solution and to convert Na_2CO_3 to $NaHCO_3$ (equation 7.2). The $NaHCO_3$ was then further titrated with 0.00100 mol L^{-1} HCl using a methyl orange indicator. As shown in equation 7.3 of the equation below, there is a 1:1 mole ratio between the HCl and the CO_2 produced in the final step. The moles of CO_2 are directly proportional to the moles of HCl used in the final titration.

$$\text{Step 1: } CO_2 + 2NaOH \rightarrow Na_2CO_3 + H_2O \qquad (7.1)$$

Step 2: $Na_2CO_3 + HCl \rightarrow NaHCO_3 + NaCl$ (7.2)

Step 3: $NaHCO_3 + HCl \rightarrow NaCl + CO_2 + H_2O$ (7.3)

Acetic acid measurements were made by titrating the anode effluent with 0.0100 mol L^{-1} NaOH solution. The background acetic acid (collected from zero current experiments) was titrated and subtracted from the measured acetic acid in each run.

All yields described in this section are faradaic yields and are calculated based only on the magnitude of current that is passed at the anode (see section 3.2.3).

7.2.5. Characterization of the Catalysts

X-ray diffraction, inductively coupled plasma optical emission spectroscopy, energy dispersive x-ray microanalysis, thermogravimetric analysis and transmission electron microscopy experiments were carried out to characterize the composition and other physical characteristics of the synthesized catalysts. The description of the processes and procedures followed for these instruments are described in section 2.5.

7.2.6. Preparation of Catalysts

7.2.6.1. Method 1 (M1)

Carbon black (CB) powder was dispersed in 0.1mol L^{-1} H_2SO_4 then collected by filtration and rinsed with distilled water. Co-deposition of Ru and Sn oxides on carbon was as follows: 0.025 mol L^{-1} (0.1513 g) $KRuO_4$ was dispersed in 0.1mol L^{-1} (30 mL) KOH. A solution of 0.025 mol L^{-1} (0.2668 g in 30 mL of 0.1mol L^{-1} KOH) of $SnCl_4 \cdot 5H_2O$ was then added to the ruthenium mixture drop wise. The RuSn solution was then added to 0.6000 g of carbon black (in 45 mL of distilled water) and was stirred vigorously for 0.5 h, collect-

ed by filtration and rinsed several times with distilled water. The Ru and Sn oxide on C powder was then dried under vacuum overnight.

Pt nanoparticles were introduced into the catalyst powder using a method similar to Yang *et. al* [24]. The $RuSnO_2$/C powder (0.2018 g) was first dispersed in 30 mL of distilled water. H_2PtCl_6 (0.1828 g) was dissolved in 10 mL of distilled water then added drop wise to the CB-RuSn mixture and stirred for 0.5 h. A 12 mL volume of 50 mmol L^{-1} trisodium citrate (0.1778 g) was then added drop wise. After mixing for 1 h, 0.0902 g of sodium borohydride was added to the solution dropwise. The entire mixture was stirred for 3 h, filtered, washed several times and was allowed to dry overnight. 0.2521 g of Pt-$RuSnO_2$/C was produced.

74.4 mg of the Pt-$RuSnO_2$/C catalyst was dispersed in 184.5 mg of 5% Nafion® solution by sonication for 30 min. The resulting ink (ca. 250 mg) was then deposited onto a 5cm^2 piece of carbon fiber paper with a micropipette and spatula and allowed to dry for 1 day. This gave the electrode a 9.74 mg cm^{-2} total catalyst loading. This number was obtained by taking the difference of the mass of the electrode prior to applying catalyst and after the catalyst was dried on the CFP (the overall loading of the catalyst and Nafion® solution). The low loading (ca. 50 mg) in comparison to the total catalyst ink produced (ca. 250 mg) is due to evaporation of the Nafion® solution upon drying and loss of catalyst during the spreading process.

7.2.6.2. Method 2 (M2)

Carbon black (CB) was first activated by adding 5 mL of concentrated HNO_3 and stirred for 0.5 hours. The carbon was then collected by filtration and washed with copious

amounts of distilled water, and dried under vacuum for 1 h. The activated carbon black (0.6028 g) was then dispersed in 50 mL of 0.1 mol L^{-1} KOH and stirred for 0.75 h. In separate beakers, 0.0513 g of $KRuO_4$ and 0.1034 g of $SnCl_4 \cdot 5H_2O$ were weighed out and each dispersed in 30 mL of 0.1 mol L^{-1} KOH forming a dark black solution and a clear colorless solution, respectively. Both the $KRuO_4$ and the $SnCl_4 \cdot 5H_2O$ solutions were stirred for 10 min. The Ru and Sn solutions were then added simultaneously dropwise to the CB solution over a one hour period. No precipitate was observed during this step. The resulting mixture was then suction filtered (3 h) and was washed with large amounts of distilled water. The modified CB was then dried under vacuum for 2 h. 0.2645 g of $RuSnO_2$/C powder was formed.

The addition of the Pt to the $RuSnO_2$/C powder was carried out using the same method as described in method 1. The $RuSnO_2$/C powder (0.2017 g) was suspended in 30 mL of distilled water. The H_2PtCl_6 (0.1853 g) was dispersed in 10 mL of distilled water. The Pt solution was then added dropwise to the $RuSnO_2$/C solution over a 15 min period. The mixture was then stirred for 15 min. 12 mL of 50 mmol L^{-1} trisodium citrate (0.1764 g) was then added dropwise to the resulting mixture and allowed to stir for an additional 0.5 h. Sodium borohydride (0.0923 g dispersed in 20 mL of distilled water) was then added dropwise to the solution. The whole solution was stirred for 3 h, filtered, washed well with distilled water and allowed to dry overnight under vacuum. The method resulted in 0.2563 g of Pt-$RuSnO_2$/C powder.

Two 5 cm^2 electrodes with loadings of 3.70 and 7.72 mg cm^{-2} were made for fuel cell testing. 21.2 and 43.5 mg of catalyst powder were mixed with 100.4 and 132.1 mg of

5% Nafion®, respectively, to form the catalyst pastes. The mixtures were sonicated for 0.5 h before being painted onto 5 cm^2 carbon fiber paper electrodes.

The synthesis methodology for the Pt-$RuSnO_2$/C catalyst was developed by Moghaddam and Pickup [25] in 2012.

7.3. Results and Discussion

7.3.1. Characterization of Catalysts

Physical properties of the prepared catalysts, M1 (method 1) and M2 (method 2), were examined and characterized using XRD, ICP-OES, EDX and TGA. Figure 7.1 illustrates the XRD patterns for the Pt-$RuSnO_2$/C made by M1 (method 1) and M2 (method 2). In both traces, a diffraction peak at ca. 25° represents the carbon (0 0 2) plane. The Pt peaks at ca. 40°, 46.5°, 67.5°, 81.5° and 86.1° represent the Pt (1 1 1), Pt (2 0 0), Pt (2 2 0), Pt (3 1 1) and Pt (2 2 2) planes respectively. In M1, peaks at ca. 34° and 53.1° are clearly observed and studies have suggested these peaks to be associated with RuO_2 [26]. There were no observed peak shifts relative to the above mentioned Pt peaks. A shift in peak position would suggest a change in the lattice constant which would be indicative of a PtRu or a PtSn alloy. Therefore, the addition of Ru and Sn to the Pt did not form an alloy. The mean particle sizes were calculated to be ca. 9.4 and 4.7 nm for M1 and M2 respectively. The mean particles sizes were calculated using the Pt (1 1 1) peak in accordance with the Scherrer equation:

$$D = \frac{0.9\lambda}{(B\cos\theta)} \tag{7.4}$$

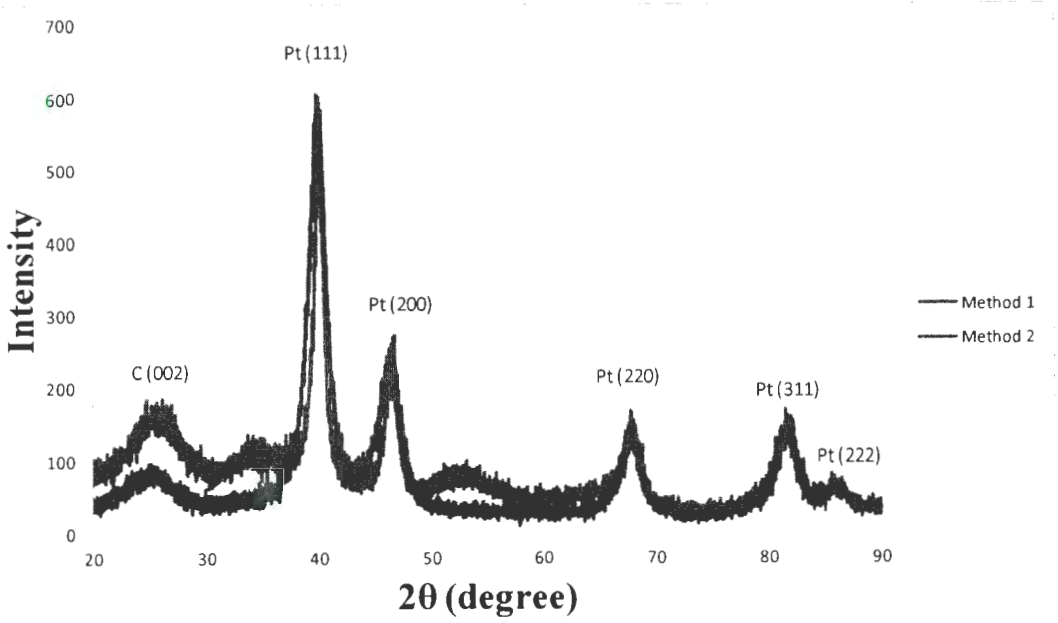

Figure 7.1: XRD patterns of the Pt-$RuSnO_2$/C catalyst powders.

where D is the mean particle diameter (nm), B is the peak width at half height (radians), λ is the X-ray wavelength (nm) and θ is the diffraction angle (degrees).

Scanning electron microscopy (SEM) was used to obtain images of the electrode surfaces. Multi-point elemental analysis was performed on the electrodes using EDX. Figure 7.2 shows the surface of the 5 cm^2 Pt-$RuSnO_2$/C catalyst (M1). The analysis focused on 10 different areas of the catalyst, giving an approximation of the catalyst composition at each area. As seen in Figure 7.2 the catalyst looks heterogeneous with small individual Pt, Ru and Sn particles on the surface of the electrode. The three different elements can be identified by their brightness. The heaviest element (Pt) produces the brightest image, showing an almost white appearance. Sn, being the second heaviest of the 3 metals, is the next brightest in the image and Ru which is the lightest of the metals

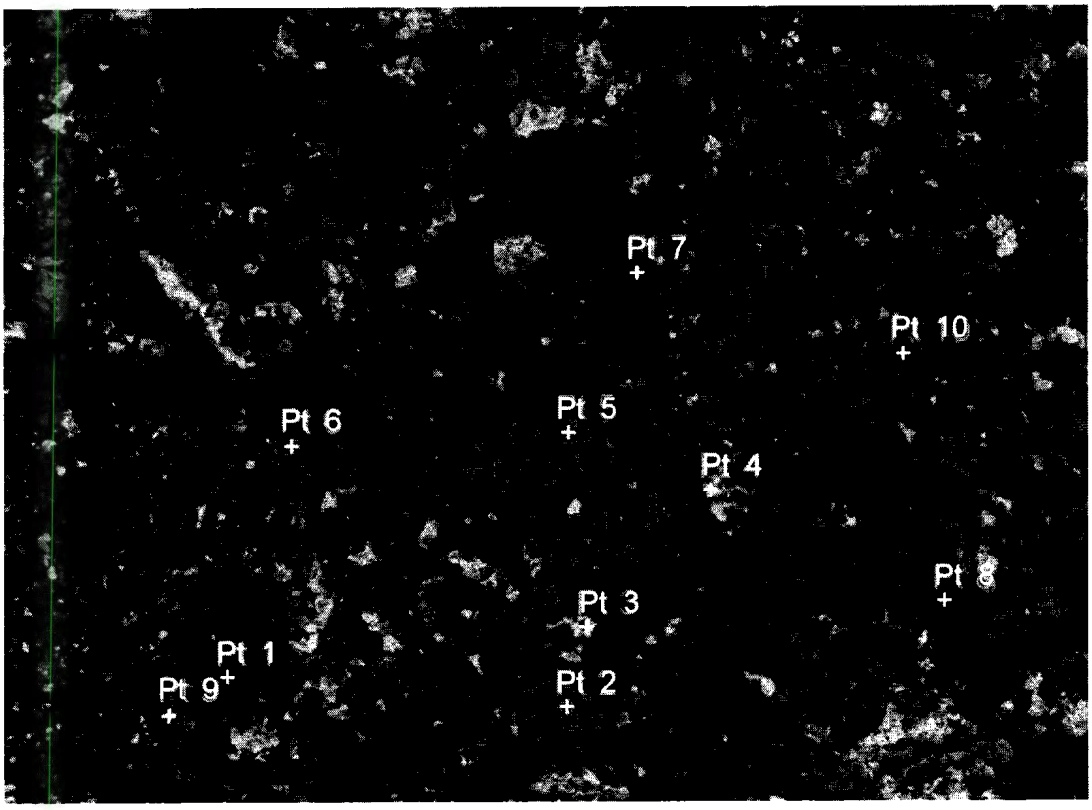

Figure 7.2: SEM image of the surface of a Pt-$RuSnO_2$/C (method 1) electrode. Points used for EDX analysis are indicated.

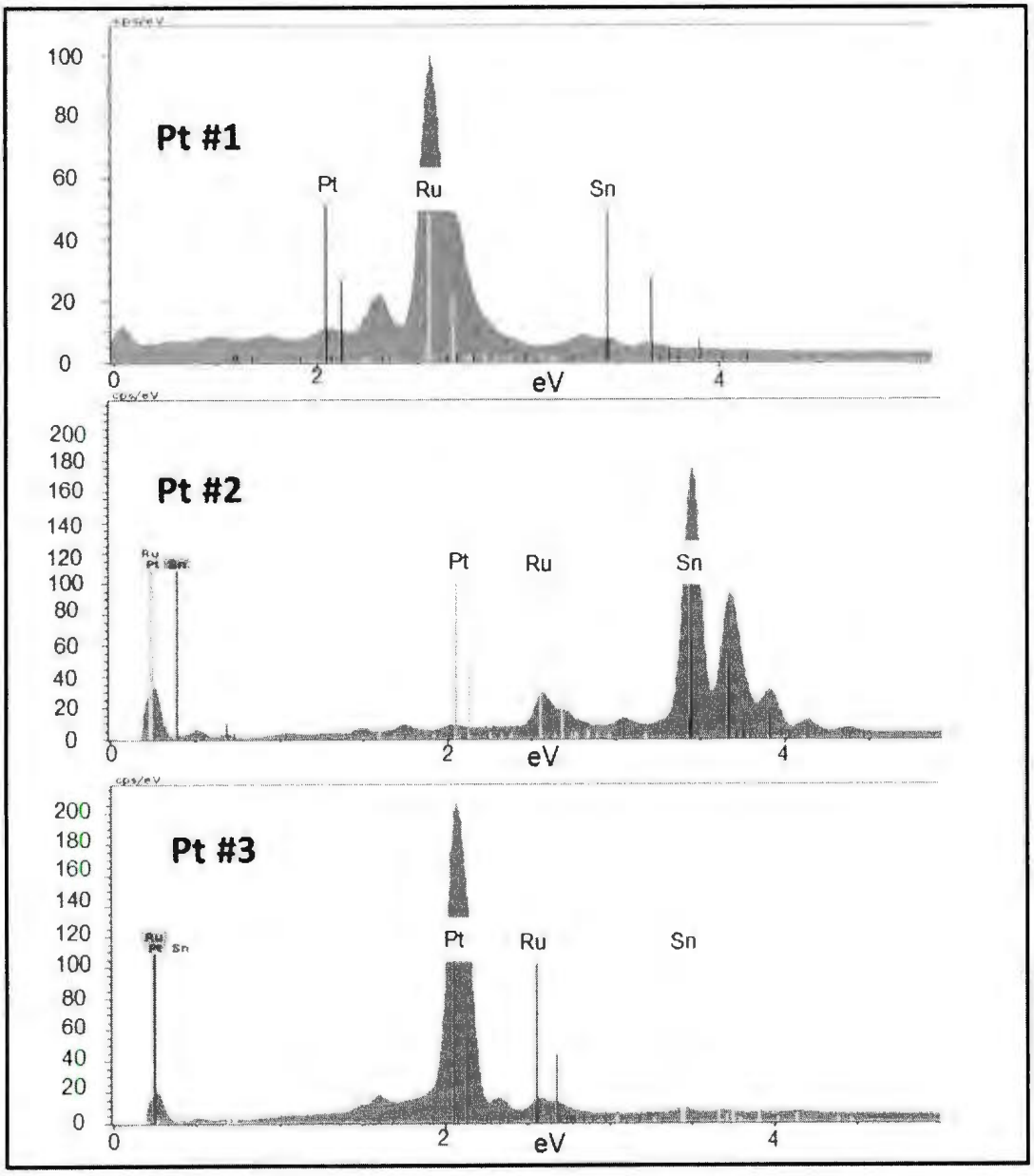

Figure 7.3: EDX spectra for points #1, 2 and 3 respectively from Figure 7.2.

is represented by the darkest spots. Figure 7.3 reveals the composition of each of the first three points on the multi-point analysis (Figure 7.2). Point #1 shows a fairly large dark particle on the surface. Its spectrum clearly shows that this particle consisted of primarily Ru and that hardly any Pt or Sn was present at this point. The second point on the multi-point diagram is much brighter; suggesting the presence of significant amounts of Pt or Sn. The spectrum analysis obtained at this point shows it to be predominately Sn. The third point on this diagram illustrates a very bright spot which is almost white in appearance. Appearing much brighter than point #2, it is most likely Pt, and only Pt is observed in the spectrum. From this multi-point analysis it is very clear that the Pt-$RuSnO_2$/C catalyst was not homogeneous. The whole surface of the catalyst is covered with particles consisting predominately of Pt, Ru and Sn with little evidence of mixing. The multi-point analysis for the Pt-$RuSnO_2$/C M2 electrode is shown in Figure 7.4 (a). It is seen from this image that the catalyst was much more homogeneous with only a few small bright Pt particles. This spectrum suggests that only small amounts of Sn and/or Ru were present in the sample. The spectrum for point #2 (Figure 7.4(b)) confirms only Pt is present in the small bright particle. The EDX spectra for all points from Figures 7.2 and 7.4 can be found in Appendix E.

To further examine the heterogeneous surface of the M1 catalyst, TEM experiments were carried out and are shown in Figure 7.5. From these images, it is clear that the Pt nanoparticles (darkest spots in top image) seem to aggregate together in about 5 different locations on the catalyst. Looking at the bottom picture, it can be seen that the Ru particles tend to remain as individual particles and the Sn is very finely divided nano-

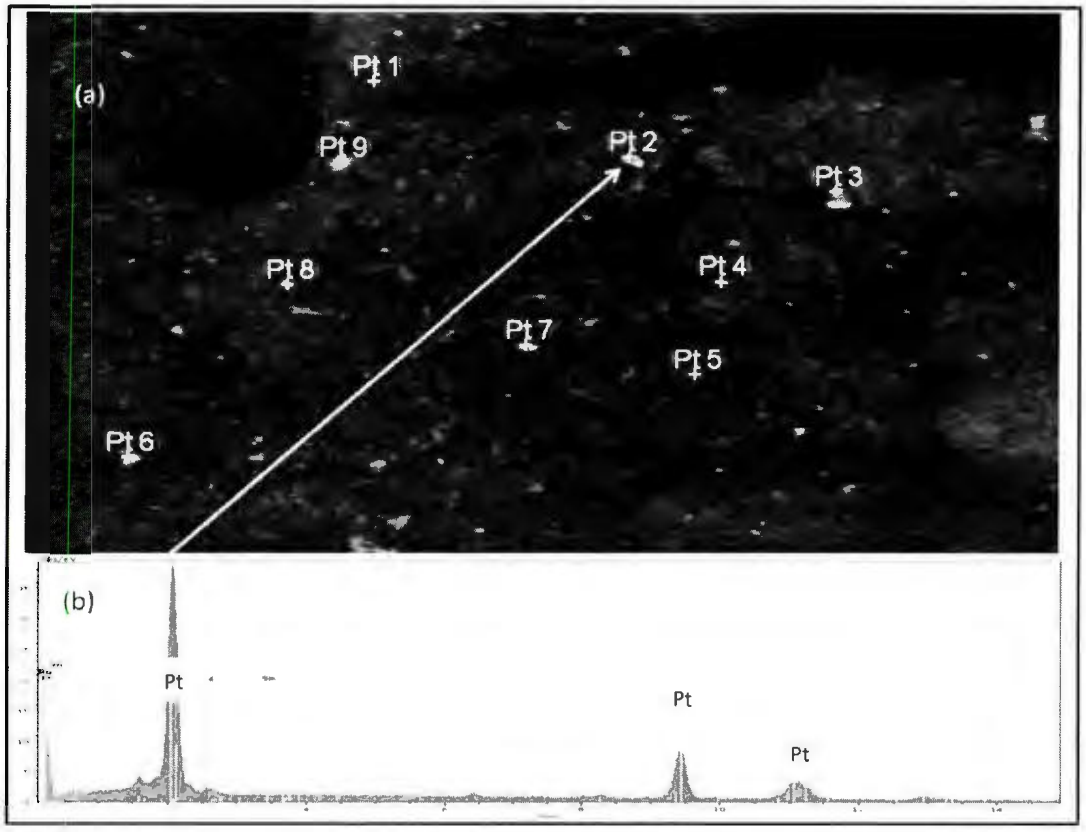

Figure 7.4: (a). SEM image of the surface of the Pt-$RuSnO_2$/C (M2) catalyst. (b). EDX analysis for metal content of the M2 catalyst.

crytalline and is smears over the whole surface of the catalyst. When examining other sections of the catalyst (images can be found in Appendix F) it was shown that some of the individual Ru particles also tend to get caught up in the Pt aggregates. These TEM

images support the SEM/EDX results showing that no Pt alloys are formed and the catalyst was heterogeneous.

To obtain the metal mass % (Pt, Ru and Sn) in the catalysts, TGA was carried out. Based on the stoichiometric amounts of each substance used in the synthesis, it was estimated that the metal mass % for the catalysts should be ca. 50% and 40% for M1 and M2, respectively (see below). For the TGA analysis, the temperature was ramped at a rate of 20° per minute from 0 to 800 °C. Once the instrument had reached 600 °C, the air flow was turned on and all of the carbon contained in the samples combusted. Taking the difference from the left over residue gave the weight % of the C, water and O functional groups in the sample. Figure 7.6.a shows the TGA data obtained for M1. It is shown that the left over residue from the catalyst powder was 55.8 % (consisting of Pt, RuO_2 and SnO_2), giving the catalyst a C, water and O functional groups a weight % of 44.2 %. Figure 7.6.b shows a catalyst residue of only 30.5 %, leading to 69.6 % of the mass corresponding to C, water and O functionality groups in the M2 catalyst powder. Based on the TGA plots in Figure 7.6, an approximation of the carbon content was made. It can be assumed that the water and O functional groups will combust prior to 600 °C (when the air was turned on to combust the carbon). Subtracting the mass from the residue and mass lost prior to the sharp decline at 600 °C, the mass of C in the sample was approximated.

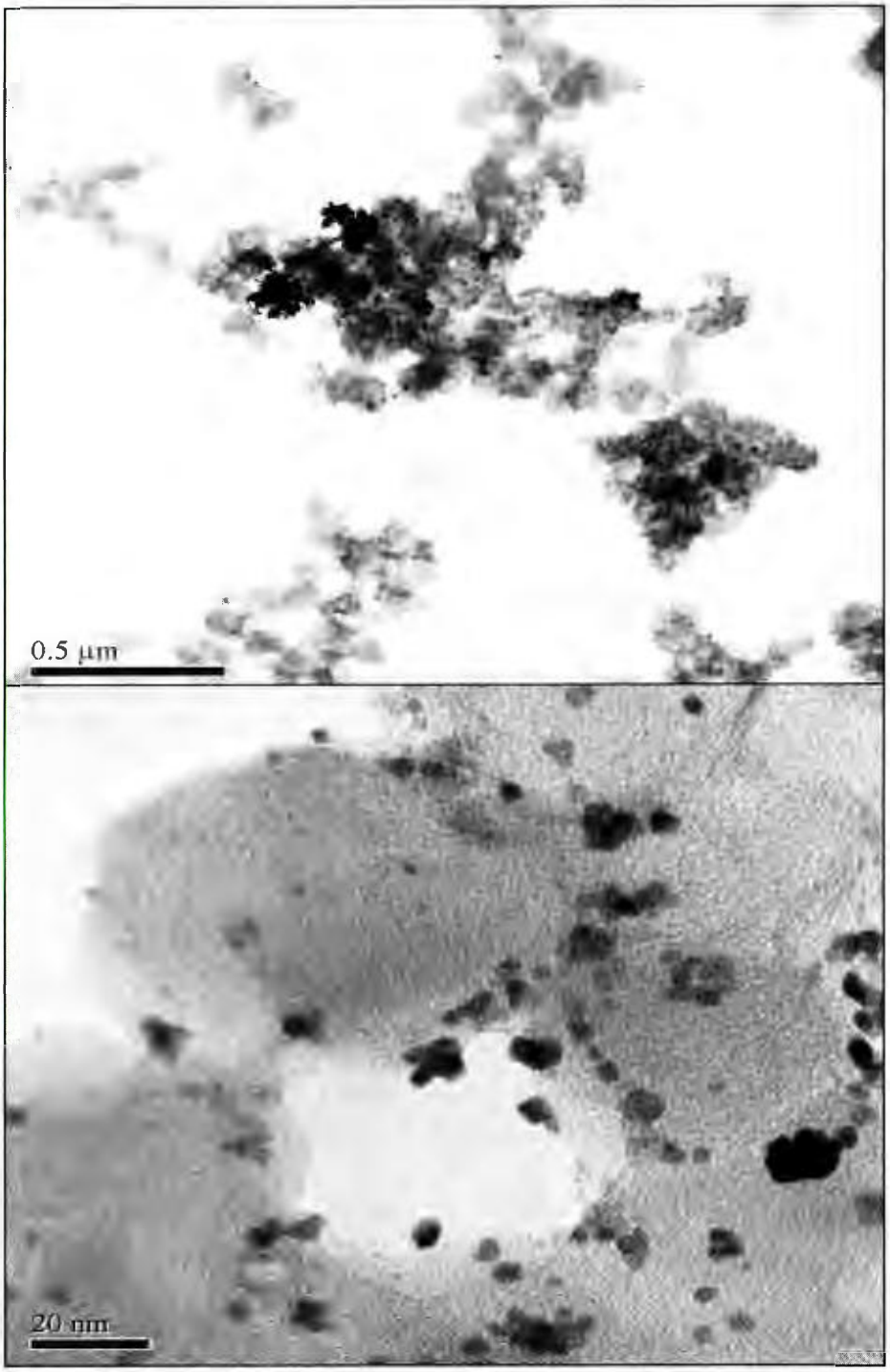

Figure 7.5: TEM images of the M1 Pt-RuSnO$_2$/C catalyst.

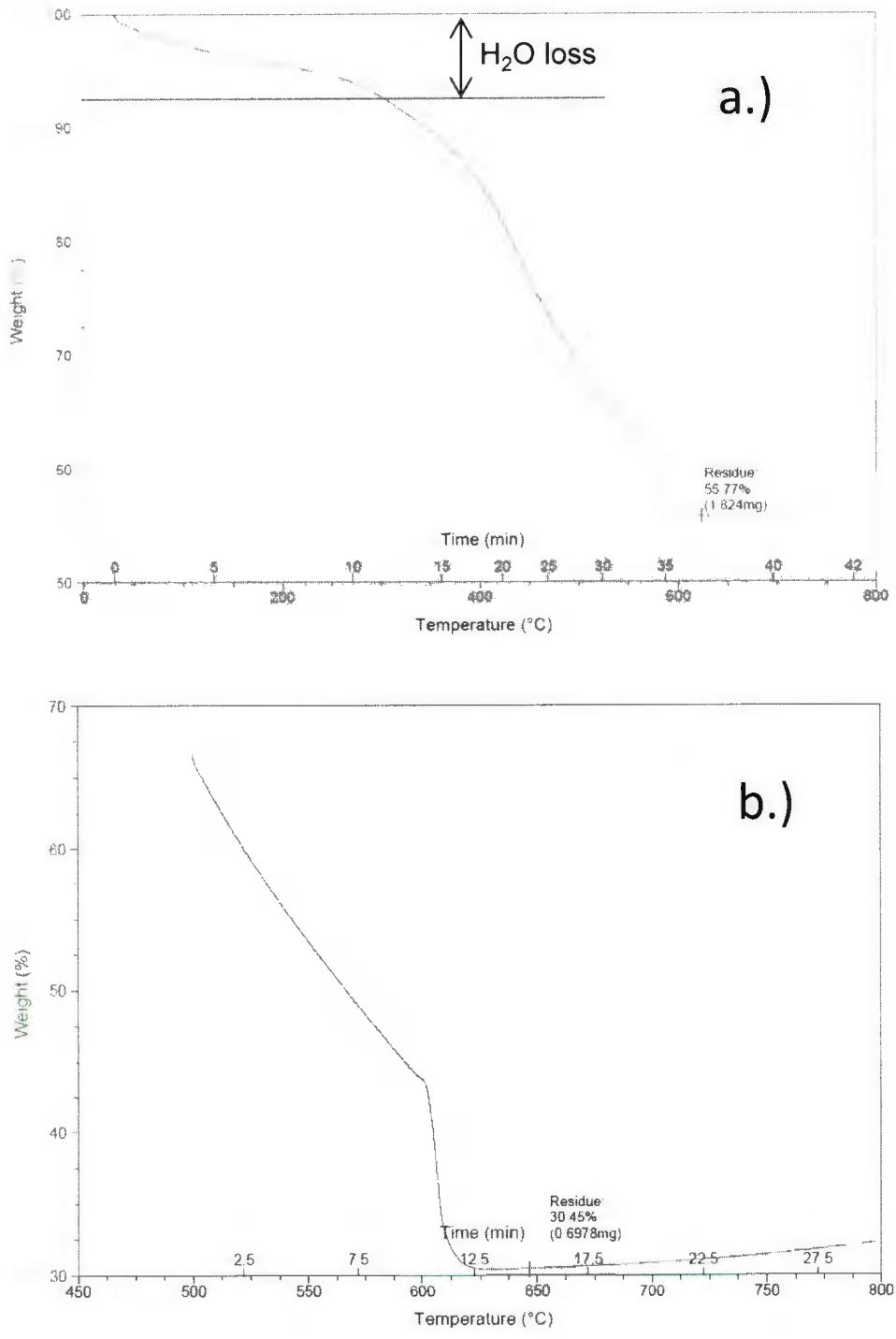

Figure 7.6: TGA results for (a) Pt-$RuSnO_2$/C (M1) and (b) Pt-$RuSnO_2$/C (M2)

Table 7.1: Composition estimates (target) for $RuSnO_2/C$ and Pt-$RuSnO_2/C$ samples calculated from stoichiometric amounts of each element used in synthesis (see section 7.2.5). Actual mass % (found) based on TGA and ICP-OES measurements.

Catalyst		Target (Mass %)				Found (Mass %)			
		Ru	Sn	Pt	"C"	Ru	Sn	Pt	"C"
$RuSnO_2/C$	(M1)	8.9	10.8	--	71.7	5.2	7.1	--	63.2
	(M2)	3.7	5.1	--	87.4	2.0	0	--	92.4
Pt-$RuSnO_2/C$	(M1)	6.3	7.5	30.1	50.1	2.6	5.1	24.6	44.2
	(M2)	2.6	3.5	30.4	60.8	1.1	0	24.8	69.6

Assumptions:
1. Sn and Ru are present as $MO_2 \cdot H_2O$
2. "C" includes impurities and surface functionalities
3. "C" from TGA is 100%-residue-H_2O based on Found Ru and Sn - O based on Found Ru.

Approximations for all metals and oxides were also made based on stoichiometric masses of each compound used in the synthesis. Assuming that all of the Ru and Sn in the catalysts were present as $MO_2 \cdot H_2O$, the compositions of the $RuSnO_2/C$ and the Pt-$RuSnO_2/C$ samples were estimated and can be seen in Table 7.1. Based on these estimations, the M1 catalyst should have been ca. 50% metal by weight with a Pt:Ru:Sn:O ratio of ca. 1:0.22:0.25:0.2. For M2 the catalyst should have been 40% metal by weight composition with a Pt:Ru:Sn:O ratio of ca. 1:0.09:0.1:0.09.

To determine the actual Pt, Sn and Ru metal contents, ICP-OES experiments were carried out. The results are also presented in Table 7.1. As shown, for both preparation methods the amounts of Ru and Sn in the samples are significantly smaller than expected. For M2, no Sn was found in the samples at all, and only a very small amount of Ru was present. The overall sum of the combined mass % for M1 was ca. 75 %. The remaining 25% can be accounted for by the oxygen combined with the Ru and Sn to form RuO_2 and SnO_2. Since only a small amount of Ru was present in sample 2, as would be expected that the additive weight % were close to 100 % as limited oxides would be formed in the sample. Based on the ICP-OES and the TGA results, the composition for M1 would be ca. 50% metal by mass and Pt:Ru:Sn:O ratios of 1:0.11:0.2:0.95. For M2, the composition would be ca. 40% metal by mass and Pt:Ru:Sn:O ratios of 1:0.05:0:0.19.

7.3.2. Electrochemical Measurements in a Liquid Electrolyte Cell

To compare the catalytic activities of the synthesized Pt-$RuSnO_2$/C catalysts for ethanol oxidation, two other electrodes were evaluated and compared. The first electrode tested was a commercial Pt black electrode donated by Ballard Power Systems (hereafter referred to as "Pt Black (Ballard)"). The second electrode used was prepared using catalyst powder that was prepared by another lab member (Reza Moghaddam) and is hereafter referred to as "RM-20% Pt"). This electrode was 20% Pt on carbon black, using Pt nanoparticles prepared in the same method as described above. The catalyst loadings for these two electrodes ranged from 2.4 – 3.2 mg cm^{-2} (4 mg cm^{-2} for Ballard), which is similar to that of the Pt-$RuSnO_2$/C catalysts used in these experiments (2.8 mg cm^{-2} and 3.0 mg cm^{-2} for M1 and M2, respectively).

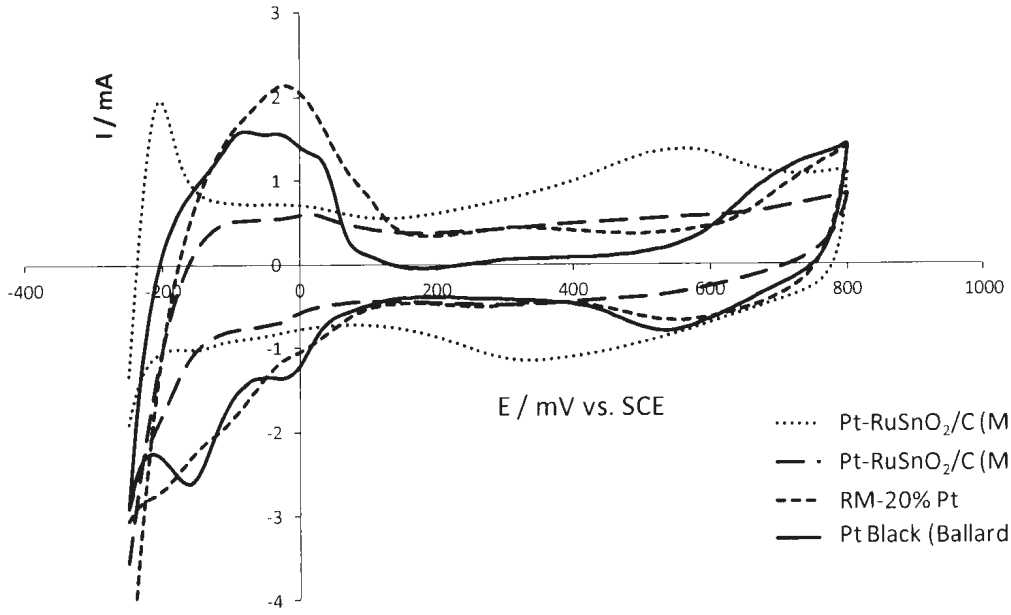

Figure 7.7: Blank cyclic voltammograms for the Pt-$RuSnO_2$/C and the Pt electrodes in 0.1 mol L^{-1} H_2SO_4 at 298 K using a scan rate of 0.01 V s^{-1}.

Blank voltammograms (no EtOH) for all four catalysts are illustrated in Figure 7.7. These were obtained by submerging the catalysts in 0.1 mol L^{-1} H_2SO_4 solution with nitrogen purging the closed system for 15 min. It can be seen from Figure 7.7 that the Pt-$RuSnO_2$/C catalysts differs significantly from the Pt black catalysts. This can be attributed to the Ru and Sn on the electrode surfaces. Pt Black (Ballard) and RM-20% Pt both illustrate a peak at ca. 0 V on the forward scan representing hydrogen desorption and another rise in current at ca. 0.6 V representing oxide formation on the Pt surface. The Pt-$RuSnO_2$/C catalysts show only a very small rise in current for the hydrogen desorption

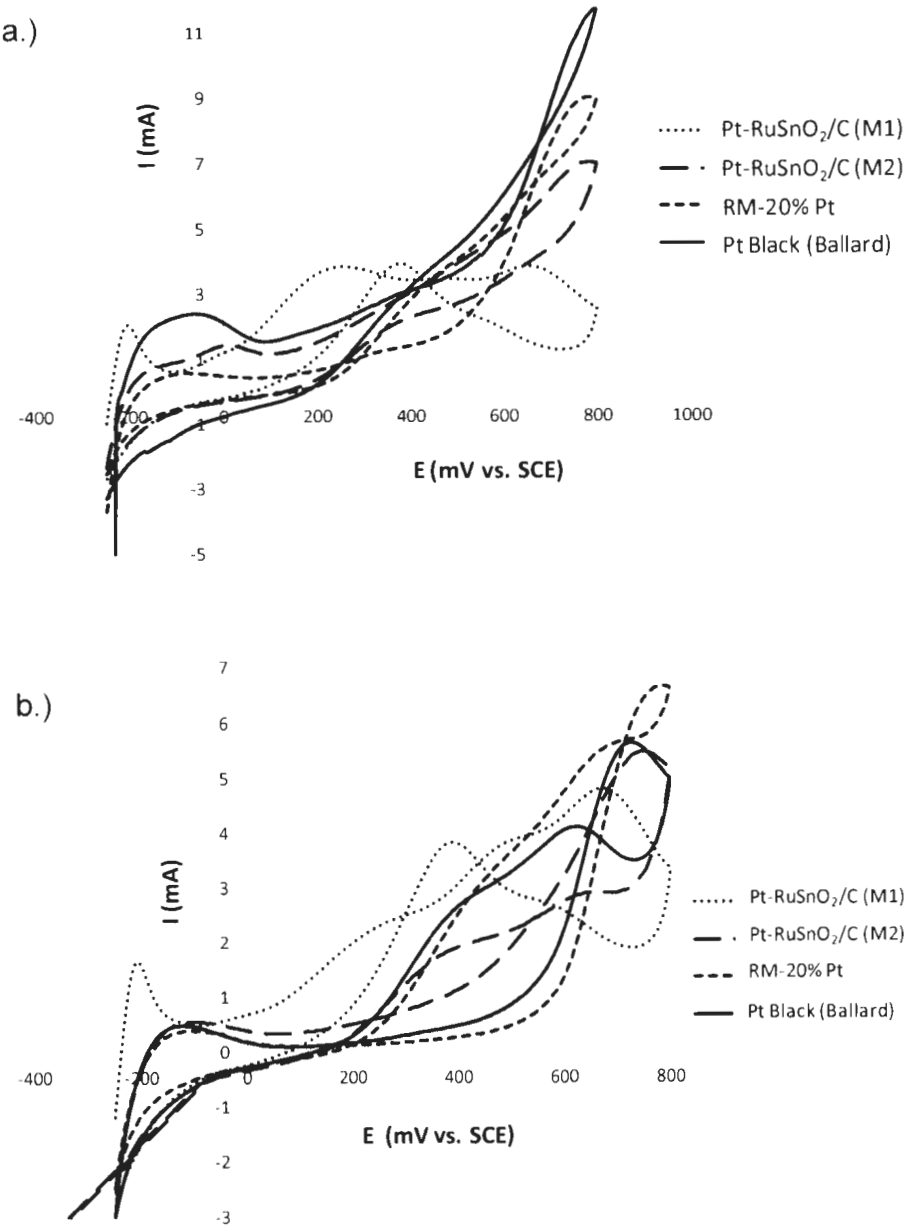

Figure 7.8: CV curves for ethanol oxidation using 0.2 mol L^{-1} ethanol solution added to 0.1 mol L^{-1} H_2SO_4 at various electrodes. (a) First cycle (b) second cycle.

peak at ca. 0 V. The absence of this peak could indicate that the addition of Ru and Sn onto the Pt surface can reduce the amount of hydrogen adsorbed and desorbed on the surface of the electrode.

The main purpose of the CV experiments was to obtain information about the catalytic activity of the Pt-$RuSnO_2$/C catalysts for ethanol oxidation. Thus, 0.2 mol L^{-1} ethanol was added to the H_2SO_4 and the results of the first cycle for each electrode can be seen in Figure 7.8 (a). It can easily be seen here that the onset of the ethanol oxidation peak seemed to occur at a much lower potential with the Pt-$RuSnO_2$/C (M1) electrode than for the M2 and Pt/C electrodes. For the Pt-$RuSnO_2$/C (M1) electrode, the onset potential occurs at ca. -0.1 V whereas for the other electrodes, it occurs at ca. 0.1 V. In the lower potential region from ca. 100- 400 mV vs. SCE, the M1 electrode showed a significant increase in current compared to the other 3 electrodes. This behavior is typical when Sn is added to Pt electrodes in the low potential region. Since the M2 electrode was shown to have no Sn and only little Ru content, its performance would most likely be similar to the Pt black electrodes, which is observed in this first cycle.

When comparing the first cycle to the second cycle of the M2 and Pt black electrodes, it can be seen that there is a significant decrease in the anodic peak current. This can be explained by the electrode being poisoned by CO_{ads}. It has been well documented that Pt electrode loses efficiency with time due to this poisoning effect [27,28] in DAFCs. When the electrode surface is covered with CO_{ads}, there are limited sites for ethanol or oxygen containing species to adsorb onto the surface and oxidized the CO to CO_2, decreasing the current density. It is shown from figure 7.8 (b) that the Pt-$RuSnO_2$/C (M1)

electrode exhibits the opposite effect. The second cycle and subsequent cycles exhibit a higher current density for the oxidation reaction, suggesting that this catalyst has the ability to limit or even eliminate the poisoning of the electrode from strongly adsorbed intermediates. It is also worth noting that the same is true for the reverse reaction. It is shown that for all the Pt black electrodes, the cathodic current decreases with each cycle, whereas an increase is observed for Pt-$RuSnO_2$/C (M1) electrode.

Although these quick and preliminary CV experiments looked very promising, they were not conducted in a fuel cell nor were they carried out under fuel cell conditions. Our next step was to make 5 cm^2 electrodes using the Pt-$RuSnO_2$/C catalyst powders and test the catalyst efficiency and carry out product analysis on ethanol oxidation. Many studies have shown that incorporating Ru and/or Sn into the Pt lattice of a catalyst can have both positive and negative contributions to the overall fuel cell efficiency. Due to the bifunctional mechanism and the ligand (electronic) effect, Sn and Ru increase the cell efficiency and power density by decreasing the EOR onset potential and limiting CO poisoning on the electrode. However, they tend to decrease the fuel efficiency due to their selectivity towards the partial oxidation by-products of acetic acid and acetaldehyde.

7.3.3. Activities of Electrodes in a Fuel Cell

The electrocatalytic activities for the catalysts under fuel cell conditions were evaluated by conducting polarization curves with 5 cm^2 electrodes at 80 °C, with 0.5 mol L^{-1} ethanol solution fed at the anode at 0.50 mL min^{-1} and O_2 was passed over the cathode at 50 mL min^{-1}. A Pt black cathode from Ballard Power Systems was used throughout all fuel cell experiments in this section. Polarization curves were measured

over the cell potential range 0.6 – 0 V. The potential was started at 0.6 V and decreased in 0.05 V increments every 5 min. Measurements were taking at the 5 min mark at each potential.

It was found that the M1 catalyst showed the best performance of the three (M1, M2 and Pt Black (Ballard)). At high cell potential and low current density, all 3 electrodes showed similar performance. In the low cell potential region, where the current is the highest, the M1 and M2 catalysts showed a significant increase in performance compared to the Pt black electrode. As mentioned in the introduction of this work, a Pt catalyst favors the formation of acetaldehyde due to the poisoning of the electrode and the very high overpotentials needed for the dissociation of water. Although Pt has shown the highest yields towards CO_2 (transferring 12 electrons), large acetaldehyde yields (transferring 2 electrons) severely decreases their performance. When Sn and/or Ru are added to the Pt electrode, the dissociation of water occurs at much lower overpotentials leading to large amounts of OH_{ads}, and very high yields of acetic acid (4 electron transfer). Since it has been shown that at low cell potentials and high current densities, the formation of acetic acid is dominant for these Pt alloyed catalysts, the performances at high current densities would be expected to be much greater than that of the Pt black. This is exactly what was observed in the low cell potential region. The limiting current for the M1 and M2 Pt-$RuSnO_2$/C catalysts were 67% and 54% higher limiting currents than for the Pt black, respectively.

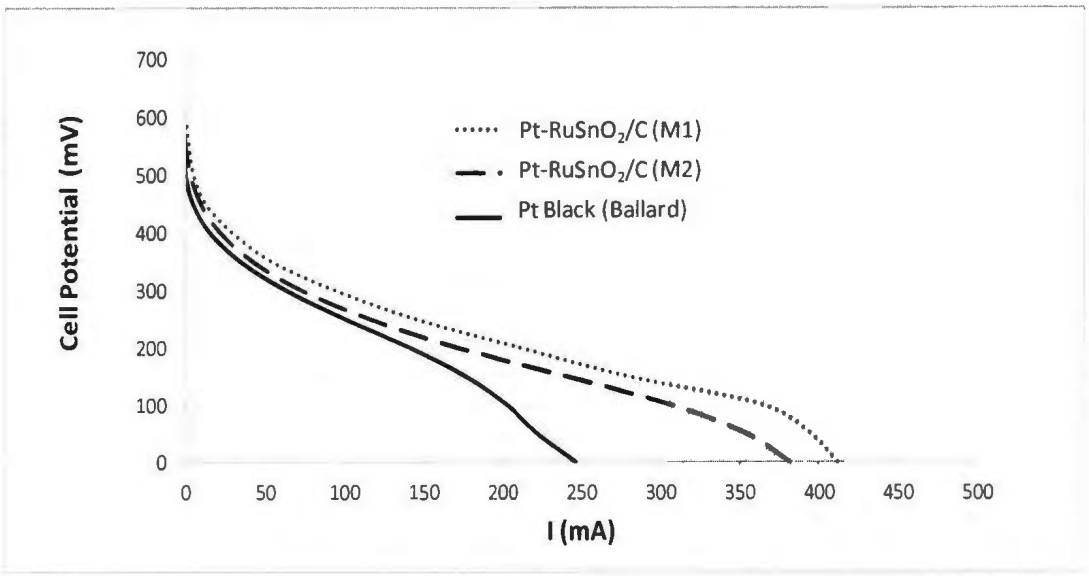

Figure 7.9: Polarization curves for the M1, M2 and Pt Black (Ballard) anode electrode in a DEFC. 0.5 mol L^{-1} ethanol solution was used as the fuel, O_2 was used as the oxidant gas and curves were conducted at 80 °C.

7.3.4. Product Analysis and CO_2 Selectivity

As mentioned in the introduction of this chapter, the enhancement of cell performance in a DEFC with the incorporation of Sn and/or Ru has been shown in numerous papers. However, in most cases, the selectivity towards CO_2 and the complete oxidation of ethanol tends to diminish. Synthesizing a catalyst that increases the cell performance while maintaining or increasing the selectivity towards CO_2 has been a hot topic of research in DEFCs.

The product analyses for the M1 and M2 electrodes along with the Pt black (Ballard) electrode are shown in Table 7.2. These experiments were performed in 0.5 h runs

Table 7.2: Faradaic yields from titration (AA) and NDIR (CO_2) measurements from combined anode and cathode exhausts with various anode catalysts. AAL yields were calculated based on the faradaic charge balance. The cathode gas was O_2. Fuel cell temperature was 80 °C and 0.5 mol L^{-1} ethanol solution was used. Titration and NDIR measurements were corrected for blank measurements at open circuit where no current was flowing.

Catalyst	Product Analysis				
	Current (mA)	CO_2 Yield (%)	AA Yield (%)	AAL Yield (%)*	Cell Potential (mV)
Pt Black (Ballard)	50	34.1	29.5	36.4	294
	100	29.5	36.8	33.7	178
	150	19.9	40.6	39.5	78
Pt-$RuSnO_2$/C (M1)	50	31.4	69.9	0	338
	100	32.2	55.0	12.8	264
	150	26.2	46.8	27.0	204
Pt-$RuSnO_2$/C (M2)	50	29.3	53.4	17.3	305
	100	21.0	53.9	25.1	208
	150	21.4	45.8	32.8	142

* Calculated from Faradaic charge balance

using 0.5 mol L^{-1} ethanol at the anode and O_2 at the cathode at 80 °C. These galvanostatic experiments used 50, 100 and 150 mA of constant current. From this table it is shown that the faradaic yields of CO_2 for both the M1 and M2 catalysts are very comparable with those of the Pt catalyst. At low current (50 mA), the M1 and M2 Pt-$RuSnO_2$/C catalysts exhibited only a 7.9 and 14.1% drop in CO_2 yield in comparison to the Pt catalysts, respectively. However, as the current was increased the difference in yields diminished and in some cases the M1 and M2 CO_2 yields were higher than those of the Pt electrode. The trend in AA yield is also in good agreement with previous reports. For the pure Pt catalyst, the AA yield tended to increase with increasing current. When Ru and Sn are introduced into the catalyst, a significant increase in AA yield (ca. 5-40%) throughout the current range was observed. The significant drop in AAL yields and the increase in AA

yields can suggest that the dissociation of water on the electrode becomes more kinetically favored with the addition of Ru and Sn, resulting in less CO poisoning of the electrode. All CO_2 traces for Table 7.3 can be found in Appendix G.

7.4. Conclusions

Using a Pt nanoparticle deposition onto a layer of $RuSnO_2$, gave significant increases in cell performance while maintaining or increasing the selectivity towards CO_2 production. Figure 7.9 and table 7.3 show that the M1 catalyst performed best amongst the catalysts tested while also having the highest CO_2 yield during the 80-150 mA constant current experiments. SEM/EDX and TEM results show a non-homogeneous surface for M1, with Pt particles aggregating, Ru oxide particles acting independently and Sn finely dispersed throughout the catalyst. It has been shown that this catalyst has the ability to increase selectivity towards CO_2 (comparable to Pt). The Sn and Ru on the surface are able to dissociate H_2O at lower overpotentials and oxidize adsorbed species on the surface, respectively, leading to an increase in the electrochemical performance. The M2 catalyst also showed enhancements in cell performance. SEM/EDX results show a much more homogeneous surface, however ICP-OES analysis revealed only a small amount of Ru and no observed Sn. The methodology used in this paper for synthesizing Pt-$RuSnO_2$/C catalyst could very well be a starting point for making effective catalysts for ethanol oxidation that overcomes both the cell performance and the product selectivity barriers.

7.5. References

[1] Lamy, C.; Lima, A.; LeRhun, V.; Delime, F.; Coutanceau, C.; Leger, J. M. *J. Power Sources* **2002**, *105*, 283-296.

[2] Vigier, F.; Rousseau, S.; Coutaneau, C.; Leger, J. M.; Lamy, C. *Top. Catal.* **2006**, *40*, 111-121.

[3] Antolini, E. *J. Power Sources* **2007**, *170*, 1-12.

[4] Song, S. Q.; Maragou, V.; Tsiakaras, P. *J. Fuel Cell Sci. Technol.* **2007**, *4*, 203-210.

[5] Demirci, U. B. *J. Power Sources* **2007**, *169*, 239-246.

[6] Thomas, S. C.; Ren, X. M.; Gottsfeld, S.; Zelenay, P. *Electrochim. Acta* **2002**, *47*, 3741-3748.

[7] Welsch, F. G.; Stöwe, K.; Maier, W. F. *Catal. Today* **2011**, *159*, 108-119.

[8] Ren, X.; Wilson, M. S.; Gottsfeld, S. *J. Electrochem. Soc.* **1996**, *143*, L12-L15.

[9] Demirbas, A. *Prog. Energy Combust. Sci.* **2007**, *33*, 1-18.

[10] Sen Gupta, S.; Singh, S.; Datta, *J. Mater. Chem. Phys.* **2010**, *120*, 682-688.

[11] Ghumman, A.; Li, G.; Bennett, D. V.; Pickup, P. G. *J. Power Sources* **2006**, *194*, 286-290.

[12] Arico, A. S.; Creti, P.; Antonucci, P. L.; Antonucci, V. Electrochem. *Solid. State. Lett.* **1998**, *1*, 66-68.

[13] Rousseau, S.; Coutanceau, C.; Lamy, C.; Léger, J. M. *J. Power Sources* **2006**, *158*, 18-24.

[14] Kowal, A.; Li, M.; Shao, M.; Sasaki, K.; Vukmirovic, M. B.; Zhang, J.; Marinkovic, N. S.; Liu, P.; Frenkel, A. I.; Adzic, R. R. *Nature Materials* **2009**, *8*, 325-330.

[15] Vigier, F.; Coutanceau, C.; Hahn, F.; Belgsir, E. M.; Lamy, C. *J. Electroanal.Chem.* **2004**, *563*, 81-89.

[16] Gonzalez, M. J.; Hable, C. T.; Wrighton, M. S. *J. Phys. Chem. B.* **1998**, *102*, 9881-9890.

[17] Vigier, F.; Coutanceau, C.; Perrard, A.; Beldsir, E. M.; Lamy, C. *J. Appl. Electrochem.* **2004**, *34*, 439-446.

[18] Fujiwara, N.; Friedrich, K. A.; Stimming, U. *J. Electroanal. Chem.* **1999**, *472*, 120-125.

[19] Neto, A. O.; Giz, M. J.; Perez, J.; Ticianelli, E. A.; Gonzalez, E. R. *J. Electrochem. Soc.* **2002**, *149*, A272-279.

[20] Colmati, F.; Antolini, E.; Gonzalez, E. R. *J. Power Sources* **2006**, *157*, 98-103.

[21] Antolini, E.; Colmati, F.; Gonzalez, E. R. *Electrochem. Commun.* **2007**, *9*, 398-404.

[22] Liu, C.-W.; Chang, Y.-W.; Wei, Y.-C.; Wang, K.-W. *Electrochim. Acta*, **2011**, *56*, 2574-2581.

[23] James, D. D.; Pickup, P. G. *Electrochim. Acta* **2012**, *78*, 274-278.

[24] Yang, J.; Lee, J. Y.; Too, H.-P. *Anal. Chim. Acta* **2006**, *571*, 206-210.

[25] Moghaddam, R. B.; Pickup, P. G. *Electrochim. Acta* **2012**, *65*, 210-215.

[26] Cunha, E. M.; Ribeiro, J.; Kokoh, K. B.; de Andrade, A. R. *Int. J. Hydrogen Energy* **2011**, *36*, 11034-11039.

[27] Ciureanu, M.; Wang, H. *J. New Mater. Electrochem. Syst.* **2000**, *3*, 107-119.

[28] Oetjen, H.-F.; Schmidt, V. M.; Stimming, U.; Trila, F. *J. Electrochem. Soc.* **1996**, *143*, 3838-3842.

CHAPTER 8

Summary and Future Work

8.1 Summary

A new methodology for determining product distribution in a direct ethanol fuel cell was developed that allowed for easy and quick real time analysis of products. The accuracy of the system was tested using previously reported methodology and results were found to be in good agreement. Furthermore, the volatile acetaldehyde product, which is very hard to detect, was shown to be accurately quantified using the charged passed at the anode. To further improve the accuracy of the system, a "crossover mode" for operating a fuel cell was examined. It was found that this method reduced the inaccuracies that are caused from fuel and product crossover through the proton exchange membrane. Surprisingly, this method also showed a significant increase in faradaic CO_2 yield at low fuel concentration, suggesting this method may decrease the poisoning at the anode.

An in-depth examination of ethanol and product crossover was carried out. It was found that using O_2 as the oxidant gas lead to worrisome discrepancies in product distributions. Ethanol crossing through the membrane and reacting chemically with oxygen created an excess in products that are unaccounted for when calculating faradaic yields. Since the release of this research, many research groups calculating product yields (using O_2 at the cathode) have corrected for these crossover products by subtracting the measured background products. To further eliminate the effects of ethanol crossover, H_2/N_2 gas was passed through the anode in many of our experiments. Also, each by-product of the EOR was examined for crossover effects. It was shown that when acetic acid is produced as a consequence of ethanol crossover, it migrates from the cathode to the anode (due to its low volatility) and exits in the anode effluent. This causes a large overestima-

tion of acetic acid. When acetaldehyde is produced, it was shown that a significant amount is lost due to crossover from anode to cathode and exiting in the cathode stream, resulting in an underestimation of acetaldehyde yield. The effects of CO_2 crossover were also examined. It was shown that the CO_2 produced at the anode is able to migrate through the membrane and desorb into the cathode gas stream, leading to an underestimation of the CO_2 yield. Our results have shown that to obtain the most accurate product distributions, it is imperative to operate the cell using H_2/N_2 or just N_2 at the cathode and collect both the anode and cathode exhausts for analysis.

With the development of the online product analysis system, we were able to perform anode stripping experiments. It was shown that the apparent faradaic CO_2 yields were dependent on the pulsing times. Only short pulsing times were needed to oxidize CO adsorbates into CO_2 resulting in a large production of CO_2. At higher pulsing times, it was shown that the yields decrease due to the clean electrode surface favoring the dissociation and oxidation of ethanol into acetic acid and acetaldehyde after the quick initial strip. The time between intervals, when the system returned to open circuit, did not seem to be influential towards the CO_2 yields. This suggests that the dissociation and adsorption of ethanol on the electrode surface is a very quick process.

Finally, a Pt-$RuSnO_2$/C catalyst was developed using a Pt nanoparticle deposition on a $RuSnO_2$ layer. This catalyst showed unusual behavior as it increased the performance of the cell while maintaining selectivity towards complete oxidation (and in some cases improved the selectivity), compared to the typical Pt electrode.

8.2 Future Work

Based on the results obtained in this work, there are some areas that should be further explored. To fully complete our methodology for product analysis, real time monitoring of acetaldehyde should be obtained. The charge balance equation (equation 3.6) should be validated for high temperature experiments. One way of achieving this would be to use an on-line DEMS system with H_2/N_2 at the cathode. The combined anode and cathode outlet stream would be combined and directly fed to the mass spectrometer. By combining the two outlets, all of the acetaldehyde lost from crossover would be accounted for and the measured concentration would be accurate.

To enable researchers to conduct stripping experiments at high temperatures, the CO_2 detection system must be altered in a way that the detector is less susceptible to moisture. A few ways to overcome this problem are to examine the electrical components of the detector and design a sealed casing to enclose the wiring, to equip the NDIR detector with a small gas separation (drying) column or a small bore tube, or to switch the type of detector to one with a liquid injection inlet. Lower pulsing times (< 0.5 s) should be examined to optimize the system during the stripping experiments. A wider range of fuel concentrations should also be tested to gain more insight into the poisoning mechanism occurring at the anode of the fuel cell.

The calculation of the faradaic CO_2 yields during stripping experiments should also be revisited. As mentioned in chapter 6, the n value is most likely lower than 6 due to a significant portion of the CO_2 attributed to CO oxidation on the electrode (n=2). A

formula could be derived where the n value is altered depending on the length of the pulse, leading to more accurate calculation of CO_2 yields.

The method used to develop the Pt-$RuSnO_2$/C catalyst should be further examined. The content of each metal should be altered in a trial and error manner, and tested in the fuel cell for performance and CO_2 selectivity. Optimizing the composition of this catalyst could lead to a significant breakthrough in catalyst development for a DEFC.

APPENDIX A

CO_2 and Current Traces for Rest Interval Dependence on CO_2 Yield

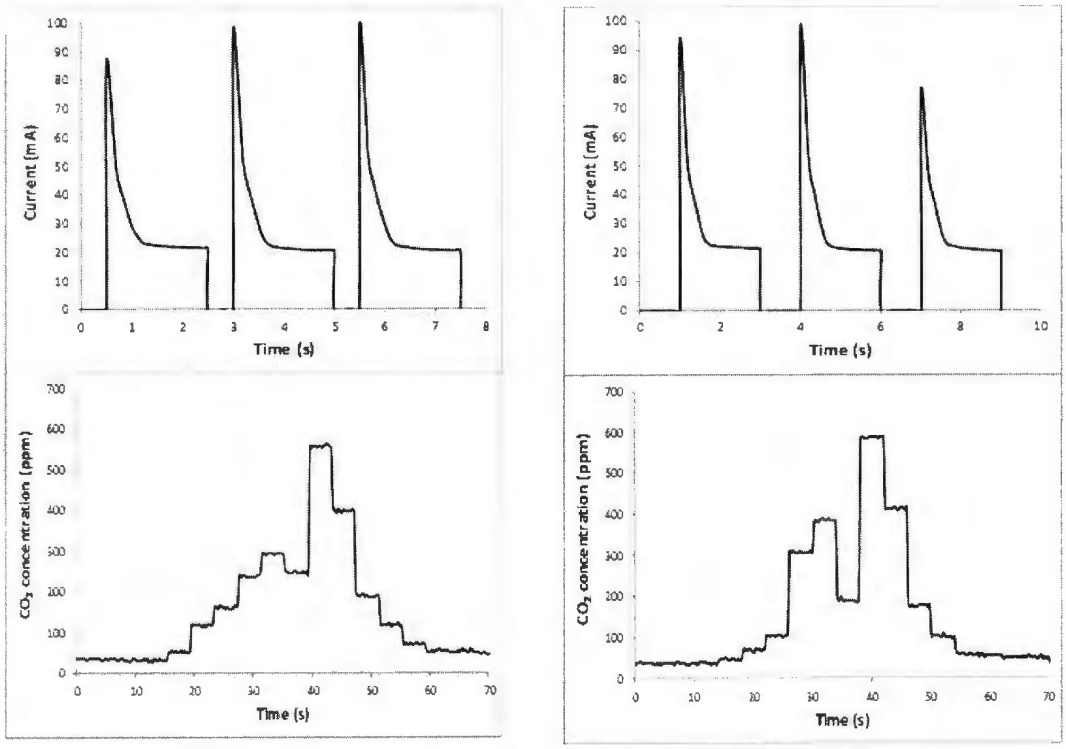

Figure A.1: Current and CO_2 vs. time traces for pulsing experiments using 2 s pulses of 0.8 V (vs. H_2) with 0.5 s (left) and 1 s (right) resting intervals at OCP between pulses.

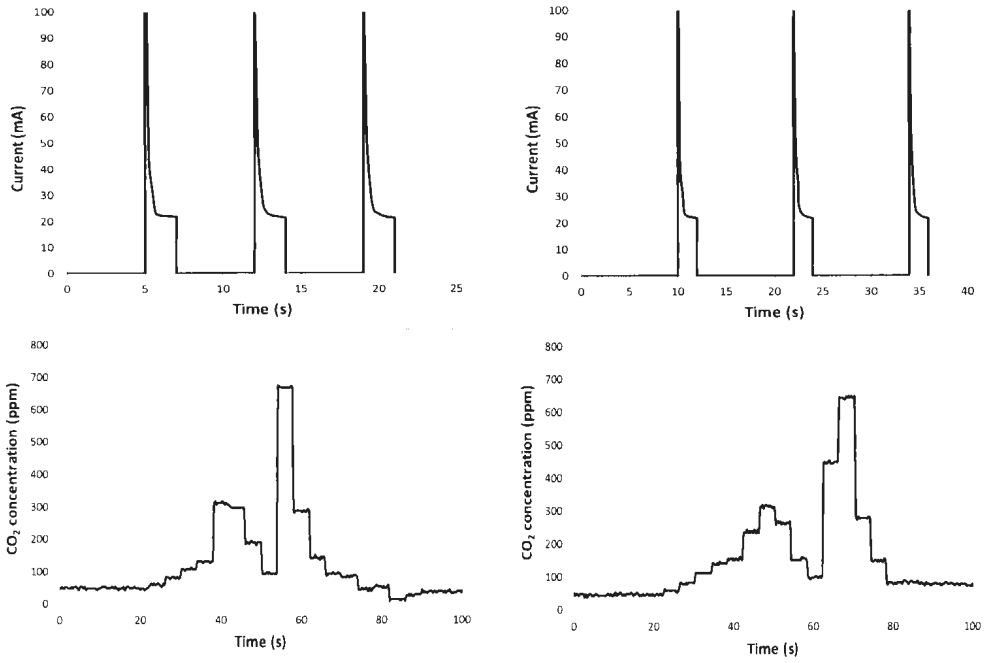

Figure A.2: Current and CO_2 vs. time traces for pulsing experiments using 2 s pulses of 0.8 V (vs. H_2) with 5 s (left) and 10 s (right) resting intervals at OCP between pulses. (All background CO_2 readings were corrected for using the pure CO_2 method described in chapter 4.)

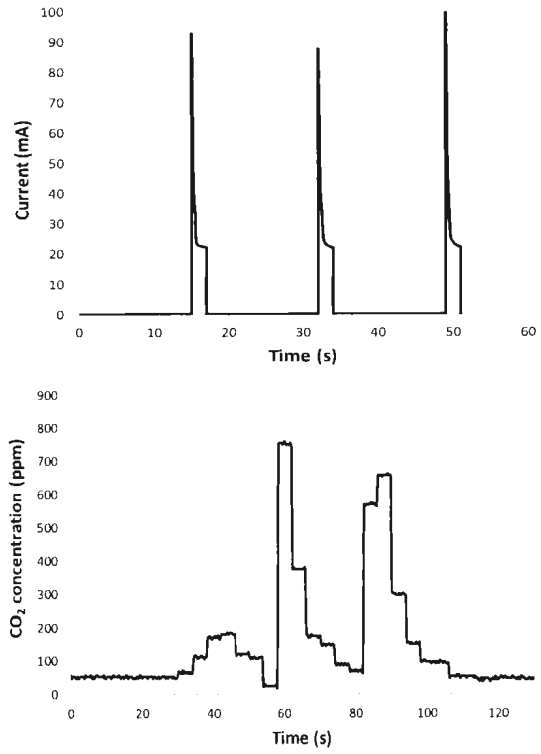

Figure A.3: Current and CO_2 vs. time traces for pulsing experiments using 2 s pulses of 0.8 V (vs. H_2) with 15 s resting intervals at OCP between pulses. (All background CO_2 readings were corrected for using the pure CO_2 method described in chapter 4.)

APPENDIX B

CO_2 and Current Traces for CO_2 Yield Dependence on Pulse Time

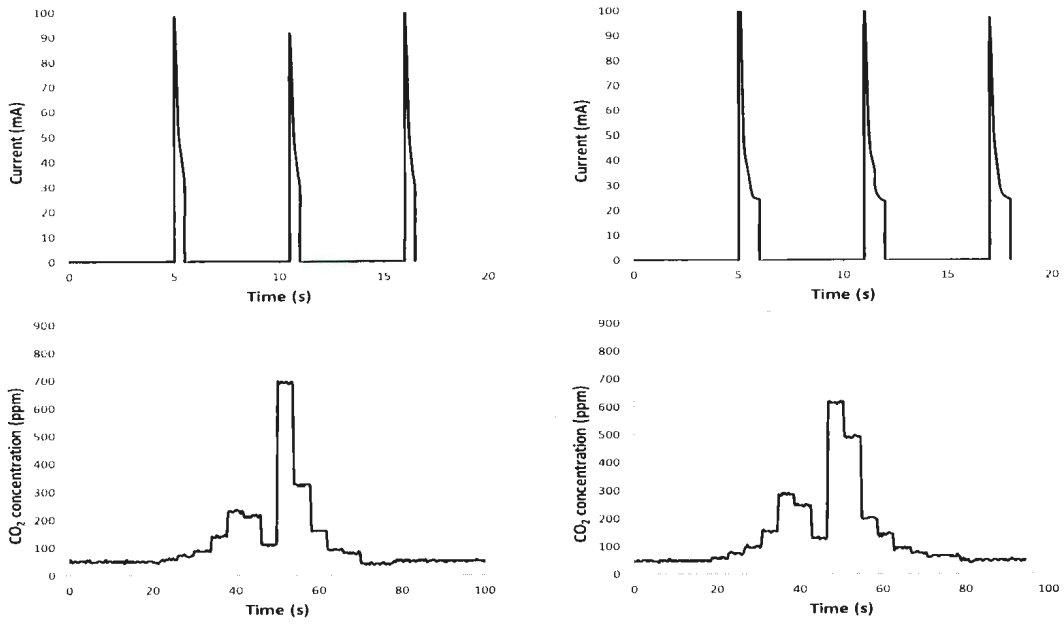

Figure B.1: Current and CO_2 vs. time traces for pulsing experiments using 0.5 s (left) and 1 s (right) pulses of 0.8 V (vs. H_2) with 5 s resting intervals at OCP between pulses. (All background CO_2 readings were corrected for using the pure CO_2 method described in chapter 4.)

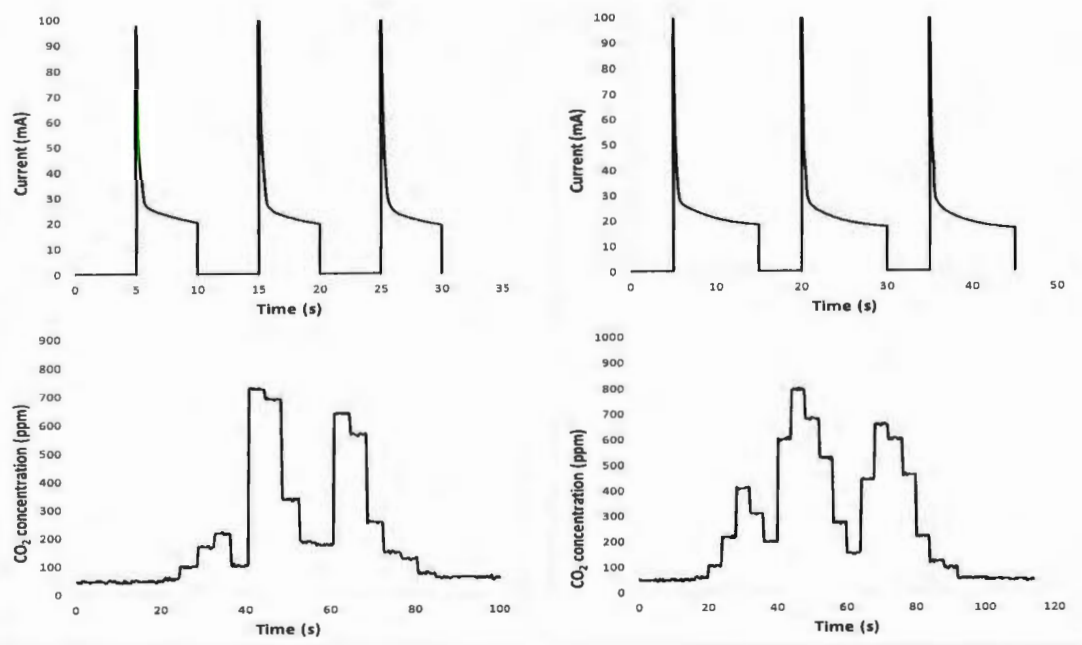

Figure B.2: Current and CO_2 vs. time traces for pulsing experiments using 5 s (left) and 10 s (right) pulses of 0.8 V (vs. H_2) with 5 s resting intervals at OCP between pulses. (All background CO_2 readings were corrected for using the pure CO_2 method described in chapter 4.)

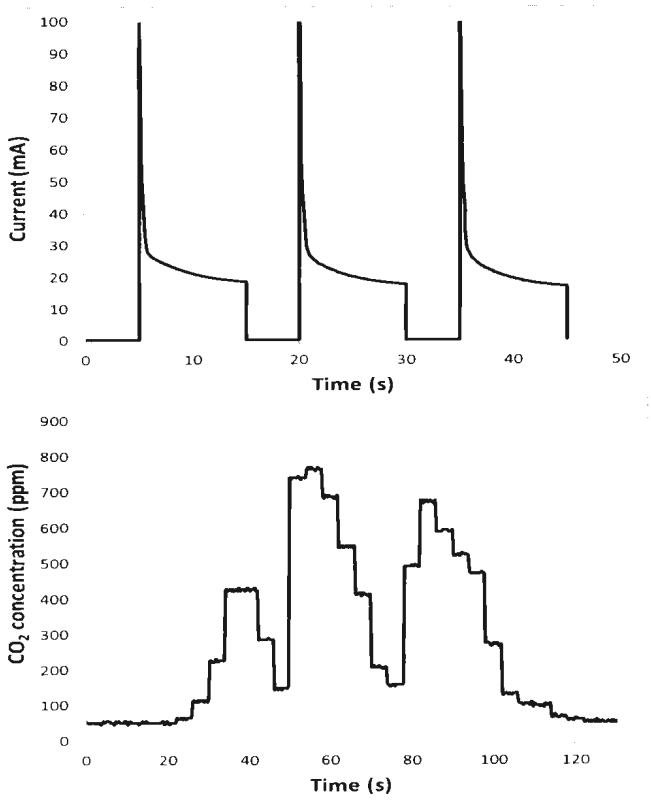

Figure B.3: Current and CO_2 vs. time traces for pulsing experiments using 15 s pulses of 0.8 V (vs. H_2) with 5 s resting intervals at OCP between pulses. (All background CO_2 readings were corrected for using the pure CO_2 method described in chapter 4.)

APPENDIX C

CO_2 and Current Traces for Crossover Mode Pulsing Experiments

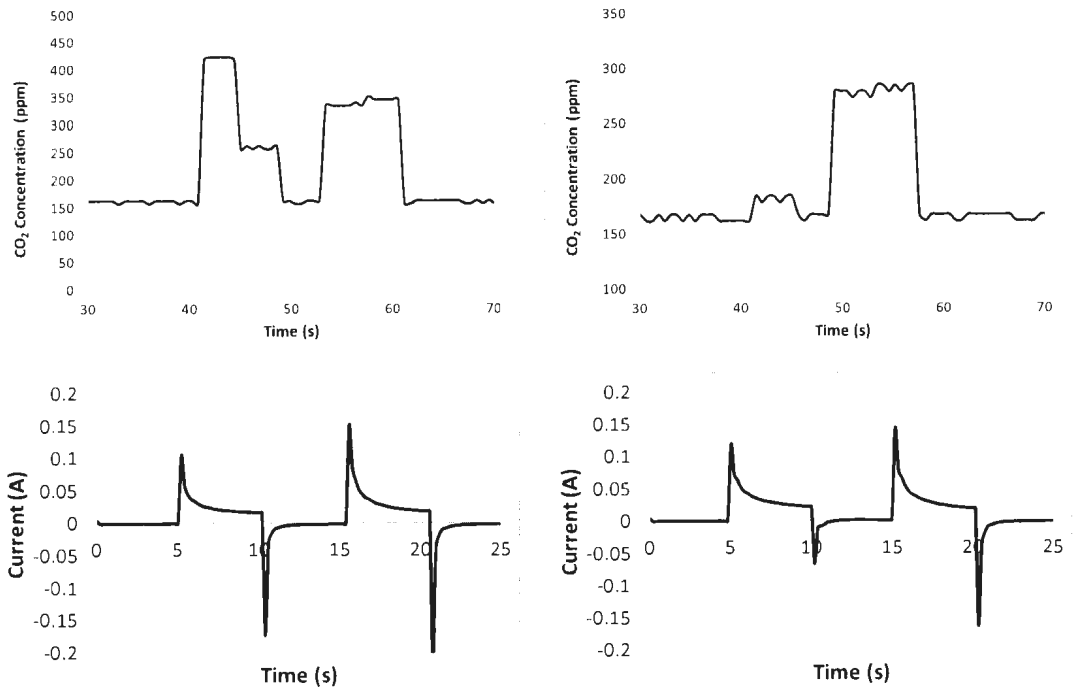

Figure C.1: CO_2 concentration and current vs. time traces for pulsing experiments in crossover mode using 0.1 mol L^{-1} aqueous ethanol solution with 700 mV (left) and 800 mV (right) of potential applied. Pulse time was 5 s and rest time was 5 s at OCP. (All background CO_2 readings were corrected for using the pure CO_2 method described in chapter 4.)

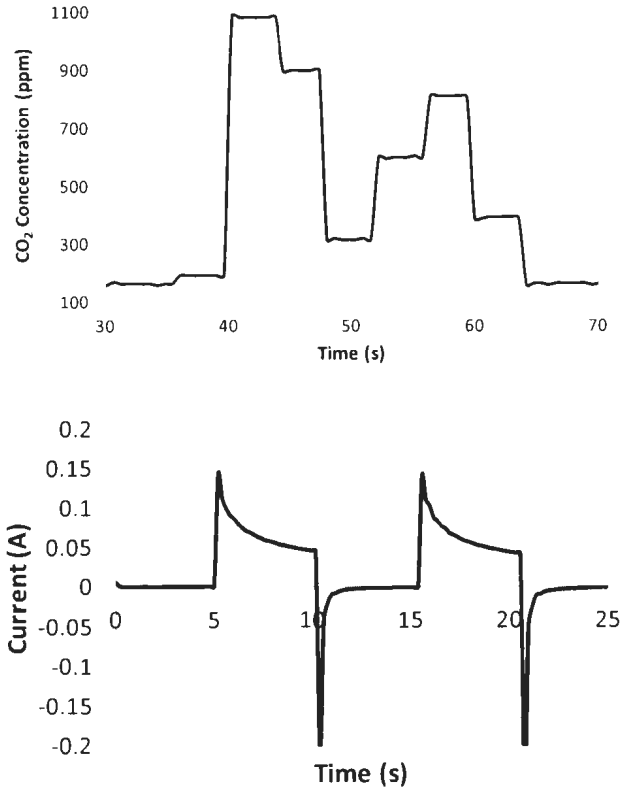

Figure C.2: CO_2 concentration and current vs. time traces for pulsing experiments in crossover mode using 0.1 mol L^{-1} aqueous ethanol solution with 900 mV of potential applied. Pulse time was 5 s and rest time was 5 s at OCP. (All background CO_2 readings were corrected for using the pure CO_2 method described in chapter 4.)

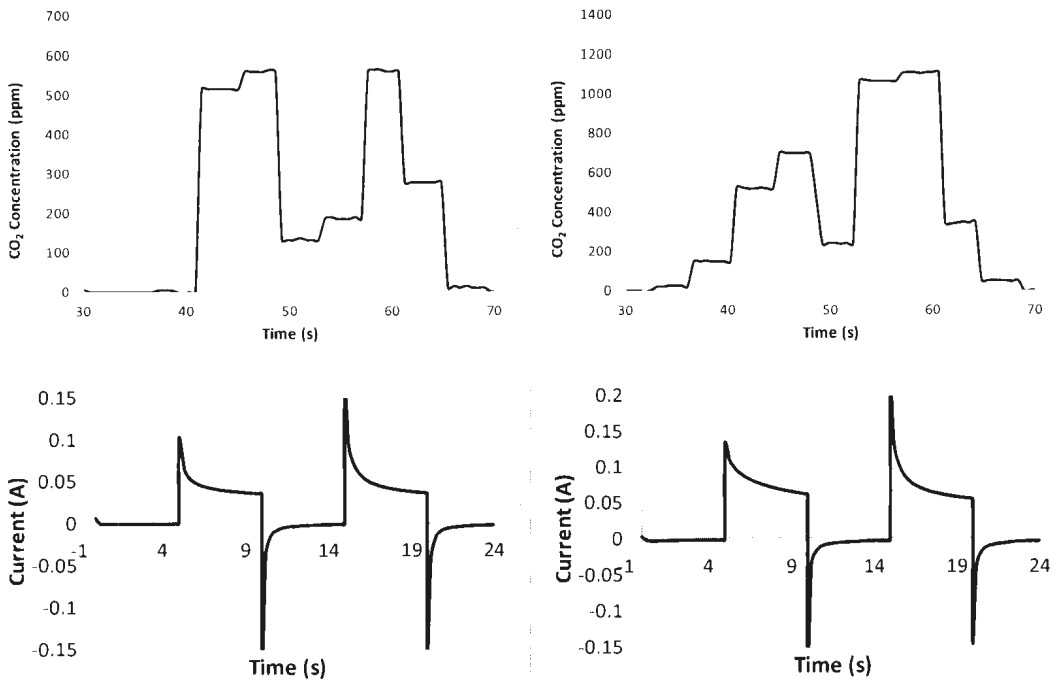

Figure C.3: CO_2 concentration and current vs. time traces for pulsing experiments in crossover mode using 0.5 mol L^{-1} aqueous ethanol solution with 700 mV (left) and 800 mV (right) of potential applied. Pulse time was 5 s and rest time was 5 s at OCP. (All background CO_2 readings were corrected for using the pure CO_2 method described in chapter 4.)

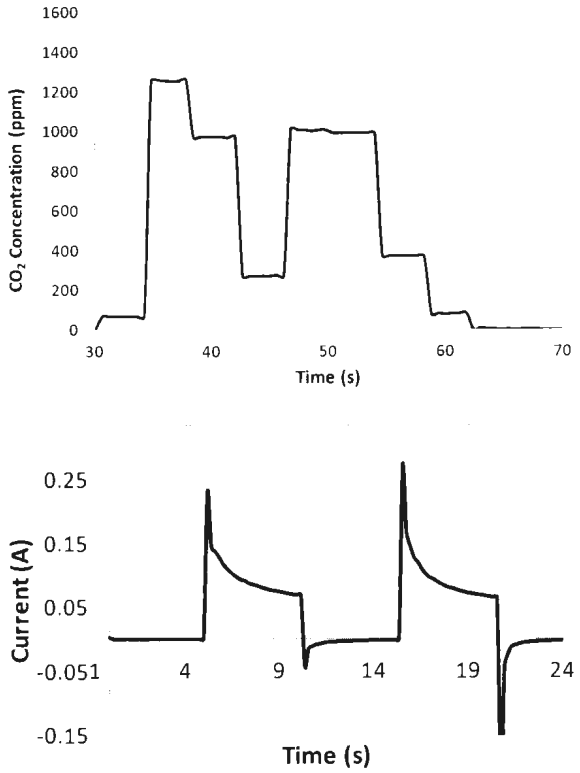

Figure C.4: CO_2 concentration and current vs. time traces for pulsing experiments in crossover mode using 0.5 mol L^{-1} aqueous ethanol solution with 900 mV of potential applied. Pulse time was 5 s and rest time was 5 s at OCP. (All background CO_2 readings were corrected for using the pure CO_2 method described in chapter 4.)

APPENDIX D

CO_2 Traces for Acetaldehyde Oxidation

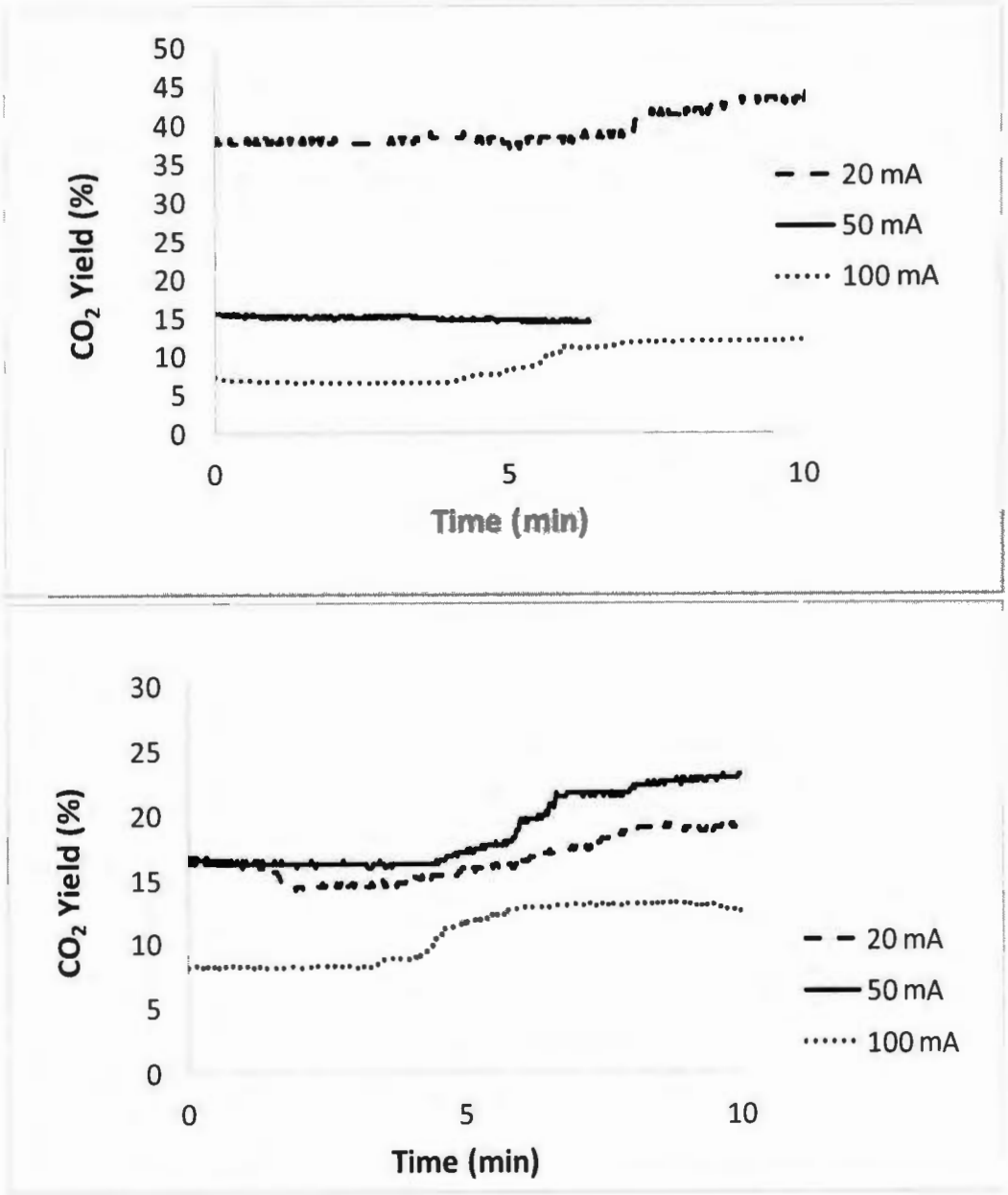

Figure D.1: CO_2 yield traces obtained from the oxidation of 0.5 mol L^{-1} acetaldehyde at ambient temperature (top) and 40 °C (bottom). (All background CO_2 readings were corrected for using the pure CO_2 method described in chapter 4.)

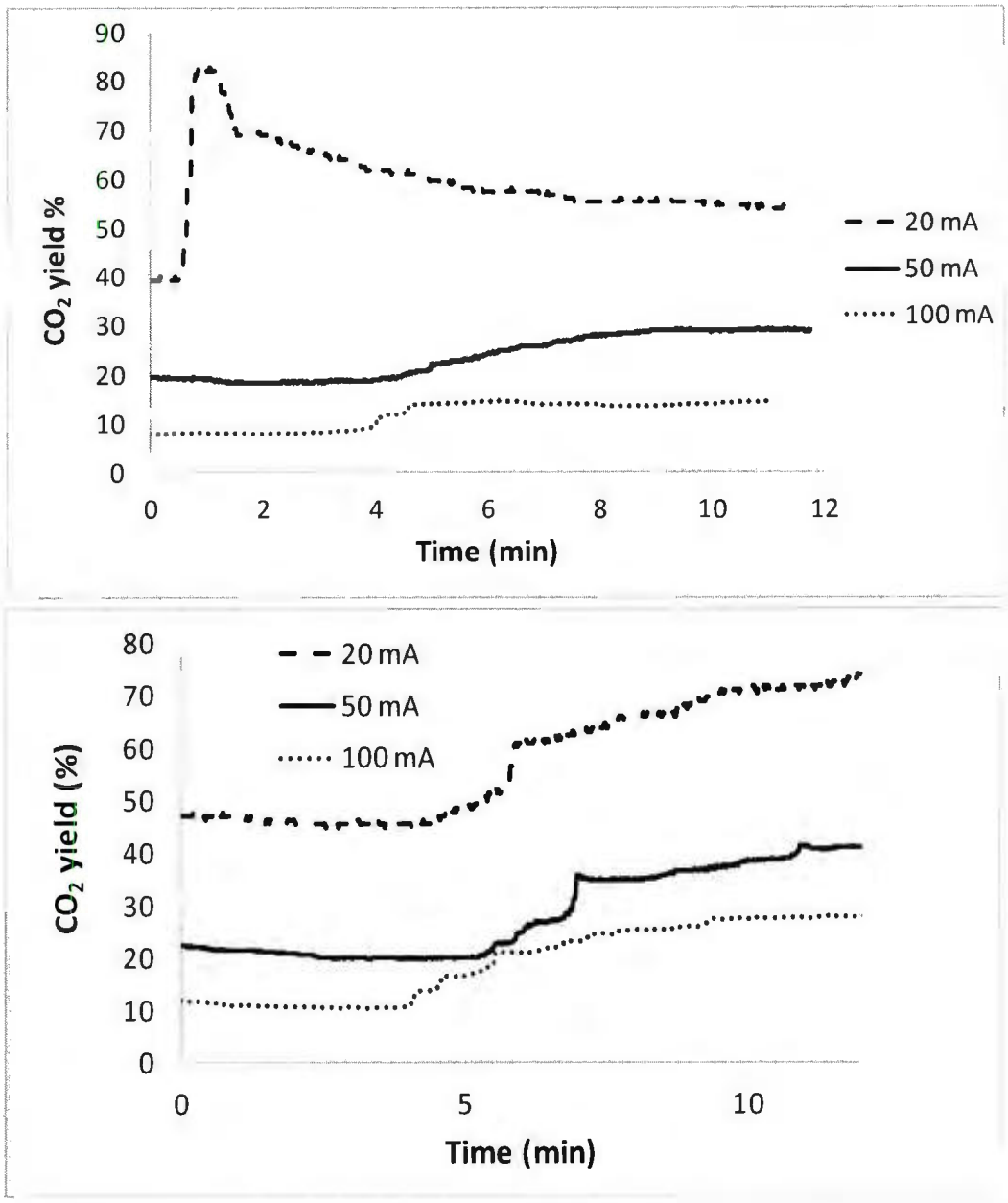

Figure D.2: CO_2 yield traces obtained from the oxidation of 0.5 mol L^{-1} acetaldehyde at 60 °C (top) and 80 °C (bottom). (All background CO_2 readings were corrected for using the pure CO_2 method described in chapter 4.)

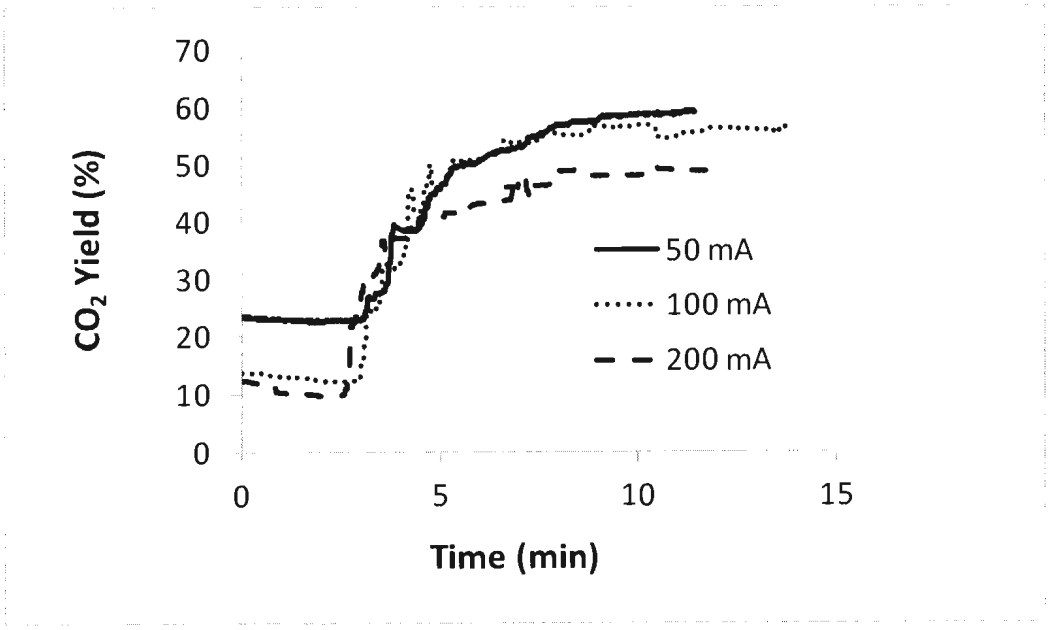

Figure D.3: CO_2 yield traces obtained from the oxidation of 0.5 mol L^{-1} acetaldehyde at 100 °C. (All background CO_2 readings were corrected for using the pure CO_2 method described in chapter 4.)

APPENDIX E

EDX Spectra

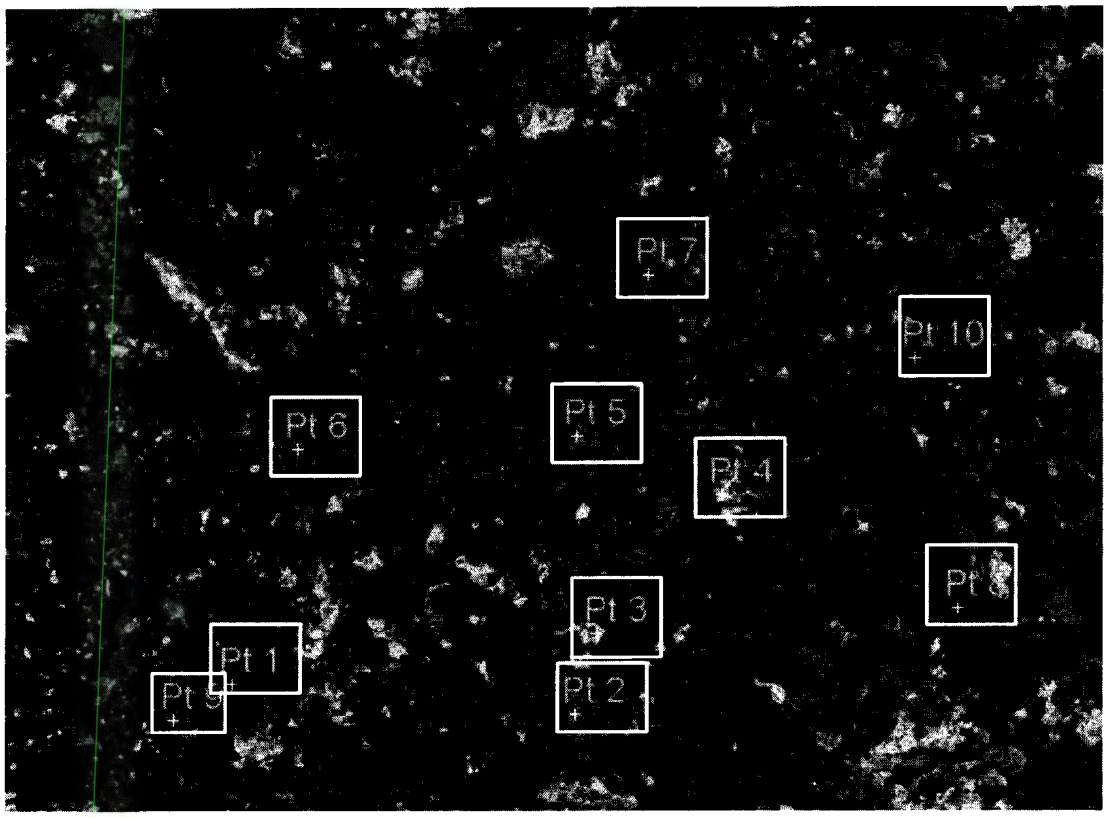

Figure E.1: SEM image for Pt-$RuSnO_2$/C (M1) catalyst surface for multi-point EDX analysis in designated areas on image (points 1-10).

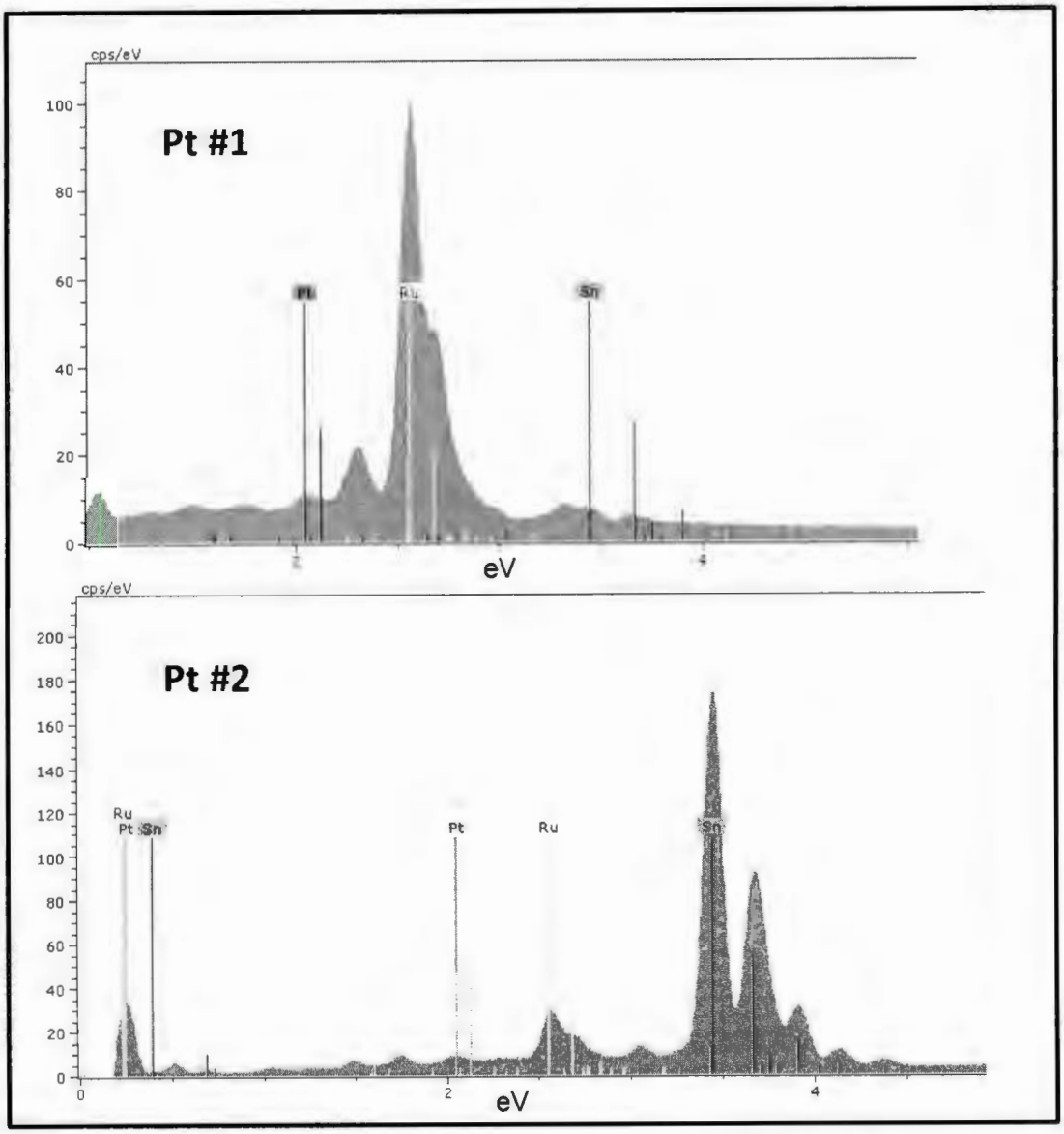

Figure E.2: EDX spectra for points #1 and 2 of Figure E.1.

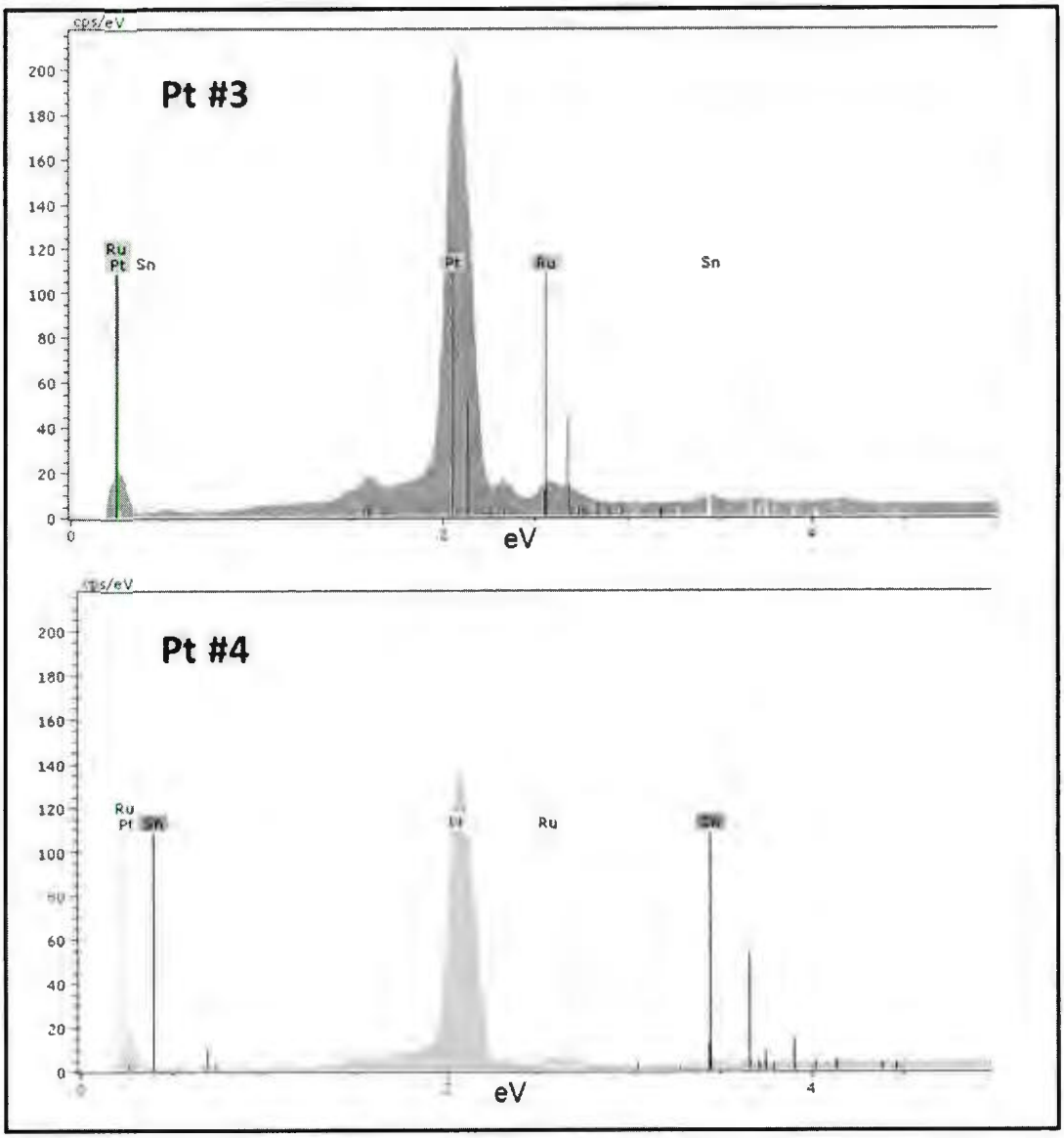

Figure E.3: EDX spectra for points #3 and 4 of Figure E.1.

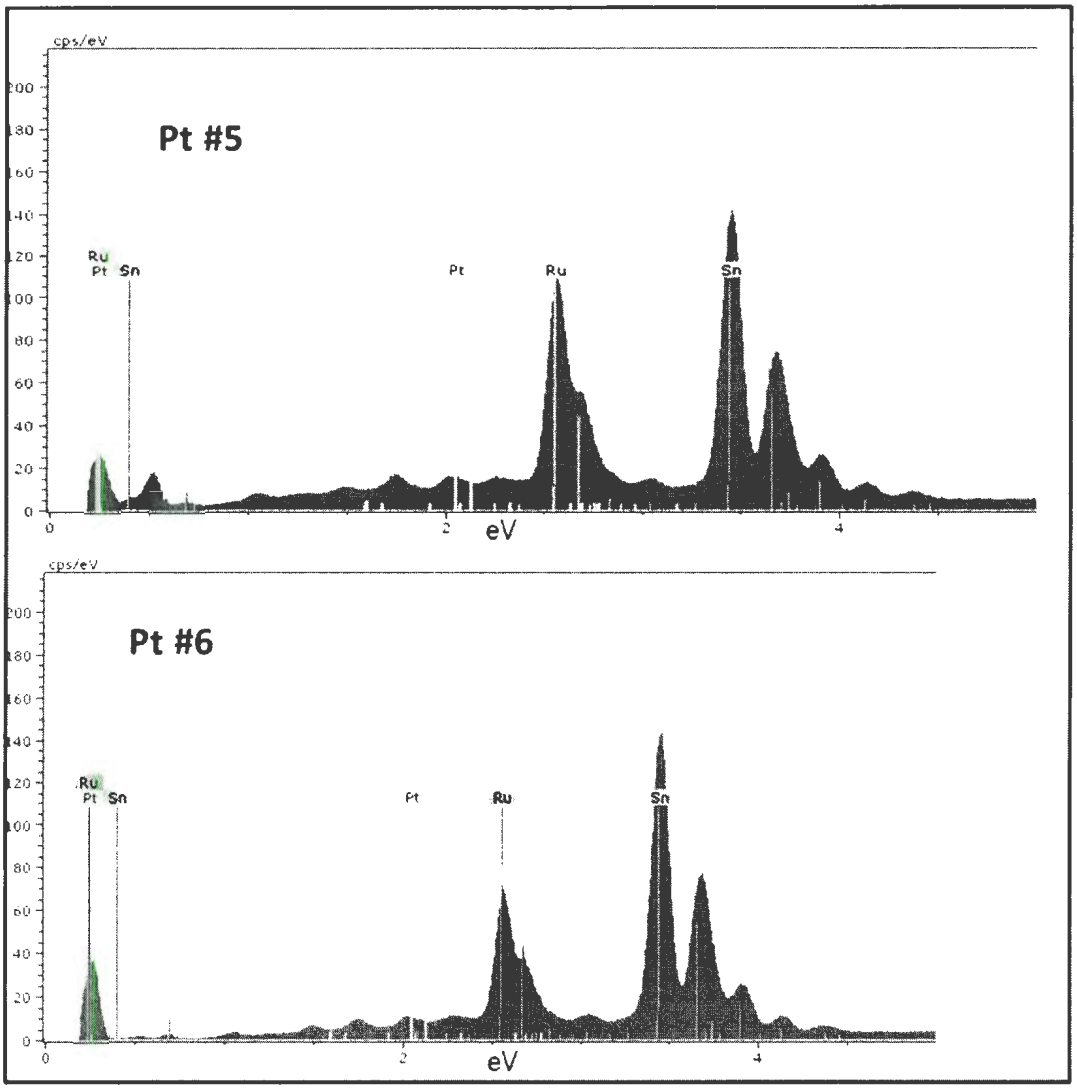

Figure E.4: EDX spectra for points #5 and 6 of Figure E.1.

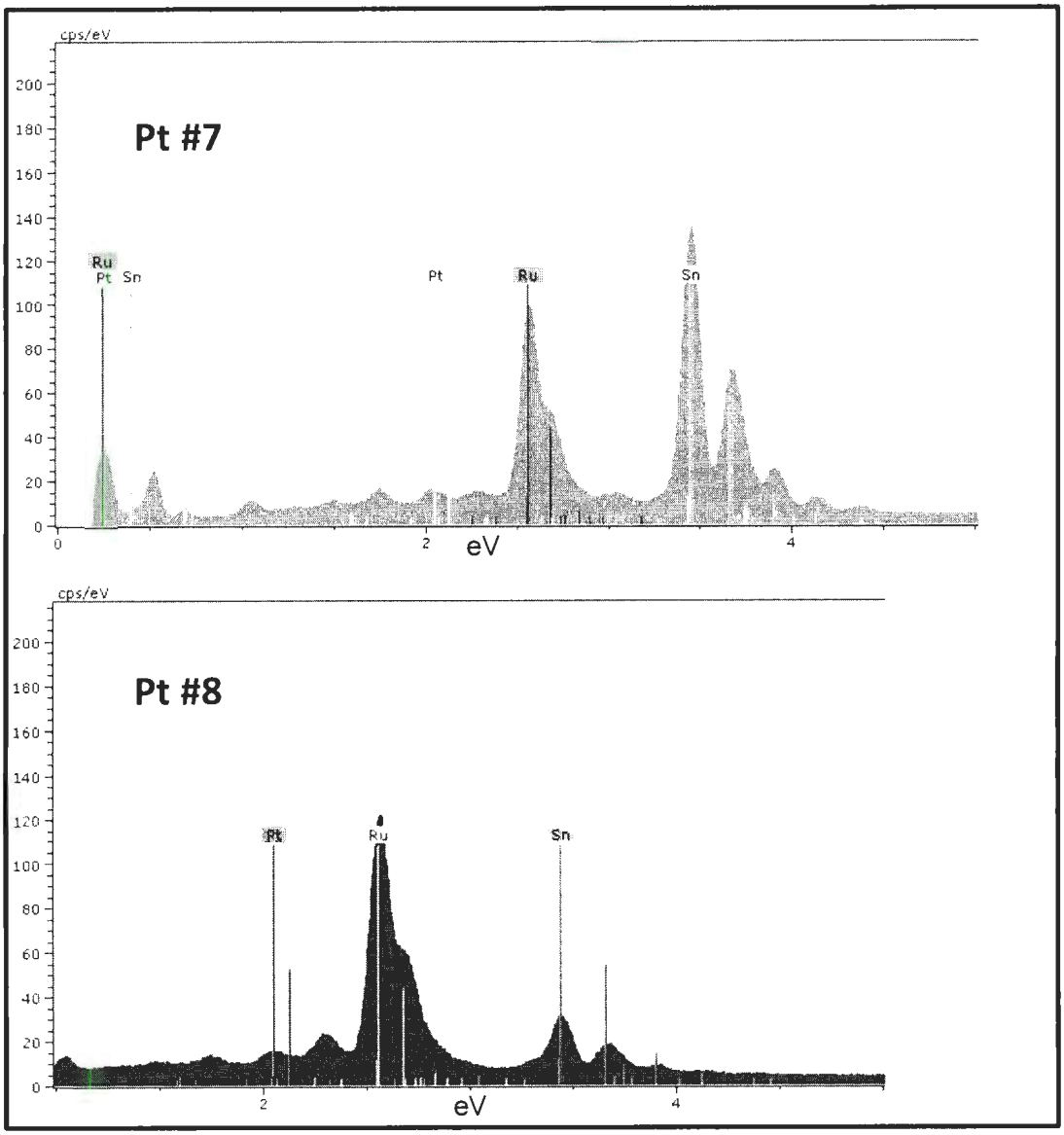

Figure E.5: EDX spectra for points #7 and 8 of Figure E.1.

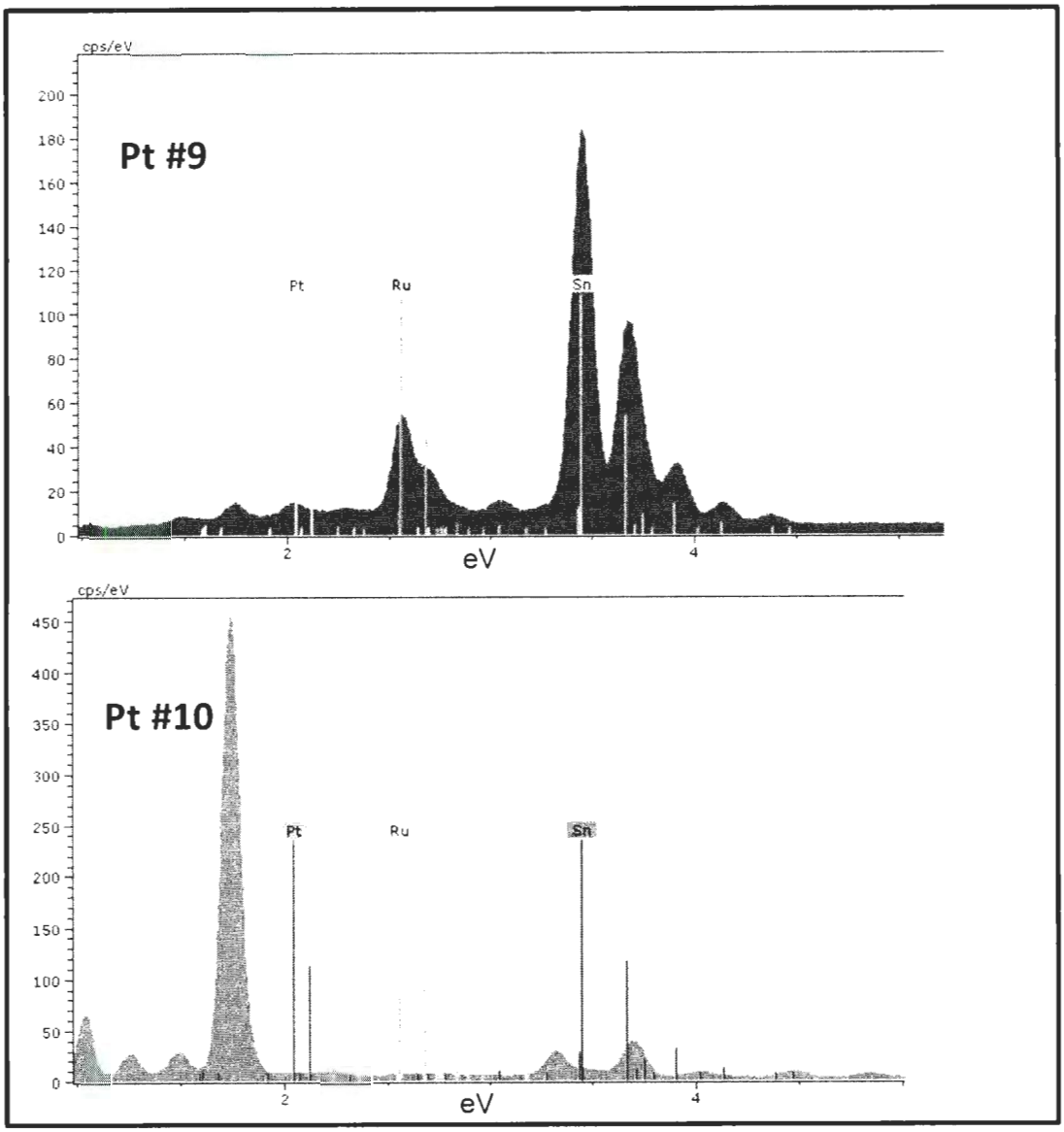

Figure E.6: EDX spectra for points #9 and 10 of Figure E.1.The large peak at ca. 1.75 eV was shown to be a silicon impurity in the sample.

APPENDIX F

TEM Images

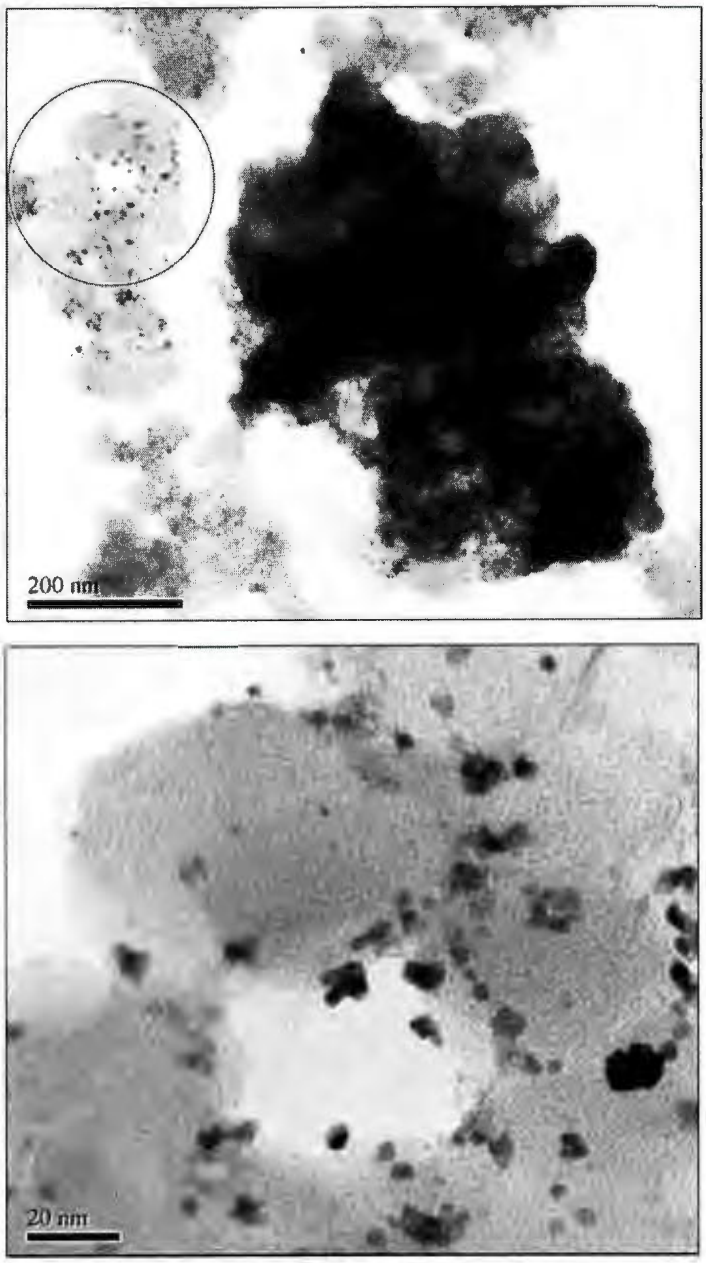

Figure F.1: TEM image of the Pt-$RuSnO_2$/C (M1) catalyst powder focusing in on the Ru and Sn particles.

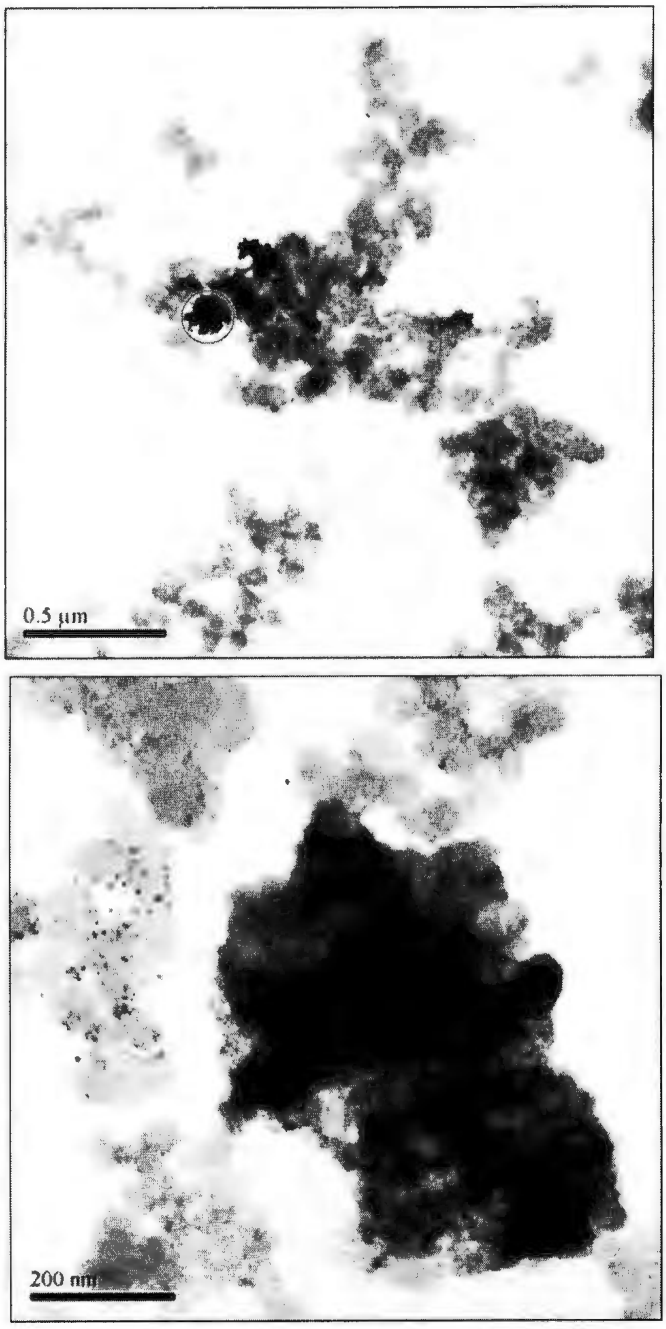

Figure F.2: TEM images of the Pt-$RuSnO_2$/C (M1) catalyst powder focusing on the Pt aggregates.

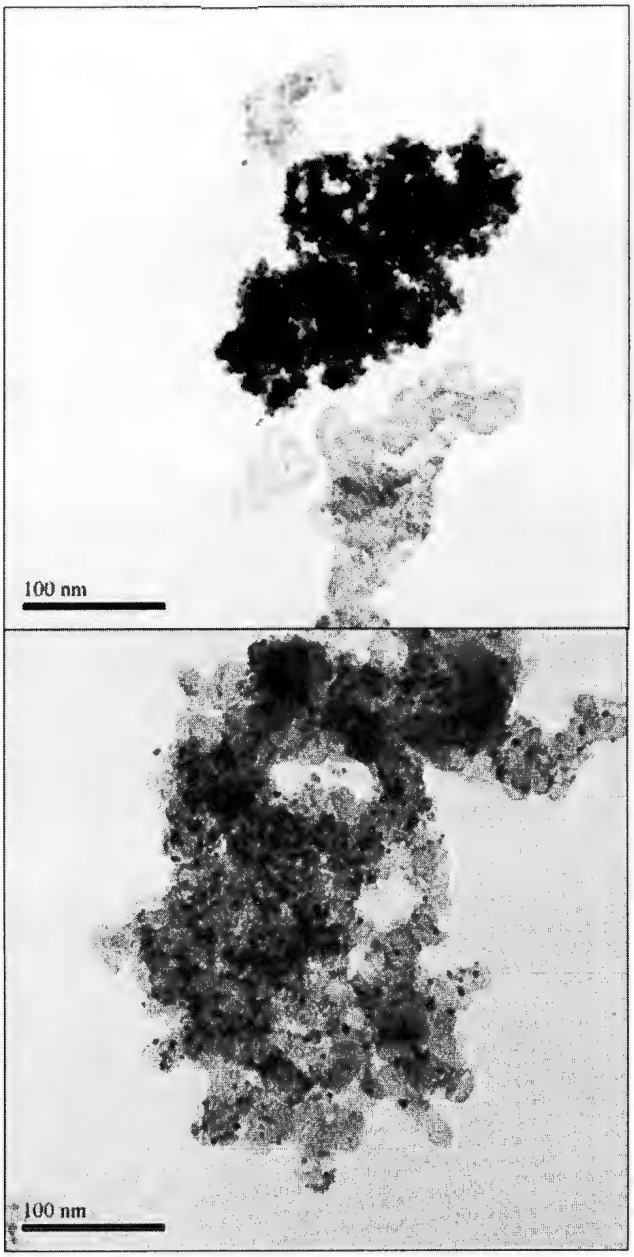

Figure F.3: TEM image of the Pt-$RuSnO_2$/C (M1) catalyst powder.

APPENDIX G

CO_2 Traces for Ballard, M1 and M2 Catalysts

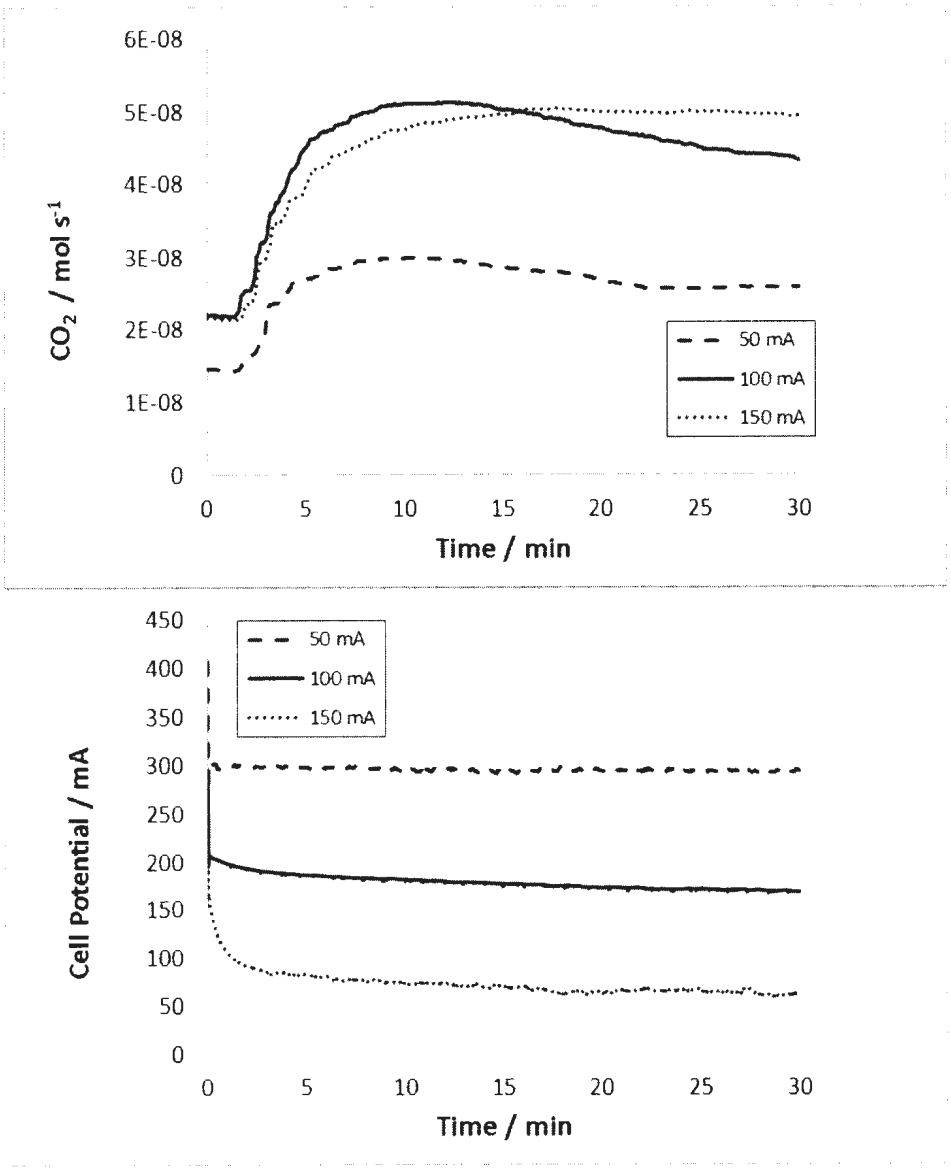

Figure G.1: CO_2 and potential traces for Pt Ballard electrode reported in Table 6.3.

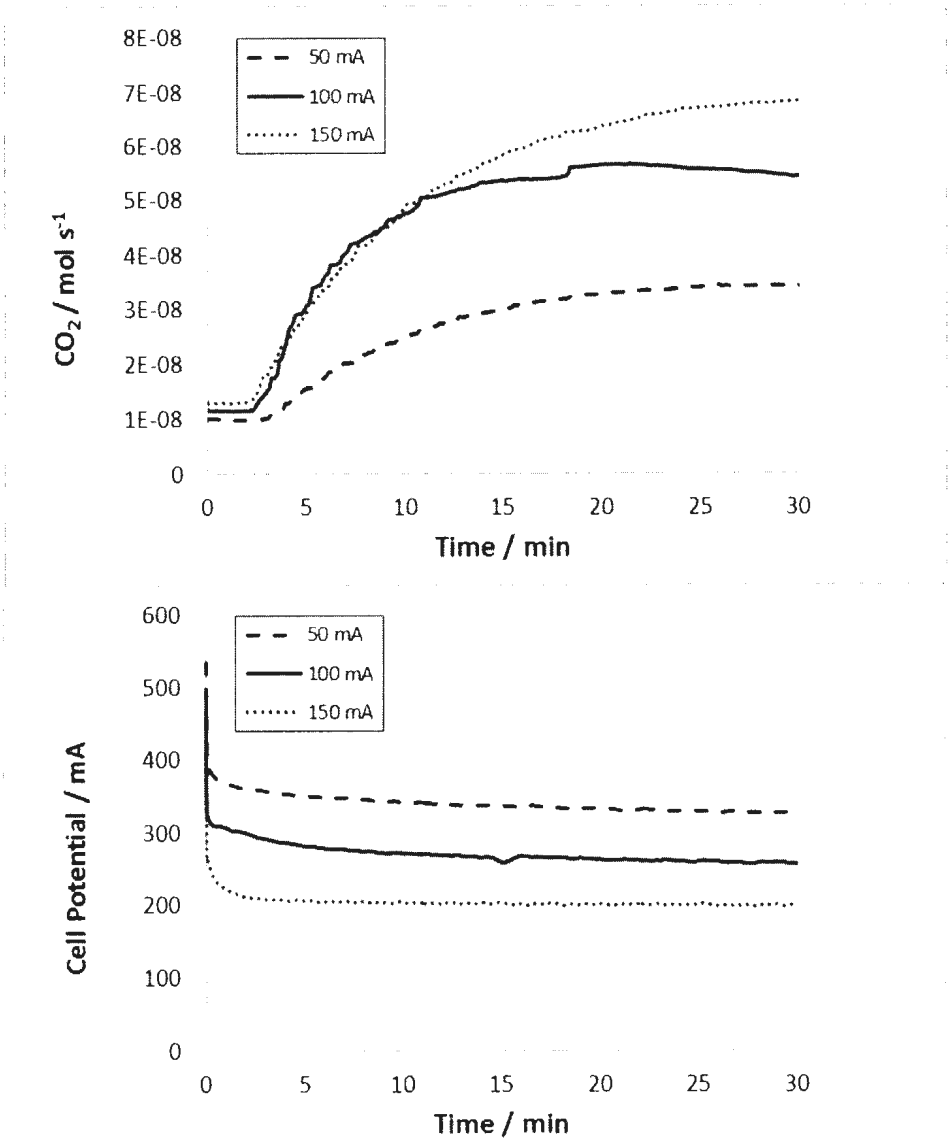

Figure G.2: CO_2 and potential traces for Pt-$RuSnO_2$/C (M1) electrode reported in Table 6.3.

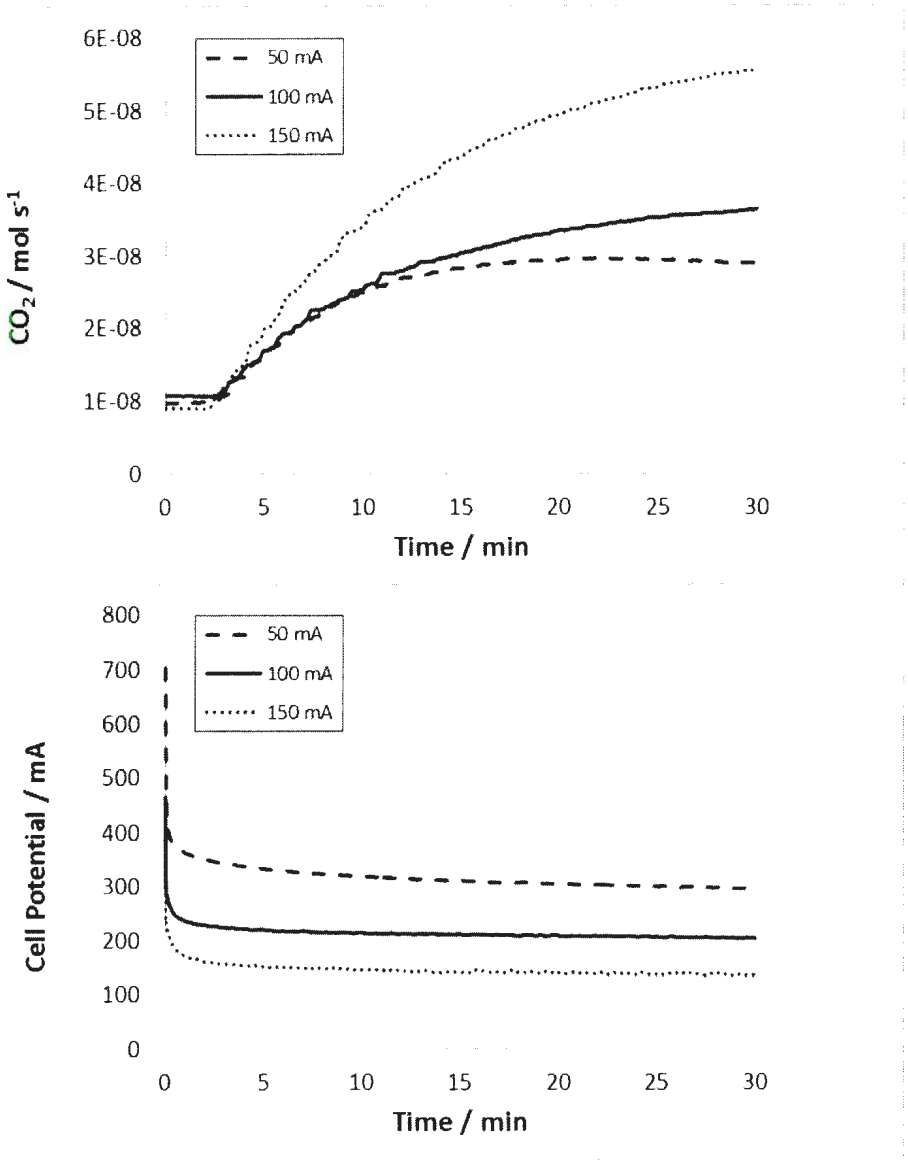

Figure G.3: CO_2 and potential traces for Pt-$RuSnO_2$/C (M2) electrode reported in Table 6.3.